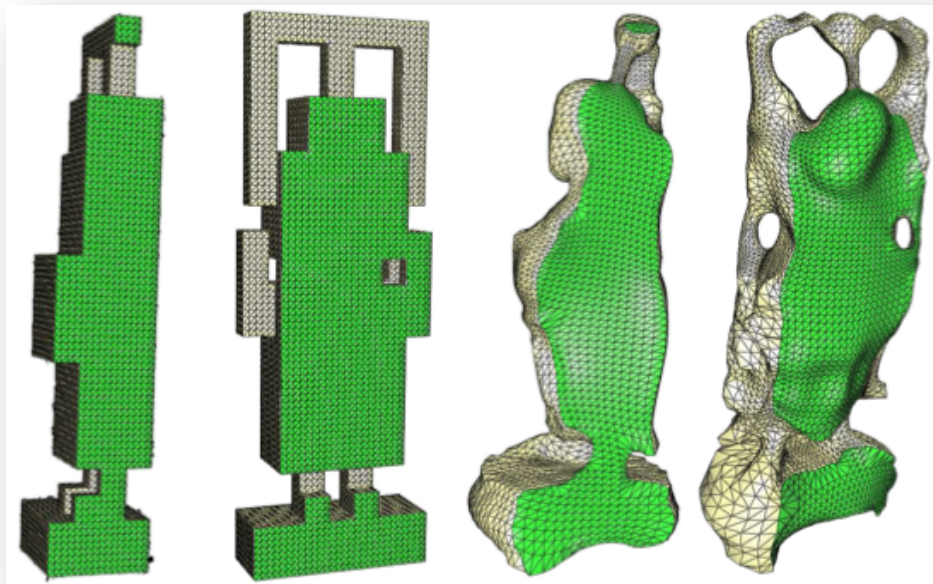**SIGGRAPH Asia 2014 – Course "An Introduction to Ricci Flow and Volumetric Approximation with Applications to Shape Modeling"**

G. Patanè (CNR-IMATI, Italy), X.S. Li (Lousiana State Univ., USA), X.D. Gu (Stony Brook Univ., USA)

Table of Contents

SIGGRAPH Asia 2014 – Course "An Introduction to Ricci Flow and Volumetric Approximation with Applications to Shape Modeling"

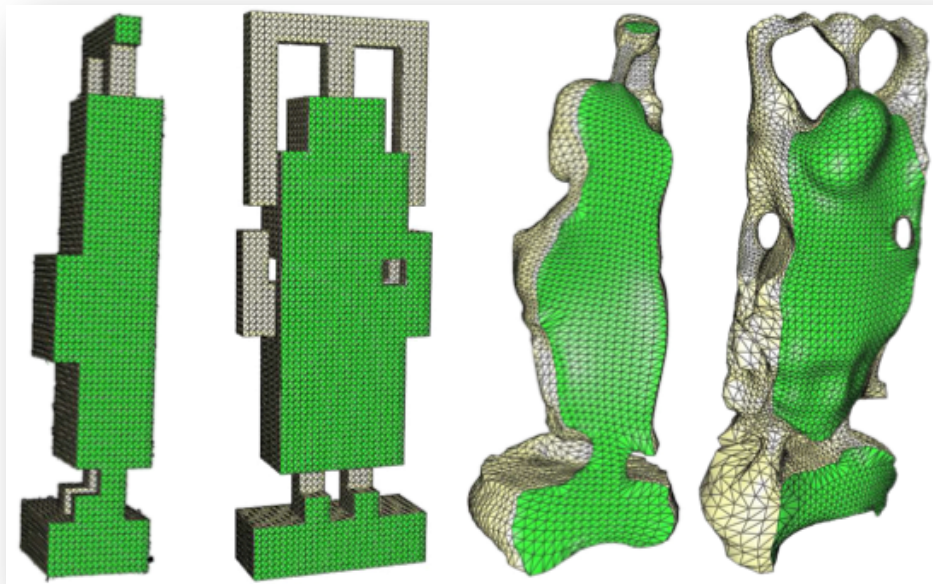G. Patanè (CNR-IMATI, Italy), X.S. Li (Lousiana State Univ., USA), X.D. Gu (Stony Brook Univ., USA)

Course Overview

SIGGRAPH Asia 2014 − Course Notes
An Introduction to Ricci Flow and Volumetric Approximation with Applications to Shape Modeling

Giuseppe Patané[*]   Xin Shane Li[†]   David Xianfeng Gu[‡]

Abstract

Extending a shape-driven map to the interior of the input shape and to the surrounding volume is a difficult problem since it typically relies on the integration of shape-based and volumetric information, together with smoothness conditions, interpolating constraints, preservation of feature values at both a local and global level. This survey discusses the main volumetric approximation schemes for both 3D shapes and d-dimensional data, and provides a unified discussion on the integration of surface-based and volume-based shape information. Then, it describes the application of shape-based and volumetric techniques to shape modeling through volumetric parameterization and polycube splines; feature-driven approximation through kernels and radial basis functions. We also discuss the Hamilton's Ricci flow, which is a powerful tool to compute the conformal shape structure and to design Riemannian metrics of manifolds by prescribed curvatures. We conclude the presentation by discussing applications to shape analysis and medicine.

Keywords: Riemannian surface and metric; Ricci flow; conformal structure; Laplace-Beltrami operator; heat diffusion equation; implicit approximation; volume parameterization; shape modeling; medicine

1 Course description

Shape modeling typically handles a 3D shape as a two-dimensional surface, which describes the shape boundary and is represented as a triangular mesh or a point cloud. However, in several applications a volumetric representation is more suited to handle the complexity of the input shape. For instance, volumetric representations accurately model the behavior of non-rigid deformations and volume constraints are imposed to avoid deformation artifacts. In shape matching, volumetric descriptors, such as Laplacian eigenfunctions, heat kernels, and diffusion distances, are defined starting from their surface-based counterparts.

In the aforementioned applications, the underlying problem requires the prolongation of the surface-based information, which is typically represented as a shape-driven map, to the interior of the input shape or, more generally, to the surrounding volume. Extending a surface-based scalar function to a volumetric map is a difficult problem since it typically relies on the integration of shape-based and volumetric information, together with smoothness conditions, interpolating constraints, preservation of features at both a local and global level. Besides the underlying complexity and degrees of freedom in the definition of volumetric approximations of surface-based maps, *volumetric approximations* (e.g., the extension of a surface-based scalar function to a volume-based approximation) are

essential to address a wide range of problems. For instance, volumetric Laplacian eigenfunctions are suited to define volumetric descriptors, which are consistent with their surface-based counterparts. In a similar way, harmonic volumetric functions have been applied to volumetric parameterization and to the definition of polycube splines.

This survey discusses the main volumetric approximation schemes for both 3D shapes and d-dimensional data, and provides a unified discussion on the integration of surface-based and volume-based shape information. It also describes the application of shape-based and volumetric techniques to shape processing with volumetric parameterization and to the feature-driven approximation with moving least-squares techniques and radial basis functions. While previous work has addressed the processing and analysis of 3D shapes through methods that exploit either their surface-based or volumetric representations, this survey presents a unified overview on these works through volumetric approximations of surface-based scalar functions. This unified scheme also provides a basis for generalizing those methods that have been primarily defined on surfaces but are open to and benefit of the integration with volumetric information. Furthermore, it systematically presents the theory, algorithm, and applications of discrete Ricci flow. In the following, we provide a detailed description of the main parts of our contribution.

Part I − Introduction

We present the outline and the main aims of this course on spectral surface-based and volume-based techniques, and discrete curvature flow methods for shape modeling and analysis.

Part II − Differential operators and spaces for shape modeling

We start with an introduction to the spectral surface-based and volume-based techniques, and discrete curvature flow methods for shape modeling, together with a presentation of the background underlying the main spectral and curvature flow techniques for shape modeling. Key concepts from smooth geometry, such as Riemannian metric, Gaussian curvature, Laplace-Beltrami operator, heat diffusion equation, and Ricci flow are systematically introduced. We also present the main results on the convergence and the uniqueness of the solution to Ricci flow and the geometric approximation theorem. Starting from this background on the main differential properties of manifolds, we define and discuss the properties of the harmonic maps, the Laplacian eigenfunctions, and the solutions to the heat equation.

Part III − From surface-based to volume-based shape modeling

Using the concepts introduced in Part II, we address the volumetric approximation problem. After an overview on the aims of the volumetric approximation in the context of shape modeling and analysis, we classify the main approaches proposed by previous work and detail the following approximation schemes: (i) linear precision methods through generalized barycentric coordinates; (ii) im-

---

[*]Consiglio Nazionale delle Ricerche, Istituto di Matematica Applicata e Tecnologie Informatiche, Genova, Italy, `patane@ge.imati.cnr.it`

[†]Louisiana State University, School of Electrical Engineering & Computer Science, USA, `xinli@cct.lsu.edu`

[‡]State University of New York at Stony Brook, Department of Computer Science, New York, USA, `gu@cs.sunysb.edu`

plicit methods with radial basis functions; (iii) surface-based and cross-volume parameterization; (iv) polycube splines; (v) moving least squares techniques. More precisely, we introduce the computation of the inter-surface harmonic map, extend it to volumetric harmonic map, and construct the polycube shape parameterization and splines. Then, we discuss volumetric approximations through radial basis function with constraints on the approximation error and the preservation of the critical points.

Part IV − **Applications** & **Conclusions**

Once the continuous and discrete settings have been introduced, we focus on the main applications of the volumetric approximation to shape modeling and medicine. In the context of shape modeling, we outline how the Laplacian eigenvectors of a given surface are extended into the shape interior, thus providing the basis for the definition of shape-aware barycentric coordinates and of volumetric descriptors, such as the volumetric global point signature, biharmonic and diffusion embeddings, which have been primarily defined for the surface setting. We also present template-based shape descriptors and the computation of harmonic volumetric mappings between solid objects with the same topology for volumetric parameterization, solid texture mapping, and hexahedral remeshing. In the context of medicine, we discuss applications to respiratory motion modeling, medical and forensic skull modeling and facial reconstruction. Finally, we conclude the course with a discussion of open problems and future perspectives, also addressing questions and answers with all presenters.

2 Schedule

Part I − **Introduction** (10 *minutes*)

1. Outline and motivations (*10 minutes: D. Gu, G. Patanè*)

Part II − **Differential operators and spaces for shape modeling** (80 *minutes*)

1. Mappings on Riemann surfaces (*20 minutes: D. Gu*)

   - Riemannian metric, isothermal coordinates
   - Holomorphic differentials
   - Quasi-conformal mapping and Beltrami equation

2. Ricci flow (*30 minutes: D. Gu*)

   - Yamabe equation and convergence theorem of Ricci flow
   - Discrete Ricci flow, convergence, uniqueness
   - Discrete conformal mapping and metric deformation

3. Laplacian operator and spectral processing (*30 minutes: G. Patanè*)

   - Laplace-Beltrami operator on 3D shapes
   - Harmonic equation, Laplacian eigenproblem, and heat diffusion equation
   - Spectral distances and kernels: commute-time, biharmonic, and diffusion distances

Part III − **From surface-based to volume-based shape modeling** (70 *minutes*)

1. The volumetric approximation problem (*5 minutes: G. Patanè*)

   - Definition
   - Aims and motivations

2. Main approaches (*25 minutes: G. Patanè*)

   - Linear precision methods and generalized barycentric coordinates
   - Function approximation with radial basis functions
   - Moving least-squares approximation

   [Break (*15 minutes*)]

3. From cross-surface to cross-volume mapping (*40 minutes: X. Li*)

   - Cross-surface and cross-volume mapping
   - Volumetric harmonic mapping
   - Polycube parameterization

Part IV − **Applications** & **Conclusions** (50 *minutes*)

1. Applications to shape modeling and analysis (*20 minutes: D. Gu, G. Patanè*)

   - Surface-based and volume-based descriptors for shape correspondence and comparison
   - Volume preserving mappings between surfaces and image restoration

2. Applications to medicine (*20 minutes: D. Gu, X. Li*)

   - Motion modeling for radiotherapy planning
   - Skull and facial modeling and restoration
   - Conformal brain mapping and brain cortex analysis
   - Virtual colonoscopy

3. Conclusions, Questions & Answers (*10 minutes: G. Patanè, X. Li, D. Gu*)

3 Targeted audience and background

Intended audience   The target audience of this tutorial includes graduate students and researchers interested in Riemannian geometry, spectral geometry processing, and implicit modeling. Our goals are threefold: (i) to show the possibility of integrating shape-based and volume-based information; (ii) to introduce and discuss the fundamental results and its applications that are relevant to shape modeling and, more generally, computer graphics; (iii) to identify open problems and future work. The main topics cover volumetric parameterization and polycube splines; implicit modeling with radial basis functions and kernel methods; spectral shape analysis through descriptors and distances; discrete Ricci flow; applications to medicine. Several topics are of interest for a wider audience; among them, we mention shape correspondence, descriptors and comparison; shape driven scalar functions for shape and volume analysis.

Prerequisites Knowledge about differential geometry, mesh processing, function approximation.

Level of difficulty: Advanced course.

4 Course Rationale

Tutorial originality While previous tutorials have addressed the processing and analysis of 3D shapes through methods that exploit either their surface-based or volumetric representations, we will present a unified overview on these works through volumetric approximations of surface-based scalar functions. This unified scheme will also provide a basis for generalizing those methods that have been primarily defined on surfaces but are open to and benefit of the integration with volumetric information. Furthermore, it is the first tutorial that systematically presents the theory, algorithm, and applications of discrete Ricci flow. In the following, we provide a list of previous work on the topics that is related to this tutorial.

Related tutorials organized by the lecturers

(T1) SIGGRAPH Asia 2013 Course "*Surface-Based and Volume-Based Techniques for Shape Modeling and Analysis*" (G. Patanè, X.S. Li, X.D. Gu);

(T2) Shape Modeling International'2012 Tutorial "*Spectral, Curvature Flow Surface-Based and Volume-Based Techniques for Shape Modeling and Analysis*" (G. Patanè, X.D. Gu, X.S. Li, M. Spagnuolo);

(T3) Eurographics'2007 Tutorial "*3D shape description and matching based on properties of real functions*" (S. Biasotti, B. Falcidieno, P. Frosini, D. Giorgi, C. Landi, S. Marini, G. Patanè, M. Spagnuolo);

(T4) ICIAM'2007 Mini-Symposium "*Geometric-Topological Methods for 3D Shape Classification and Matching*" (M. Spagnuolo, G. Patanè);

(T5) SMI'2008 Mini-Symposium on "*Shape Understanding via Spectral Analysis Techniques*" (B. Levy, R. Zhang, M. Retuer, G. Patanè, M. Spagnuolo).

This course proposal revises and extends our T1 SIGGRAPH Asia 2013 Course "*Surface-Based and Volume-Based Techniques for Shape Modeling and Analysis*". According to recent results of the authors and the feedback to the previous course, additional material on (i) spectrum-free computation of the heat kernel and diffusion distances; (ii) applications to medicine have been included in the notes and slides of this new course proposal. Tutorial T2 addressed the main volumetric approximation schemes for both 3D shapes and n-dimensional data, and provides a unified discussion on the integration of surface-based and volume-based shape information. Tutorials T3 and T4 covered a variety of methods for 3D shape matching and retrieval, which are characterized by the use of a real-valued function defined on the shape to derive its signature. Tutorial T5 addressed spectral analysis for shape understanding and several applications, which include surface parameterization, deformation, compression, and non-rigid shape retrieval.

Related tutorials

(T6) SIGGRAPH'2013 Course "*Geometry Processing with Discrete Exterior Calculus* " (F. de Goes, K. Crane, M. Desbrun, P. Schroeder);

(T7) SIGGRAPH Asia'2010 "*Spectral Geometry Processing*" (B. Levy, R. H. Zhang);

(T8) Eurographics'2010 State if the Art Reports "*A Survey on Shape Correspondence* (O. van Kaick, R. H. Zhang, G. Hamarneh, D. Cohen-Or).

Course T6 focused on the discrete exterior calculus and its relation with digital geometry processing and discrete differential geometry. Tutorial T7 presented the main concepts behind spectral mesh processing on 3D shapes and its applications to filtering, shape matching, remeshing, segmentation, and parameterization. Tutorial T8 reviewed the main methods for the computation of the correspondences between geometric shapes.

5 Lecturers biographies

David Xiangfeng Gu

Affiliation	State Univ. of New York at Stony Brook
e-mail	gu@cs.stonybrook.edu
URL	http://www.cs.sunysb.edu/ gu/

David Gu is an associate professor in Computer Science department, Stony Brook University. He received a Ph.D. from Harvard university (2003), supervised by a Fields medalist, Prof. Shing-Tung Yau. His research focuses on computational conformal geometry, and its applications in graphics, vision, geometric modeling networks and medical imaging.

Xin Shane Li

Affiliation	Louisiana State University
e-mail	xinli@cct.lsu.edu
URL	http://www.ece.lsu.edu/xinli

Xin Li is an assistant professor in School of Electrical Engineering and Computer Science, Louisiana State University. He received his Ph.D. in Computer Science from Stony Brook University (SUNY) in 2008. His research focus is on geometric modeling and computing, and their applications in graphics, vision, medical imaging, and computational forensics.
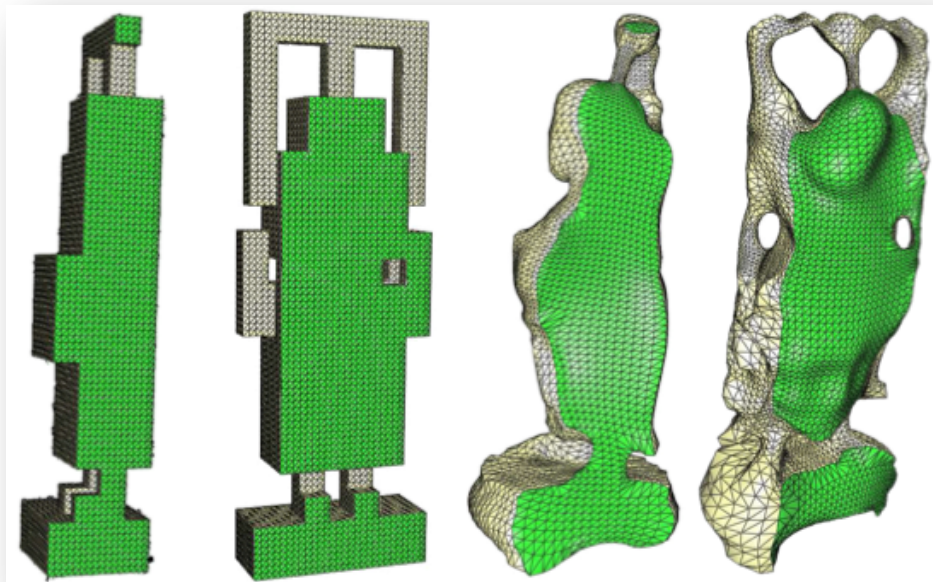
Giuseppe Patanè

Affiliation	CNR-IMATI, Genova, Italy
e-mail	patanel@ge.imati.cnr.it
URL	http://www.ge.imati.cnr.it

Giuseppe Patanè is researcher at CNR-IMATI (2001-today). He received a Ph.D. in "Mathematics and Applications" from the University of Genova (2005) and a Post Lauream Degree Master from the "F. Severi National Institute for Advanced Mathematics" (2000). From 2001, his research activities have been focused on the definition of paradigms and algorithms for modeling and analyzing digital shapes and multidimensional data.

SIGGRAPH Asia 2014 – Course "An Introduction to Ricci Flow and Volumetric Approximation with Applications to Shape Modeling"

G. Patanè (CNR-IMATI, Italy), X.S. Li (Lousiana State Univ., USA), X.D. Gu (Stony Brook Univ., USA)

Course Notes

Course Notes – Index

Contents

SIGGRAPH Asia 2014 − Course Notes
An Introduction to Ricci Flow and Volumetric Approximation with Applications to Shape Modeling

Giuseppe Patané* David Xianfeng Gu† Xin Shane Li‡

Abstract

Extending a shape-driven map to the interior of the input shape and to the surrounding volume is a difficult problem since it typically relies on the integration of shape-based and volumetric information, together with smoothness conditions, interpolating constraints, preservation of feature values at both a local and global level. This survey discusses the main volumetric approximation schemes for both 3D shapes and d-dimensional data, and provides a unified discussion on the integration of surface-based and volumetric shape information. Then, it describes the application of surface-based and volumetric techniques to shape modeling through volumetric parameterization and polycube splines; feature-driven approximation through kernels and radial basis functions. We also discuss the Hamilton's Ricci flow, which is a powerful tool to compute the conformal shape structure and to design Riemannian metrics of manifolds by prescribed curvatures. We conclude the presentation by discussing applications to shape analysis and medicine.

Keywords: Riemannian surface and metric; Ricci flow; conformal structure; Laplace-Beltrami operator; heat diffusion equation; implicit approximation; volume parameterization; shape modeling; medicine

1 Introduction

Shape modeling typically handles a 3D shape as a two-dimensional surface, which describes the shape boundary and is represented as a triangular mesh or a point cloud. However, in several applications a volumetric representation is more suited to handle the complexity of the input shape. For instance, volumetric representations accurately model the behavior of non-rigid deformations and volume constraints are imposed to avoid deformation artifacts. In shape matching, volumetric descriptors, such as Laplacian eigenfunctions, heat kernels, and diffusion distances, are defined starting from their surface-based counterparts.

In the aforementioned applications, the underlying problem requires the prolongation of the surface-based information, which is typically represented as a shape-driven map, to the interior of the input shape or, more generally, to the surrounding volume. Extending a surface-based scalar function to a volumetric map is a difficult problem since it typically relies on the integration of shape-based and volumetric information, together with smoothness conditions, interpolating constraints, preservation of features at both a local and global level. Besides the underlying complexity and degrees of freedom in the definition of volumetric approximations of surface-based maps, *volumetric approximations* (e.g., the extension of a surface-based scalar function to a volume-based approximation) are essential to address a wide range of problems. For instance, volumetric Laplacian eigenfunctions are suited to define volumetric descriptors, which are consistent with their surface-based counterparts. In a similar way, harmonic volumetric functions have been applied to volumetric parameterization and to the definition of polycube splines.

This survey discusses the main volumetric approximation schemes for both 3D shapes and d-dimensional data, and provides a unified discussion on the integration of surface-based and volumetric information. It also describes the application of shape-based and volumetric techniques to shape processing with volumetric parameterization and to the feature-driven approximation with moving least-squares techniques and radial basis functions. While previous work has addressed the processing and analysis of 3D shapes through methods that exploit either their surface-based or volumetric representations, this survey presents a unified overview on these works through volumetric approximations of surface-based scalar functions. This unified scheme also provides a basis for generalizing those methods that have been primarily defined on surfaces but are open to and benefit of the integration with volumetric information. Furthermore, it systematically presents the theory, algorithm, and applications of discrete Ricci flow. In the following, we provide a detailed description of the main parts of our contribution.

---

*Consiglio Nazionale delle Ricerche, Istituto di Matematica Applicata e Tecnologie Informatiche, Genova, Italy, `patane@ge.imati.cnr.it`

†State University of New York at Stony Brook, Department of Computer Science, New York, USA, `gu@cs.sunysb.edu`

‡Louisiana State University, School of Electrical Engineering & Computer Science, USA, `xinli@cct.lsu.edu`
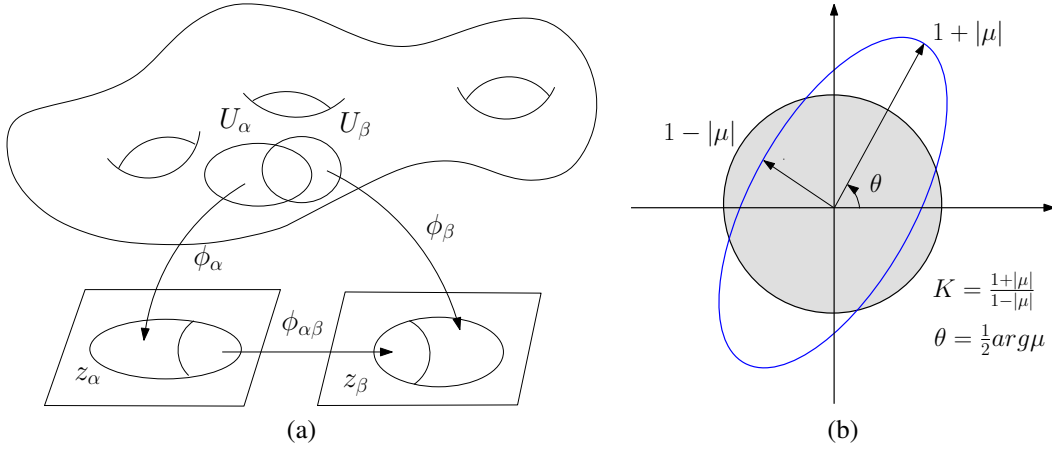
Figure 1: *(a) Riemann surface. All transitions $\phi_{\alpha\beta}$ are biholomorphic. (b) Beltrami coefficient.*

Outline and contribution We start with an introduction to the spectral surface-based and volumetric techniques, and discrete curvature flow methods for shape modeling, together with a presentation of the background underlying the main spectral and curvature flow techniques for shape modeling (Sect. 2). Key concepts from smooth geometry, such as Riemannian metric, Gaussian curvature, Laplace-Beltrami operator, heat diffusion equation, and Ricci flow are systematically introduced (Sect. 3). We also present the main results on the convergence and the uniqueness of the solution to Ricci flow and the geometric approximation theorem. Starting from this background on the main differential properties of manifolds, we define and discuss the properties of the harmonic maps, the Laplacian eigenfunctions, and the solutions to the heat equation.

After an overview on the aims of the volumetric approximation in the context of shape modeling and analysis, we classify the main approaches proposed by previous work and detail the following approximation schemes (Sect. 4): (i) linear precision methods through generalized barycentric coordinates; (ii) implicit methods with radial basis functions; (iii) surface-based and cross-volume parameterization; (iv) polycube splines; (v) moving least squares techniques; (vi) and topology-driven approximation. More precisely, we introduce the computation of the inter-surface harmonic map, extend it to volumetric harmonic map, and construct the polycube shape parameterization and splines. Then, we discuss volumetric approximations through radial basis function with constraints on the approximation error and the preservation of the critical points.

Once the continuous and discrete settings have been introduced, we focus on the main applications of the volumetric approximation to shape modeling and medicine (Sect. 5). In the context of shape modeling, we outline how the Laplacian eigenvectors of a given surface are extended into the shape interior, thus providing the basis for the definition of shape-aware barycentric coordinates and of volumetric descriptors, such as the volumetric global point signature, biharmonic and diffusion embeddings, which have been primarily defined for the surface setting. We also present template-based shape descriptors and the computation of harmonic volumetric mappings between solid objects with the same topology for volumetric parameterization, solid texture mapping, and hexahedral remeshing. In the context of medicine, we discuss applications to respiratory motion modeling, medical and forensic skull modeling and facial reconstruction. Finally (Sect. 6), we conclude the presentation by discussing open problems and future perspectives.

2 Riemann surfaces and Ricci flow

Firstly, we introduce mappings on Riemann surfaces, and quasi-conformal mapping and Teichmuller spaces (Sect. 2.1). Then, we discuss the surface Ricci flow and its discretization (Sect. 2.2).

2.1 Mappings on Riemann Surfaces

Suppose $\mathcal{N}$ be a differential manifold of dimension n. A *Riemannian metric* on $\mathcal{N}$ is a family of inner products $\mathbf{g_p} : T_\mathbf{p}\mathcal{N} \times T_\mathbf{p}\mathcal{N} \to \mathbb{R}$, $\mathbf{p} \in \mathcal{N}$, such that, for all differentiable vector fields X, Y on $\mathcal{N}$, $\mathbf{p} \to \mathbf{g_p}(X(\mathbf{p}), Y(\mathbf{p}))$ defines a smooth surface $\mathcal{N} \to \mathbb{R}$. Selecting a set of local coordinates $(x^1, x^2, \cdots, x^n)$, the metric tensor can be written as $\mathbf{g} = \sum_{i,j} g_{ij} dx^i dx^j$. Considering the differential map $f : (\mathcal{M}, \mathbf{g}) \to (\mathcal{N}, \mathbf{h})$ between two Riemannian manifolds, the *pull back* metric on $\mathcal{M}$ induced by f is given by $f^*\mathbf{h} = J^T \mathbf{h} J$, where $J = (\frac{\partial y^i}{\partial x^j})$ is the Jacobian matrix of f. Surfaces are examples of 2 dimensional manifolds.
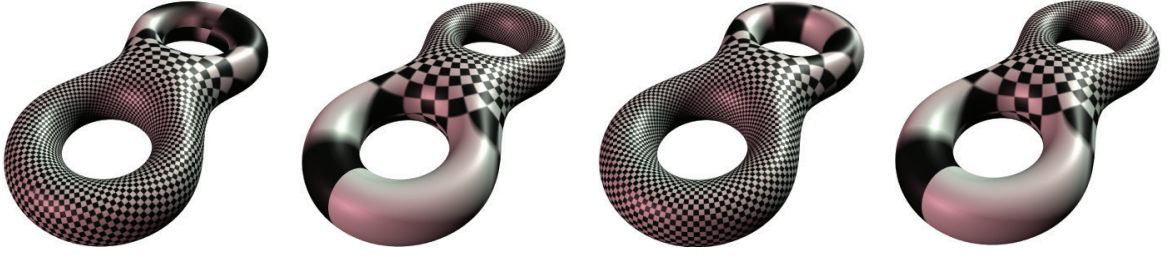
Figure 2: *Holomorphic 1-form basis on a genus two surface.*

Suppose $\mathcal{N}$ is an orientable surface embedded in $\mathbb{E}^3$ and $\mathbf{g}$ the induced Euclidean metric; let (x, y) be the local parameters of the metric surface $(\mathcal{N}, \mathbf{g})$. If the Riemannian metric has the local representation $\mathbf{g} = e^{2\lambda(x,y)}(dx^2 + dy^2)$, then (x, y) is called *isothermal coordinates* of the surface. In particular, $\lambda : \mathcal{N} \to \mathbb{R}$ is called the *conformal factor*. The following theorem shows the existence of isothermal coordinates [Chern 1955].

Theorem 2.1 *Suppose $(\mathcal{N}, \mathbf{g})$ is a smooth oriented metric surface, then for each point $\mathbf{p}$ there exists a neighborhood $U(\mathbf{p})$ of $\mathbf{p}$ such that local coordinates exist on $U(\mathbf{p})$.*

Through the isothermal coordinates, we introduce the Gaussian coordinates as follows. Let $(\mathcal{N}, \mathbf{g})$ be an oriented surface with a Riemannian metric and (u, v) an isothermal coordinates. Then, the *Gaussian curvature* of the surface is given by

$$K(u, v) = -\Delta_{\mathbf{g}}\lambda, \quad \Delta_{\mathbf{g}} = e^{-2\lambda(u,v)}\left(\frac{\partial^2}{\partial u^2} + \frac{\partial^2}{\partial v^2}\right),$$

where $\Delta_{\mathbf{g}}$ is the Laplace-Beltrami operator induced by $\mathbf{g}$. The Gauss curvature is intrinsic to the Riemannian metric and the total curvature is a topological invariant. According to the Gauss-Bonnet theorem [Schoen and Yau 1994; DoCarmo 1976], the total Gaussian curvature is given by

$$\int_{\mathcal{N}} K dA + \int_{\partial\mathcal{N}} k_{\mathbf{g}} ds = 2\pi\chi(\mathcal{N}),$$

where $\chi(\mathcal{N})$ is the Euler number of the surface, $k_{\mathbf{g}}$ is the geodesic curvature on the boundary, and $\partial\mathcal{N}$ is the boundary of the surface.

Holomorphic Differentials We now introduce holomorphic 1-forms on Reimannian surfaces. Suppose $f : \hat{\mathbb{C}} \to \hat{\mathbb{C}}$ be a complex function, where $\hat{\mathbb{C}} = \mathbb{C} \cup \{\infty\}$ is the extended complex plane. Defining the complex differential operators,

$$\frac{\partial}{\partial z} = \frac{1}{2}\left(\frac{\partial}{\partial x} - i\frac{\partial}{\partial y}\right), \qquad \frac{\partial}{\partial\bar{z}} = \frac{1}{2}\left(\frac{\partial}{\partial x} + i\frac{\partial}{\partial y}\right),$$

the function f is called *holomorphic* if $\frac{\partial f}{\partial\bar{z}} = 0$ everywhere. If f is invertible and f^{-1} is also holomorphic, then f is called *bi-holomorphic*. If f is treated as a mapping between complex planes, then holomorphic functions are *angle-preserving*, namely, *conformal*.

Suppose $\mathcal{N}$ is a topological surface, with an atlas $\{(U_k, \phi_k)\}$, where $\phi_k : U_k \to \mathbb{C}$ is a local complex coordinate chart. If all the local coordinate transitions (Fig. 1(a))

$$\phi_{ij} = \phi_j \circ \phi_i^{-1} : \phi_i(U_i \cap U_j) \to \phi_j(U_i \cap U_j),$$

are bi-holomorphic, then the atlas is called a *conformal atlas* and the surface $\mathcal{N}$ is called a *Riemann surface*. We recall that all oriented metric surfaces are Riemann surfaces.

Suppose $(\mathcal{N}, \mathbf{g})$ is an oriented surface with a Riemannian metric, the atlas formed by local isothermal coordinate charts is a conformal structure. Hence, all oriented metric surfaces are Riemann surfaces, their Riemannian metrics induce conformal structures. A *holomorphic 1-form* on a Riemann surface $\mathcal{N}$ is an assignment of a function $\phi_i(z_i)$ on each chart z_i such that if z_j is another local coordinate, then $\phi_i(z_i) = \phi_j(z_j)\left(\frac{dz_j}{dz_i}\right)$. All holomorphic 1-forms form a group with $2g$ real dimension, denoted as $\Omega(\mathcal{N})$, where g is the genus of $\mathcal{N}$. Fig. 2 shows the basis of holomorphic 1-forms on a genus two surface. A holomorphic 1-form can be decomposed to two real harmonic 1-forms. According to Hodge theory [Schoen and Yau 1997],

Figure 3: *(a) Conformal mapping versus (b) quasi-conformal mapping.*

each cohomological class of the surface has a unique harmonic 1-form. This property leads to the computational algorithm described in [Jin et al. 2004].

Quasi-conformal mapping and Beltrami equation Suppose $(\mathcal{N}_k, \mathbf{g}_k)$, $k = 1, 2$, are orientable surfaces with Riemannian metrics. A diffeomorphism $f : (\mathcal{N}_1, \mathbf{g}_1) \to (\mathcal{N}_2, \mathbf{g}_2)$ is *conformal*, if the pull back metric $f^*\mathbf{g}_2$ induced by f differs the original metric $\mathbf{g}_1$ by a scalar function $f^*\mathbf{g}_2 = e^{2\lambda}\mathbf{g}_1$, where $e^{2\lambda}$ is the conformal factor. Geometrically, a conformal mapping is *angle-preserving* and maps infinitesimal circles on the source to infinitesimal circles on the target. In contrast, general diffeomorphisms transforms infinitesimal circles to infinitesimal ellipses. Fig. 3 illustrates a conformal mapping and a quasiconformal mapping for a human face surface.

A generalization of conformal maps is the *quasi-conformal maps*, which are orientation preserving homeomorphisms between Riemann surfaces with bounded conformality distortion, in the sense that their first order approximations takes small circles to small ellipses of bounded eccentricity. Mathematically, $f : \mathbb{C} \to \mathbb{C}$ is quasiconformal such that it satisfies the Beltrami equation

$$\frac{\partial f}{\partial \bar{z}} = \mu(z)\frac{\partial f}{\partial z}, \tag{1}$$

for some complex-valued function μ satisfying $\|\mu\|_\infty < 1$. The term μ is called the *Beltrami coefficient*, which is a measure of non-conformality. It measures how far the map at each point is deviated from a conformal map. In particular, the map f is conformal around a small neighborhood of $\mathbf{p}$ when $\mu(\mathbf{p}) = 0$. Conventional Riemann mapping theorem can be generalized to quasi-conformal mappings.

Theorem 2.2 (Measurable Riemann Mapping) *Let $f : \hat{\mathbb{C}} \to \hat{\mathbb{C}}$, further more f fixes three points $\{0, 1, \infty\}$. Suppose $\mu : \hat{\mathbb{C}} \to \mathbb{R}$ be a measurable function, $\|\mu\|_\infty < 1$, then the solution to the Beltrami equation (1) uniquely exists.*

Computational algorithms for solving Beltrami equation can be found in [Zeng et al. 2009b]. As shown in Fig. 1(b), the orientation of the ellipse is the double of the argument of μ, the *dilation* of the map is defined as the ratio between the major axis and the minor axis of the infinitesimal ellipse. The maximal dilation of f is given by

$$K_f = \frac{1 + \|\mu\|_\infty}{1 - \|\mu\|_\infty}.$$

A homeomorphism whose dilation is less than K is called a K-quasiconformal mapping. Let μ, σ, and τ be the Beltrami coefficients of quasiconformal maps f^μ, f^σ, and f^τ with $f^\tau = f^\sigma \circ (f^\mu)^{-1}$, then

$$\tau = \left(\frac{\sigma - \mu}{1 - \bar{\mu}\sigma}\frac{1}{\theta}\right) \circ (f^\mu)^{-1},$$

where $p = \frac{\partial}{\partial z}f^\mu(z)$ and $\theta = \bar{p}/p$. For diffeomorphisms between Riemann surfaces, the concept of Beltrami coefficient needs to be replaced by *Beltrami differential* with local representation $\mu\frac{d\bar{z}}{dz}$.

The space of all Beltrami differential on a Riemann surface $\mathcal{N}$ is denoted as $B(\mathcal{N})$. The space of Beltrami differential $B(\mathcal{N})$ is one representation of the mapping spaces between two Riemann surfaces. Given two Beltrami differentials μ and ν, $\|\mu\|_\infty < 1$, $\|\nu\|_\infty < 1$, denote their respective normalized Beltrami equation solutions as $f^\mu : \mathcal{S} \to \mathcal{N}_1$ and $f^\nu : \mathcal{N} \to \mathcal{N}_2$. Then, the differentials are called *globally equivalent* if $\mathcal{N}_1 = \mathcal{N}_2$, and the identity map of $\mathcal{N}_2$ is homotopic to $f^\nu \circ (f^\mu)^{-1}$ via a homotopy consisting of quasiconformal homeomorphisms. The Beltrami differentials globally equivalent to zero are called *global trivial differentials* and denoted as $N(\mathcal{N}) := \{\mu \in B(\mathcal{N}) | \mu \sim 0\}$.
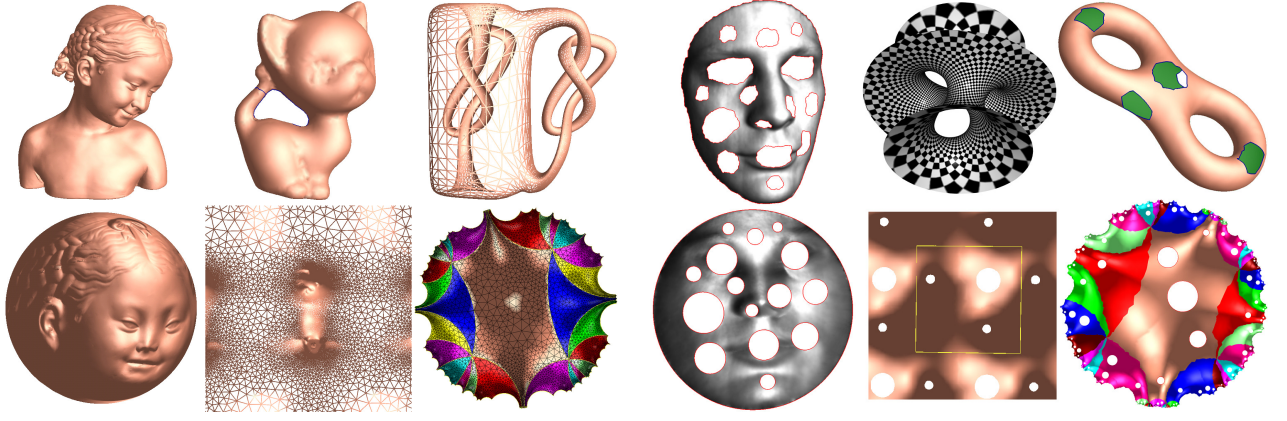
Figure 4: *Surface uniformization induced by Ricci flow.*

Teichmüller Space Let $\mathcal{N}$ be a topological surface of genus g with b boundaries, two Riemannian metrics $\mathbf{g}_1$ and $\mathbf{g}_2$ on $\mathcal{N}$ are Teichmüller equivalent $\mathbf{g}_1 \sim \mathbf{g}_2$ if there exists a conformal mapping $f : (\mathcal{N}, \mathbf{g}_1) \to (\mathcal{N}, \mathbf{g}_2)$. Furthermore, f is homotopic to the identity map. The Teichmüller space $T^{g,b}$ is formed by the equivalence classes of Riemannian metrics,

$$T^{g,b} := \{\text{all Riemannian metrics on } \mathcal{N}\}/\sim .$$

Equivalently, all Riemann surfaces of genus g with b boundaries can be classified by conformal equivalence. Two Riemann surfaces are conformally equivalent if there exists a conformal mapping between them. All conformal equivalence classes form the *Moduli Space*. The universal covering space of the Moduli space is the Teichmüller space. Holomorphic quadratic differentials $Q(\mathcal{N})$ can be treated as the tangent space of Teichmüller space.

Suppose μ is a Beltrami differential on a Riemann surface $\mathcal{N}$, on each local chart z_i of $\mathcal{N}$, μ has the local representation μ_i, then the solution to the Beltrami equation $\partial_{\bar{z}} \zeta_i = \mu_i \partial_z \zeta_i$ exists. Then, the collection of local charts $\{\zeta_i\}$ form another conformal structure of $\mathcal{N}$. Namely, μ deforms the Riemann surface $(\mathcal{N}, \{z_i\})$ to another $(\mathcal{N}, \{\zeta_i\})$. If μ_1 and μ_2 differ by a global trivial Beltrami differential, then they deform $\mathcal{N}$ to the same Riemann surface. Therefore, the Teichmüller space can be represented as the quotient space $T(\mathcal{N}) = B(\mathcal{N})/N(\mathcal{N})$. Teichmüller space is a Riemannian manifold and the Riemannian metric is given by the Teichmüller map. The computational algorithm for finding the Teichmüller coordinates for a given surface is explained in [Jin et al. 2009b].

2.2 Surface Ricci flow

Suppose $\bar{\mathbf{g}} = e^{2\lambda}\mathbf{g}$ is a conformal metric on the surface, then Gaussian curvatures induced by $\mathbf{g}$ and $\bar{\mathbf{g}}$ are K and $\bar{K}$ respectively, then the so-called Yamabe equation is given by $\bar{K} = e^{-2\lambda}(-\Delta_{\mathbf{g}}\lambda + K)$; similarly, the geodesic curvatures are given by $\bar{k}_g = e^{-\lambda}(-\partial_n \lambda + k_{\mathbf{g}})$. Yamabe equations are highly non-linear. Hamiton's Ricci flow is able to solve them. Suppose the metric tensor is $\mathbf{g} = (g_{ij})$. Hamilton [Hamilton 1988] introduced surface Ricci flow

$$\frac{dg_{ij}}{dt} = (\rho - 2K)g_{ij}, \tag{2}$$

where ρ is the mean value of the scalar curvature $\rho = \frac{4\pi\chi(M)}{A(0)}$. The term $A(0)$ is the total area of M at time $t = 0$. During the flow, the Gauss curvature will evolve according to a heat diffusion process

$$\frac{\partial K(t)}{\partial t} = \Delta_{\mathbf{g}(t)} K(t) + K(t)(2K(t) - \rho).$$

Therefore, the curvature evolves according to a non-linear heat diffusion process. Hamilton and Chow proved that surface Ricci flow converges to the constant curvature metric.

Theorem 2.3 ([Hamilton 1988]) *Let $(\mathcal{M}^2, g_0)$ be compact. If $\rho \leq 0$, or if $R(0) \geq 0$ on all of $\mathcal{M}^2$, then the solution to (2) exists for all $t \geq 0$ and converges to a metric of constant curvature.*

Theorem 2.4 ([Chow 1991]) *If g_0 is any metric on $\mathcal{S}^2$, then its evolution under (2) develops positive scalar curvature in finite time, and hence by Theorem 2.3 converges to the round metric as t goes to ∞.*

This property gives another approach to proving the Poincaré uniformization theorem.

Theorem 2.5 (Uniformization) *All closed surfaces can be conformally deformed to one of the three canonical spaces, the unit sphere $\mathbb{S}^2$, the plane $\mathbb{E}^2$, or the hyperbolic space $\mathbb{H}^2$.*

Ricci flow induces the conformal mappings for general surfaces, as shown in Fig. 4. Surfaces with boundaries are conformally deformed to constant curvature surfaces with circular holes.

Discrete Surface Ricci Flow Discrete surface Ricci flow algorithm has been introduced in [Jin et al. 2008; Yang et al. 2009] and applied for shape analysis in [Zeng et al. 2010b], surface registration [Wang et al. 2007; Zeng et al. 2008], computational topology [Zeng et al. 2009a], geometric modeling [Gu et al. 2007], image processing [Lui et al. 2010], virtual colonoscopy [Zeng et al. 2010a], and many other applications. In engineering fields, smooth surfaces are often approximated by simplicial complexes (triangle meshes). For more details on applications, we refer the reader to Sect. 5.2.

Major concepts, such as metrics, curvature, and conformal deformation in the continuous setting, can be generalized to the discrete setting. To this end, we denote a triangle mesh as $\mathcal{M}$, a vertex set as $\mathcal{P}$, an edge set as $\mathcal{E}$, and a face set as $\mathcal{F}$. The edge connecting vertices $\mathbf{p}_i$ and $\mathbf{p}_j$ is indicated as e_{ij}, and f_{ijk} denotes the face formed by $\mathbf{p}_i$, $\mathbf{p}_j$, and $\mathbf{p}_k$. Each triangle face can be assumed to be Euclidean $\mathbb{E}^2$, spherical $\mathbb{S}^2$ or hyperbolic $\mathbb{H}^2$, and the edge lengths and angles satisfy Euclidean, spherical or hyperbolic cosine laws,

$$\begin{cases} \cos l_i &= \frac{\cos\theta_i+\cos\theta_j\cos\theta_k}{\sin\theta_j\sin\theta_k} & \mathbb{S}^2 \\ \cosh l_i &= \frac{\cosh\theta_i+\cosh\theta_j\cosh\theta_k}{\sinh\theta_j\sinh\theta_k} & \mathbb{H}^2 \\ 1 &= \frac{\cos\theta_i+\cos\theta_j\cos\theta_k}{\sin\theta_j\sin\theta_k} & \mathbb{E}^2. \end{cases}$$

We say the mesh is with Euclidean, spherical, or hyperbolic background metric. In the following discussion, we will explicitly specify the background geometry for a mesh when it is needed. Otherwise, the concept or the algorithm is appropriate for all kinds of the background geometries.

A Riemannian metric on a mesh $\mathcal{M}$ is a piecewise constant metric with cone singularities. A metric on a mesh with Euclidean background geometry is a Euclidean metric with cone singularities. Each vertex is a cone singularity. Similarly, a metric on a mesh with spherical background geometry is a spherical metric with cone singularities; a metric on a mesh with hyperbolic background geometry is a hyperbolic metric with cone singularities. The edge lengths of a mesh $\mathcal{M}$ are sufficient to define this Riemannian metric $l : \mathcal{E} \to R^+$ as long as, for each face f_{ijk}, the edge lengths satisfy the triangle inequality: $l_{ij} + l_{jk} > l_{ki}$. The *discrete Gaussian curvature K_i* on a vertex $\mathbf{p}_i \in \sigma$ is computed from the angle deficit,

$$K_i = \begin{cases} 2\pi - \sum_{[\mathbf{p}_i,\mathbf{p}_j,\mathbf{p}_k]\in\mathcal{M}}\theta_i^{jk}, & \mathbf{p}_i \notin \partial\mathcal{M} \\ \pi - \sum_{[\mathbf{p}_i,\mathbf{p}_j,\mathbf{p}_k]\in\mathcal{M}}\theta_i^{jk}, & \mathbf{p}_i \in \partial\mathcal{M} \end{cases}$$

where θ_i^{jk} represents the corner angle attached to vertex $\mathbf{p}_i$ in the face $[\mathbf{p}_i,\mathbf{p}_j,\mathbf{p}_k]$, and $\partial\mathcal{M}$ represents the boundary of the mesh. The discrete Gaussian curvatures are determined by the discrete metrics.

The Gauss-Bonnet theorem states that the total curvature is a topological invariant and it still holds on meshes as follows

$$\sum_{\mathbf{p}_i\in\mathcal{P}} K_i + \lambda \sum_{f_i\in\mathcal{F}} A_i = 2\pi\chi(M), \tag{3}$$

where A_i denotes the area of face f_i, and λ represents the constant curvature for the background geometry; $+1$ for the spherical geometry, 0 for the Euclidean geometry, and -1 for the hyperbolic geometry. Conformal metric deformations preserve infinitesimal circles and the intersection angles among them. The discrete *conformal metric deformation* of metrics uses circles with finite radii to approximate the infinitesimal circles.

The concept of the circle packing metric was introduced by Thurston in [Thurston 1980]. Let Γ be a function defined on the vertices, $\Gamma : \mathcal{P} \to \mathbb{R}^+$, which assigns a radius γ_i to the vertex $\mathbf{p}_i$. Similarly, let Φ be a function defined on the edges, $\Phi : \mathcal{E} \to [0, \frac{\phi}{2}]$, which assigns an acute angle ϕ_{ij} to each edge e_{ij} and is called a weight function on the edges. The pair of vertex radius function and edge weight function on a mesh $\mathcal{M}$, (Γ, Φ), is called a circle packing metric of $\mathcal{M}$. Fig. 3 illustrates the circle packing metrics. Each vertex $\mathbf{p}_i$ has a circle whose radius is γ_i. For each edge e_{ij}, the intersection angle ϕ_{ij} is defined by the two circles of $\mathbf{p}_i$ and $\mathbf{p}_j$, which either intersect or are tangent. The edge length is given by $l_{ij}^2 = \gamma_i^2 + \gamma_j^2 + 2\cos\phi_{ij}\gamma_i\gamma_j$.

Two circle packing metrics (Γ_1, Φ_1) and (Γ_2, Φ_2) on the same mesh are conformally equivalent if $\Phi_1 \equiv \Phi_2$. A conformal deformation of a circle packing metric only modifies the vertex radii and preserves the intersection angles on the edges. There

are different ways to define discrete conformal metric deformation. Details can be found in [Gu and Yau 2007] and [Luo et al. 2007].

Admissible Curvature Space A mesh $\mathcal{M}$ with edge weight Φ is called a weighted mesh, which is denoted as $(\mathcal{M}, \Phi)$. In the following, we want to clarify the spaces of all possible circle packing metrics and all possible curvatures of a weighted mesh. Let the vertex set be $\mathscr{P} = \{\mathbf{p}_1, \mathbf{p}_2, \ldots, \mathbf{p}_n\}$, and the radii be $\Gamma = \{\gamma_1, \gamma_2, \ldots, \gamma_n\}$. Let u_i be

$$u_i = \begin{cases} \log \gamma_i & \mathbb{E}^2 \\ \log \tanh \frac{\gamma_i}{2} & \mathbb{H}^2 \\ \log \tan \frac{\gamma_i}{2} & \mathbb{S}^2 \end{cases}$$

where $\mathbb{E}^2$, $\mathbb{H}^2$, and $\mathbb{S}^2$ indicate the background geometry of the mesh. We represent a circle packing metric on $(\mathcal{M}, \Phi)$ by a vector $\mathbf{u} = (u_1, u_2, \ldots, u_n)^T$. Similarly, we represent the Gaussian curvatures at mesh vertices by the curvature vector $k(K_1, K_2, \ldots, K_n)^T$. All the possible $\mathbf{u}$ form the admissible metric space, and all the possible ks form the admissible curvature space.

According to the Gauss-Bonnet theory (c.f., Eq. (3)), the total curvature must be $2\pi\chi(\mathcal{M})$, and therefore the curvature space is $n-1$ dimensional. We add one linear constraint to the metric vector $\mathbf{u}$, $\mathcal{M}\mathbf{u}_i = 0$, for the normalized metric. As a result, the metric space is also $n-1$ dimensional. If all the intersection angles are acute, then the edge lengths induced by a circle packing satisfy the triangle inequality. There is no further constraint on $\mathbf{u}$. Therefore, the admissible metric space is simply $\mathbb{R}^{n-1}$. A curvature vector k is admissible if there exists a metric vector $\mathbf{u}$, which induces k. The admissible curvature space of a weighted mesh $(\mathcal{M}, \Phi)$ is a convex polytope, specified by the following theorem. The detailed proof can be found in [Chow and Luo 2003].

Theorem 2.6 *Suppose $(\mathcal{M}, \Phi)$ is a weighted mesh with Euclidean background geometry, I is a proper subset of vertices, F_I is the set of faces whose vertices are in I, and the link set $Lk(I) = \{(e, v) | e \cap I = \emptyset, v \in I\}$ is formed by faces (e, v), where e is an edge and v is the third vertex in the face. Then, a curvature vector k is admissible if and only if*

$$\sum_{\mathbf{p}_i \in I} K_i > - \sum_{(e,v) \in Lk(I)} (\pi - \phi(e)) + 2\phi\chi(F_1).$$

The admissible curvature spaces for weighted meshes with hyperbolic or spherical background geometries are more complicated. We refer readers to [Luo et al. 2007] for detailed discussions.

Discrete Surface Ricci Flow Suppose $(\mathcal{M}, \Phi)$ is a weighted mesh with an initial circle packing metric. The discrete Ricci flow is defined as

$$\frac{du_i(t)}{dt} = (\bar{K} - K_i), \tag{4}$$

where $\bar{k} = (\bar{K}_1, \bar{K}_2, \ldots, \bar{K}_n)^T$ is the user defined target curvature. Discrete Ricci flow is in the exact same form as the smooth Ricci flow, which deforms the circle packing metric according to the Gaussian curvature, as in Eq. (4). Discrete Ricci flow can be formulated in the variational setting, namely, it is a negative gradient flow of a special energy form. Let $(\mathcal{M}, \Phi)$ be a weighted mesh with spherical (Euclidean or hyperbolic) background geometry. For two arbitrary vertices $\mathbf{p}_i$ and $\mathbf{p}_j$, the following symmetric relation holds $\frac{\partial K_i}{\partial u_j} = \frac{\partial K_j}{\partial u_i}$.

Let $\omega = \sum_{i=1}^{n} K_i du_i$ be a differential one-form. The symmetric relation guarantees that the one-form is closed (curl free) in the metric space; i.e.,

$$d\omega = \sum_{ij} \left(\frac{\partial K_i}{\partial u_j} - \frac{\partial K_j}{\partial u_i} \right) du_i \wedge du_j = 0.$$

By Stokes theorem, the following integration is path independent,

$$f(\mathbf{u}) = \int_{u_0}^{u} \sum_{i=1}^{n} n(\bar{K}_i - K_i) du_i, \tag{5}$$

where u_0 is an arbitrary initial metric. Therefore, the above integration is well defined, so called the *discrete Ricci energy*. The discrete Ricci flow is the negative gradient flow of the discrete Ricci energy. The discrete metric which induces $\bar{k}$ is the minimizer of the energy.

Computing the desired metric with user-defined curvature $\bar{k}$ is equivalent to minimizing the discrete Ricci energy. For the Euclidean (or hyperbolic) case, the discrete Ricci energy (c.f., Eq. (5)) has been proven to be strictly convex (namely, its

Hessian is positive definite) in [Chow and Luo 2003]. The global minimum uniquely exists, corresponding to the metric $\bar{\mathbf{u}}$, which induces $\bar{k}$. The discrete Ricci flow converges to this global minimum.

Theorem 2.7 (Euclidean and hyperbolic Ricci energy) *The Ricci energy satisfies the following properties.*

- *The Euclidean Ricci energy $f(u)$ on the space of the normalized metric $\sum u_i = 0$ is strictly convex.*

- *The hyperbolic Ricci energy is strictly convex.*

Although the spherical Ricci energy is not strictly convex, the desired metric $\mathbf{u}$ is still a critical point of the energy. Finally, the solution can be reached using Newton's method.

Harmonic maps on manifolds Let $(\mathcal{M}, \sigma(z)dzd\bar{z})$ and $(\mathcal{N}, \rho(w)dwd\bar{w})$ be metric surfaces, where z and w refer to the local isothermal coordinates, $\sigma(z)$ and $\rho(w)$ are conformal factors. For a Lipschitz map $f : (\mathcal{M}, \sigma|dz|^2) \rightarrow (\mathcal{M}, \rho|dw|^2)$, the *harmonic energy density* of f is defined as

$$\omega(f; \sigma, \rho) = \frac{\rho(w(z))}{\sigma(z)}(|w_z|^2 + |w_{\bar{z}}|^2).$$

The *harmonic energy* of the mapping is given by

$$E(f; \sigma, \rho) := \int_{\mathcal{M}} \omega(f; \sigma, \rho)\sigma(z)\frac{dz \wedge d\bar{z}}{-2i}$$
$$= \int_{\mathcal{M}} \rho(w(z))(|w_z|^2 + |w_{\bar{z}}|^2)dxdy,$$

where $\sigma(z)\frac{dz \wedge d\bar{z}}{-2i}$ is the area element induced by the Riemannian metric $\sigma(z)dzd\bar{z}$. From the definition, it is obvious that the harmonic energy $E(f; \sigma, \rho)$ solely depends on the conformal structure $\{z\}$ on the source and the Riemannian metric $\rho(w)dwd\bar{w}$ on the target. A critical point of the harmonic energy functional is called a *harmonic map*. If f is harmonic, then $w_{z\bar{z}} + (\log \rho)_w w_z w_{\bar{z}} \equiv 0$.

The pull back metric on $\mathcal{M}$ induced by f is given by

$$f^*\rho = \rho(w_z dz + w_{\bar{z}}d\bar{z})\overline{(w_z dz + w_{\bar{z}}d\bar{z})}.$$

Therefore,

$$f^*\rho = \rho(w_z\overline{w_{\bar{z}}}dz^2 + (|w_z|^2 + |w_{\bar{z}}|^2)dzd\bar{z} + w_{\bar{z}}\overline{w_z}d\bar{z}^2).$$

Suppose $f : (\mathcal{M}, \sigma) \rightarrow (\mathcal{N}, \rho)$ is a mapping, then the *Hopf differential* induced by f is given by

$$\Phi(f) := \rho(w(z))w_z\overline{w_{\bar{z}}}dz^2.$$

The mapping $f : (\mathcal{M}, \sigma) \rightarrow (\mathcal{N}, \rho)$ is harmonic, if and only $\Phi(f)$ is a holomorphic quadratic differential. The mapping is conformal, if and only if $\Phi(f)$ is zero. The following facts are important for surface harmonic maps, the detailed proofs can be found in [Schoen and Yau 1997],

Theorem 2.8 (Rado's theorem) *Suppose $f : S \rightarrow \Omega$ is a harmonic map, where S is a simply connected surface with a single boundary, Ω is a convex planar domain, such that the restriction of f on the boundary ∂S is a homeomorphism, then the mapping is a diffeomorphism.*

Theorem 2.9 *Suppose $f : S \rightarrow \mathbb{S}^2$ is a harmonic map, where S is a genus zero closed surface, then it is conformal.*

Theorem 2.10 *Suppose $f : (S, \mathbf{g}) \rightarrow (T, \mathbf{h})$ is a degree one harmonic map, where S, T are closed high genus surfaces, $\mathbf{h}$ induces negative Gaussian curvature everywhere, then f is diffeomorphic.*

In Sect. 3.1, we specialize harmonic maps on surfaces and discuss their discretization on 3D shapes represented as trianle meshes. As further discussed in Sect. 5.2, harmonic functions have been applied to brain mapping [Gu et al. 2004] and shape registration [Wang et al. 2007].

3   Differential operators and spaces for shape modeling

In the following, we introduce harmonic maps, the Laplacian eigenfunctions, and the solution to the heat diffusion equation in the continuous (Sect. 3.1) and discrete (Sect. 3.2) case.

3.1 Laplace-Beltrami operator on 3D shapes

Three main classes of maps are associated to the Laplace-Beltrami operator $\Delta : \mathscr{C}^2(\mathscr{N}) \rightarrow \mathscr{C}^0(\mathscr{N})$, where $\mathscr{C}^k(\mathscr{N})$ is the class of functions with regularity of degree k: the harmonic maps; the Laplacian eigenfunctions; and the solutions to the heat diffusion equation [Rosenberg 1997]. Since the Laplace-Beltrami operator is self-adjoint and semi-positive definite [Rosenberg 1997], it admits an *orthonormal eigensystem* $\mathscr{B} := \{(\lambda_i, \varphi_i)\}_i$, $\Delta \varphi_i = \lambda_i \varphi_i$, $\lambda_i \leq \lambda_{i+1}$, in the space $\mathscr{L}^2(\mathscr{N})$ of square integrale functions defined on $\mathscr{N}$.

The *harmonic function* $h : \mathscr{N} \rightarrow \mathbb{R}$ is the solution of the Laplace equation $\Delta h = 0$ with Dirichlet boundary conditions $h|_{\mathscr{S}} = h_0$, $\mathscr{S} \subset \mathscr{N}$, where h_0 is the initial condition. In particular, it minimizes the *Dirichlet energy* $E := \int_{\mathscr{N}} \|\nabla h(\mathbf{p})\|_2^2 \mathrm{d}\mathbf{p}$ and satisfies the *locality property*; i.e., if $\mathbf{p}$ and $\mathbf{q}$ are two distinct points, then $\Delta h(\mathbf{p})$ is not affected by the value of h at $\mathbf{q}$. According to the *maximum principle* [Rosenberg 1997], a harmonic function has no local extrema other than at constrained vertices. In the case that all constrained minima are assigned the same global minimum value and all constrained maxima are assigned the same global maximum value, all the constraints will be extrema in the resulting field. We briefly recall that the critical points of h are defined as those points $\mathbf{p} \in \mathscr{N}$ such that $\nabla h(\mathbf{p}) = \mathbf{0}$ and h is *Morse* if the Hessian matrix of h at any critical point is not singular [Biasotti et al. 2008; Milnor 1963]. The critical point is classified as a maximum or a minimum if the corresponding Hessian matrix has zero or three positive eigenvalues, respectively; otherwise, it is a saddle.

The *scale-based representation* $H : \mathscr{N} \times \mathbb{R}^+ \rightarrow \mathbb{R}$ of the map $h : \mathscr{N} \rightarrow \mathbb{R}$ is the solution to the *heat diffusion equation*

$$\begin{cases} \partial_t H(\mathbf{p},t) = -\Delta H(\mathbf{p},t) \\ H(\mathbf{p},0) = h(\mathbf{p}) \end{cases} \quad \mathbf{p} \in \mathscr{N}, \quad t \in \mathbb{R},$$

and it can be written through the convolution operator $\star$ as

$$\begin{cases} H(\mathbf{p},t) := k_t(\mathbf{p},\cdot) \star h = \int_{\mathscr{N}} k_t(\mathbf{p},\mathbf{q}) h(\mathbf{q}) d\mathbf{q} \\ k_t(\mathbf{p},\mathbf{q}) := \sum_{i=1}^{+\infty} \exp(-\lambda_i t) \varphi_i(\mathbf{p}) \varphi_i(\mathbf{q}) \end{cases}$$

where $k_t(\cdot,\cdot)$ is the *heat diffusion kernel*. From the spectral decomposition of $k_t(\cdot,\cdot)$ and disregarding the ordering of the Laplacian eigenvalues, it follows that the heat diffusion and the Laplace-Beltrami operator have the same eigenfunctions $\{\varphi_i\}_{i=1}^{+\infty}$ and $(\exp(-\lambda_i t))_{i=1}^n$ are the corresponding eigenvalues.

3.2 Laplacian matrix and equations

Let us consider a triangle mesh $\mathscr{M} := (\mathscr{P}, T)$, which discretizes a manifold $\mathscr{N}$, where $\mathscr{P} := \{\mathbf{p}_i\}_{i=1}^n$ is the set of n vertices and T is the connectivity graph. Then, the piecewise linear scalar function $f : \mathscr{M} \rightarrow \mathbb{R}$ is defined by linearly interpolating the values $\mathbf{f} := (f(\mathbf{p}_i))_{i=1}^n$ of f at the vertices using barycentric coordinates. If $f(\mathbf{p}_i) \neq f(\mathbf{p}_j)$, for each edge (i, j), then f is called *general*.

We represent the Laplace-Beltrami operator on triangle meshes and point sets in a unified way as $\tilde{\mathbf{L}} := \mathbf{B}^{-1}\mathbf{L}$, where $\mathbf{B}$ is a positive definite matrix and $\mathbf{L}$ is symmetric, positive semi-definite. On triangle meshes, the Laplacian matrix is defined as $\tilde{\mathbf{L}} := \mathbf{B}^{-1}\mathbf{L}$, where $\mathbf{L}$ is the Laplacian matrix with cotangent weights and $\mathbf{B}$ is the diagonal matrix whose entries are the areas of the Voronoi regions of the mesh vertices (*Voronoi-cot weights*) [Desbrun et al. 1999], which extend the cot weights intruduced in [Pinkall and Polthier 1993]. Alternatively, $\mathbf{B}$ is the FEM mass matrix (*linear FEM weights*) [Reuter et al. 2006; Vallet and Levy 2008], which measures the variation of the triangle areas. On polygonal meshes, we consider the Laplacian discretization proposed in [Alexa and Wardetzky 2011], which provides a generalization of the Laplacian matrix with cot-weights to surface meshes with non-planar, non-convex faces.

In [Belkin and Niyogi 2003; Belkin and Niyogi 2006; Belkin and Niyogi 2008; Liu et al. 2012], the Laplace-Beltrami operator for a function $f : \mathscr{P} \rightarrow \mathbb{R}$ defined on a point set $\mathscr{P} := \{\mathbf{p}_i\}_{i=1}^n$, is discretized as the linear operator $\mathbf{f} \mapsto \tilde{\mathbf{L}}\mathbf{f}$, where $\tilde{\mathbf{L}} := (L(i,j))_{i,j=1}^n$ is the Laplacian matrix. In [Liu et al. 2012], the Laplacian matrix is defined as $\tilde{\mathbf{L}} := \mathbf{B}^{-1}\mathbf{L}$, where $\mathbf{L}$ is the Gram matrix associated to the Gaussian kernel and $\mathbf{B}$ is the diagonal matrix whose entries are areas of the Voronoi cells associated to the points of $\mathscr{P}$. The Voronoi cell of $\mathbf{p}_i$ is approximated by projecting the points of a neighbor of $\mathbf{p}_i$ on the estimated tangent plane at $\mathbf{p}_i$. This discretization still converges to the Laplace-Beltrami operator of the underlying manifold, as the sampling density increases and t tends to zero. If $\mathbf{B} := \mathbf{I}$, then this discretization, which applies a fine approximation of the local geometry of the surface at each point through its Voronoi cell, reduces to the discretizations of the Laplace-Beltrami operator proposed in [Belkin and Niyogi 2003; Belkin and Niyogi 2006; Belkin and Niyogi 2008; Liu et al. 2012] and that are based on the heat diffusion kernel. In both cases, $\mathbf{L}\mathbf{f}$ converges to Δf, on $\mathscr{P}$, as $t \rightarrow 0^+$.

(a) $n = 152K$, $m = 1$ (b) $m = 2$, $M = 2$ (c) $m = 3$, $M = 3$
$M = 1$, $s = 0$ $s = 2$ $s = 4$
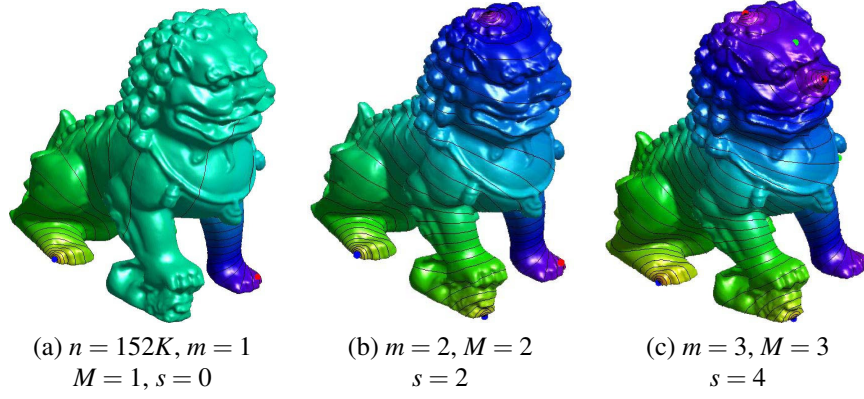
Figure 5: *Level-sets and critical points of harmonic maps with (a) two, (b) four, and (c) six Dirichlet boundary conditions, which are shown in blue and red. Red, blue, and green points indicate the maxima, minima, and saddles of each map. The insertion of new boundary constraints locally affects the resulting harmonic map.*

Critical points Let $f : \mathcal{M} \to \mathbb{R}$ be a piecewise linear and general scalar function. As $\alpha \in \mathbb{R}$ varies, the behavior of f is conveyed by the corresponding level sets $f^{-1}(\alpha)$ and the critical points of f, at which the number of connected components of the level sets changes. The critical points of $f : \mathcal{M} \to \mathbb{R}$ are computed by analyzing the distribution of the f-values on the neighborhood of each vertex [Banchoff 1967]. Under the assumption that f is a regular map, the *Euler formula* gives the link between the critical points of $(\mathcal{M}, f)$, the Euler characteristic $\chi(\mathcal{M}) = m - s + M$ of $\mathcal{M}$ [Banchoff 1967; Milnor 1963], and the genus $g = \frac{1}{2}(2 - \chi(\mathcal{M}))$ of $\mathcal{M}$. Here, m and M is the number of minima and maxima, respectively; the $s := \sum_{\mathbf{p}_i \text{ saddle}} m_i$ saddle points of f are counted with their multiplicity m_i. The computational cost of the classification of the critical points is $O(n)$, where n is the number of vertices; in fact, we need to visit all the 1-stars of $\mathcal{M}$ and compare the f-values along their edges.

Harmonic equation According to the Euler formula, the number of critical points of a harmonic map depends on the number of Dirichlet boundary conditions, which determine the corresponding maxima and minima of the resulting harmonic map. In particular, a harmonic function with exactly one maximum and one minimum has a minimal number of $2g$ saddle points, which are located on the topological handles of $\mathcal{M}$. Fig. 5 shows a family of harmonic functions achieved by increasing the number of Dirichlet boundary conditions. In Fig. 5(a), we applied two boundary conditions, which identify the maximum and minimum of f; in (b), we added two new boundary conditions, while maintaining the previous ones. According to the locality property, the resulting harmonic function and its level-sets remain unchanged in a neighborhood of the Dirichlet points related to the previous step. An analogous remark applies to (b,c), where in (c) we added two constraints to the set of Dirichlet conditions used in (b).

While the position of the extrema is determined *a-priori* by the Dirichlet boundary conditions, only the number of saddles and not their locations on the input surface are determined through the Euler formula. As shown in the deformed surfaces of Fig. 6, the harmonic functions with the same Dirichlet boundary conditions share an equal number of critical points and level-sets of similar shape. The stability is also confirmed by the examples in Fig. 7, where the input shape has been modified by a non-isometric deformation. This result is due to the uniqueness of the harmonic function, once we have fixed the Dirichlet boundary conditions. Indeed, quasi-isometric changes of $\mathcal{M}$ and a different choice of the weights influence the local behavior of f without affecting its global structure.

Laplacian eigenproblem In the discrete case, the eigenproblem related to the linear FEM Laplacian matrix $\tilde{\mathbf{L}} := \mathbf{B}^{-1}\mathbf{L}$ can be written as $\mathbf{L}\mathbf{x} = \lambda\mathbf{B}\mathbf{x}$ and the corresponding eigenvectors $\{\mathbf{x}_i\}_{i=1}^{n}$ are orthonormal with respect to the scalar product $\langle \cdot, \cdot \rangle_{\mathbf{B}}$ induced by $\mathbf{B}$; i.e., $\langle \mathbf{x}_i, \mathbf{x}_j \rangle_{\mathbf{B}} = \mathbf{x}_i^\top \mathbf{B}\mathbf{x}_j = \delta_{ij}$, or equivalently $\mathbf{X}^\top \mathbf{B}\mathbf{X} = \mathbf{I}$, with $\mathbf{X} := [\mathbf{x}_1, \ldots, \mathbf{x}_n]$ the matrix of the eigenvectors. In matrix form, the generalized eigen-decomposition is rewritten as $\mathbf{L}\mathbf{X} = \mathbf{B}\mathbf{X}\Gamma$, where $\Gamma := \text{diag}(\lambda_i)_{i=1}^{n}$ is the diagonal matrix of the Laplacian eigenvalues. Lumping the mass matrix $\mathbf{B}$ [Vallet and Levy 2008], $\tilde{\mathbf{L}}$ reduces to the normalized Laplacian matrix $\mathbf{D}^{-1}\mathbf{L}$. Here, $\mathbf{D}$ is the diagonal matrix whose entries are the areas of the Voronoi regions; i.e., $D(i,i) = \frac{1}{3}\sum_{t \in N(i)} |t|$, $i = 1, \ldots, n$.

The eigenvector corresponding to the smallest non-zero eigenvalue of the Laplacian graph (i.e., the *Fiedler vector*) has been used in graph theory for partitioning graphs into sub-graphs [Fiedler 1973; Mohar and Poljak 1993], which are handled in parallel [Alpert et al. 1999]; in numerical linear algebra, for reordering sparse matrices and reducing their bandwidth [Barnard et al. 1993]; in machine learning, for clustering [Schoelkopf and Smola 2002] (§ 14) and dimensionality reduction [Belkin

Figure 6: *Common behavior of harmonic functions with the same Dirichlet boundary conditions on four deformed surfaces. Each scalar function has 3 maxima, 5 minima, and 6 saddles.*

and Niyogi 2003]; in computer graphics, for graph/mesh layout [Díaz et al. 2002; Koren 2003] and image segmentation [Shi and Malik 1997]. In digital geometry processing, the spectral properties of the uniform discrete Laplacian has been used to design low-pass filters [Taubin 1995]. Successively, this formulation has been refined to include the local geometry of the input surface [Desbrun et al. 1999; Kim and Rossignac 2005; Pinkall and Polthier 1993]. Further applications include implicit mesh fairing [Desbrun et al. 1999; Kim and Rossignac 2005; Zhang and Fiume 2003], mesh watermarking [Ohbuchi et al. 2001; Ohbuchi et al. 2002], and geometry compression [Karni and Gotsman 2000; Sorkine et al. 2003]. Moreover, the spectral properties of the Laplacian matrix are at the basis of the definition of fairing functionals [Kobbelt et al. 1998; Mallet 1989], which optimize the triangles' shape and/or the surface smoothnesss [Nealen et al. 2006].

The eigenvectors of the Laplacian matrix have been used for embedding a surface of arbitrary genus into the plane [Zhou et al. 2004; Zigelman et al. 2002] and mapping a closed 0-genus surface into a spherical domain [Gotsman et al. 2003]. In the frequency space, mesh segmentation [Liu and Zhang 2007; Zhang and Liu 2005], shape correspondence [Jain and Zhang 2007; Jain et al. 2007] and comparison [Jain and Zhang 2007; Reuter et al. 2006] have been successfully addressed. Mesh Laplacian operators are also associated to a set of differential coordinates for surface deformation [Sorkine et al. 2004] and quadrangulation with harmonic maps and Laplacian eigenfunctions [Dong et al. 2005; Dong et al. 2006; Belkin and Niyogi 2003; Ni et al. 2004]. Recent applications of the Laplacian spectrum include shape segmentation and analysis through nodal domains [Reuter et al. 2009] and constrained smoothing of scalar functions [Patanè and Falcidieno 2009]. Finally, theoretical results on the sensitivity of the Laplacian spectrum against geometry changes, irregular sampling density, and connectivity variations have been presented in [Hildebrandt et al. 2006; Xu 2007]. All these works have been accompanied by several surveys on mesh filtering [Taubin 1999]; surface coding and spectral partitioning [Karni and Gotsman 2000]; 3D shape deformation based on differential coordinates [Sorkine 2006]; spectral methods [Zhang et al. 2007] and Laplacian eigenfunctions [Levy 2006] for mesh processing and shape analysis.

Heat diffusion equation On the space of piecewise linear scalar functions defined on $\mathcal{M}$, let us consider the *weighted scalar product* $\langle \mathbf{f}, \mathbf{g} \rangle_{\mathbf{B}} := \mathbf{f}^{\top} \mathbf{B} \mathbf{g}$, which is induced by the mass matrix $\mathbf{B}$ associated to the linear FEM discretization [Reuter et al. 2006; Vallet and Levy 2008] of the Laplace-Beltrami operator. This scalar product is intrinsic to the surface on which the scalar functions are defined and is adapted to the local sampling of $\mathcal{M}$ through the variation of the triangle areas.

For the discretization of the solution to the heat diffusion equation, we consider the linear FEM Laplacian matrix instead of Voronoi-cot Laplacian matrix. According to [Patanè 2013b; Patanè and Falcidieno 2010], the *scale-based representation of* $f : \mathcal{M} \to \mathbb{R}$ is $\mathbf{F}(t) := (F(\mathbf{p}_i, t))_{i=1}^{n} = \sum_{i=1}^{n} \exp(-\lambda_i t) \langle \mathbf{f}, \mathbf{x}_i \rangle_{\mathbf{B}} \mathbf{x}_i$, which is re-written in matrix form as $\mathbf{F}(t) = \mathbf{K}_t \mathbf{f}$, where $\mathbf{K}_t := \mathbf{X} \mathbf{D}_t \mathbf{X}^{\top} \mathbf{B}$, and $\mathbf{D}_t := \mathrm{diag}\left(\exp(-\lambda_i t)\right)_{i=1}^{n}$ is the *weighted linear FEM* (wFEM) *heat kernel matrix*. Lumping the mass matrix $\mathbf{B}$, we get the diagonal matrix whose entries are the areas of the Voronoi regions of $\mathcal{M}$, and $\mathbf{K}_t$ becomes equal to the *Voronoi*-cot (or *lumped FEM*) *heat kernel* $\mathbf{K}_t^{\star} := \mathbf{X} \mathbf{D}_t \mathbf{X}^{\top} \mathbf{D}$, $\mathbf{L} \mathbf{X} = \mathbf{X} \Gamma$, used by previous work [Bronstein et al. 2011; Ovsjanikov et al. 2010; Rustamov 2007; Sun et al. 2009; Vaxman et al. 2010]. Finally, the weighted heat diffusion kernel is still the exponential $\mathbf{K}_t := \exp(-t \mathbf{B}^{-1} \mathbf{L})$ of the linear FEM Laplacian matrix.

Indicating with $\mathbf{e}_i$ the i-th vector of the canonical basis of $\mathbb{R}^n$, $\mathbf{K}_t \mathbf{e}_i$ is the map achieved by applying the diffusion process to the function that takes value one at the *anchor* $\mathbf{p}_i$ and zero otherwise. We compare the basis function $\mathbf{K}_t^{\star} \mathbf{e}_i$ and $\mathbf{K}_t \mathbf{e}_i$, which are induced by the Voronoi-cot and wFEM heat kernel, respectively. As shown in Fig. 8, irregularly-sampled patches on $\mathcal{M}$
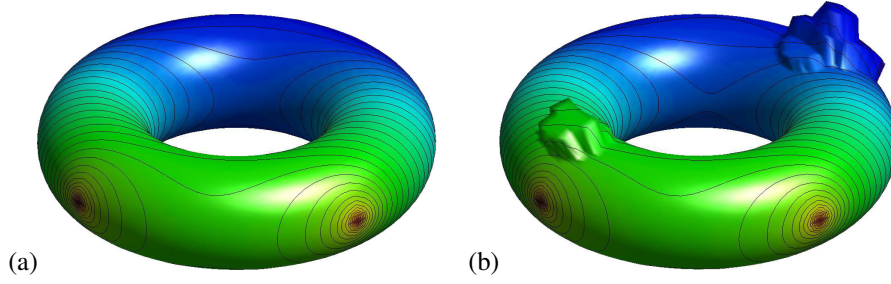
Figure 7: *Level-sets of the harmonic function with four Dirichlet boundary conditions on a (a) smooth and (b) deformed shapes. In (b), the corresponding harmonic maps is slightly affected by surface changes.*

generally affect the smoothness of $\mathbf{K}_t^\star \mathbf{e}_i$ at smaller scales; increasing t improves the smoothness of $\mathbf{K}_t^\star \mathbf{e}_i$ in terms of regularity of the level-sets and of a lower number of critical points. On the contrary, the smoothness of $\mathbf{K}_t \mathbf{e}_i$ is guaranteed through all the scales in spite of the discretization of $\mathcal{M}$. The heat kernels $\mathbf{K}_t$ and $\mathbf{K}_t^\star$ are intrinsically scale-covariant (i.e., without shape or kernel normalization) and scale-invariant through a normalization of the Laplacian eigenvalues. In [Bronstein et al. 2010b; Bronstein et al. 2010c], these properties and the robustness of the wFEM heat kernel against shape transformation, sampling, and noise have been verified by testing the matching performances of the wFEM heat kernel descriptors on the SHREC'10 data set. For more details, we refer the reader to Sect. 5.1.

Once the Laplacian eigensystem is known, the computation of $F(\cdot,t)$ takes $O(n)$-time. However, using the whole spectrum is computationally unfeasible. To overcome this limitation, we consider only the contribution related to the first k eigenvalues; i.e., $\mathbf{F}_k(t) = \sum_{i=1}^{k} \exp(-\lambda_i t) \langle \mathbf{f}, \mathbf{x}_i \rangle_\mathbf{B} \mathbf{x}_i$. Applying the computation described in [Vallet and Levy 2008], these eigenpairs are computed in super-linear time. If $t := 0$, then the map $\mathbf{F}_k(0) = \sum_{i=1}^{k} \langle \mathbf{f}, \mathbf{x}_i \rangle_\mathbf{B} \mathbf{x}_i$ is the least-squares approximation of f in the linear space generated by the first k eigenfunctions and with respect to the norm $\| \cdot \|_\mathbf{B}$. Indeed, both the parameters k and t define the hierarchy of approximations. In fact, reducing the number of Laplacian eigenfunctions results in a smoothing of the input map and a further simplification of its critical points, with more emphasis on those with a low persistence value. A spectrum-free computation of the heat diffusion kernel, which is based on the Chebyshev approximation of the exponential matrix, has been recently proposed in [Patanè 2013b; Patanè and Spagnuolo 2013a]. For an interactive comparison of Laplacian spectral kernels and distances, we refer the reader to [Patanè and Spagnuolo 2013b].

The discrete heat diffusion kernel is central for shape segmentation [de Goes et al. 2008] and comparison [Bronstein and Kokkinos 2010; Bronstein et al. 2011; Dey et al. 2010; Gebal et al. 2009; Ovsjanikov et al. 2010] through heat kernel shape descriptors, auto-diffusion maps [Gebal et al. 2009], and diffusion distances [Bronstein et al. 2010a; Coifman and Lafon 2006; Lafon et al. 2006]; dimensionality reduction [Belkin and Niyogi 2003; Xiaoa et al. 2010] with spectral embeddings; the computation of the gradient of discrete maps [Wang 2009] and the multi-scale approximation of functions [Patanè and Falcidieno 2010]. In [Vaxman et al. 2010], prolongation operators have been applied to extend the values of the heat diffusion kernel computed on a low resolution representation of $\mathcal{M}$ to higher resolutions through the hierarchy associated to multiresolutive simplification algorithms. Recently, the heat equation and the associated diffusion metric have been used to define multi-scale shape signatures [Sun et al. 2009], compare 3D shapes [Mèmoli 2009], and approximate the gradients of scalar functions defined on triangulated surfaces and point sets [Wang 2009]. Combining the smoothness of the Laplacian eigenfunctions with the multi-scale structure induced by the time parameter of the heat kernel on a 3D shape $\mathcal{M}$, it is possible to compute a smooth approximations of scalar functions defined on $\mathcal{M}$ and define new function spaces for shape analysis.

Heat diffusion and spectral distances Through the Laplacian spectrum, previous work has defined several spectral distances (e.g., commute-time, bi-harmonic, and diffusion distances), which are intrinsic to the input shape, invariant to isometries, shape-aware, robust to noise and tessellation. Bi-harmonic [Ovsjanikov et al. 2012; Lipman et al. 2010; Rustamov 2011b] distances provide a trade-off between a nearly-geodesic behavior for small distances and global shape-awareness for large distances, thus guaranteeing an intrinsic multi-scale characterization of the input shape. The heat diffusion distances have been used in the context of spectral graph theory [Chung 1997] (Ch. 10), manifold learning [Belkin and Niyogi 2003; Coifman and Lafon 2006; Lafon et al. 2006], and shape comparison [Bronstein et al. 2010a; Bronstein and Kokkinos 2010; Bronstein et al. 2011; Bronstein and Bronstein 2011; Dey et al. 2010; Gebal et al. 2009; Mahmoudi and Sapiro 2009; Mèmoli 2009; Ovsjanikov et al. 2010; Rustamov 2007; Sun et al. 2009] through multi-scale and density invariant embeddings. Additional applications include shape segmentation [de Goes et al. 2008], the computation of the gradient of discrete maps [Wang 2009] and the multi-scale approximation of functions [Patanè and Falcidieno 2010]. For an interactive comparison of spectral distances, we refer the reader to [Patanè and Spagnuolo 2013b].
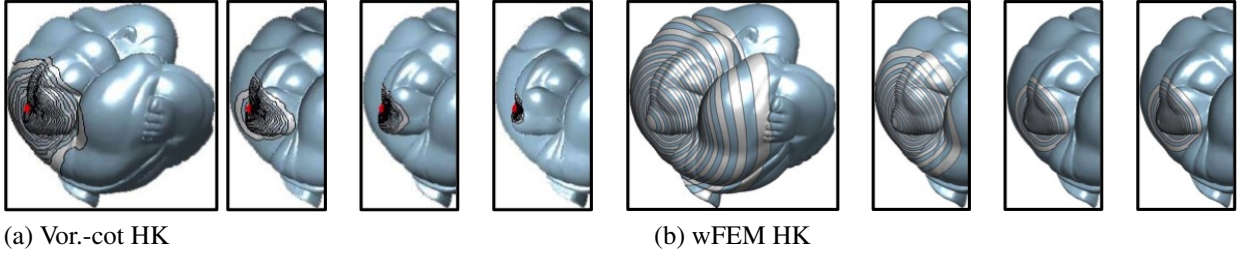
Figure 8: *Level-sets of the basis $K_t\mathbf{e}_i$ induced by the (a) Voronoi-cot and (b) wFEM heat kernel on an irregularly-sampled surface with respect to different values of the time parameter.*

4 From surface-based to volume-based shape modeling

Shape modeling typically handles a 3D shape as a two-dimensional surface, which describes the shape boundary and is represented as a triangular mesh or a point cloud. However, in several applications a volumetric surface representation is more suited to handle the complexity of the input shape. For instance, volumetric representations accurately model the behavior of non-rigid deformations and volume constraints are imposed to avoid deformation artifacts. In shape matching, volumetric descriptors, such as Laplacian eigenfunctions, heat kernels, and diffusion distances, are defined starting from their surface-based counterparts. In these cases, a surface-based information, which is typically represented as a shape-driven map, is extended to the interior of the input shape or, more generally, to the surrounding volume. This step typically relies on the integration of shape-based and volumetric information, together with smoothness conditions, interpolating constraints, preservation of feature values at both a local and global level.

Besides the underlying complexity and degrees of freedom in the definition of volumetric approximations of surface-based maps, volumetric approximations (i.e., the extension of a surface-based scalar function to a volume-based approximation) are essential to address a wide range of problems. For instance, the approximation of spatio-physico-chemical properties measured or simulated on a molecular surface to the surrounding volume could be used to predict the interactions among proteins [Cipriano and Gleicher 2007]. Computing corresponding feature elements [Jain and Zhang 2007], harmonic volumetric mappings [Li et al. 2009a; Li et al. 2010b; Martin et al. 2008b; Martin and Cohen 2010], and volumetric [Rustamov 2011a] shape descriptors by extending the surface-based Laplacian eigenvectors to the surrounding volume [Rustamov 2011b] avoids the evaluation of volumetric descriptors directly on a tessellation of the input shape. In this way, the computational cost, which is generally high in case of volumetric meshes, is effectively reduced. Furthermore, descriptors primarily defined on surfaces (e.g., GPS embedding [Rustamov 2007], biharmonic distances [Lipman et al. 2010; Rustamov 2011b], and heat kernel signatures [Sun et al. 2009]) can be approximated to measure volumetric information.

Given a piecewise linear scalar function $f : \mathcal{M} \to \mathbb{R}$, we want to define a *volumetric approximation $F : \mathbb{R}^3 \to \mathbb{R}$* that satisfies different types of conditions, such as interpolation of the f-values, approximation accuracy, smoothness, preservation of the critical points. To this end, we focus on the following volumetric approximation schemes: (i) linear precision methods through generalized barycentric coordinates (Sect. 4.1); (ii) implicit methods with radial basis functions (Sect. 4.2); (iii) integration of surface- and cross-volume parameterization (Sect. 4.3); (iv) polycube splines (Sect. 4.4); (v) moving least-squares techniques (Sect. 4.5); (vi) topology-driven approximation (Sect. 4.6). Finally, we compare the computation cost of the aforementioned approximations (Sect. 4.7).

4.1 Linear precision approximation

Barycentric coordinates provide a standard technique for interpolating discrete scalar, vector, or even multidimensional fields from the boundary of a domain over its interior, and are useful in a variety of applications in computer graphics, such as texture mapping [Desbrun et al. 2002], deformation [Ju et al. 2005; Lipman et al. 2007], texture synthesis [Takayama et al. 2010], and image composition [Farbman et al. 2009]. For instance [Rustamov 2011a], the Laplacian eigenvectors of a given surface are extended into the shape interior using piecewise linear interpolation with barycentric coordinates. These volumetric eigenvectors provide the basis for the definition of shape-aware barycentric coordinates and of volumetric shape descriptors, such as the volumetric global point signature (GPS), biharmonic and diffusion embeddings. In particular, they generalize the GPS embedding, the biharmonic distances, and the heat kernel signatures, which have been primarily defined on surfaces.

Barycentric coordinates are commonly computed through the solution of a linear system, the minimization of an energy functional with constraints, or a closed form. Over the last two decades, many closed-form barycentric coordinates have been

developed for convex [Dasgupta and Wachspress 2008; Pinkall and Polthier 1993; Floater 2003] and arbitrary [Hormann and Floater 2006] shapes. Variants include mean value [Floater 2003; Hormann and Floater 2006; Ju et al. 2005], Green [Lipman et al. 2008], and Poisson [Li and Hu 2013] coordinates. Recently, these coordinates have been enriched with constraints on their regularity and accuracy [Li et al. 2013b], harmonicity [Joshi et al. 2007; Hormann and Sukumar 2008; Weber et al. 2012; Jacobson et al. 2011; Lipman et al. 2008], and positiveness [Lipman et al. 2007]. We also mention the maximum entropy coordinates [Hormann and Sukumar 2008], which are computed by solving a linear system or through an iterative process, and recent generalizations of barycentric coordinates to the complex plane [Weber et al. 2009; Weber and Gotsman 2010; Weber et al. 2011].

4.2 Function approximation with RBFs

In the following, we review global approximation scheme with radial basis functions (RBFs) and globally-supported or locally-supported kernels.

Interpolating constraints Choosing a kernel $\varphi : \mathbb{R}^+ \to \mathbb{R}$, the volumetric approximation $F : \mathbb{R}^3 \to \mathbb{R}$ of $f : \mathcal{M} \to \mathbb{R}$ is defined as [Aronszajn 1950; Poggio and Girosi 1990]

$$F(\mathbf{p}) := \sum_{i=1}^{n} \alpha_i \varphi_i(\mathbf{p}) + \pi(\mathbf{p}), \quad \mathbf{p} := (x, y, z), \tag{6}$$

that is, a linear combination of the radial basis functions $\varphi_i(\mathbf{p}) := \varphi(\|\mathbf{p} - \mathbf{p}_i\|_2)$, centered at $\{\mathbf{p}_i\}_{i=1}^n$, plus a first-degree polynomial $\pi(\mathbf{p}) := \beta_0 + \beta_1 x + \beta_2 y + \beta_3 z$. The second term π in (6) is used to fit f over regions of $\mathscr{P}$ where it is linear. Then, the coefficients in (6) that uniquely satisfy the interpolating conditions $F(\mathbf{p}_i) = f(\mathbf{p}_i)$, $i = 1, \ldots, n$, are the solution of the following $(n+4) \times (n+4)$ square linear system

$$\begin{bmatrix} a_{11} & \ldots & a_{1n} & p_1^x & p_1^y & p_1^z & 1 \\ \vdots & \ddots & \vdots & \vdots & \vdots & \vdots & \vdots \\ a_{n1} & \ldots & a_{nn} & p_n^x & p_n^y & p_n^z & 1 \\ p_1^x & \ldots & p_n^x & 0 & 0 & 0 & 0 \\ p_1^y & \ldots & p_n^y & 0 & 0 & 0 & 0 \\ p_1^z & \ldots & p_n^z & 0 & 0 & 0 & 0 \\ 1 & \ldots & 1 & 0 & 0 & 0 & 0 \end{bmatrix} \alpha = \begin{bmatrix} f(\mathbf{p}_1) \\ \vdots \\ f(\mathbf{p}_n) \\ 0 \\ 0 \\ 0 \\ 0 \end{bmatrix}, \tag{7}$$

$$\alpha = \begin{bmatrix} \alpha_1 & \ldots & \alpha_n & \beta_0 & \beta_1 & \beta_2 & \beta_3 \end{bmatrix}^\top,$$

with $a_{ij} := \varphi(\|\mathbf{p}_i - \mathbf{p}_j\|_2)$ and $\mathbf{p}_i := (p_i^x, p_i^y, p_i^z)$. The last four rows of the full matrix in (7) correspond to the *natural additional constraints*

$$\sum_{i=1}^n \alpha_i p_i^x = 0, \quad \sum_{i=1}^n \alpha_i p_i^y = 0, \quad \sum_{i=1}^n \alpha_i p_i^z = 0.$$

These relations guarantee that the coefficient matrix in Eq. (7) is invertible; in fact, the $n \times n$ sub-matrix $\mathbf{A} := (a_{ij})_{i,j}$ is conditionally positive-definite on the subspace of vectors that are orthogonal to the last four rows of the full matrix.

Least-squares constraints To reduce the amount of memory storage and computation time of the implicit approximation, sparsification methods select a set of centers such that the associated function F approximates the f-values within a target accuracy. This aim is usually achieved through *a-posteriori* updates of the approximating function, which are guided by the local approximation error [Carr et al. 2001; Chen and Wigger 1995; Kanai et al. 2006; Ohtake et al. 2005b; Shen et al. 2004], or by solving a constrained optimization problem [Girosi 1998; Patanè 2006; Steinke et al. 2005; Walder et al. 2006]. Clustering techniques can also be applied to group those points that satisfy a common "property" and center a basis function at a representative point of each cluster. Main clustering criteria are the planarity and closeness, measured in the Euclidean space using the k-means clustering [Lloyd 1982] and the principal component analysis [Jolliffe 1986] (PCA). As an alternative, kernel methods [Cortes and Vapnik 1995] evaluate the correlation among points with respect to the scalar product induced by a positive-definite kernel. In this case, the PCA and the k-means algorithm lead to efficient clustering techniques, such as the kernel PCA and the Voronoi tessellation of the feature space [Schoelkopf and Smola 2002] (Ch. 1). Finally [Weiler et al. 2005], the set of centers can be enriched by including the peaks and low frequency regions of the input data.

Once the centers $\mathscr{B} := \{\mathbf{c}_i\}_{i=1}^r$ of the globally-supported basis functions have been selected, we can also compute the best approximation of f with respect to the least-squares error between the piecewise linear restriction $F_{\mathscr{P}}$ of F to $\mathscr{P}$ and f. We

notice that $\mathscr{B}$ might be a subset of $\mathscr{P}$. To this end, we search the function $F(\mathbf{p}) := \sum_{i \in \mathscr{I}} \alpha_i \varphi_i(\mathbf{p})$ that minimizes the least-squares approximation error $\mathscr{E} := \sum_{i=1}^n |F(\mathbf{p}_i) - f(\mathbf{p}_i)|^2$. Let $\mathbf{A}$ be the $n \times r$ matrix defined using the new set $\mathscr{B}$ of selected centers and the set $\mathscr{P}$ of samples. Then, the minimum of the least-squares error $\mathscr{E}$ is attained at the solution α of the normal equation $\mathbf{A}^\top \mathbf{A} \alpha = \mathbf{A}^\top \mathbf{b}$; i.e., $\alpha = \mathbf{A}^\dagger \mathbf{b}$, with $\mathbf{A}^\dagger := (\mathbf{A}^\top \mathbf{A})^{-1} \mathbf{A}$ pseudoinverse of $\mathbf{A}$. Assuming that n is large, we do not construct the $n \times r$ matrix $\mathbf{A}$ but we store only the $r \times r$ coefficient matrix $\mathbf{A}^\top \mathbf{A}$ and the right-hand vector $\mathbf{A}^\top \mathbf{b}$. Finally, the solution of the corresponding linear system is computed using direct or iterative solvers without explicitly storing the pseudoinverse.

Choice of the kernel Depending on the properties of φ and of the corresponding approximation scheme, we distinguish globally-supported [Carr et al. 2001; Turk and O'Brien 2002] and compactly-supported [Wendland 1995; Morse et al. 2001; Ohtake et al. 2005a] supported radial basis functions, and the partition of unity [Ohtake et al. 2003; Xie et al. 2004]. We briefly remind that the *support* of an arbitrary map $g : \mathbb{R}^3 \to \mathbb{R}$ is defined as the set $\text{supp}(g) := \overline{\{\mathbf{p} \in \mathbb{R}^3 : F(\mathbf{p}) \neq 0\}}$. If $\text{supp}(g) := \mathbb{R}^3$, then g has *global support*. Common choices of kernels with global support are the Gaussian $\varphi(t) := \exp(-t)$, the harmonic $\varphi(t) := |t|^{-1}$, and the bi-harmonic $\varphi(t) := |t|^3$ kernel. Main examples of locally-supported kernels are $\varphi(t) := (1-t)^2$ [Morse et al. 2001] and $\varphi(t) := (1-t)^4(4t+1)$ [Wendland 1995]. Globally-supported kernels are associated to full coefficient matrices, which require a prohibitive storage and computational cost with respect to compactly-supported kernels. Selecting compactly-supported basis functions generally provide sparse coefficient matrices and a lower computation cost (Sect. 4.7). However, the corresponding volumetric approximation $F : \mathbb{R}^3 \to \mathbb{R}$ has several and small iso-surfaces that have artifacts where the supports of the basis functions intersect. Therefore, the selection of a compact support might result in a poor visualization of F and a coarse approximation of f on $\mathscr{P}$. Furthermore, the support selection is not trivial and a local definition of F would not extrapolate the behavior of f on the interior and exterior of $\mathscr{P}$.

The variance and width parameters of Gaussian [Co et al. 2003; Jang et al. 2004; Weiler et al. 2005] and ellipsoidal [Jang et al. 2006; Hong et al. 2006] basis functions, which are best suited to fit data that are not radially symmetric, are computed using the Levenberg-Marquardt optimization method [Madsen et al. 2004]. The maximum principle of harmonic maps is easily applied to the approximation scheme with interpolating and least-squares constraints. In fact, the values of F in the interior of $\mathscr{P}$ are fully determined by its boundary conditions, which are selected among the f-values. Since the function $\varphi_i(\mathbf{p}) := \|\mathbf{p} - \mathbf{p}_i\|_2^{-1}$ is not defined at $\mathbf{p}_i$, the harmonic kernel is centered at the offset points $\mathbf{c}_i$ previously introduced. In particular, F is harmonic (i.e., $\Delta F = 0$) in $\mathscr{D} := \mathbb{R}^3 \setminus \mathscr{B}$, with $\mathscr{B} := \{\mathbf{c}_i\}_{i=1}^r$, as superposition of harmonic functions. Under these assumptions, $F : \mathscr{D} \to \mathbb{R}$ is the unique solution of the Laplace equation $\Delta F(\mathbf{p}) = 0$, $\mathbf{p} \in \mathscr{D}$, with Dirichlet boundary conditions $F(\mathbf{p}_i) = f(\mathbf{p}_i)$, $i \in \mathscr{I}$. Once the boundary constraints have been fixed, the function F minimizes the Dirichlet energy $\int_{\mathscr{D}} \|\nabla F(\mathbf{p})\|_2^2 d\mathbf{p}$.

4.3 From surface- to cross-volume parameterization

Using the volumetric harmonic maps previously introduced, we now discuss the cross-volume paramterization, which is computed extending a harmonic map from the input surface to the surrounding space.

Cross-surface parameterization Cross-surface parameterization is an important tool in surface modeling. It computes a bijective correspondence between two surfaces $f : \mathscr{N}_1 \to \mathscr{N}_2$. This correspondence enables numerous applications such as shape analysis, interpolation, comparison, and texturing. Given two surfaces $\mathscr{N}_1, \mathscr{N}_2 \subset \mathbb{R}^3$, their cross-surface mapping can be computed and measured by the composition of their parameterization over a common geometrically homogeneous domain Ω. Suppose we have the parametric representations $\phi : \Omega \to \mathscr{N}_1$ and $\varphi : \Omega \to \mathscr{N}_2$ for $\mathscr{N}_1$ and $\mathscr{N}_2$, respectively,

$$\phi(u_1, u_2) = (\phi_1(u_1, u_2), \phi_2(u_1, u_2), \phi_3(u_1, u_2)),$$
$$\varphi(u_1, u_2) = (\varphi_1(u_1, u_2), \varphi_2(u_1, u_2), \varphi_3(u_1, u_2)),$$

where (u_1, u_2) is a point in a parametric domain Ω in $\mathbb{R}^2$. With the same coordinate (u_1, u_2) on Ω, each point

$$\mathbf{p} = (\phi_1(u_1, u_2), \phi_2(u_1, u_2), \phi_3(u_1, u_2)) \in \mathscr{N}_1$$

is mapped to its image point

$$f(\mathbf{p}) = (\varphi_1(u_1, u_2), \varphi_2(u_1, u_2), \varphi_3(u_1, u_2)) \in \mathscr{N}_2$$

by the composition $f := \varphi \circ \phi^{-1}$.

A mapping $f : \mathscr{N}_1 \to \mathscr{N}_2$ is *isometric* or *length-preserving* if any arc on $\mathscr{N}_1$ has the same length as its image on $\mathscr{N}_2$. Such a mapping is called an isometry. The map f is *conformal* or *angle-preserving* if the angle of intersection of every pair of intersecting arcs on $\mathscr{N}_1$ is the same as that on $\mathscr{N}_2$ (Sect. 2.1). The map f is *equiareal* or *area-preserving* if each region on $\mathscr{N}_1$ has the same area of its image on $\mathscr{N}_2$. An *isometric* map is both *conformal* and *equiareal*. It is usually desirable to minimize

Figure 9: *Solving cross-surface mapping for high-genus surfaces. (a) Mapping by divide-and-conquer through consistent surface decomposition [Li et al. 2009a], (b) global optimization on the covering space with uniformization metrics [Li et al. 2008].*

the metric distortion of the map, i.e., to seek for the isometric map that is both angle-preserving and area-preserving. However, isometry rarely exists between the two arbitrarily given surfaces. In practice, users usually minimize length distortion, angle distortion, or a trade-off between the angle and area distortions.

According to the Riemannian uniformization theorem (Sect. 2.2), for any simply connected surface, one of the following three canonical domains: a *sphere*, the *complex plane*, and an *open disk* can be used for the mapping composition. According to topological types of the given surface, different surface parameterization techniques should be utilized. Examples of cross-surface mappings are shown in Fig. 9. Inter genus-0 surface mapping can be composed over a common sphere [Kent et al. 1992; Alexa 1999; Asirvatham et al. 2005; Kobbelt et al. 1999] or planar disk [Kanai et al. 1998; Haker et al. 2000] domain. For *closed genus-0 surfaces*, i.e., the topological spheres, many effective spherical parameterization techniques that minimize angle distortion [Haker et al. 2000; Gu and Yau 2003; Sheffer et al. 2004; Stephenson 2005; Zeng et al. 2007], or a balance between angle and area distortions [Isenburg et al. 2001; Gotsman et al. 2003; Saba et al. 2005; Friedel and Desbrun 2005; Zayer et al. 2006] have been developed. Efficient multi-resolution algorithms [Shapiro and Tal 1998; Praun and Hoppe 2003; Wan et al. 2012] are also used to reduce the number of local minima and accelerate the expensive nonlinear optimization on the sphere. For *open genus-0 surfaces*, i.e., the topological disks, their parameterization over planar domains [Floater and Hormann 2005; Sheffer et al. 2006; Hormann et al. 2007] has been extensively studied and many efficient algorithms can be adopted directly.

For *high genus surfaces*, finding a simple canonical domain becomes nontrivial. There are two general approaches to compute their cross-surface parameterization. One approach is to first segment surfaces $\mathcal{N}_i, i = 1, 2$, into two consistent sets of subregions, $\mathcal{N}_i = \bigcup_{j=1}^m \widetilde{\mathcal{N}_{i,j}}$, then obtain the global mapping by composing local maps between corresponding subregions: $f_k : \widetilde{\mathcal{N}_{1,k}} \to \widetilde{\mathcal{N}_{2,k}}$. To enable such a divide-and-conquer mapping approach, the decomposition should satisfy that (a) each subregion has simple topology (e.g., topological disks) and geometry (e.g., flat, convex, etc.) so that the subregion mapping can be computed efficiently, and (b) the partitioning is topologically consistent, i.e. the dual graphs of the two decompositions are isomorphic to each other. This decomposition is referred to as the *consistent decomposition*. A few semi-automatic or automatic effective consistent decomposition algorithms have been proposed [Kwok et al. 2012; Kraevoy and Sheffer 2004; Schreiner et al. 2004; Li et al. 2009a; Zhang and Li 2012; Shalom et al. 2008; Kraevoy et al. 2007; Zhang et al. 2012]. Mapping computation through divide-and-conquer is efficient, and locally the mapping quality can be significantly improved. Its challenge is the effective handling of the distortion and discontinuity across the decomposition boundary. Also, the mapping result is directly dictated by the decomposition quality.

The second approach for inter high-genus surface mapping is to directly compute the global mapping through one global domain with certain desirable Riemannian metrics. For example, the domain Ω for high genus surfaces can be Riemannian surfaces of non-positive constant curvature [Schoen and Yau 1997] by deforming the target surface $\mathcal{N}_2$ to tile the complex plane $\mathscr{C}^2$ (if surface $\mathcal{N}_2$ is genus-1) or tile the unit hyperbolic disk $\mathscr{H}^2$ (if surface $\mathcal{N}_2$ is genus-n, $n > 1$). Upon such an Ω, a harmonic map can be computed through an global optimization. A key advantage of using such a uniformization metric is that the objective function does not have local minima and one can obtain a globally optimal solution [Li et al. 2008]. Other types of canonical domain Ω with good geometric regularity/simplicity, such as polycubes [Wan et al. 2011] or N-hole tori [Grimm and Hughes 2003], can also be used to compose cross-surface mapping.

From surface to cross-volume parameterization Many real-world data are volumetric and have both boundary surface geometry and interior texture or material attributes. To model such volumetric data, their interior material, intensity, or other
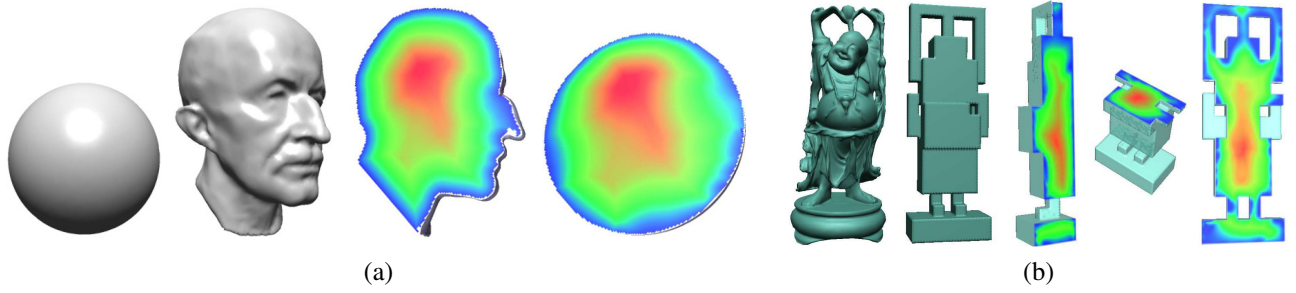
Figure 10: *Extending cross-surface mapping to cross-volume mapping [Li et al. 2007] on (a) genus-0 and (b) high-genus surfaces.*

structural information, should be considered and volumetric parameterization needs to be studied. Inter volume mapping can be extended from the boundary surface mapping. Given two volumetric regions $\mathscr{V}_1$ and $\mathscr{V}_2$, the volumetric mapping $f : \mathscr{V}_1 \rightarrow \mathscr{V}_2$ consists of three scalar fields $\Phi := (\phi_1, \phi_2, \phi_3)$ defined on $\mathscr{V}_1$. To measure the *quality* of Φ, we consider two criteria: geometric distortion and feature alignment.

- *Geometric distortion.* Similar to the surface map, the distortion of a volumetric map can be also measured by the metric changes between the original and the transformed spaces. It is often desirable to have the geodesic distances, angles, and volumes preserved under the mapping.

- *Feature alignment.* The volumetric data usually possess nonuniform interior materials/layers, and their mapping should incorporate these nonuniform structures. For example, feature curves, feature surfaces, and other sub-structures (such as local landmarks or global symmetry pattern) often encode important information. Hence, the scalar fields $\{\phi_j, j = 1, 2, 3\}$ may need to satisfy some extra constraints, and their gradients $\{\nabla \phi_j\}$ should align with (be parallel or perpendicular to) some given directions.

Wang *et al.* [Wang et al. 2004] discretized the volumetric harmonic energy over tetrahedral mesh, and generalize the spherical surface mapping to the volumetric harmonic sphere mapping. Such a discrete Laplacian discretization was also used for extending polycube surface parameterization to the mapping of given model's entire volume space [Han et al. 2010; Xia et al. 2010]. Li *et al.* [Li et al. 2007; Li et al. 2009b; Li et al. 2010a; Xu et al. 2013] used the surface mapping as the boundary condition and extend the cross-surface map to a cross-volume map using the fundamental solution method. Martin *et al.* [Martin et al. 2008b] parameterized the surface model onto a cylinder, then extend the parameterization into the interior volume using the finite element method; later, they also generalized the algorithm to more complicated models with medial surfaces [Martin et al. 2012].

There are also quite a few volumetric parameterization algorithms that directly solve the mapping between two volume regions, without first computing boundary surface mapping. Such an approach, avoiding pre-computing a boundary condition, can usually result in smaller mapping distortion. However, the problem reduces to a big non-linear optimization problem with both integer and certain linear/nonlinear constraints, hence it is much more expensive to solve [Nieser et al. 2011; Huang et al. 2011; Li et al. 2012]. Fig. 10 shows the extension of cross-surface to cross-volume mappings.

4.4 Polycube parameterization and polycube splines

An alternative to volumetric approximation with RBFs is given by the polycube splines, which are defined starting from the volumetric parameterziation of the input surface.

Polycube parameterization The *polycube* can serve as a special desirable domain for shape modeling. A *polycube* can be formally defined as an orthogonal polyhedron where three mutually-perpendicular axis-parallel edges meet at every corner vertex. Polycube mapping was first introduced by Tarini *et al.* [Tarini et al. 2004] for seamless texture mapping, in which polycube domain is constructed manually and the mapping is constructed by iteratively minimizing a deformation energy. Wang *et al.* [Wang et al. 2008] introduced an intrinsic polycube parameterization method based on discrete harmonic maps, which guarantees the mapping bijectivity and reduces the mapping distortion. Xia *et al.* [Xia et al. 2011] proposed an editable polycube mapping method which provides a regular and artist-controllable quad mesh with a parameterized subdivision scheme. Li *et al.* [Li et al. 2010a] proposed the generalized polycube parameterization upon the so called *generalized polycube* domain, which is composed of a set of locally glued topological cubes that can be geometrically curved and non-axis aligned. A key

| (a) Face charts | (b) Edge charts | (c) Singularities | (d) Edge charts and singularities |
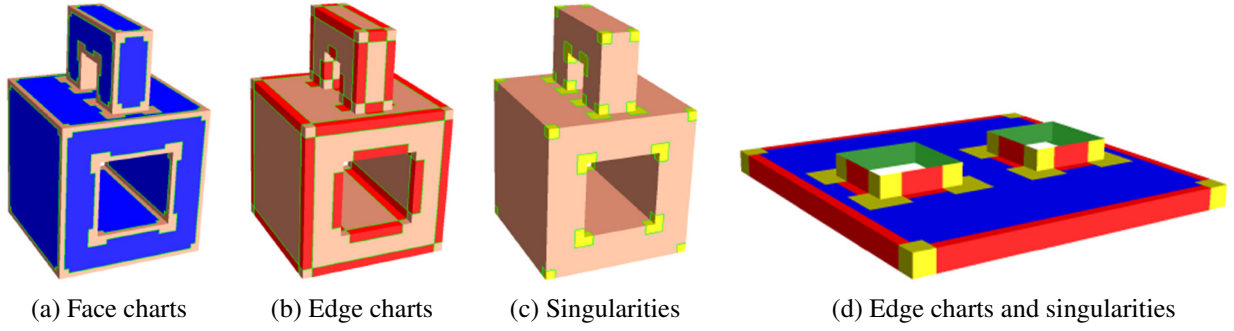
Figure 11: *Polycube Splines construction [Wang et al. 2008]. The Polycube is covered by face and edge charts (a,b). The polycube corners (yellow) are singularities which are not covered by any charts (c). In (d), one face chart was highlighted with its associated edge charts and singularities.*

difficulty in polycube parameterization is the construction of desirable polycube domain shape.

The aforementioned manual or semi-manual polycube construction algorithms could be tedious when modeling shapes with complicated geometry. Lin *et al.* [Lin et al. 2008] proposed a polycube parameterization algorithm using the Reeb graph. This method can automatically construct polycubes for models with simple topology and geometry. He *et al.* [He et al. 2009] used a line-scanning-like strategy to construct polycubes. This approach is sensitive to the object's orientation and off-axis features and could result in over-refined polycubes with many corner points. Gregson *et al.* [Gregson et al. 2011] proposed a rotation-driven and position-driven deformation algorithm to construct polycubes. To get rid of topologically erroneous wedges, a non-trivial post-processing is needed. Wan *et al.* [Wan et al. 2011] proposed a topology-preserving polycube mapping optimization algorithm that simultaneously optimizes the polycube domain shape and surface mapping. More recently, Li *et al.* [Li et al. 2013a] presented an effective polycube construction and optimization algorithm using 3D homotopic morphological operations.

Polycube splines These polycube parameterizations can be used for *polycube spline* construction [Wang et al. 2008; Li et al. 2013a; Wang et al. 2012]. An affine atlas can be constructed from the polycube map in the following way. Each face and edge on the polycube domain Ω are associated with its own local chart. Each *face chart* covers only interior points of corresponding face and leaves off all the edges of the face. Each *edge chart* covers interior points of the edge but leaves off corner vertices. Furthermore, there are overlaps between face charts and edge charts. The transition functions between overlapped edge and face charts are simply translations and rotations. Note that there is no vertex chart for the corner vertex, i.e., the corners are singular points, denoted by C. Therefore, by removing all the corners, polycube map naturally induces the affine structure [Wang et al. 2008] and spline surfaces can be directly defined on polycube domain. These concepts are illustrated in Fig. 11.

The key advantage for defining splines over polycube maps is that each face chart of the polycube is nothing more than a union of rectangles. Tensor-product splines can be naturally defined over rectangular regions. Using the T-splines [Sederberg et al. 2003], we can flexibly control the hierarchical and level-of-detail refinement in spline constructions. For every control point in the T-mesh, the covering region of its basis function is a rectangle, whose side lengths (knot vectors) are determined by the connectivity of the T-mesh. On each chart, the basis functions are enforced to vanish outside the boundary of the chart. Thus, the face charts are totally separate from each other. Each edge chart connects two face charts (one face chart if it is a boundary edge and not shared by two faces). Therefore, given an arbitrary parameter $u \in \Omega \backslash C$, it may be covered by a single face chart, or a single edge chart, or by one face chart and one edge chart. On each (edge and face) chart (U_i, ϕ_i), the spline patch is defined as a point-based spline whose control points form a T-mesh.

The *polycube spline* can be formally defined as $\mathbf{F}(\mathbf{p}) = \sum_i \mathbf{F}_i(\mathbf{p})$, $\mathbf{p} \in \Omega \backslash C$, where $\mathbf{F}_i(\mathbf{p}) = \sum_j \mathbf{c}_j B_j(\phi_i(\mathbf{p}))$ is the spline surface patch defined on an edge or face chart (U_i, ϕ_i) and $\mathbf{c}_j \in \mathbb{R}^3$ are the control points, and B_j are the basis functions. The spline fitting can be formulated as minimizing a linear combination of interpolation and fairness functionals, i.e., $\min\{E_{dist} + \lambda E_{fair}\}$. The first part is the least-squares approximation error $E_{dist} = \sum_{i=1}^m \|\mathbf{F}(\mathbf{p}_i) - \mathbf{p}_i\|^2$, where $\mathbf{p}_i \in \mathcal{M}$ is the parameter for $\mathbf{p}_i$, $i = 1, \ldots, m$. The second part is a smoothing term. A frequently used example is the thin-plate energy

$$E_{fair} = \int \int_M (\mathbf{F}_{uu}^2 + \mathbf{F}_{uv}^2 + \mathbf{F}_{vv}^2)^2 dudv.$$

A few polycube spline surfaces are illustrated in Fig. 12. Similarly, the polycube surface splines can be generalized to volumetric splines for solid models [Wang et al. 2012].

| Polycube map | T-spline | T-junction | Control points |
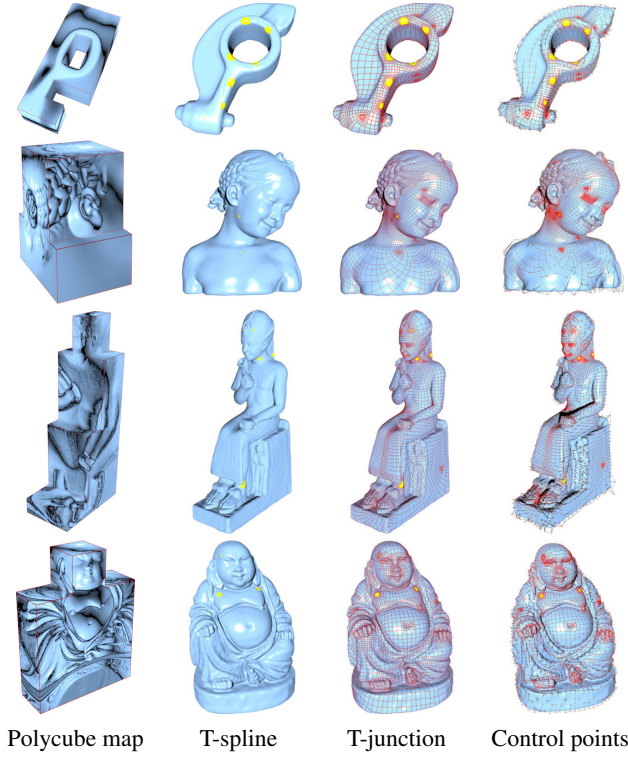
Figure 12: *Polycube Spline surface examples [Wang et al. 2008].*

4.5 Moving least-squares and local approximation

As an alternative to the global approximation schemes previously introduced, we review two local methods that are based on the moving least-squares (MLS) approximation with polynomials and the local approximation with RBFs.

MLS approximation with polynomials The key element of the MLS approximation is the solution of a linear system, whose size is proportional to the degree of the polynomials that are reproduced by the method [Farwig 1986; Levin 1998]. To this end, we search the approximation $F : \mathbb{R}^3 \to \mathbb{R}$ in the linear space $\mathscr{F} := \mathrm{span}\{\varphi_1(\mathbf{p}), \dots, \varphi_r(\mathbf{p})\}$ generated by the monomials $\varphi_i(\mathbf{p})$, $\mathbf{p} := (x, y, z)$, $i = 1, \dots, r$, of degree lower than s. In the space $\mathscr{F}$, the norm $\| \cdot \|_{W(\mathbf{p})}$ is induced by the weighted l_2 scalar product

$$\langle f, g \rangle_{W(\mathbf{p})} := \sum_{i=1}^{n} f(\mathbf{p}_i) g(\mathbf{p}_i) W(\mathbf{p}, \mathbf{p}_i) = \mathbf{f}^\top W(\mathbf{p}) \mathbf{g}, \tag{8}$$

with $W(\mathbf{p}) := \mathrm{diag}(W(\mathbf{p}, \mathbf{p}_i))_{i=1}^n$ positive-definite diagonal matrix and arrays $\mathbf{f} := (f(\mathbf{p}_i))_{i=1}^n$, $\mathbf{g} := (g(\mathbf{p}_i))_{i=1}^n$. A common choice is the exponential map $W(\mathbf{p}, \mathbf{p}_i) := \exp(-\|\mathbf{p} - \mathbf{p}_i\|_2 / \sigma(\mathbf{p}))$ of width $\sigma(\mathbf{p})$. Then, the MLS approximation F is the solution to the quadratic minimization problem $\min_{F \in \mathscr{F}} \{\|F - f\|_{W(\mathbf{p})}\}$. Deriving the energy $\mathscr{E}(\alpha) := \sum_{i=1}^n |F(\mathbf{p}_i) - f(\mathbf{p}_i)|_2^2 W(\mathbf{p}, \mathbf{p}_i)$, with respect to the unknown $\alpha(\mathbf{p}) := (\alpha_i(\mathbf{p}))_{i=1}^r$, we get that the stationary points of $\mathscr{E}$ solve the equations $\partial_{\alpha_i(\mathbf{p})} \mathscr{E} = 0$, $i = 1, \dots, r$, if and only if the following system of equations is satisfied

$$\left[\Phi^\top W(\mathbf{p}) \Phi \right] \alpha(\mathbf{p}) = \Phi^\top W(\mathbf{p}) \mathbf{f}. \tag{9}$$

Here, the Gram matrix Φ associated to the kernel that generates the RBFs and the vector of the f-values are $\Phi := (\varphi_{ij})_{i=1,\dots,n}^{i=1,\dots,r}$, $\varphi_{ij} := \varphi_j(\mathbf{p}_i)$. Since the kernel φ is positive-definite and the matrix $W(\mathbf{p})$ is diagonal, the $r \times r$ coefficient matrix $\Phi^\top W(\mathbf{p}) \Phi$ is symmetric and positive definite. In particular, Eq. (9) has a unique solution.

Finally, we notice that the MLS approximation generalizes the Partition of the Unity. In fact, considering only constant polynomials $\{\varphi_i(\mathbf{p})\}_{i=1}^r$, the MLS approximation $F(\cdot)$ reduces to the *partition of the unity* (PU) [Jin et al. 2009a]. Since the MLS scheme reproduces a class of functions larger than the constant ones, the accuracy of the MLS approximation is generally higher than the PU scheme.
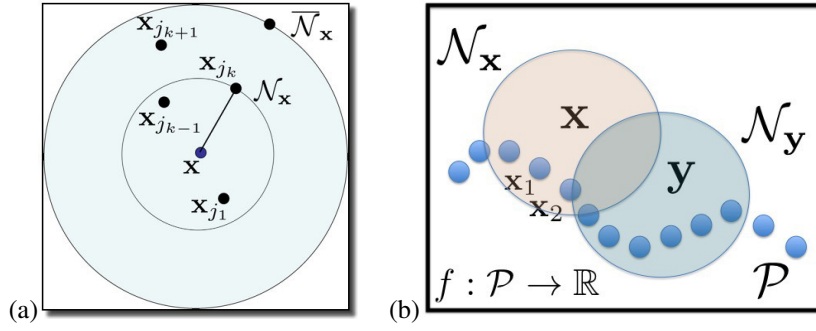
Figure 13: *(a,b) Neighbors $\mathcal{N}_{\mathbf{p}}$ and $\overline{\mathcal{N}}_{\mathbf{p}}$ of $\mathbf{p}$, $\mathcal{N}_{\mathbf{p}} \subseteq \overline{\mathcal{N}}_{\mathbf{p}}$, used for the computation of the value $F(\mathbf{p})$.*

Associating a weight $W(\mathbf{p}, \mathbf{p}_i)$ to each point $\mathbf{p}_i$ with respect to $\mathbf{p}$ allows us to adapt the least-squares constraints to the local distribution of the points, thus including both the f-values and the local the local distribution of points in the computation of $F(\mathbf{p})$. Since the weight function $W(\cdot, \cdot)$ rapidly decreases to zero, the indices of the sum in (8) and in the following equations are restricted to those of the points that belong to a neighbor $\mathcal{N}_{\mathbf{p}} := \{\mathbf{p}_{j_s}\}_{s=1}^{k}$ of $\mathbf{p}$, which includes those points of $\mathcal{P}$ that fall inside the sphere of center $\mathbf{p}$ and radius $\sigma(\mathbf{p})$; i.e., $\|\mathbf{p}_{j_s} - \mathbf{p}\|_2 \leq \sigma(\mathbf{p})$, $s = 1, \ldots, k$ (Fig. 13(a)). Here, the value $\sigma(\mathbf{p})$ is chosen according to the local sampling density of $\mathcal{P}$ [Pauly et al. 2003]. For simplicity, we omit the dependence of the number k of points in $\mathcal{N}_{\mathbf{p}}$ from $\mathbf{p}$ and $\sigma(\mathbf{p})$. This choice makes the approximation scheme *local*; improves the efficiency of the computation of $F(\mathbf{p})$; avoids to sample every basis function φ_i at $\mathbf{p}$; and generally reduces the conditioning number of the coefficient matrix in each normal equation.

**Local approximation with RBFs** Since MLS approximations [Dyn et al. 1986; Micchelli 1986; Wendland 1995] and the multi-level PU [Ohtake et al. 2003] involve a polynomial basis, they cannot interpolate the f-values in an easy way. In fact, the degree of the fitting polynomial determines the number of interpolating conditions and not *viceversa*. For instance, in 3D a polynomial of degree two or three requires to impose ten or twenty interpolating constraints; however, we might have a different number of points in different neighbors. Furthermore, in case of uneven sampling fixing the number of points in each neighbor instead of its radius, or increasing the polynomial degree, provides unstable results due to the ill-conditioning of the corresponding Gram matrices [Golub and VanLoan 1989].

The idea behind the local approximation [Patané and Spagnuolo 2012] is to apply the MLS approximation with RBFs. Using a set of radial instead of polynomial basis functions allows us to combine interpolating constraints for feature preservation and LS conditions for noise removal. In fact, the number of local interpolating constraints is equal to the number of RBFs and no more related to the degree of the polynomial used for the local approximation. For the evaluation of $F(\mathbf{p})$, we consider as interpolating or least-squares constraints only the f-values at those points of $\mathcal{P}$ that belong to $\mathcal{N}_{\mathbf{p}}$. This choice is motivated by the observation that the behavior of any approximation of f at $\mathbf{p}$ is mainly controlled by the f-values in $\mathcal{N}_{\mathbf{p}}$. Indeed, the evaluation point $\mathbf{p}$ drives the selection of a set of interpolating conditions and the construction of the local approximation F in $\mathcal{N}_{\mathbf{p}}$ (Fig. 13(b)). In $\mathcal{N}_{\mathbf{p}}$, we approximate the input scalar function $f : \mathcal{M} \to \mathbb{R}$ with the implicit map $F : \mathbb{R}^3 \to \mathbb{R}$, which is the linear combination of the RBFs $\mathcal{B} := \{\varphi_{j_s}(\mathbf{p}) := \varphi(\|\mathbf{p} - \mathbf{p}_{j_s}\|_2)\}_{s=1}^{k}$; i.e.,

$$\begin{cases} F(\mathbf{p}) := \sum_{s=1}^{k} \beta_s(\mathbf{p}) \varphi_{j_s}(\mathbf{p}) = \beta^\top(\mathbf{p}) \tilde{\varphi}(\mathbf{p}), \\ \beta(\mathbf{p}) := (\beta_s(\mathbf{p}))_{s=1}^{k}, \quad \tilde{\varphi}(\mathbf{p}) := (\varphi_{j_s}(\mathbf{p}))_{s=1}^{k}. \end{cases} \tag{10}$$

Each function φ_{j_s} is generated by a map $\varphi : \mathbb{R}^+ \to \mathbb{R}$ and centered at $\mathbf{p}_{j_s}$ [Dyn et al. 1986; Micchelli 1986]. The local LS approximation takes into account the f-values at the points of a neighbor $\overline{\mathcal{N}}_{\mathbf{p}}$ larger than $\mathcal{N}_{\mathbf{p}}$. Generally, $\overline{\mathcal{N}}_{\mathbf{p}}$ is the neighbor of $\mathbf{p}$ whose radius is twice the radius of $\mathcal{N}_{\mathbf{p}}$. Then, F is computed by minimizing the error $\sum_{s=1}^{h} |F(\mathbf{p}_{j_s}) - f(\mathbf{p}_{j_s})|^2$ through the normal equation

$$(\Phi^\top \Phi) \beta(\mathbf{p}) = \Phi^\top \mathbf{f}_h, \quad \Phi := (\varphi_{sr})_{s=1,\ldots,h}^{r=1,\ldots,k}, \tag{11}$$

where $\varphi_{sr} := \varphi(\|\mathbf{p}_{j_r} - \mathbf{p}_{j_s}\|_2)^2$, $\overline{\mathcal{N}}_{\mathbf{p}} := \{\mathbf{p}_{j_s}\}_{s=1}^{h}$, $k \leq h \leq n$, and $\mathbf{f}_h := (f(\mathbf{p}_{j_s}))_{s=1}^{h}$ is the $h \times 1$ right-hand side vector. Since Φ is a full-rank matrix, $(\Phi^\top \Phi)$ is invertible and Eq. (11) has a unique solution. If $\overline{\mathcal{N}}_{\mathbf{p}} \equiv \mathcal{N}_{\mathbf{p}}$, then the normal equation (11) reduces to $\Phi \beta(\mathbf{p}) = \mathbf{f}_h$. Indeed, in $\mathcal{N}_{\mathbf{p}}$ we compute the function $F : \mathbb{R}^3 \to \mathbb{R}$ that interpolates the values of f at the points of $\mathcal{N}_{\mathbf{p}}$; i.e., $F(\mathbf{p}_{j_s}) = f(\mathbf{p}_{j_s})$, $s = 1, \ldots, k$. To test the extrapolation capability, the local approximation underlying the input data in Fig. 14(a) is resampled on a higher resolution grid with interpolating (Fig. 14(b)) and LS (Fig. 14(c)) constraints. Increasing the neighbor size we get a larger number of basis functions in Eq. (10), which might introduce local and small perturbations to

| (a) Input res.: 50×50 | (b) Interp.: 100×100 | (c) LS: 100×100 | (d) Approx. err. |
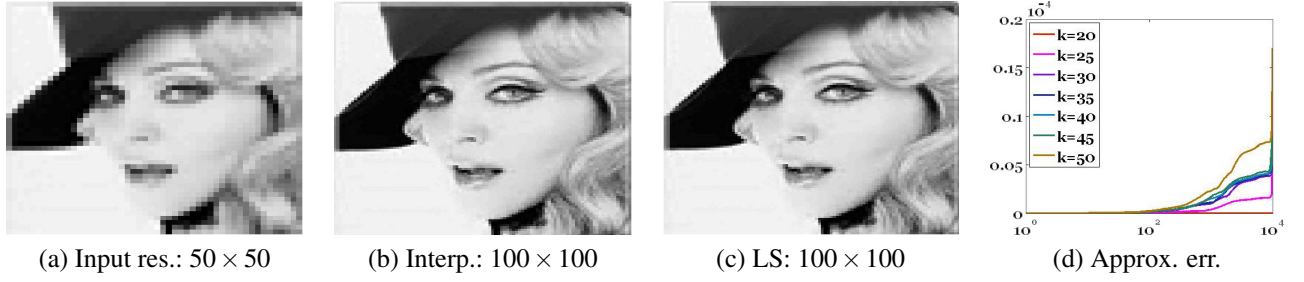
Figure 14: *(a) Input $f : \mathscr{P} \to \mathbb{R}$ and local approximation $F : \mathbb{R}^2 \to \mathbb{R}$ with RBFs and (b) interpolating or (c) LS constraints. (d) $\mathscr{L}^\infty$ error (y-axis) at each pixel (x-axis) of (c) with respect to a different k-nearest neighbor.*

the evaluation of the F-values. As a result, the approximation error slightly increases but remains lower than 10^{-4} (Fig. 14(d)).

4.6 Topology-driven approximation

Traditional approaches to function approximation are mainly driven by a numerical error estimation: from our perspective, instead, the critical points are a natural choice to guide the approximation scheme as they usually represent very relevant information about the phenomena coded by f. For instance, in biomolecular simulation the maxima of the electrostatic charge are those features that guide the interaction and that should be preserved for a correct analysis of the phenomenon. Approximating the electrostatic charge on a molecular surface without preserving the distribution of its maxima and minima introduces artifacts in the modeling of those interactions that are guided by the energy extrema. Indeed, our aim is to compute a smooth function $F : \mathbb{R}^3 \to \mathbb{R}$ such that the piecewise linear map $F_{\mathscr{P}}$, which interpolates the values of F at the vertices of $\mathscr{P}$, approximates the piecewise linear scalar function $f : \mathscr{M} \to \mathbb{R}$ within a prescribed error and preserves its critical points. The *topology-driven approximation* [Patanè and Falcidieno 2009] computes $F := F_1 + F_2$ as the sum of two components $F_1, F_2 : \mathbb{R}^3 \to \mathbb{R}$ such that

- F_1 captures the global structure of f in terms of its critical points; i.e., the piecewise linear scalar function $f_1 := F_{1,\mathscr{P}}$ that interpolates the values of F_1 at the vertices of $\mathscr{P}$ has the same critical points of f. On the basis of this property, we refer to f_1 as the *global component* of f;

- F_2 recovers the local details of f; i.e., the piecewise linear scalar function $f_2 := F_{2,\mathscr{P}}$, which interpolates the values of F_2 at the vertices of $\mathscr{P}$, guarantees that the error between f and $f_1 + f_2$ is below the target approximation accuracy. On the basis of this property, we refer to f_2 as the *local component* of f.

The function F_1 is computed as a linear combination of globally-supported radial basis functions [Aronszajn 1950; Bloomenthal and Wyvill 1997; Dyn et al. 1986; Poggio and Girosi 1990], whose centers are selected through an iterative procedure which converges in a generally low number of steps. The function F_2 is generated as a linear combination of locally-supported radial basis functions, using as error metric the $\mathscr{L}^\infty$-norm or a local comparison measure [Biasotti et al. 2007; Edelsbrunner et al. 2004].

The choice of globally-supported and compactly-supported radial basis functions enable to adapt the construction of the approximation to specific problem constraints, such as the number of input samples, the local accuracy, and the degree of smoothness of the final approximation. The approximation method can also be applied to smooth the function f by selecting only the critical points that are perceived as informative ones. For instance, f might exhibit *differential noise*, such a high number of critical points with very close positions and low variation of the f-values, which is typically due to a low quality of the discrete representations of the input data, unstable computations, or noisy measurements.

Whenever the scalar function f has a large number of critical points associated to a low variation of the f-values, it is useful to simplify them and compute a smooth approximation of f with a lower number of critical points. Then, the idea is to build the volumetric approximation by using only the critical points of f that describe its global behavior and neglecting those that are redundant. To this end, we use the persistence-based simplification to identify the set of critical points which guide the implicit approximation of f. In some cases, it might happen that we get a function $h := F_{\mathscr{P}}$ whose set of critical points *strictly* includes the preserved maxima, minima, and saddles of f. In Fig. 15, we show the topology-driven approximation of a noisy scalar functions on a 3D shape.

| (a) $(\mathscr{P}, f), g = 7$ | (b) f | (c) $h := g_{\mathscr{P}}$ | (d) h | (e) g |
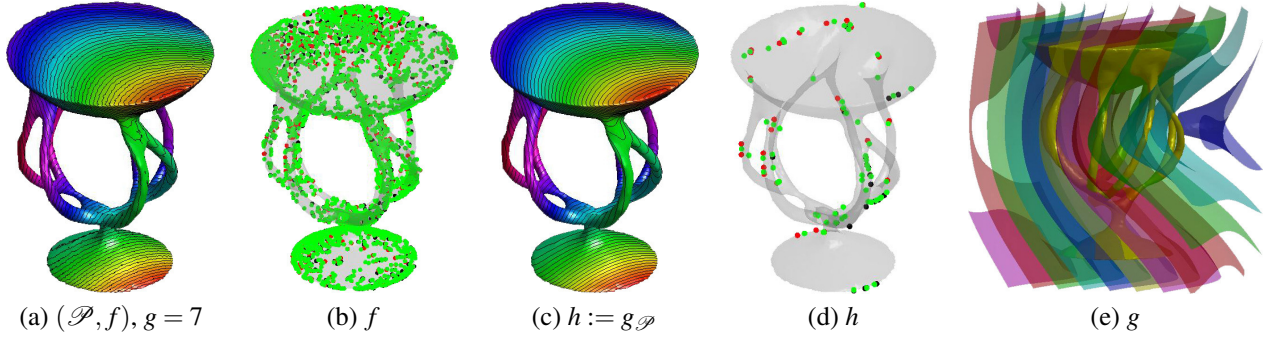
Figure 15: *Level sets and critical points of (a,b) a noisy map f with $m = 1426$ minima, $M = 1550$ maxima, $s = 2988$ saddles and (c,d) its smoothed approximation $h := g_{\mathscr{P}}$ of f. Here, h has $m = 28$ minima, $M = 25$ maxima, and $s = 65$ saddles. In h, the critical points of f with low-persistence have been smoothed out by the topology-driven approximation and the $\mathscr{L}^{\infty}$-error between f and h is below 0.001. (e) Iso-surfaces of g. Note that the level sets in (c) and the iso-surfaces in (e) smoothly resemble the noisy level sets in (a).*

4.7 Computational cost

Approximation schemes [Dyn et al. 1986; Micchelli 1986; Wendland 1995; Martin et al. 2008a; Turk and O'Brien 2002] apply interpolating or LS constraints globally; then, the resulting approximation is evaluated at any sample point. Since a $n \times n$ linear system is solved once, the computational cost of the approximation with globally- and locally-supported RBFs is $O(n^3)$ and $O(n \log n)$, respectively. Selecting k centers through spectral clustering and sparse representations (e.g., [Patanè 2013a]) and applying the least-squares approach take $O(n \log n)$ and $O(k^3)$ time, respectively.

The computation of the nearest neighbor graph takes $O(n \log n)$ time [Arya et al. 1998]. Assuming that the neighbor $\mathcal{N}_{\mathbf{p}}$ contains k points, the evaluation of $F(\mathbf{p})$ with the MLS and local approximation scheme requires to solve a $k \times k$ linear system, where k is generally small (i.e., $20 \leq k \leq 30$) and much lower than n. Its solution takes $O(k^3)$ time with direct solvers and varies from $O(k)$ to $O(k^2)$ in case of sparse coefficient matrix and iterative solvers [Golub and VanLoan 1989]. Then, the evaluation of F at s sample points varies from $O(sk^3)$ to $O(sk)$.

According to Table 1, the computational cost of the MLS and local approximation with RBFs is generally lower than the approximation with globally-supported and locally-supported RBFs. It also reduces the memory storage from $O(n^3)$ and $O(kn)$ to $O(k^3)$. Finally, our method has the same order of computational complexity of local approximation schemes, such as the MLS approximation [Dyn et al. 1986; Micchelli 1986; Wendland 1995] and the multi-level PU [Ohtake et al. 2003].

5 Applications

We focus on the main applications of the volumetric approximation of surface-based and volume-based scalar functions to shape modeling and analysis (Sect. 5.1) and medicine (Sect. 5.2).

5.1 Shape modeling and analysis

Among the several applications of surface-based and volume-based methods in shape modeling and analysis, we have outlined how the Laplacian eigenvectors of a given surface are extended into the shape interior using piecewise linear interpolation with barycentric coordinates (Sect. 4.1). These volumetric eigenvectors provide the basis for the definition of shape-aware barycentric coordinates and of volumetric shape descriptors, such as the volumetric global point signature, biharmonic and diffusion embeddings, which have been primarily defined for the surface setting. Furthermore, we have discussed how shape correspondences are computed by matching manifold harmonics or mapping the surface features onto a template using barycentric coordinates with first order precision (Sect. 4.3). We have also presented template-based shape descriptors and the computation of harmonic volumetric mappings between solid objects with the same topology for volumetric parameterization, solid texture mapping, and hexahedral remeshing. In the following, we focus our attention on the integration of surface-based and volume-based descriptors for shape comparison.

Surface-based and volume-based descriptors for shape comparison. In [Bronstein et al. 2010b; Bronstein et al. 2010c; Bronstein et al. 2011], the performances of surface-based and volume-based descriptors for shape matching have been tested
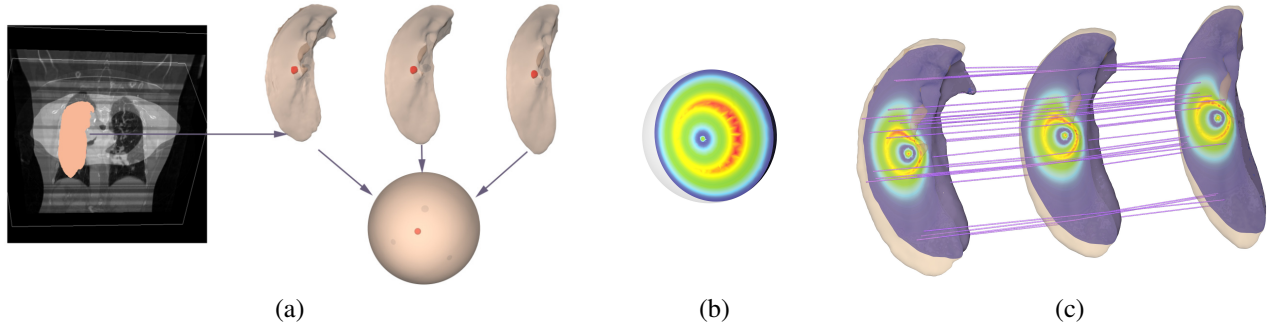
Figure 16: *Parameterization of sequential lung/tumor volumes over a common domain [Xu et al. 2013]. (a) The dynamically deforming lung/tumor models and their parameterization onto a sphere domain; (b) the transferred distance field from one lung model to the sphere domain; (c) the correspondence among sequential models induced by the volumetric parameterization.*

Table 1: *Computational cost of different approximations: solution of the normal equation (LSys.); evaluation of F at* $\mathbf{p}$ *(Ev.* $\mathbf{p}$*) and a set* $\mathscr{S}$ *of s samples (Ev.* $\mathscr{S}$*). The column (Con.) indicates the type of constraints; i.e., interpolating (In.) and least-squares (LS.). Approximation methods include MLS with RBFs, MLS with polynomial functions [Dyn et al. 1986; Micchelli 1986; Wendland 1995], Partition of the Unity (PU) [Ohtake et al. 2003], locally [Morse et al. 2001] and globally-supported RBFS [Turk and O'Brien 2002].*

Approx. Scheme	LSys.	Ev. p	Ev. $\mathscr{S}$	Con.
MLS with RBFs	$O(k^3)$	$O(k)$	$O(sk^3)$	In./Ls.
MLS	$O(k^3)$	$O(k)$	$O(sk^3)$	Ls.
PU	$O(k^3)$	$O(k)$	$O(sk^3)$	Ls.
LocS-RBF	$O(n^2)$	$O(n)$	$O(sk^3)$	In./Ls.
GS-RBF	$O(n^3)$	$O(n)$	$O(sk^3)$	In./Ls.

on the SHREC'10 data set. It consists of shapes modified through transformations of different strength. The transformations are: *null transformation*, *isometry* (non-rigid almost isometric deformations), *topology* (welding of shape vertices resulting in different triangulation), *micro holes* and *big holes*, *global* and *local scaling*, *additive Gaussian noise*, *shot noise*, *down-sampling* (less than 20% of the original points), *partial occlusion*, and *mixed transformation*.

For the robust feature detection and description benchmark [Bronstein et al. 2010b], the number of transformations *per* shape was 45 and the total data set size was 138. Three classes of feature description methods have been compared: (i) the heat kernel signature [Sun et al. 2009] with Voronoi-cot weights and feature points detected as local maxima of the signature without/with (SHK1/SHK2) simplification based on persistence homology [Zomorodian and Carlsson 2005]; (ii) the dense signature [Bronstein et al. 2011] based on the Voronoi-cot (DHK1) and wFEM (DHK2) heat kernel; (iii) the spin image signatures [Johnson and Hebert 1999] (SP). The heat kernel signatures show the best results among the compared algorithms; on average, the wFEM heat kernel provides the highest robustness among all the transformations of different strength. According to the results and discussion reported in [Bronstein et al. 2010b; Bronstein et al. 2010c], among sparse descriptors (SHK1, SHK2, and spin images SI) the best results in average repeatability are achieved by SHK1. Furthermore, the best results in average repeatability in local scale and sampling classes are achieved by SHK1; in micro holes and scale, the best results are provided by SHK2; in isometry, holes, noise classes, SHK1 and SHK2 have similar performances; and spin image (SI) feature descriptor performs the best in topology and shot noise classes. Among dense descriptors (DHK1 − 3), DHK1 and DHK2 show equal average performance, with FEM-based descriptor (DH2) being slightly better in the topology, local scale, sampling, and noise classes; the scale-invariant heat kernel signatures (DHK3) perform the best in the scale class.

For the robust large-scale shape retrieval benchmark [Bronstein et al. 2010c], the total number of transformations per shape was 55 and the total number of query shapes was 715. Three classes of methods have been compared: visual similarity [Lian et al. 2010a; Lian et al. 2010b]; part-based bags of features [Toldo et al. 2009]; Shape-Google [Bronstein et al. 2011] based on the heat kernel shape descriptor using Voronoi-cot [Desbrun et al. 1999; Pinkall and Polthier 1993] or wFEM weights (Sect. 3.2), with or without kernel normalization [Bronstein and Kokkinos 2010]. For the evaluation of the results, we have used the *mean average precision (mAP)*; i.e., $mAP := \sum_i P(i)rel(i)$, where $rel(i)$ is the relevance of a single rank and the *precision* $P(i)$ is computed as the percentage of relevant shapes in the first i top-ranked retrieved shapes. Ideal retrieval performance results in
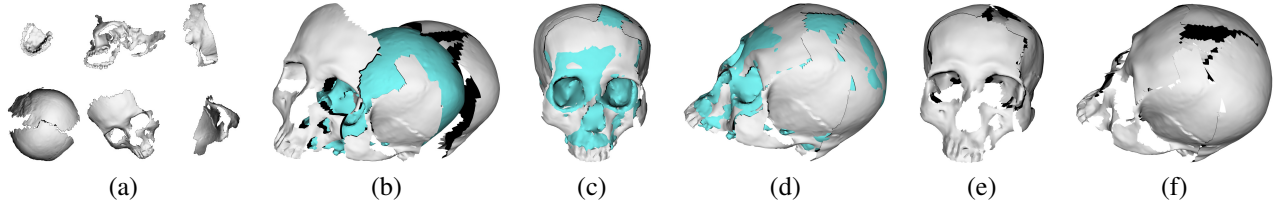
Figure 17: *Template-guided fragment reassembly. [Yin et al. 2011]. (a-d) Fragments (grey) are reassembled using a template template skull (blue); (e-f) show the assembly results.*

$mAP = 100\%$.

On average, HKS local descriptor computed with Voronoi-cot weights and 96 bit similarity sensitive hash and Shape-Google using scale-invariant heat-kernel signatures, which represents 3D shapes as binary codes through bag-of-features embedded in the Hamming space, have the best performances on all class of transformations. In this case, we have $98,27\%$ mAP on the full query set. Second best in all strengths is Visual Similarity with 94.33% mAP and at the third place we have SI-HKS local descriptor computed with Voronoi-cot weights with 90.79% mAP. Finally, VS2 and Shape-Google using heat kernel shape descriptors based on the wFEM discretization have the best robustness to sampling density; visual similarity based on clock matching bag of features without modified manifold ranking also has the best performance in mixed transformation class.

5.2 Medical applications

In the context of medicine, we discuss how the volumetric approximations and harmonic maps can be used for conformal brain mapping, lung tumor respiratory motion modeling, medical and forensic skull modeling and facial reconstruction.

Respiratory motion modeling for lung tumor radiotherapy Cross-volume mapping can facilitate the design of next generation radiotherapy management system. Cancer patients often need to be treated by external beam radiation therapy. The radiation should target at the solid tumor and avoid damaging surrounding normal tissues. Recently, with the improved understanding of radiobiology and enhanced radiation hardware systems, radiotherapy planning and delivery guided by scanned-images becomes a important research direction in medical imaging [Iyengar et al. 2012]. For example, lung cancer is one of the most common human cancer, whose effective radiation treatment is critical but challenging due to the highly dynamic motions of the tumor and surrounding tissues during respiratory cycles.

Sequentially scanned volumetric CT/MR images can be parameterized on a common domain, to model and predict the deformation of the lung tumor and surrounding tissues. This is referred to as the *4D parameterization* of dynamic data [Metz et al. 2011; Xu et al. 2012]. Formally, given sequential volumetric data $\mathcal{M}_i \subset \mathbb{R}^3$ taken at different time $t_i, i = 1, \ldots, m$, the goal is to build a 4D parametric deformation model $\Psi(\mathbf{p}, t) : \Omega \times \mathbb{R} \to \mathbb{R}^3$, where $\mathbf{p} \in \Omega \subset \mathbb{R}^3$ and $t \in \mathbb{R}$, so that: (i) spatially, it interpolates the sample frames (i.e., $\Psi(\Omega, t_i) = \mathcal{M}_i$) and the deformation (which is a 3D volumetric mapping between $\Psi(\mathbf{p}, t)$ and $\Psi(\mathbf{p}, t + \delta t)$) should minimize the geometric distortion; (ii) temporally, the motion $\partial \Psi / \partial t$ should be smooth so that the trajectory would be smooth. With this 4D parameterization, we can understand and predict how the data change by interpolating/extrapolating their geometry or trajectory on any given time T. Fig. 16 shows the computation of correspondences among sequential lung/tumor volumes induced by volumetric paramterizations over a common domain.

Medical and forensic skull modeling and facial reconstruction Facial reconstruction is a process of recreating faces of decedents from their skeletal remains. Its main stimuli have sprung from various forensic, clinical, and academic fields. For example, in law enforcement, it is an important enabling tool to identify victims or suspects [Manhein et al. 2000]; in craniofacial orthopedics, it can improve pre-operative surgical planning [Berar et al. 2005]; in archaeology, it helps create visual images of historic figures or ancient people [Benazzi et al. 2009b; Benazzi et al. 2009a]. The empirical foundation for facial reconstruction results from academic human anatomy. The common fundamental objective is to seek the best shape approximation of the face from the skull. Direct creation of facial geometry from a limited set of anthropological rules can result in a search on a overly large shape space. With effective surface and volume matching, we can use skull and soft-tissue templates [Greef et al. 2005; Vandermeulen et al. 2005] to help guide skull and face shape modeling and synthesis.

Skull Modeling. The fragmented or incomplete skulls can be restored with the help of subject-template matching [Yin et al. 2011; Li et al. 2011; Yu et al. 2012]. The fragment reassembly problem can be formulated as follows. Given a set of fragment surfaces S_i, fragments $\mathcal{M}_i^S, i = 1, 2, \ldots, n$, the *reassembly* process is to compute a set of transformations Φ_i that compose fragments into a whole skull $\mathcal{M}^S = \bigcup_{i=1}^n \Phi_i(\mathcal{M}_i^S)$. Fig. 17 illustrates an example of fragmented skull reassembly. Using
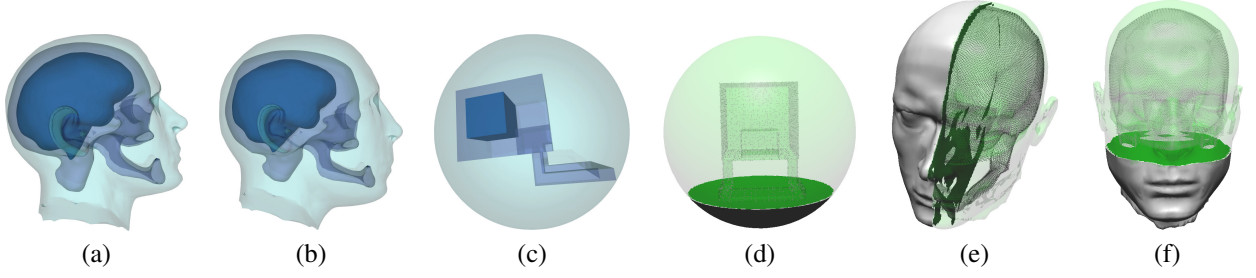
Figure 18: *Volumetric head modeling [Li et al. 2010b]. (a) The parameterization of a head template model onto a sphere domain (c). The 50% linear interpolation (b) illustrates the mapping effect. (d-f) visualize the modeling of the head model (e) over the parametric domain (d).*

a complete template skull $\mathcal{M}^T$ as guidance and the fragment-template matching, one can develop effective 3D reassembly algorithm. When the object and fragments can be considered as *thin shells* and approximated as surface patches. We can solve Φ_i for $\mathcal{M}_i^S, i = 1, \dots, n$, so that each $\Phi_i(\mathcal{M}_i^S)$ matches with a subregion of $\mathcal{M}^T$. The maps Φ_i are used to assemble the fragments, and they can be solved by a optimization

$$\begin{cases} \{\Phi_i\} = \mathrm{argmin}_{\{\Phi_i\}} \, D(\mathcal{M}^T, \bigcup_{i=1}^n \Phi_i(\mathcal{M}_i^S)) \\ \Phi_i(\mathcal{M}_i^S) \bigcap \Phi_j(\mathcal{M}_j^S) = \emptyset, \forall i, j, \end{cases}$$

where the *objective function* $D(\mathcal{M}, \mathcal{N})$ measures the geometric deviation between shapes $\mathcal{M}$ and $\mathcal{N}$, (i.e., here deviation between $\mathcal{M}^T$ and the composition of transformed fragments); the *constraints* mean that composed fragments should not intersect with each other.

Facial Reconstruction. The subject face can also be synthesized by transforming template face onto a subject skull, preserving common facial geometric characteristics [Kähler et al. 2003]. Given a template skull surface $\mathcal{M}^T$ and its corresponding face surface $\mathcal{H}^T$, the template soft tissue $\mathcal{V}^T$ is the volumetric region bounded by $\mathcal{M}^T$ and $\mathcal{H}^T$. Denote the inner and outer boundaries of $\mathcal{V}^T$ as $\partial_i \mathcal{V}^T = \mathcal{M}^T$ and $\partial_o \mathcal{V}^T = \mathcal{H}^T$. We can synthesize the facial tissue V^S on the subject skull $\mathcal{M}^S$ using a bijective transformation Φ applied on $\mathcal{V}^T$, that enforces $\Phi(\partial_i \mathcal{V}^T)$ conform with the subject skull surface $\mathcal{M}^S$. Then, the transformed template outer boundary, $\Phi(\partial_o \mathcal{V}^T)$, will synthesize the subject face. This reduces to a *volumetric mapping* $\Phi : \mathcal{V}^T \to V^S$ satisfying a set of synthesis constraints, such as inner boundary constraint ($\Phi(\mathcal{M}^T) = \mathcal{M}^S$), tissue-depth constraints (to enforce tissue thickness over skull anthropometric points), anthropometric or aesthetic constraints (to preserve general face geometric characteristics), and structural alignment constraints (to preserve nonuniform muscle/gland layers). Generally, Φ can be formulated as a minimizer of the following energy:

$$\min_{\Phi} \int_{\mathcal{V}^T} \|\nabla \Phi(\mathbf{p}) - G(\mathbf{p})\|^2 d\mathbf{p},$$

subject to the given synthesis constraints. Here, a matrix tensor field G is used to control the gradient of the deformation Φ. Without considering any directional alignment, one can set $G = 0$. One can also synthesize the inhomogeneous tissues (e.g., muscles and glands) by setting different material stiffness and using different G. An example of volumetric head modeling is shown in Fig. 18

6 Conclusions and future work

While previous work has addressed the processing and analysis of 3D shapes through methods that exploit either their surface-based or volumetric representations, this survey has presented a unified overview on these works through volumetric approximations of surface-based scalar functions. This unified scheme has also provided a basis for generalizing those methods that have been primarily defined on surfaces but are open to and benefit of the integration with volumetric information. Furthermore, it has systematically presented the theory, algorithm, and applications of discrete Ricci flow.

References

ALEXA, M., AND WARDETZKY, M. 2011. Discrete Laplacians on general polygonal meshes. *ACM Transactions on Graphics 30*, 4.

ALEXA, M. 1999. Merging polyhedral shapes with scattered features. In *Proc. of the Int. Conf. on Shape Modeling and Applications*, 202–210.

ALPERT, C. J., KAHNG, A. B., AND YAO, S.-Z. 1999. Spectral partitioning with multiple eigenvectors. *Discrete Applied Mathematics 90*, 1-3, 3–26.

ARONSZAJN, N. 1950. Theory of reproducing kernels. *Trans. of the American Mathematical Society 68*, 337–404.

ARYA, S., MOUNT, D. M., NETANYAHU, N. S., SILVERMAN, R., AND WU, A. Y. 1998. An optimal algorithm for approximate nearest neighbor searching fixed dimensions. *Journal of the ACM 45*, 6, 891–923.

ASIRVATHAM, A., PRAUN, E., AND HOPPE, H. 2005. Consistent spherical parameterization. In *Int. Conf. on Computational Science (2)*, 265–272.

BANCHOFF, T. 1967. Critical points and curvature for embedded polyhedra. *Journal of Differential Geometry 1*, 245–256.

BARNARD, S. T., POTHEN, A., AND SIMON, H. D. 1993. A spectral algorithm for envelope reduction of sparse matrices. In *Proc. of the ACM Supercomputing*, 493–502.

BELKIN, M., AND NIYOGI, P. 2003. Laplacian eigenmaps for dimensionality reduction and data representation. *Neural Computations 15*, 6, 1373–1396.

BELKIN, M., AND NIYOGI, P. 2006. Convergence of Laplacian eigenmaps. In *NIPS*, 129–136.

BELKIN, M., AND NIYOGI, P. 2008. Towards a theoretical foundation for Laplacian-based manifold methods. *Journal of Computer System Sciences 74*, 8, 1289–1308.

BENAZZI, S., FANTINI, M., CRESCENZIO, F. D., MALLEGNI, G., MALLEGNI, F., PERSIANI, F., AND GRUPPIONI, G. 2009. The face of the poet Dante Alighieri reconstructed by virtual modelling and forensic anthropology techniques. *Journal of Archaeological Science 36*, 278–283.

BENAZZI, S., STANSFIELD, E., MILANI, C., AND GRUPPIONI, G. 2009. Geometric morphometric methods for three-dimensional virtual reconstruction of a fragmented cranium: the case of Angelo Poliziano. *Int. Journal of Legal Medicine 123*, 333–344.

BERAR, M., DESVIGNES, M., BAILLY, G., AND PAYAN, Y. 2005. 3D statistical facial reconstruction. In *Image and Signal Processing and Analysis, 2005. ISPA 2005. Proc. of the 4th Int. Symposium on*, 365–370.

BIASOTTI, S., PATANÈ, G., SPAGNUOLO, M., AND FALCIDIENO, B. 2007. Analysis and comparison of real functions on triangulated surfaces. *Curve and Surface Fitting Modern Methods in Mathematics*, 41–50.

BIASOTTI, S., FALCIDIENO, B., DE FLORIANI, L., FROSINI, P., GIORGI, D., LANDI, C., PAPALEO, L., AND SPAGNUOLO, M. 2008. Describing shapes by geometric-topological properties of real functions. *ACM Computing Surveys 40*, 4.

BLOOMENTHAL, J., AND WYVILL, B., Eds. 1997. *Introduction to Implicit Surfaces*. Morgan Kaufmann Publishers Inc.

BRONSTEIN, M. M., AND BRONSTEIN, A. M. 2011. Analysis of diffusion geometry methods for shape recognition. *Trans. on Patter Analysis and Machine Intelligence*, In press.

BRONSTEIN, M. M., AND KOKKINOS, I. 2010. Scale-invariant heat kernel signatures for non-rigid shape recognition. *Proc. Computer Vision and Pattern Recognition*, 1704 – 1711.

BRONSTEIN, A., BRONSTEIN, M., KIMMEL, R., MAHMOUDI, M., AND SAPIRO, G. 2010. A Gromov-Hausdorff framework with diffusion geometry for topologically-robust non-rigid shape matching. *Int. Journal of Computer Vision 2-3*, 266–286.

BRONSTEIN, A. M., BRONSTEIN, M. M., BUSTOS, B., CASTELLANI, U., CRISANI, M., FALCIDIENO, B., GUIBAS, L. J., I. KOKKINOS, V. M., ISIPIRAN, I., OVSJANIKOV, M., PATANÈ, G., SPAGNUOLO, M., AND SUN, J. 2010. SHREC 2010: robust feature detection and description benchmark. *Eurographics Workshop on 3D Object Retrieval*.

BRONSTEIN, A. M., BRONSTEIN, M. M., CASTELLANI, U., FALCIDIENO, B., FUSIELLO, A., GODIL, A., GUIBAS, L., KOKKINOS, I., LIAN, Z., OVSJANIKOV, M., PATANÈ, G., SPAGNUOLO, M., AND TOLDO, R. 2010. SHREC 2010: robust large-scale shape retrieval benchmark. *Eurographics Workshop on 3D Object Retrieval*.

BRONSTEIN, A. M., BRONSTEIN, M. M., OVSJANIKOV, M., AND GUIBAS, L. J. 2011. Shape Google: geometric words and expressions for invariant shape retrieval. *ACM Trans. on Graphics 30*, 1.

CARR, J. C., BEATSON, R. K., CHERRIE, J. B., MITCHELL, T. J., FRIGHT, W. R., MCCALLUM, B. C., AND EVANS, T. R. 2001. Reconstruction and representation of 3D objects with radial basis functions. In *ACM Siggraph*, 67–76.

CHEN, S., AND WIGGER, J. 1995. Fast orthogonal least squares algorithm for efficient subset model selection. *IEEE Trans. on Signal Processing 43*, 7, 1713–1715.

CHERN, S. 1955. An elementary proof of the existence of isothermal parameters on a surface. *Proc. of the American Mathematical Society 6*, 5, 771–782.

CHOW, B., AND LUO, F. 2003. Combinatorial Ricci flows on surface. *Journal Differential Geometry 63*, 1, 97–129.

CHOW, B. 1991. The Ricci flow on the 2-sphere. *Journal of Differential Geometry 33*, 2, 325–334.

CHUNG, F. R. K. 1997. *Spectral graph theory*. American Mathematical Society.

CIPRIANO, G., AND GLEICHER, M. 2007. Molecular surface abstraction. *IEEE Trans. on Visualization and Computer Graphics 13*, 6, 1608–1615.

CO, C. S., HECKEL, B., HAGEN, H., HAMANN, B., AND JOY, K. 2003. Hierarchical clustering for unstructured volumetric scalar fields. In *IEEE Visualization*, 43.

COIFMAN, R. R., AND LAFON, S. 2006. Diffusion maps. *Applied and Computational Harmonic Analysis 21*, 1, 5–30.

CORTES, C., AND VAPNIK, V. 1995. Support-vector networks. *Machine Learning 20*, 3, 273–297.

DASGUPTA, G., AND WACHSPRESS, E. L. 2008. Basis functions for concave polygons. *Computer Math. Appl. 56*, 2, 459–468.

DE GOES, F., GOLDENSTEIN, S., AND VELHO, L. 2008. A hierarchical segmentation of articulated bodies. *Computer Graphics Forum 27*, 5, 1349–1356.

DESBRUN, M., MEYER, M., SCHRÖDER, P., AND BARR, A. H. 1999. Implicit fairing of irregular meshes using diffusion and curvature flow. In *ACM Siggraph*, 317–324.

DESBRUN, M., MEYER, M., AND ALLIEZ, P. 2002. Intrinsic parameterizations of surface meshes. *Computer Graphics Forum 21*, 4, 209–218.

DEY, T. K., RANJAN, P., AND WANG, Y. 2010. Convergence, stability, and discrete approximation of Laplace spectra. *ACM Symposium Discrete Algorithms*, 650–663.

DÍAZ, J., PETIT, J., AND SERNA, M. 2002. A survey of graph layout problems. *ACM Computing Surveys 34*, 3, 313–356.

DOCARMO, M. P. 1976. *Differential Geometry of Curves and Surfaces*, 1 ed. Pearson, February.

DONG, S., KIRCHER, S., AND GARLAND, M. 2005. Harmonic functions for quadrilateral remeshing of arbitrary manifolds. *Computer Aided Geometric Design 22*, 5, 392–423.

DONG, S., BREMER, P.-T., GARLAND, M., PASCUCCI, V., AND HART, J. C. 2006. Spectral surface quadrangulation. *ACM Siggraph*, 1057–1066.

DYN, N., LEVIN, D., AND RIPPA, S. 1986. Numerical procedures for surface fitting of scattered data by radial functions. *SIAM Journal on Scientific and Statistical Computing 7(2)*, 639–659.

EDELSBRUNNER, H., HARER, J., NATARAJAN, V., AND PASCUCCI, V. 2004. Local and global comparison of continuous functions. In *IEEE Visualization*, 275–280.

FARBMAN, Z., HOFFER, G., LIPMAN, Y., COHEN-OR, D., AND LISCHINSKI, D. 2009. Coordinates for instant image cloning. *Proc. ACM Siggraph*, 67:1–9.

FARWIG, R. 1986. Multivariate interpolation of arbitrarily spaced data by moving least squares methods. *Journal of Computational and Applied Mathematics 16*, 1, 79–93.

FIEDLER, M. 1973. Algebraic connectivity of graphs. *Czechoslovak Mathematical Journal 23*, 98, 298–305.

FLOATER, M. S., AND HORMANN, K. 2005. Surface parameterization: a tutorial and survey. In *Advances in Multiresolution for Geometric Modelling*, Mathematics and Visualization. Springer, 157–186.

FLOATER, M. S. 2003. Mean value coordinates. *Computer Aided Geometric Design 20*, 1, 19–27.

FRIEDEL, I. SCHRÖDER, P., AND DESBRUN, M. 2005. Unconstrained spherical parameterization. In *ACM Siggraph*, 134.

GEBAL, K., BÆRENTZEN, J. A., AANÆS, H., AND LARSEN, R. 2009. Shape analysis using the auto diffusion function. *Computer Graphics Forum 28*, 5, 1405–1413.

GIROSI, F. 1998. An equivalence between sparse approximation and support vector machines. *Neural Computation 10*, 6, 1455–1480.

GOLUB, G., AND VANLOAN, G. 1989. *Matrix Computations*. John Hopkins University Press, 2nd Edition.

GOTSMAN, C., GU, X., AND SHEFFER, A. 2003. Fundamentals of spherical parameterization for 3D meshes. In *ACM Siggraph 2003*, 358–363.

GREEF, S. D., CLAES, P., MOLLEMANS, W., LOUBELE, M., VANDERMEULEN, D., SUETENS, P., AND WILLEMS, G. 2005. Semi-automated ultrasound facial soft tissue depth registration: Method and validation. *Journal of Forensic Sciences 50*, 1282–1288.

GREGSON, J., SHEFFER, A., AND ZHANG, E. 2011. All-hex mesh generation via volumetric polycube deformation. *Computer Graphics Forum 30*, 5.

GRIMM, C., AND HUGHES, J. 2003. Parameterizing n-holed tori. In *Mathematics of Surfaces X*, 14–29.

GU, X., AND YAU, S.-T. 2003. Global conformal surface parameterization. In *Proc. Symp. Geometry Processing*, 127–137.

GU, X., AND YAU, S.-T. 2007. Computational conformal geometry. *High Education Press and Int. Press*.

GU, X., WANG, Y., CHAN, T., THOMPSON, P. M., AND S.-T, Y. 2004. Genus zero surface conformal mapping and its application to brain surface mapping. *IEEE Trans. on Medical Imaging 23*, 8, 949–958.

GU, X., HE, Y., JIN, M., F. LUO, H. Q., AND YAU, S.-T. 2007. Manifold splines with single extraordinary point. *ACM Symposium on Solid and Physics Modeling*, 61–72.

HAKER, S., ANGENENT, S., TANNENBAUM, A., KIKINIS, R., SAPIRO, G., AND HALLE, M. 2000. Conformal surface parameterization for texture mapping. *IEEE Trans. on Visualization and Computer Graphics 6*, 2, 181–189.

HAMILTON, R. 1988. Ricci flow on surfaces. *Mathematics and General Relativity, Contemporary Mathematics AMS, Providence, RI, 71*, 237–261.

HAN, S., XIA, J., AND HE, Y. 2010. Hexahedral shell mesh construction via volumetric polycube map. In *Proc. ACM Symposium on Solid and Physical Modeling*, 127–136.

HE, Y., WANG, H., FU, C.-W., AND QIN, H. 2009. A divide-and-conquer approach for automatic polycube map construction. *Computer Graphics 33*, 3, 369–380.

HILDEBRANDT, K., POLTHIER, K., AND WARDETZKY, M. 2006. On the convergence of metric and geometric properties of polyhedral surfaces. *Geometria Dedicata*, 89–112.

HONG, W., NEOPYTOU, N., AND KAUFMAN, A. 2006. Constructing 3D elliptical gaussian for irregular data. In *Mathematical Foundations of Scientific Visualization, Computer Graphics, and Massive Data Visualization*.

HORMANN, K., AND FLOATER, M. S. 2006. Mean value coordinates for arbitrary planar polygons. *ACM Trans. on Graphincs 25*, 4, 1424–1441.

HORMANN, K., AND SUKUMAR, N. 2008. Maximum entropy coordinates for arbitrary polytopes. In *Proc. of the Symposium on Geometry Processing*, 1513–1520.

HORMANN, K., LÉVY, B., AND SHEFFER, A. 2007. Mesh parameterization: Theory and practice. In *ACM Siggraph 2007 Course*, vol. 11, 1–87.

HUANG, J., TONG, Y., WEI, H., AND BAO, H. 2011. Boundary aligned smooth 3D cross-frame field. *ACM Trans. on Graphics 30*, 6, 143.

ISENBURG, M., GUMHOLD, S., AND GOTSMAN, C. 2001. Connectivity shapes. In *IEEE Visualization*, 135–142.

IYENGAR, S. S., LI, X., XU, H., MUKHOPADHYAY, S., BALAKRISHNAN, N., SAWANT, A., AND IYENGAR, P. 2012. Toward more precise radiotherapy treatment of lung tumors. *IEEE Computer 45*, 59–65.

JACOBSON, A., BARAN, I., POPOVIĆ, J., AND SORKINE, O. 2011. Bounded biharmonic weights for real-time deformation. *Proc. ACM Siggraph 30*, 4, 78:1–8.

JAIN, V., AND ZHANG, H. 2007. A spectral approach to shape-based retrieval of articulated 3D models. *Computer Aided Design 39*, 398–407.

JAIN, V., ZHANG, H., AND VAN KAICK, O. 2007. Non-rigid spectral correspondence of triangle meshes. *Int. Journal on Shape Modeling 13*, 1, 101– 124.

JANG, Y., WEILER, M., HOPF, M., HUANG, J., EBERT, D. S., GAITHER, K. P., AND ERTL, T. 2004. Interactively visualizing procedurally encoded scalar fields. In *Proc. of Symposium on Visualization*, 35–44.

JANG, Y., BOTCHEN, R. P., LAUSER, A., EBERT, D. S., GAITHER, K. P., AND ERTL, T. 2006. Enhancing the interactive visualization of procedurally encoded multifield data with ellipsoidal basis functions. *Computer Graphics Forum 25*, 3, 587–596.

JIN, M., WANG, Y., YAU, S.-T., AND GU, X. 2004. Optimal global conformal surface parameterization. In *IEEE Visualization 2004*, 267–274.

JIN, M., KIM, J., LUO, F., AND GU, X. 2008. Discrete surface Ricci flow. *IEEE Trans. on Visualization and Computer Graphics 14*, 5, 1030–1043.

JIN, J., GARLAND, M., AND RAMOS, E. A. 2009. MLS-based scalar fields over triangle meshes and their application in mesh processing. In *Proc. of the Symposium on Interactive 3D Graphics and Games*, 145–153.

JIN, M., ZENG, W., LUO, F., AND GU, X. 2009. Computing teichmüller shape space. *IEEE Trans. on Visualization and Computer Graphics 15*, 3, 504–517.

JOHNSON, A. E., AND HEBERT, M. 1999. Using spin images for efficient object recognition in cluttered 3D scenes. *IEEE Trans. on Pattern Analysis and Machine Intelligence 21*, 5, 433–449.

JOLLIFFE, I. T. 1986. Principal component analysis. In *Principal Component Analysis*. Springer Verlag.

JOSHI, P., MEYER, M., DEROSE, T., GREEN, B., AND SANOCKI, T. 2007. Harmonic coordinates for character articulation. *ACM Trans. Graphics 26*, 3 (July).

JU, T., SCHAEFER, S., AND WARREN, J. 2005. Mean value coordinates for closed triangular meshes. *ACM Trans. on Graphics*, 561–566.

KÄHLER, K., HABER, J., AND SEIDEL, H.-P. 2003. Reanimating the dead: reconstruction of expressive faces from skull data. *ACM Trans. on Graphics 22*, 3, 554–561.

KANAI, T., SUZUKI, H., AND KIMURA, F. 1998. Three-dimensional geometric metamorphosis based on harmonic maps. *The Visual Computer 14*, 4, 166–176.

KANAI, T., OHTAKE, Y., AND KASE, K. 2006. Hierarchical error-driven approximation of impplicit surfaces from polygonal meshes. In *Proc. of Symposium on Geometry Processing*, 21–30.

KARNI, Z., AND GOTSMAN, C. 2000. Spectral compression of mesh geometry. In *ACM Siggraph 2000*, 279–286.

KENT, J., CARLSON, W., AND PARENT, R. 1992. Shape transformation for polyhedral objects. In *ACM Siggraph*, 47–54.

KIM, B., AND ROSSIGNAC, J. 2005. Geofilter: Geometric selection of mesh filter parameters. *Computer Graphics Forum 24*, 3, 295–302.

KOBBELT, L., CAMPAGNA, S., VORSATZ, J., AND SEIDEL, H.-P. 1998. Interactive multi-resolution modeling on arbitrary meshes. In *ACM Siggraph*, 105–114.

KOBBELT, L., VORSATZ, J., U.LABSIK, AND SEIDEL, H.-P. 1999. A shrink wrapping approach to remeshing polygonal surfaces. *Computer Graphics Forum 18*, 3, 119–130.

KOREN, Y. 2003. On spectral graph drawing. In *Proc. of the 9th Int. Computing and Combinatorics Conf.*, Lecture Notes in Computer Science, Vol. 2697, Springer Verlag, 496–508.

KRAEVOY, V., AND SHEFFER, A. 2004. Cross-parameterization and compatible remeshing of 3D models. *ACM Trans. on Graphics 23*, 3, 861–869.

KRAEVOY, C., JULIUS, D., AND SHEFFER, A. 2007. Shuffler: Modeling with interchangeable parts. *The Visual Computer*.

KWOK, T.-H., ZHANG, Y., AND WANG, C. C. 2012. Efficient optimization of common base domains for cross-parameterization. *IEEE Trans. on Visualization and Computer Graphics 18*, 914–924.

LAFON, S., KELLER, Y., AND COIFMAN, R. R. 2006. Data fusion and multicue data matching by diffusion maps. *IEEE Trans. on Pattern Analysis Machine Intelligence 28*, 11, 1784–1797.

LEVIN, D. 1998. The approximation power of moving least-squares. *Mathematics of Computation 67*, 224, 1517–1531.

LEVY, B. 2006. Laplace-Beltrami eigenfunctions: towards an algorithm that understands geometry. In *Proc. of Shape Modeling and Applications*, 13.

LI, X.-Y., AND HU, S.-M. 2013. Poisson coordinates. *IEEE Trans. on Visualization and Computer Graphics 19*, 2, 344 –352.

LI, X., GUO, X., WANG, H., HE, Y., GU, X., AND QIN, H. 2007. Harmonic volumetric mapping for solid modeling applications. In *Proc. ACM Symp. on Solid and Physical Modeling*, 109–120.

LI, X., BAO, Y., GUO, X., JIN, M., GU, X., AND QIN, H. 2008. Globally optimal surface mapping for surfaces with arbitrary topology. *IEEE Trans. on Visualization and Computer Graphics 14*, 4, 805–819.

LI, X., GU, X., AND QIN, H. 2009. Surface mapping using consistent pants decomposition. *IEEE Trans. on Visualization and Computer Graphics 15*, 4, 558–571.

LI, X., GUO, X., WANG, H., HE, Y., GU, X., AND QIN, H. 2009. Meshless harmonic volumetric mapping using fundamental solution methods. *IEEE Trans. on Automation Science and Engineering 6*, 3.

LI, B., LI, X., WANG, K., AND QIN, H. 2010. Generalized polycube trivariate splines. *Int. Conf. on Shape Modeling and Applications*, 261–265.

LI, X., XU, H., WAN, S., YIN, Z., AND YU, W. 2010. Feature-aligned harmonic volumetric mapping using MFS. *Computers & Graphics*, 242–251.

LI, X., YIN, Z., WEI, L., WAN, S., YU, W., AND LI, M. 2011. Symmetry and template guided completion of damaged skulls. *Computers and Graphics 35*, 4, 885–893.

LI, Y., LIU, Y., XU, W., WANG, W., AND GUO, B. 2012. All-hex meshing using singularity-restricted field. *ACM Trans. on Graphics 31*, 6, 177:1–177:11.

LI, B., LI, X., WANG, K., AND QIN, H. 2013. Surface mesh to volumetric spline conversion with generalized polycubes. *IEEE Transactions on Visualization and Computer Graphics 19*, 1539–1551.

LI, X., J., T., AND HU, S.-M. 2013. Cubic mean value coordinates. *ACM Siggraph*.

LIAN, Z., GODIL, A., AND SUN, X. 2010. Visual similarity based 3D shape retrieval using bag-of-features. In *Proc. of Shape Modeling Int.*, 25–36.

LIAN, Z., ROSIN, P., AND SUN, X. 2010. Rectilinearity of 3D meshes. *Int. Journal of Computer Vision 89*, 2, 130–151.

LIN, J., JIN, X., FAN, Z., AND WANG, C. C. L. 2008. Automatic polycube-maps. In *Proc. Geometric modeling and processing*, 3–16.

LIPMAN, Y., KOPF, J., COHEN-OR, D., AND LEVIN, D. 2007. GPU-assisted positive mean value coordinates for mesh deformations. In *Proc. of Symposium on Geometry Processing*, 117–123.

LIPMAN, Y., LEVIN, D., AND COHEN-OR, D. 2008. Green coordinates. *ACM Trans. on Graphics 27*, 3, 78:1–78:10.

LIPMAN, Y., RUSTAMOV, R., AND FUNKHOUSER, T. 2010. Biharmonic distance. *ACM Trans. on Graphics 29*, 3.

LIU, R., AND ZHANG, H. 2007. Mesh segmentation via spectral embedding and contour analysis. *Eurographics 2007 26*, 385–394.

LIU, Y., PRABHAKARAN, B., AND GUO, X. 2012. Point-based manifold harmonics. *IEEE Transactions on Visualization and Computer Graphics 18*, 10, 1693 –1703.

LLOYD, S. 1982. An algorithm for vector quantizer design. *IEEE Trans. on Communications 28*, 7, 84–95.

LUI, L. M., ZENG, W., CHAN, T., YAU, S.-T., AND GU, X. 2010. Shape representation of planar objects with arbitrary topologies using conformal geometry. In *11th European Conf. on Computer Vision*.

LUO, F., GU, X., AND J.DAI. 2007. Variational principles for discrete surfaces. *High Education Press and Int. Press*.

MADSEN, K., NIELSEN, H. B., AND TINGLEFF, O. 2004. *Methods for Non-Linear Least Squares Problems, 2nd Edition*. Informatics and Mathematical Modelling, Technical University of Denmark, DTU.

MAHMOUDI, M., AND SAPIRO, G. 2009. Three-dimensional point cloud recognition via distributions of geometric distances. *Graphical Models 71*, 1, 22–31.

MALLET, J.-L. 1989. Discrete smooth interpolation. *ACM Trans. on Graphics 8*, 2, 121–144.

MANHEIN, M., LISTI, G., BARSLEY, R., MUSSELMAN, R., BARROW, N., AND UBELAKER, D. 2000. In vivo facial tissue depth measurements for children and adults. *Journal of Forensic Science 45*, 1, 48–60.

MARTIN, T., AND COHEN, E. 2010. Volumetric parameterization of complex objects by respecting multiple materials. *Computer Graphics 34*, 187–197.

MARTIN, S., KAUFMANN, P., BOTSCH, M., WICKE, M., AND GROSS, M. 2008. Polyhedral finite elements using harmonic basis functions. *Computer Graphics Forum 27*, 5, 1521–1529.

MARTIN, T., COHEN, E., AND KIRBY, M. 2008. Volumetric parameterization and trivariate b-spline fitting using harmonic functions. In *Proc. of the ACM Symposium on Solid and Physical Modeling*, 269–280.

MARTIN, T., CHEN, G., MUSUVATHY, S., COHEN, E., AND HANSEN, C. D. 2012. Generalized swept mid-structure for polygonal models. *Computer Graphics Forum 31*, 2, 805–814.

MÈMOLI, F. 2009. Spectral Gromov-Wasserstein distances for shape matching. In *Workshop on Non-Rigid Shape Analysis and Deformable Image Alignment*.

METZ, C., KLEIN, S., SCHAAP, M., VAN WALSUM, T., AND NIESSEN, W. 2011. Nonrigid registration of dynamic medical imaging data using nD+tB-splines and a groupwise optimization approach. *Medical Image Analysis 15*, 238 – 249.

MICCHELLI, C. A. 1986. Interpolation of scattered data: Distance matrices and conditionally positive definite functions. *Constructive Approximation 2*, 11–22.

MILNOR, J. 1963. *Morse Theory*, vol. 51 of *Annals of Mathematics Studies*. Princeton University Press.

MOHAR, B., AND POLJAK, S. 1993. Eigenvalues in combinatorial optimization. *Combinatorial and graph-theoretical problems in linear algebra 23*, 98, 107–151.

MORSE, B. S., YOO, T. S., CHEN, D. T., RHEINGANS, P., AND SUBRAMANIAN, K. R. 2001. Interpolating implicit surfaces from scattered surface data using compactly supported radial basis functions. In *IEEE Shape Modeling and Applications*, 89–98.

NEALEN, A., IGARASHI, T., SORKINE, O., AND ALEXA, M. 2006. Laplacian mesh optimization. In *Proc. of Computer graphics and interactive techniques*, 381–389.

NI, X., GARLAND, M., AND HART, J. C. 2004. Fair morse functions for extracting the topological structure of a surface mesh. In *ACM Siggraph 2004*, 613–622.

NIESER, M., REITEBUCH, U., AND POLTHIER, K. 2011. Cubecover - parameterization of 3D volumes. *Computer Graphics Forum 30*, 5, 1397–1406.

OHBUCHI, R., TAKAHASHI, S., MIYAZAWA, T., AND MUKAIYAMA, A. 2001. Watermarking 3D polygonal meshes in the mesh spectral domain. In *Graphics Interface 2001*, 9–17.

OHBUCHI, R., MUKAIYAMA, A., AND TAKAHASHI, S. 2002. A frequency-domain approach to watermarking 3D shapes. *Computer Graphics Forum 21*, 3.

OHTAKE, Y., BELYAEV, A., ALEXA, M., TURK, G., AND SEIDEL, H.-P. 2003. Multi-level partition of unity implicits. *ACM Siggraph 22*, 3, 463–470.

OHTAKE, Y., BELYAEV, A., AND SEIDEL, H.-P. 2005. 3D scattered data interpolation and approximation with multilevel compactly supported RBFs. *Graphical Models 67*, 3, 150–165.

OHTAKE, Y., BELYAEV, A. G., AND ALEXA, M. 2005. Sparse low-degree implicits with applications to high quality rendering, feature extraction, and smoothing. In *Proc. of Symposium on Geometry Processing*, 149–158.

OVSJANIKOV, M., MÉRIGOT, Q., MÉMOLI, F., AND GUIBAS, L. 2010. One point isometric matching with the heat kernel. *ACM Symposium on Discrete Algorithms*, 650–663.

OVSJANIKOV, M., BEN-CHEN, M., SOLOMON, J., BUTSCHER, A., AND GUIBAS, L. J. 2012. Functional maps: a flexible representation of maps between shapes. *ACM Trans.s on Graphics 31*, 4, 30.

PATANÈ, G., AND FALCIDIENO, B. 2009. Computing smooth approximations of scalar functions with constraints. *Computer & Graphics 33*, 3, 399 – 413.

PATANÈ, G., AND FALCIDIENO, B. 2010. Multi-scale feature spaces for shape processing and analysis. In *Proc. of Shape Modeling Int.*, 113–123.

PATANÉ, G., AND SPAGNUOLO, M. 2012. Local approximation of scalar functions on 3D shapes and volumetric data. *Computers & Graphics 36*, 5, 387 – 397.

PATANÈ, G., AND SPAGNUOLO, M. 2013. Heat diffusion kernel and distance on surface meshes and point sets. *Computers & Graphics 37*, 6, 676 – 686.

PATANÈ, G., AND SPAGNUOLO, M. 2013. An interactive analysis of harmonic and diffusion equations on discrete 3D shapes. *Computer & Graphics*.

PATANÈ, G. 2006. SIMS: a multi-level approach to surface reconstruction with sparse implicits. In *Proc. of Shape Modeling and Applications*, 222–233.

PATANÈ, G. 2013. Multi-resolutive sparse approximations of *d*-dimensional data. *International Journal of Computer Vision 117*, 4, 418–428.

PATANÈ, G. 2013. wFEM heat kernel: Discretization and applications to shape analysis and retrieval. *Computer Aided Geometric Design*.

PAULY, M., KEISER, R., KOBBELT, L. P., AND GROSS, M. 2003. Shape modeling with point-sampled geometry. *ACM Trans. on Graphics 22*, 3, 641–650.

PINKALL, U., AND POLTHIER, K. 1993. Computing discrete minimal surfaces and their conjugates. *Experimental Mathematics 2*, 1, 15–36.

POGGIO, T., AND GIROSI, F. 1990. Networks for approximation and learning. *Proc. of the IEEE 78*, 9, 1481–1497.

PRAUN, E., AND HOPPE, H. 2003. Spherical parametrization and remeshing. In *Siggraph '03*, 340–349.

REUTER, M., WOLTER, F.-E., AND PEINECKE, N. 2006. Laplace-Beltrami spectra as Shape-DNA of surfaces and solids. *Computer-Aided Design 38*, 4, 342–366.

REUTER, M., BIASOTTI, S., GIORGI, D., PATANÈ, G., AND SPAGNUOLO, M. 2009. Discrete Laplace-Beltrami operators for shape analysis and segmentation. *Computer & Graphics 33*, 3, 381–390.

ROSENBERG, S. 1997. *The Laplacian on a Riemannian Manifold*. Cambridge University Press.

RUSTAMOV, R. M. 2007. Laplace-Beltrami eigenfunctions for deformation invariant shape representation. In *Proc. of the Symposium on Geometry processing*, 225–233.

RUSTAMOV, R. M. 2011. Interpolated eigenfunctions for volumetric shape processing. *The Visual Computer 27*, 11, 951–961.

RUSTAMOV, R. M. 2011. Multiscale biharmonic kernels. *Computer Graphics Forum 30*, 5, 1521–1531.

SABA, S., YAVNEH, I., GOTSMAN, C., AND SHEFFER, A. 2005. Practical spherical embedding of manifold triangle meshes. In *Int. Conf. on Shape Modeling and Applications*, 258–267.

SCHOELKOPF, B., AND SMOLA, A. J. 2002. *Learning with Kernels*. The MIT Press.

SCHOEN, R., AND YAU, S.-T. 1994. *Lecture on Differential Geometry*, vol. 1. Int. Press Incorporated, Boston.

SCHOEN, R., AND YAU, S. T. 1997. *Lectures on harmonic maps*. Int. Press.

SCHREINER, J., ASIRVATHAM, A., PRAUN, E., AND HOPPE, H. 2004. Inter-surface mapping. *Siggraph. 23*, 3, 870–877.

SEDERBERG, T. W., ZHENG, J., BAKENOV, A., AND NASRI, A. 2003. T-splines and T-NURCCs. *ACM Trans. on Graphics 22*, 3 (July), 477–484.

SHALOM, S., SHAPIRA, L., SHAMIR, A., AND COHEN-OR, D. 2008. Part analogies in sets of objects. In *Proc. of Eurographics Symposium on 3D Object Retrieval*, 33–40.

SHAPIRO, A., AND TAL, A. 1998. Polyhedron realization for shape transformation. *The Visual Computer 14*, 8.

SHEFFER, A., GOTSMAN, C., AND DYN, N. 2004. Robust spherical parameterization of triangular meshes. *Computing 72*, 1-2, 185–193.

SHEFFER, A., PRAUN, E., AND ROSE, K. 2006. Mesh parameterization methods and their applications. *Found. Trends. Computer Graphics Vis. 2*, 2, 105–171.

SHEN, C., O'BRIEN, J. F., AND SHEWCHUK, J. R. 2004. Interpolating and approximating implicit surfaces from polygon soup. *ACM Trans. on Graphics 23*, 3, 896–904.

SHI, J., AND MALIK, J. 1997. Normalized cuts and image segmentation. In *Proc. of the Conf. on Computer Vision and Pattern Recognition*, 731.

SORKINE, O., COHEN-OR, D., AND TOLEDO, S. 2003. High-pass quantization for mesh encoding. In *Proc. of the Symposium on Geometry Processing*, 42–51.

SORKINE, O., LIPMAN, Y., COHEN-OR, D., ALEXA, M., ROESSL, C., AND SEIDEL, H.-P. 2004. Laplacian surface editing. In *Proc. of the Symposium on Geometry Processing*, 179–188.

SORKINE, O. 2006. Differential representations for mesh processing. *Computer Graphics Forum 25*, 4, 789–807.

STEINKE, F., SCHÖLKOPF, B., AND BLANZ, V. 2005. Support vector machines for 3D shape processing. *Computer Graphics Forum 24*, 3, 285–294.

STEPHENSON, K. 2005. *Introduction to circle packing*. Cambridge University Press.

SUN, J., OVSJANIKOV, M., AND GUIBAS, L. J. 2009. A concise and provably informative multi-scale signature based on heat diffusion. *Computer Graphics Forum 28*, 5, 1383–1392.

TAKAYAMA, K., SORKINE, O., NEALEN, A., AND IGARASHI, T. 2010. Volumetric modeling with diffusion surfaces. *ACM Trans.s on Graphics*, 180:1–8.

TARINI, M., HORMANN, K., CIGNONI, P., AND MONTANI, C. 2004. Polycube-maps. In *ACM Siggraph*, 853–860.

TAUBIN, G. 1995. A signal processing approach to fair surface design. In *ACM Siggraph 1995*, 351–358.

TAUBIN, G. 1999. 3D geometry compressionand progressive transmission. In *Eurographics Tutorials*.

THURSTON, W. P. 1980. Geometry and topology of three-manifolds. *Lecture Notes at Princeton university*.

TOLDO, R., CASTELLANI, U., AND FUSIELLO, A. 2009. Visual vocabulary signature for 3D object retrieval and partial matching. *Proc. Eurographics Workshop on 3D Object Retrieval*.

TURK, G., AND O'BRIEN, J. F. 2002. Modelling with implicit surfaces that interpolate. *ACM Siggraph 21*, 4, 855–873.

VALLET, B., AND LEVY, B. 2008. Manifold harmonics. *Computer Graphics Forum 27(2)*.

VANDERMEULEN, D., CLAES, P., SUTENS, P., DEGREEF, S., AND WILLEMS, G. 2005. Volumetric deformation face models for cranio-facial reconstruction. In *Proc. of the Int. Symposium on Image and Signal Processing and Analysis*, 353–358.

VAXMAN, A., BEN-CHEN, M., AND GOTSMAN, C. 2010. A multi-resolution approach to heat kernels on discrete surfaces. *ACM Trans. on Graphics 29*, 4, 1–10.

WALDER, C., SCHÖLKOPF, B., AND CHAPELLE, O. 2006. Implicit surface modelling with a globally regularised basis of compact support. *Computer Graphics Forum 25*, 3, 635–644.

WAN, S., YIN, Z., ZHANG, K., ZHANG, H., AND LI, X. 2011. A topology-preserving optimization algorithm for polycube mapping. *Computers and Graphics 35*, 3, 639–649.

WAN, S., YE, T., LI, M., ZHANG, H., AND LI, X. 2012. Efficient spherical parametrization using progressive optimization. In *Computational Visual Media*, S.-M. Hu and R. Martin, Eds., vol. 7633 of *Lecture Notes in Computer Science*. Springer Berlin / Heidelberg, 170–177.

WANG, Y., GU, X., CHAN, T. F., THOMPSON, P. M., AND YAU, S. T. 2004. Volumetric harmonic brain mapping. In *IEEE Int. Symp. on Biomedical Imaging: Macro to Nano.*, 1275–1278.

WANG, S., WANG, Y., JIN, M., GU, X. D., AND SAMARAS, D. 2007. Conformal geometry and its applications on 3D shape matching, recognition, and stitching. *IEEE Trans. om Pattern Analysis and Machince Intelligence 29*, 7, 1209–1220.

WANG, H., HE, Y., LI, X., GU, X., AND QIN, H. 2008. Polycube splines. *Computer Aided Design 40*, 6, 721–733.

WANG, K., LI, X., LI, B., XU, H., AND QIN, H. 2012. Restricted trivariate polycube splines for volumetric data modeling. *IEEE Trans. on Visualization and Computer Graphics 18*, 703–716.

WANG, Y. 2009. Approximating gradients for meshes and point clouds via diffusion metric. *Computer Graphics Forum 28*, 1497–1508(12).

WEBER, O., AND GOTSMAN, C. 2010. Controllable conformal maps for shape deformation and interpolation. *ACM Trans. Graphics 29*, 78:1–78:11.

WEBER, O., BEN-CHEN, M., AND GOTSMAN, C. 2009. Complex barycentric coordinates with applications to planar shape deformation. *Computer Graphics Forum 28*, 2, 587–597.

WEBER, O., BEN-CHEN, M., GOTSMAN, C., AND HORMANN, K. 2011. A complex view of barycentric mappings. *Computer Graphics Forum 30*, 5, 1533–1542.

WEBER, O., PORANNE, R., AND GOTSMAN, C. 2012. Biharmonic coordinates. *Computer Graphics Forum 31*, 8, 2409–2422.

WEILER, M., BOTCHEN, R., STEGMAIER, S., ERTL, T., HUANG, J., JANG, Y., EBERT, D., AND GAITHER, K. 2005. Hardware-assisted feature analysis and visualization of procedurally encoded multifield volumetric data. *Computer Graphics Applications 25*, 5, 72–81.

WENDLAND, H. 1995. Real piecewise polynomial, positive definite and compactly supported radial functions of minimal degree. *Advances in Computational Mathematics 4(4)*, 389–396.

XIA, J., HE, Y., YIN, X., HAN, S., AND GU, X. 2010. Direct-product volumetric parameterization of handlebodies via harmonic fields. *Int. Conf. on Shape Modeling and Applications*, 3–12.

XIA, J., GARCÍA, I., HE, Y., XIN, S. Q., AND PATOW, G. 2011. Editable polycube map for gpu-based subdivision surfaces. In *Symposium on Interactive 3D Graphics and Games*, 151–158.

XIAOA, B., HANCOCK, E. R., AND WILSONB, R. 2010. Geometric characterization and clustering of graphs using heat kernel embeddings. *Image and Vision Computing 28*, 6, 1003 – 1021.

XIE, H., MCDONNELL, K. T., AND QIN, H. 2004. Surface reconstruction of noisy and defective data sets. In *IEEE Visualization*, 259–266.

XU, H., CHEN, P., YU, W., S., A., IYENGAR, S., AND LI, X. 2012. Feature-aligned 4D spatiotemporal image registration. In *Proc. Int. Conf. on Pattern Recognition*, 2639–2642.

XU, H., YU, W., GU, S., AND LI, X. 2013. Biharmonic volumetric mapping using fundamental solutions. *IEEE Transactions on Visualization and Computer Graphics 19*, 787–798.

XU, G. 2007. Discrete Laplace-Beltrami operators and their convergence. *Computer Aided Geometric Design 8*, 21, 398–407.

YANG, Y.-L., GUO, R., LUO, F., HU, S.-M., AND GU, X. 2009. Generalized discrete ricci flow. *Computer Graphics Forum. 28*, 7, 2005–2014.

YIN, Z., WEI, L., MANHEIN, M., AND LI, X. 2011. An automatic assembly and completion framework for fragmented skulls. In *Int. Conf. on Computer Vision*, 2532–2539.

YU, W., LI, M., AND LI, X. 2012. Fragmented skull modeling using heat kernels. *Graphical Models 74*, 4, 140 – 151.

ZAYER, R., ROSSL, C., AND SEIDEL, H.-P. 2006. Curvilinear spherical parameterization. In *Int. Conf. on Shape Modeling and Applications*, 57–64.

ZENG, W., LI, X., YAU, S.-T., AND GU, X. 2007. Conformal spherical parameterization for high genus surfaces. *Communications in Information and Systems 7*, 3, 273–286.

ZENG, W., YIN, X. T., ZENG, Y., LAI, Y. K., GU, X., AND SAMARAS, D. 2008. 3D face matching and registration based on hyperbolic Ricci flow. In *The CVPR Workshop on 3D Face Processing (CVPR'08-3DFP)*.

ZENG, W., JIN, M., LUO, F., AND GU, X. 2009. Computing canonical homotopy class representative using hyperbolic structure. *IEEE Int. Conf. on Shape Modeling and Applications*.

ZENG, W., LUO, F., YAU, S.-T., AND GU, X. 2009. Surface quasi-conformal mapping by solving Beltrami equations. In *IMA Int. Conf. on Mathematics of Surfaces XIII*, 391–408.

ZENG, W., MARINO, J., GURIJALA, K., GU, X., AND KAUFMAN, A. 2010. Supine and prone colon registration using quasi-conformal mapping. *IEEE Trans. on Visualization and Computer Graphics 16*, 6, 1348–1357.

ZENG, W., SAMARAS, D., AND GU, X. D. 2010. Ricci flow for 3D shape analysis. *IEEE Trans. on Pattern Analysis and Machine Intelligence 32*, 4, 662–677.

ZHANG, H., AND FIUME, E. 2003. Butterworth filtering and implicit fairing of irregular meshes. In *Proc. of the Pacific Conf. on Computer Graphics and Applications*, 502.

ZHANG, K., AND LI, X. 2012. Optimizing geometry-aware pants decomposition. In *Proc. Pacific Graphics*, 11–16.

ZHANG, H., AND LIU, R. 2005. Mesh segmentation via recursive and visually salient spectral cuts. In *Proc. of Vision, Modeling, and Visualization*, 429–436.

ZHANG, H., VAN KAICK, O., AND DYER, R. 2007. Spectral methods for mesh processing and analysis. In *Eurographics State-of-the-art Report*, 1–22.

ZHANG, M., HUANG, J., LIU, X., AND BAO, H. 2012. A divide-and-conquer approach to quad remeshing. *IEEE Trans. on Visualization and Computer Graphics 99*, PrePrints, 1.

ZHOU, K., SYNDER, J., GUO, B., AND SHUM, H.-Y. 2004. Iso-charts: stretch-driven mesh parameterization using spectral analysis. In *Proc. of the Symposium on Geometry processing*, 45–54.

ZIGELMAN, G., KIMMEL, R., AND KIRYATI, N. 2002. Texture mapping using surface flattening via multidimensional scaling. *IEEE Trans. on Visualization and Computer Graphics 8*, 2, 198–207.

ZOMORODIAN, A., AND CARLSSON, G. 2005. Computing persistent homology. *Discrete Computational Geometry 33*, 2, 249–274.

SIGGRAPH Asia 2014 – Course "An Introduction to Ricci Flow and Volumetric Approximation with Applications to Shape Modeling"

G. Patanè (CNR-IMATI, Italy), X.S. Li (Lousiana State Univ., USA), X.D. Gu (Stony Brook Univ., USA)
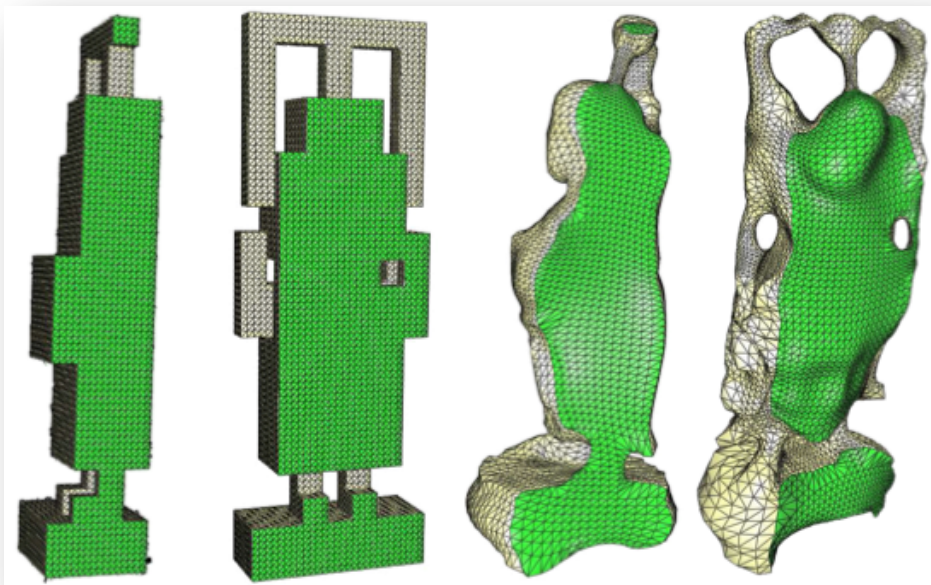
Course Slides

An Introduction to Ricci Flow and Volumetric Approximation with Applications to Shape Modeling

G. Patanè, X.D. Gu, X.S. Li

Speakers

Giuseppe Patanè
CNR-IMATI, Italy
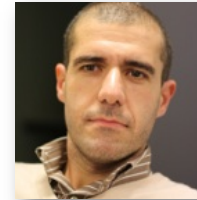
Xin Shane Li
LSU, USA
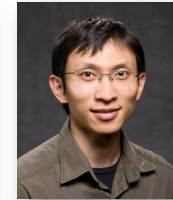
David Gu
SUNY, USA
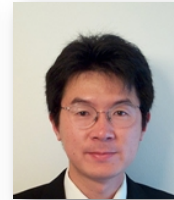
Outline

- **Introduction**
    - Outline and motivations
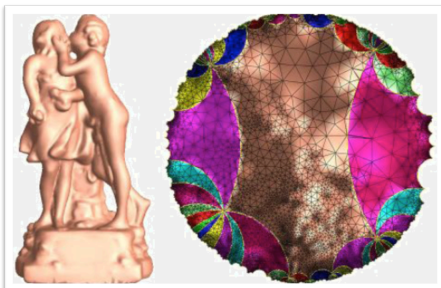
Outline

- **Introduction**
- **Differential operators and spaces for shape modeling**
    - Mappings on Riemann surfaces
    - Ricci flow
    - Laplacian operator and spectral processing
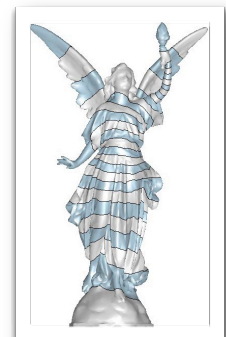
Outline

- **Introduction**
- **Differential operators and spaces for shape modeling**
  - Mappings on Riemann surfaces
  - Ricci flow
  - Spectral methods
- **From surface- to volume-based shape modeling**
  - The out-of-sample approximation problem
  - Main approaches
  - From surface- to cross-volume parameterization
  - Polycube parameterization and polycube splines
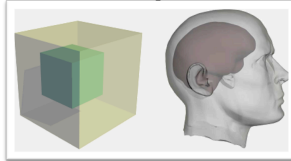
Outline

- **Introduction**
- **Differential operators and spaces for shape modeling**
  - Mappings on Riemann surfaces
  - Ricci flow
  - Spectral methods
- **From surface- to volume-based shape modeling**
  - The out-of-sample approximation problem
  - Main approaches
  - From surface- to cross-volume parameterization
  - Polycube parameterization and polycube splines
- **Applications**
  - Applications to shape modeling and analysis
  - Applications to medicine and bio-informatics

An Introduction to Volumeric Approximation and Its Applications to Shape Modeling

G. Patané[1], X. Li[2], David Gu[3]

[1]CNR-IMATI, Italy
[2]Louisiana State University, USA
[3]Stony Brook University, USA

SIGGRAPH Asia 2014 Course

David Gu   Surface Geometry

Surface Ricci Flow

David Gu   Surface Geometry

Basic Concepts

Manifold

Definition (Manifold)

M is a topological space, $\{U_\alpha\}\ \alpha \in I$ is an open covering of M, $M \subset \cup_\alpha U_\alpha$. For each U_α, $\phi_\alpha : U_\alpha \to \mathbb{R}^n$ is a homeomorphism. The pair (U_α, ϕ_α) is a chart. Suppose $U_\alpha \cap U_\beta \neq \emptyset$, the transition function $\phi_{\alpha\beta} : \phi_\alpha(U_\alpha \cap U_\beta) \to \phi_\beta(U_\alpha \cap U_\beta)$ is smooth

$$\phi_{\alpha\beta} = \phi_\beta \circ \phi_\alpha^{-1}$$

then M is called a smooth manifold, $\{(U_\alpha, \phi_\alpha)\}$ is called an atlas.

Manifold
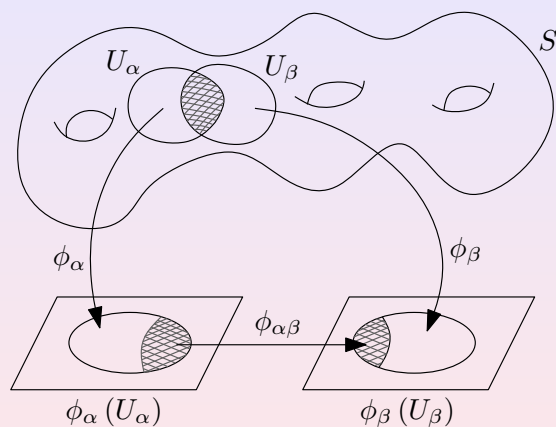
Holomorphic Function

Definition (Holomorphic Function)

Suppose $f : \mathbb{C} \to \mathbb{C}$ is a complex function, $f : x + iy \to u(x, y) + iv(x, y)$, if f satisfies Riemann-Cauchy equation

$$\frac{\partial u}{\partial x} = \frac{\partial v}{\partial y}, \frac{\partial u}{\partial y} = -\frac{\partial v}{\partial x},$$

then f is a holomorphic function.

Denote

$$dz = dx + idy, d\bar{z} = dx - idy,$$

then the dual operators

$$\frac{\partial}{\partial z} = \frac{1}{2}\left(\frac{\partial}{\partial x} - i\frac{\partial}{\partial y}\right), \frac{\partial}{\partial \bar{z}} = \frac{1}{2}\left(\frac{\partial}{\partial x} + i\frac{\partial}{\partial y}\right)$$

then if $\frac{\partial f}{\partial \bar{z}} = 0$, then f is holomorphic.

biholomorphic Function

Definition (biholomorphic Function)

Suppose $f : \mathbb{C} \to \mathbb{C}$ is invertible, both f and f^{-1} are holomorphic, then then f is a biholomorphic function.

Conformal Atlas

Definition (Conformal Atlas)

Suppose S is a topological surface, (2 dimensional manifold), $\mathfrak{A}$ is an atlas, such that all the chart transition functions $\phi_{\alpha\beta} : \mathbb{C} \to \mathbb{C}$ are bi-holomorphic, then A is called a conformal atlas.

Definition (Compatible Conformal Atlas)

Suppose S is a topological surface, (2 dimensional manifold), $\mathfrak{A}_1$ and $\mathfrak{A}_2$ are two conformal atlases. If their union $A_1 \cup A_2$ is still a conformal atlas, we say $\mathfrak{A}_1$ and $\mathfrak{A}_2$ are compatible.

Conformal Structure

The compatible relation among conformal atlases is an equivalence relation.

Definition (Conformal Structure)

Suppose S is a topological surface, consider all the conformal atlases on M, classified by the compatible relation

$$\{all\ conformal\ atlas\} / \sim$$

each equivalence class is called a conformal structure.

In other words, each maximal conformal atlas is a conformal structure.

Smooth map

Definition (Smooth map)

Suppose $f : S_1 \to S_2$ is a map between two smooth manifolds. For each point p, choose a chart of S_1, (U_α, ϕ_α), $p \in U_\alpha$. The image $f(U_\alpha) \subset V_\beta$, (V_β, τ_β) is a chart of S_2. The local representation of f

$$\tau_\beta \circ f \circ \phi_\alpha^{-1} : \phi_\alpha(U_\alpha) \to \tau_\beta(V_\beta)$$

is smooth, then f is a smooth map.

Map between Manifolds

$S_1 \subset \{(U_\alpha, \phi_\alpha)\}$ $S_2 \subset \{(V_\beta, \tau_\beta)\}$

f

U_α V_β

ϕ_α τ_β

$\tau_\beta \circ f \circ \phi_\alpha^{-1}$

z w
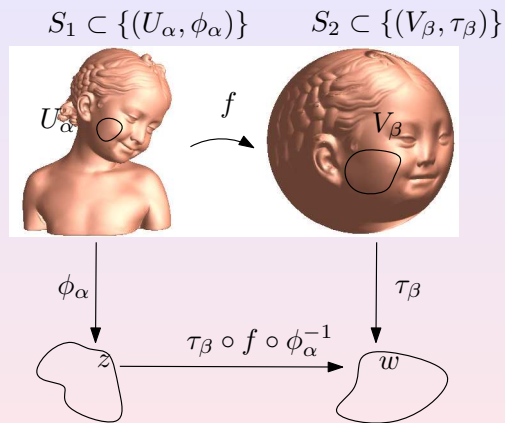
Riemannian Metric

Definition (Riemannian Metric)

A Riemannian metric on a smooth manifold M is an assignment of an inner product $g_p : T_pM \times T_pM \to \mathbb{R}$, $\forall p \in M$, such that

1. $g_p(a_1 X_1 + a_2 X_2, b_1 Y_1 + b_2 Y_2) = \sum_{i,j=1}^{2} a_i b_j g_p(X_i, Y_j)$.

2. $g_p(X, Y) = g_p(Y, X)$

3. g_p is non-degenerate.

4. $\forall p \in M$, there exists local coordinates $\{x^i\}$, such that $g_{ij} = g_p(\frac{\partial}{\partial x_i}, \frac{\partial}{\partial x_j})$ are C^∞ functions.

Pull back Riemannian Metric

Definition (Pull back Riemannian metric)

Suppose $f : (M, \mathbf{g}) \to (N, \mathbf{h})$ is a smooth mapping between two Riemannian manifolds, $\forall p \in M$, $f_* : T_pM \to T_{f(p)}N$ is the tangent map. The pull back metric $f^*\mathbf{h}$ induced by the mapping f is given by

$$f^*h(X_1, X_2) := h(f_* X_1, f_* X_2), \forall X_1, X_2 \in T_pM.$$

Local representation of the pull back metric is given by

$$f^*\mathbf{h} = \begin{pmatrix} \frac{\partial u}{\partial x} & \frac{\partial v}{\partial x} \\ \frac{\partial u}{\partial y} & \frac{\partial v}{\partial y} \end{pmatrix} \begin{pmatrix} h_{11} & h_{12} \\ h_{21} & h_{22} \end{pmatrix} \begin{pmatrix} \frac{\partial u}{\partial x} & \frac{\partial u}{\partial y} \\ \frac{\partial v}{\partial x} & \frac{\partial v}{\partial y} \end{pmatrix}$$

Conformal Structure

Definition (Conformal equivalent metrics)

Suppose $\mathbf{g}_1, \mathbf{g}_2$ are two Riemannian metrics on a manifold M, if

$$\mathbf{g}_1 = e^{2u}\mathbf{g}_2, u : M \to \mathbb{R}$$

then $\mathbf{g}_1$ and $\mathbf{g}_2$ are conformal equivalent.

Definition (Conformal Structure)

Consider all Riemannian metrics on a topological surface S, which are classified by the conformal equivalence relation,

$$\{Riemannian\ metrics\ on\ S\}/\sim,$$

each equivalence class is called a conformal structure.

Isothermal Coordinates

Relation between conformal structure and Riemannian metric

Isothermal Coordinates

A surface M with a Riemannian metric $\mathbf{g}$, a local coordinate system (u, v) is an isothermal coordinate system, if

$$\mathbf{g} = e^{2\lambda(u,v)}(du^2 + dv^2).$$
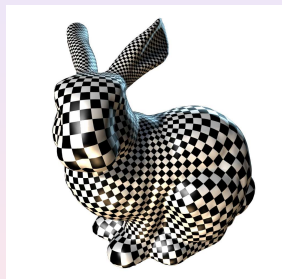
Riemannian metric vs Conformal Structure

Definition (Isothermal coordinates)

Suppose $(S, \mathbf{g})$ is a metric surface, (U_α, ϕ_α) is a coordinate chart, (x, y) are local parameters, if

$$\mathbf{g} = e^{2u}(dx^2 + dy^2),$$

then we say (x, y) are isothermal coordinates.

Theorem

Suppose S is a compact metric surface, for each point p, there exits a local coordinate chart (U, ϕ), such that $p \in U$, and the local coordinates are isothermal.

Riemannian metric and Conformal Structure

Corollary

For any compact metric surface, there exists a natural conformal structure.

Definition (Riemann surface)

A topological surface with a conformal structure is called a Riemann surface.

Theorem

All compact metric surfaces are Riemann surfaces.

Smooth Surface Ricci Flow

Isothermal Coordinates

Relation between conformal structure and Riemannian metric

Isothermal Coordinates

A surface M with a Riemannian metric $\mathbf{g}$, a local coordinate system (u, v) is an isothermal coordinate system, if

$$\mathbf{g} = e^{2\lambda(u,v)}(du^2 + dv^2).$$
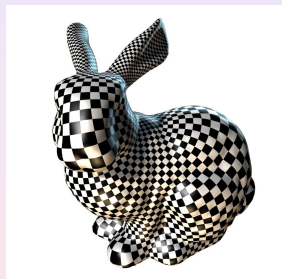
Gaussian Curvature

Gaussian Curvature

Suppose $\bar{\mathbf{g}} = e^{2\lambda}\mathbf{g}$ is a conformal metric on the surface, then the Gaussian curvature on interior points are

$$K = -\Delta_{\mathbf{g}}\lambda = -\frac{1}{e^{2\lambda}}\Delta\lambda,$$

where

$$\Delta = \frac{\partial^2}{\partial u^2} + \frac{\partial^2}{\partial v^2}$$

Conformal Metric Deformation

Definition

Suppose M is a surface with a Riemannian metric,

$$\mathbf{g} = \begin{pmatrix} g_{11} & g_{12} \\ g_{21} & g_{22} \end{pmatrix}$$

Suppose $\lambda : \Sigma \to \mathbb{R}$ is a function defined on the surface, then $e^{2\lambda}\mathbf{g}$ is also a Riemannian metric on Σ and called a conformal metric. λ is called the conformal factor.

$$\mathbf{g} \to e^{2\lambda}\mathbf{g}$$

Conformal metric deformation.
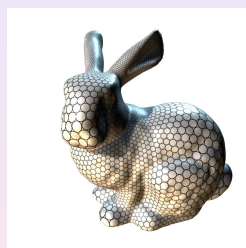
Angles are invariant measured by conformal metrics.

Curvature and Metric Relations

Yamabi Equation

Suppose $\bar{\mathbf{g}} = e^{2\lambda}\mathbf{g}$ is a conformal metric on the surface, then the Gaussian curvature on interior points are

$$\bar{K} = e^{-2\lambda}(K - \Delta_{\mathbf{g}}\lambda),$$

geodesic curvature on the boundary

$$\bar{k}_g = e^{-\lambda}(k_g - \partial_{\mathbf{g},n}\lambda).$$

Uniformization

Let $(\Sigma, \mathbf{g})$ be a compact 2-dimensional Riemannian manifold. Then there is a metric $\tilde{\mathbf{g}} = e^{2\lambda}\mathbf{g}$ conformal to $\mathbf{g}$ which has constant Gauss curvature.
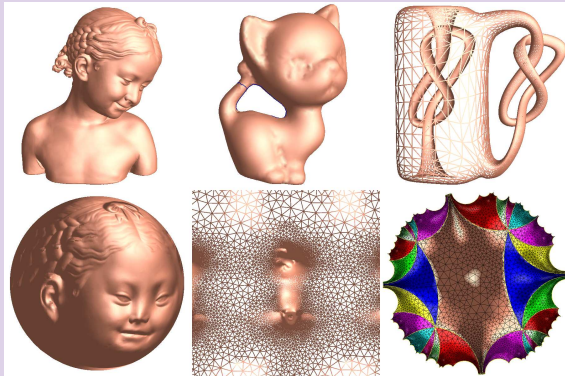
Uniformization of Open Surfaces
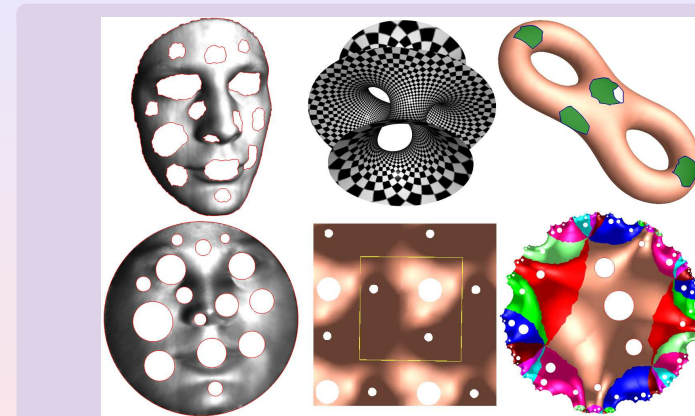
Surface Ricci Flow

Surface Ricci Flow

Surface Ricci Flow

Key Idea

$$K = -\Delta_{\mathbf{g}}\lambda,$$

Roughly speaking,

$$\frac{dK}{dt} = \Delta_{\mathbf{g}}\frac{d\lambda}{dt}$$

Let $\frac{d\lambda}{dt} = -K$,

$$\frac{dK}{dt} = \Delta_{\mathbf{g}}K + K^2$$

Heat equation!

Surface Ricci Flow

Definition (**Hamilton's Surface Ricci Flow**)

A closed surface S with a Riemannian metric $\mathbf{g}$, the Ricci flow on it is defined as

$$\frac{dg_{ij}}{dt} = \left(\frac{4\pi\chi(S)}{A(0)} - 2K \right) g_{ij}.$$

where $\chi(S)$ is the Euler characteristic number of S, $A(0)$ is the initial total area.

The ricci flow preserves the total area during the flow, converge to a metric with constant Gaussian curvature $\frac{4\pi\chi(S)}{A(0)}$.

Ricci Flow

Theorem (Hamilton 1982)

For a closed surface of non-positive Euler characteristic, if the total area of the surface is preserved during the flow, the Ricci flow will converge to a metric such that the Gaussian curvature is constant (equals to $\bar{K}$) every where.

Theorem (Bennett Chow)

For a closed surface of positive Euler characteristic, if the total area of the surface is preserved during the flow, the Ricci flow will converge to a metric such that the Gaussian curvature is constant (equals to $\bar{K}$) every where.

Summary

Surface Ricci Flow

- Conformal metric deformation

$$\mathbf{g} \to e^{2u}\mathbf{g}$$

- Curvature Change - heat diffusion

$$\frac{dK}{dt} = \Delta_{\mathbf{g}} K + K^2$$

- Ricci flow

$$\frac{du}{dt} = \bar{K} - K.$$

Discrete Surface

Generic Surface Model - Triangular Mesh

- Surfaces are represented as polyhedron triangular meshes.
- Isometric gluing of triangles in $\mathbb{E}^2$.
- Isometric gluing of triangles in $\mathbb{H}^2, \mathbb{S}^2$.

Generic Surface Model - Triangular Mesh

- Surfaces are represented as polyhedron triangular meshes.
- Isometric gluing of triangles in $\mathbb{E}^2$.
- Isometric gluing of triangles in $\mathbb{H}^2, \mathbb{S}^2$.
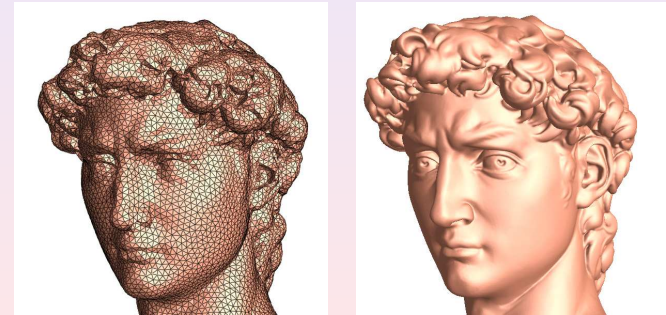
Generic Surface Model - Triangular Mesh

- Surfaces are represented as polyhedron triangular meshes.
- Isometric gluing of triangles in $\mathbb{E}^2$.
- Isometric gluing of triangles in $\mathbb{H}^2, \mathbb{S}^2$.

Discrete Generalization

Concepts

1. Discrete Riemannian Metric
2. Discrete Curvature
3. Discrete Conformal Metric Deformation

Discrete Metrics

Definition (Discrete Metric)

A Discrete Metric on a triangular mesh is a function defined on the vertices, $l : E = \{all\ edges\} \to \mathbb{R}^+$, satisfies triangular inequality.

A mesh has infinite metrics.
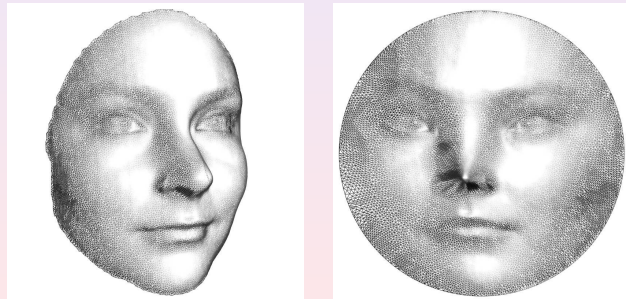
Discrete Curvature

Definition (Discrete Curvature)

Discrete curvature: $K : V = \{vertices\} \to \mathbb{R}^1$.

$$K(v) = 2\pi - \sum_i \alpha_i, v \notin \partial M; K(v) = \pi - \sum_i \alpha_i, v \in \partial M$$

Theorem (Discrete Gauss-Bonnet theorem)

$$\sum_{v \notin \partial M} K(v) + \sum_{v \in \partial M} K(v) = 2\pi\chi(M).$$
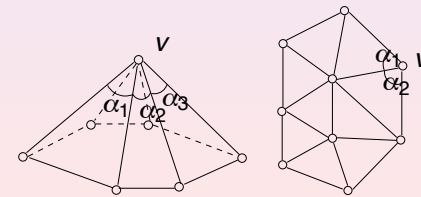
Discrete Metrics Determines the Curvatures

$$R^2 \qquad H^2 \qquad S^2$$
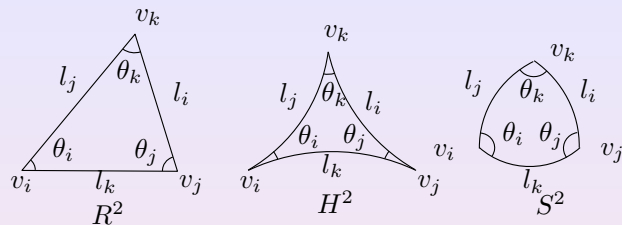
cosine laws

$$\cos l_i = \frac{\cos \theta_i + \cos \theta_j \cos \theta_k}{\sin \theta_j \sin \theta_k} \tag{1}$$

$$\cosh l_i = \frac{\cosh \theta_i + \cosh \theta_j \cosh \theta_k}{\sinh \theta_j \sinh \theta_k} \tag{2}$$

$$1 = \frac{\cos \theta_i + \cos \theta_j \cos \theta_k}{\sin \theta_j \sin \theta_k} \tag{3}$$

Derivative cosine law
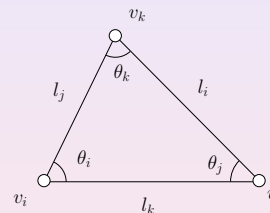
Lemma (Derivative Cosine Law)

Suppose corner angles are the functions of edge lengths, then

$$\frac{\partial \theta_i}{\partial l_i} = \frac{l_i}{A}$$

$$\frac{\partial \theta_i}{\partial l_j} = -\frac{\partial \theta_i}{\partial l_i} \cos \theta_k$$

where $A = l_j l_k \sin \theta_i$.

Discrete Conformal Structure

Discrete Conformal Metric Deformation

Conformal maps Properties
- transform infinitesimal circles to infinitesimal circles.
- preserve the intersection angles among circles.
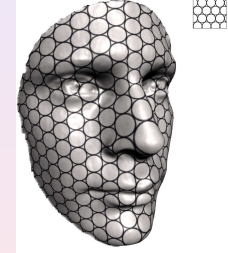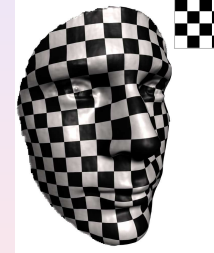
Idea - Approximate conformal metric deformation
Replace infinitesimal circles by circles with finite radii.

Discrete Conformal Metric Deformation vs CP
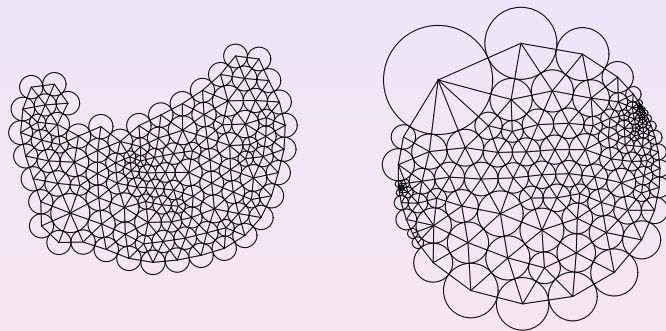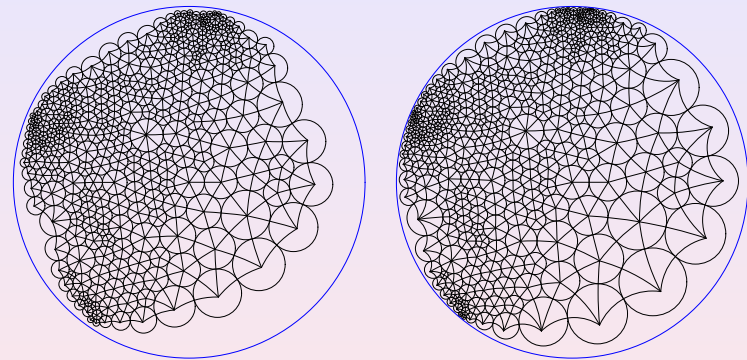
Discrete Conformal Metric Deformation vs CP

Discrete Conformal Metric Deformation vs CP
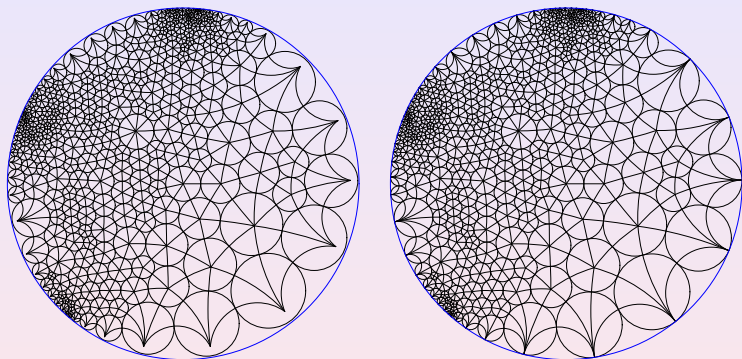
Thurston's Circle Packing Metric

Thurston's CP Metric

We associate each vertex v_i with a circle with radius γ_i. On edge e_{ij}, the two circles intersect at the angle of Φ_{ij}. The edge lengths are

$$l_{ij}^2 = \gamma_i^2 + \gamma_j^2 + 2\gamma_i\gamma_j\cos\Phi_{ij}$$

CP Metric (T, Γ, Φ), T triangulation,

$$\Gamma = \{\gamma_i | \forall v_i\}, \Phi = \{\phi_{ij} | \forall e_{ij}\}$$
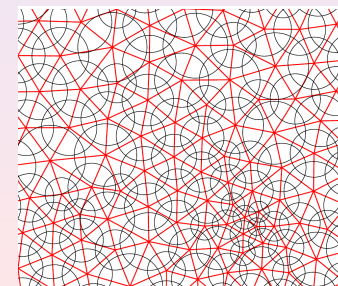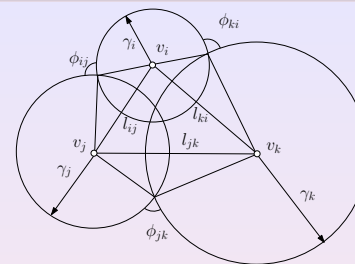
Discrete Conformal Equivalence Metrics

Definition

Conformal Equivalence Two CP metrics (T_1, Γ_1, Φ_1) and (T_2, Γ_2, Φ_2) are conformal equivalent, if they satisfy the following conditions

$$T_1 = T_2 \text{ and } \Phi_1 = \Phi_2.$$
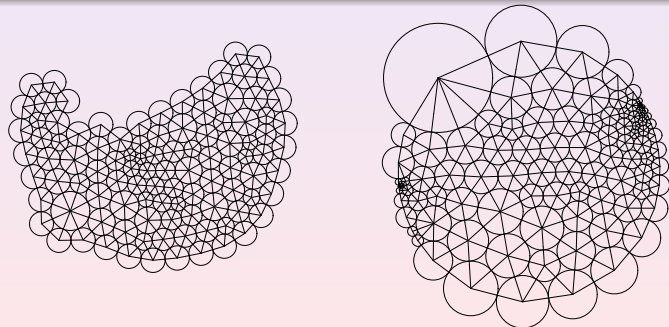
Power Circle

Definition (Power Circle)

The unit circle orthogonal to three circles at the vertices (v_i, γ_i), (v_j, γ_j) and (v_k, γ_k) is called the power circle. The center is called the power center. The distance from the power center to three edges are denoted as h_i, h_j, h_k respectively.
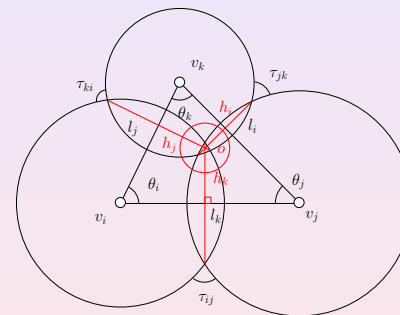
Derivative cosine law

Theorem (Symmetry)

$$\frac{d\theta_i}{du_j} = \frac{d\theta_j}{du_i} = \frac{h_k}{l_k}$$

$$\frac{d\theta_j}{du_k} = \frac{d\theta_k}{du_j} = \frac{h_i}{l_i}$$

$$\frac{d\theta_k}{du_i} = \frac{d\theta_i}{du_k} = \frac{h_j}{l_j}$$

Therefore the differential 1-form $\omega = \theta_i du_i + \theta_j du_j + \theta_k du_k$ is closed.
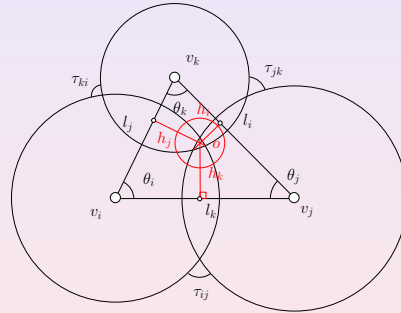
Discrete Ricci Energy

Definition (Discrete Ricci Energy)

The functional associated with a CP metric on a triangle is

$$E(\mathbf{u}) = \int_{(0,0,0)}^{(u_i,u_j,u_k)} \theta_i(\mathbf{u})du_i + \theta_j(\mathbf{u})du_j + \theta_k(\mathbf{u})du_k.$$

Geometrical interpretation: the volume of a truncated hyperbolic hyper-ideal tetrahedron.
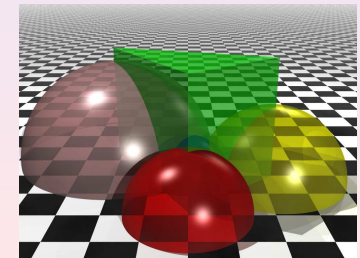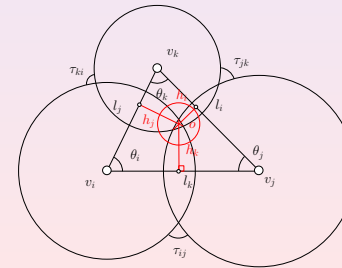
Generalized Circle Packing/Pattern

Definition (Tangential Circle Packing)

$$l_{ij}^2 = \gamma_i^2 + \gamma_j^2 + 2\gamma_i\gamma_j.$$
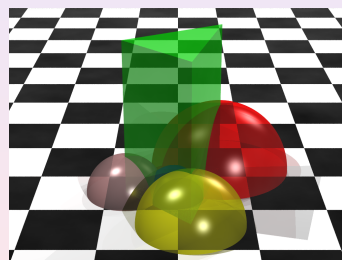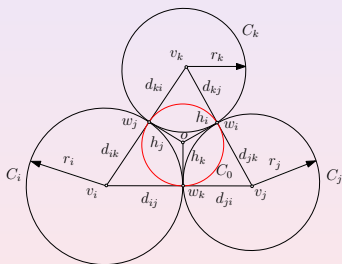
Generalized Circle Packing/Pattern

Definition (Inversive Distance Circle Packing)

$$l_{ij}^2 = \gamma_i^2 + \gamma_j^2 + 2\gamma_i\gamma_j\eta_{ij}.$$

where $\eta_{ij} > 1$.
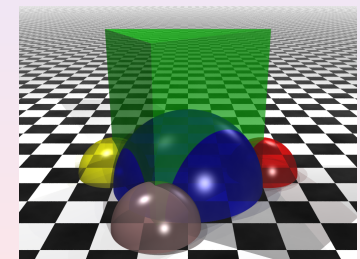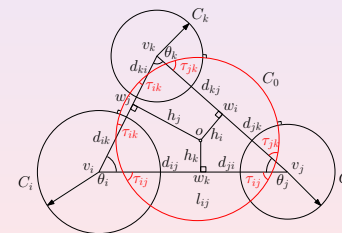
Generalized Circle Packing/Pattern

Definition (Discrete Yamabe Flow)

$$l_{ij}^2 = 2\gamma_i\gamma_j\eta_{ij}.$$

where $\eta_{ij} > 0$.
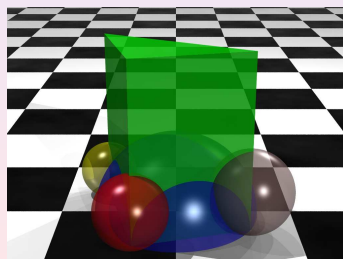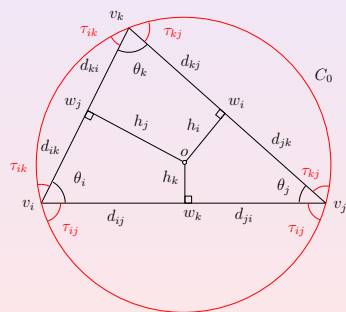
Voronoi Diagram

Definition (Voronoi Diagram)

Given $p_1, \cdots, p_k$ in $\mathbb{R}^n$, the Voronoi cell W_i at p_i is

$$W_i = \{\mathbf{x} \,|\, |\mathbf{x} - p_i|^2 \leq |\mathbf{x} - p_j|^2, \forall j\}.$$

The dual triangulation to the Voronoi diagram is called the Delaunay triangulation.
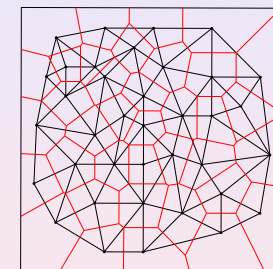
Power Distance

Power Distance

Given $\mathbf{p}_i$ associated with a sphere $(\mathbf{p}_i, r_i)$ the power distance from $\mathbf{q} \in \mathbb{R}^n$ to $\mathbf{p}_i$ is

$$pow(\mathbf{p}_i, \mathbf{q}) = |\mathbf{p}_i - \mathbf{q}|^2 - r_i^2.$$
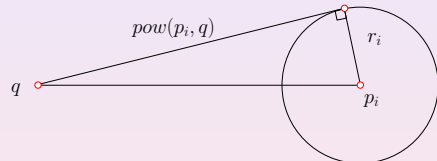
Power Diagram

Definition (Power Diagram)

Given $p_1, \cdots, p_k$ in $\mathbb{R}^n$ and sphere radii $\gamma_1, \cdots, \gamma_k$, the power Voronoi cell W_i at p_i is

$$W_i = \{\mathbf{x} \,|\, Pow(\mathbf{x}, p_i) \leq Pow(\mathbf{x}, p_j), \forall j\}.$$

The dual triangulation to Power diagram is called the Power Delaunay triangulation.
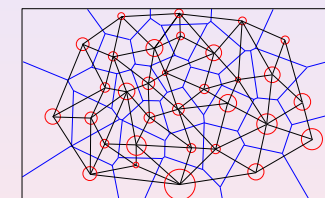
Voronoi Diagram Delaunay Triangulation

Definition (Voronoi Diagram)

Let (S, V) be a punctured surface, V is the vertex set. d is a flat cone metric, where the cone singularities are at the vertices. The Voronoi diagram is a cell decomposition of the surface, Voronoi cell W_i at v_i is

$$W_i = \{\mathbf{p} \in S | d(\mathbf{p}, v_i) \leq d(\mathbf{p}, v_j), \forall j\}.$$

The dual triangulation to the voronoi diagram is called the Delaunay triangulation.
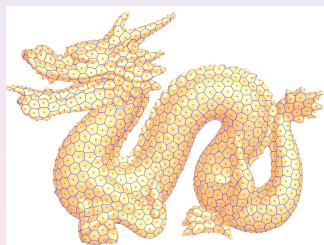
Power Voronoi Diagram Delaunay Triangulation

Definition (Power Diagram)

Let (S, V) be a punctured surface, with a generalized circle packing metric. The Power diagram is a cell decomposition of the surface, a Power cell W_i at v_i is

$$W_i = \{\mathbf{p} \in S | Pow(\mathbf{p}, v_i) \leq Pow(\mathbf{p}, v_j), \forall j\}.$$

The dual triangulation to the power diagram is called the power Delaunay triangulation.
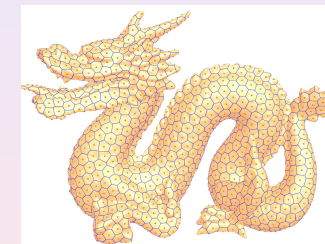
Edge Weight

Definition (Edge Weight)

(S, V, d), d a generalized CP metric. D the Power diagram, T the Power Delaunay triangulation. $\forall e \in D$, the dual edge $\bar{e} \in T$, the weight

$$w(e) = \frac{|e|}{|\bar{e}|}.$$
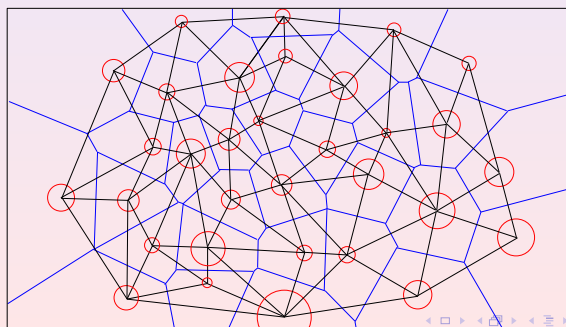
Discrete Surface Ricci Flow

Discrete Conformal Factor

Conformal Factor

Defined on each vertex $\mathbf{u} : V \to \mathbb{R}$,

$$u_i = \begin{cases} \log \gamma_i & \mathbb{R}^2 \\ \log \tanh \frac{\gamma_i}{2} & \mathbb{H}^2 \\ \log \tan \frac{\gamma_i}{2} & \mathbb{S}^2 \end{cases}$$

Discrete Surface Ricci Flow

Definition (Discrete Surface Ricci Flow with Surgery)

Suppose (S, V, d) is a triangle mesh with a generalized CP metric, the discrete surface Ricci flow is given by

$$\frac{du_i}{dt} = \bar{K}_i - K_i,$$

where $\bar{K}_i$ is the target curvature. Furthermore, during the flow, the Triangulation preserves to be Power Delaunay.

Theorem (Exponential Convergence)

The flow converges to the target curvature $K_i(\infty) = \bar{K}_i$. Furthermore, there exists $c_1, c_2 > 0$, such that

$$|K_i(t) - K_i(\infty)| < c_1 e^{-c_2 t}, |u_i(t) - u_i(\infty)| < c_1 e^{-c_2 t},$$

Discrete Conformal Metric Deformation

Properties

- Symmetry

$$\frac{\partial K_i}{\partial u_j} = \frac{\partial K_j}{\partial u_i} = -w_{ij}$$

- Discrete Laplace Equation

$$dK_i = \sum_{[v_i, v_j] \in E} w_{ij}(du_i - du_j)$$

namely

$$d\mathbf{K} = \Delta d\mathbf{u},$$

Discrete Laplace-Beltrami operator

Definition (Laplace-Beltrami operator)

Δ is the discrete Lapalce-Beltrami operator, $\Delta = (d_{ij})$, where

$$d_{ij} = \begin{cases} \sum_k w_{ik} & i = j \\ -w_{ij} & i \neq j, [v_i, v_j] \in E \\ 0 & otherwise \end{cases}$$

Lemma

Given (S, V, d) with generalized CP metric, if T is the Power Delaunay triangulation, then Δ is positive definite on the linear space $\sum_i u_i = 0$.

Because Δ is diagonal dominant.

Discrete Surface Ricci Energy

Definition (Discrete Surface Ricci Energy)

Suppose (S, V, d) is a triangle mesh with a generalized CP metric, the discrete surface energy is defined as

$$E(\mathbf{u}) = \int_{\mathbf{0}}^{\mathbf{u}} \sum_{i=1}^{k} (\bar{K}_i - K_i) du_i.$$

1. gradient $\nabla E = \bar{\mathbf{K}} - \mathbf{K}$,
2. Hessian
$$\left(\frac{\partial^2 E}{\partial u_i \partial u_j} \right) = \Delta,$$
3. Ricci flow is the gradient flow of the Ricci energy,
4. Ricci energy is concave, the solution is the unique global maximal point, which can be obtained by Newton's method.

One Example: Discrete Yamabe Flow

Delaunay Triangulation

Definition (Delaunay Triangulation)

Each PL metric d on (S, V) has a Delaunay triangulation T, such that for each edge e of T,

$$a + a' \leq \pi,$$
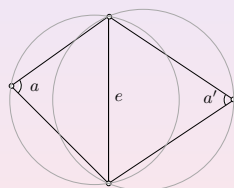
It is the dual of Voronoi decomposition of (S, V, d)

$$R(v_i) = \{x | d(x, v_i) \leq d(x, v_j) \text{ for all } v_j\}$$

Discrete Conformality

Definition (Conformal change)

Conformal factor $u : V \to \mathbb{R}$. Discrete conformal change is vertex scaling.
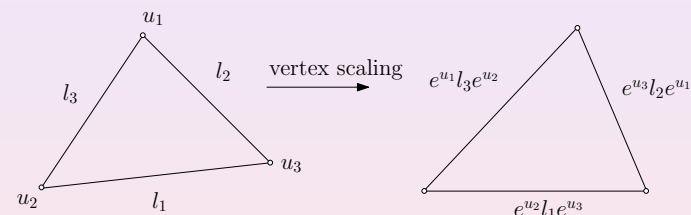
proposed by physicists Rocek and Williams in 1984 in the Lorenzian setting. Luo discovered a variational principle associated to it in 2004.

Discrete Yamabe Flow

Definition (Discrete Yamabe Flow)

$$\frac{du(v_i)}{dt} = \bar{K}(v_i) - K(v_i)$$

Theorem (Luo)

The discrete Yamabe flow converge exponentially fast,
$\exists c_1, c_2 > 0$, such that

$$|u_i(t) - u_i(\infty)| < c_1 e^{-c_2 t}, |K_i(t) - K_i(\infty)| < c_1 e^{-c_2 t},$$

Discrete Conformality

Definition (Discrete Conformal Equivalence)

PL metrics d, d' on (S, V) are discrete conformal,

$$d \sim d'$$

if there is a sequence $d = d_1, d_2, \cdots, d_k = d'$ and $T_1, T_2, \cdots, T_k$ on (S, V), such that

1. T_i is Delaunay in d_i
2. if $T_i \neq T_{i+1}$, then $(S, d_i) \cong (S, d_{i+1})$ by an isometry homotopic to *id*
3. if $T_i = T_{i+1}$, $\exists u : V \to \mathbb{R}$, such that $\forall$ edge $e = [v_i, v_j]$,

$$l_{d_{i+1}}(e) = e^{u(v_i)} l_{d_i} e^{u(v_j)}$$

Discrete Conformality

Discrete conformal metrics
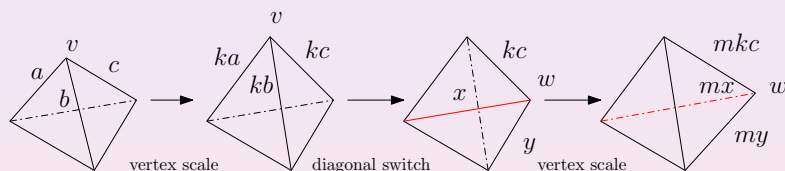
Main Theorem

Theorem (Gu-Luo-Sun-Wu (2013))

$\forall$ PL metrics d on closed (S, V) and $\forall \bar{K} : V \to (-\infty, 2\pi)$, such that $\sum \bar{K}(v) = 2\pi\chi(S)$, $\exists$ a PL metric $\bar{d}$, unique up to scaling on (S, V), such that

1. *$\bar{d}$ is discrete conformal to d*
2. *The discrete curvature of $\bar{d}$ is $\bar{K}$.*

Furthermore, $\bar{d}$ can be found from d from a discrete curvature flow.

Remark

$\bar{K} = \frac{2\pi\chi(S)}{|V|}$, discrete uniformization.

Main Theorem

1. The uniqueness of the solution is obtained by the convexity of discrete surface Ricci energy and the convexity of the admissible conformal factor space (u-space).

2. The existence is given by the equivalence between PL metrics on (S, V) and the decorated hyperbolic metrics on (S, V) and the Ptolemy identity.

X. Gu, F. Luo, J. Sun, T. Wu, "A discrete uniformization theorem for polyhedral surfaces", arXiv:1309.4175.

Algorithm

Input: a closed triangle mesh M, target curvature $\bar{K}$, step length δ, threshold ε
Output: a PL metric conformal to the original metric, realizing $\bar{K}$.

1. Initialize $u_i = 0$, $\forall v_i \in V$.
2. compute edge length, corner angle, discrete curvature K_i
3. update to Delaunay triangulation by edge swap
4. compute edge weight w_{ij}.
5. $\mathbf{u} += \delta \Delta^{-1}(\bar{\mathbf{K}} - \mathbf{K})$
6. normalize $\mathbf{u}$ such that the mean of u_i's is 0.
7. repeat step 2 through 6, until the max $|\bar{K}_i - K_i| < \varepsilon$.

Genus One Example
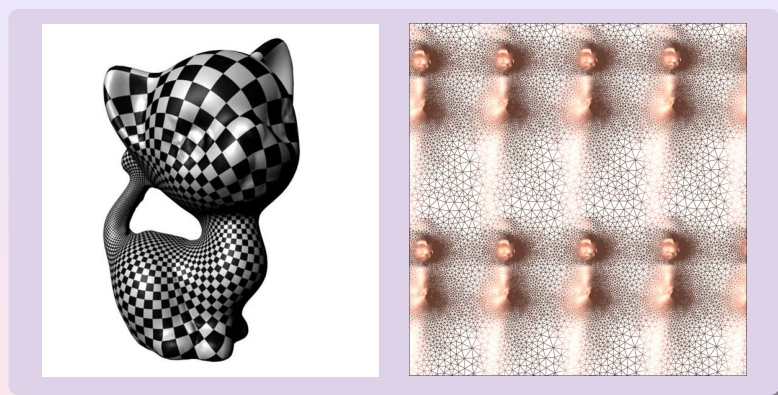
Hyperbolic Discrete Surface Yamabe Flow

Discrete conformal metric deformation:
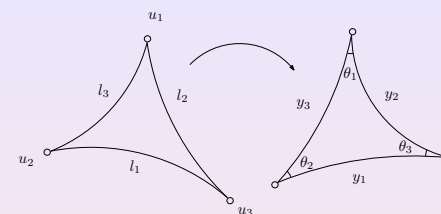
conformal factor

$$
\begin{aligned}
\frac{y_k}{2} &= e^{u_i}\frac{l_k}{2}e^{u_j} & \mathbb{R}^2 \\
\sinh\frac{y_k}{2} &= e^{u_i}\sinh\frac{l_k}{2}e^{u_j} & \mathbb{H}^2 \\
\sin\frac{y_k}{2} &= e^{u_i}\sin\frac{l_k}{2}e^{u_j} & \mathbb{S}^2
\end{aligned}
$$

Properties: $\frac{\partial K_i}{\partial u_j} = \frac{\partial K_j}{\partial u_i}$ and $d\mathbf{K} = \Delta d\mathbf{u}$.

Hyperbolic Discrete Surface Yamabe Flow

Unified framework for both Discrete Ricci flow and Yamabe flow

- Curvature flow

$$\frac{du}{dt} = \bar{K} - K,$$

- Energy

$$E(\mathbf{u}) = \int \sum_i (\bar{K}_i - K_i)\,du_i,$$

- Hessian of E denoted as Δ,

$$d\mathbf{K} = \Delta d\mathbf{u}.$$

Genus Two Example
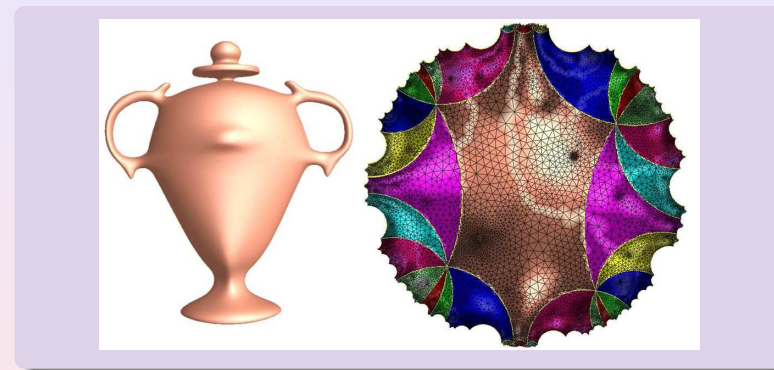
Genus Three Example
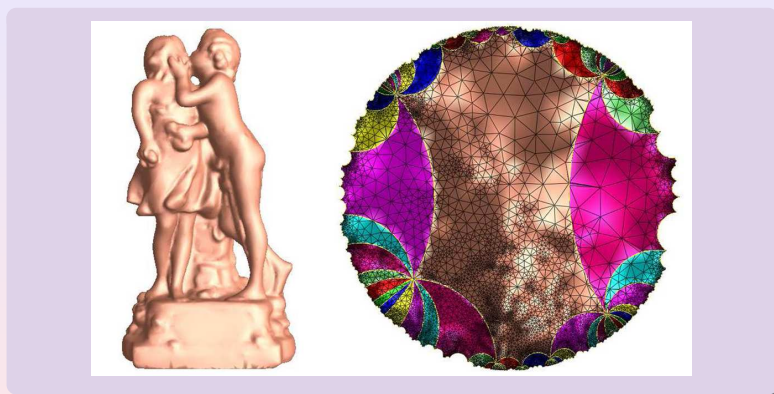
Computational Algorithms

Topological Quadrilateral

Topological Quadrilateral
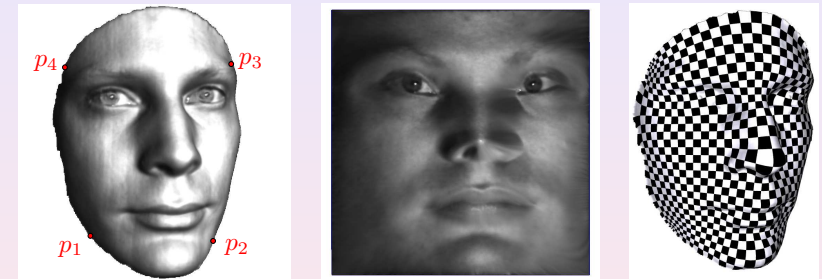
Figure: Topological quadrilateral.

Topological Quadrilateral

Definition (Topological Quadrilateral)

Suppose S is a surface of genus zero with a single boundary, and four marked boundary points $\{p_1, p_2, p_3, p_4\}$ sorted counter-clock-wisely. Then S is called a topological quadrilateral, and denoted as $Q(p1, p2, p3, p4)$.

Theorem

Suppose $Q(p1, p2, p3, p4)$ is a topological quadrilateral with a Riemannian metric $\mathbf{g}$, then there exists a unique conformal map $\phi : S \to \mathbb{C}$, such that ϕ maps Q to a rectangle, $\phi(p_1) = 0$, $\phi(p_2) = 1$. The height of the image rectangle is the conformal module of the surface.

Algorithm: Topological Quadrilateral

Input: A topological quadrilateral M
Output: Conformal mapping from M to a planar rectangle
$\phi : M \to \mathbb{D}$

1. Set the target curvatures at corners $\{p_0, p_1, p_2, p_3\}$ to be $\frac{\pi}{2}$,
2. Set the target curvatures to be 0 everywhere else,
3. Run ricci flow to get the target conformal metric $\bar{\mathbf{u}}$,
4. Isometrically embed the surface using the target metric.

Topological Annulus

Topological Annulus
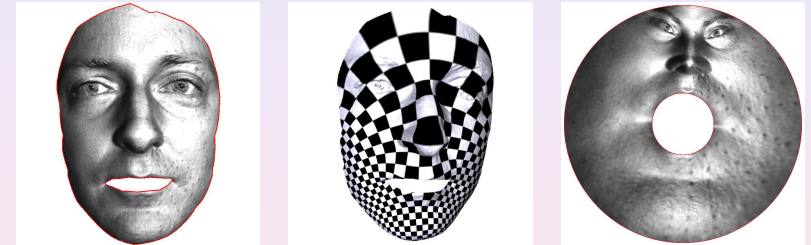
Figure: Topological annulus.

Topological Annulus

Definition (Topological Annulus)

Suppose S is a surface of genus zero with two boundaries, the S is called a topological annulus.

Theorem

Suppose S is a topological annulus with a Riemannian metric **g**, *the boundary of S are two loops* $\partial S = \gamma_1 - \gamma_2$, *then there exists a conformal mapping* $\phi : S \to \mathbb{C}$, *which maps S to the canonical annulus,* $\phi(\gamma_1)$ *is the unit circle,* $\phi(\gamma_2)$ *is another concentric circle with radius* γ. *Then* $-\log\gamma$ *is the conformal module of S. The mapping* ϕ *is unique up to a planar rotation.*

Algorithm: Topological Annulus

Input: A topological annulus M, $\partial M = \gamma_0 - \gamma_1$
Output: a conformal mapping from the surface to a planar annulus $\phi : M \to \mathbb{A}$

1. Set the target curvature to be 0 every where,
2. Run Ricci flow to get the target metric,
3. Find the shortest path γ_2 connecting γ_0 and γ_1, slice M along γ_2 to obtain $\bar{M}$,
4. Isometrically embed $\bar{M}$ to the plane, further transform it to a flat annulus

$$\{z | r \le Re(z) \le 0\}/\{z \to z + 2k\sqrt{-1}\pi\}$$

    by planar translation and scaling,
5. Compute the exponential map $z \to \exp(z)$, maps the flat annulus to a canonical annulus.

Riemann Mapping

Conformal Module

Simply Connected Domains

Topological Disk

Definition (Topological Disk)

Suppose S is a surface of genus zero with one boundary, the S is called a topological disk.

Theorem

Suppose S is a topological disk with a Riemannian metric $\mathbf{g}$, then there exists a conformal mapping $\phi : S \to \mathbb{C}$, which maps S to the canonical disk. The mapping ϕ is unique up to a Möbius transformation,

$$z \to e^{i\theta} \frac{z - z_0}{1 - \bar{z}_0 z}.$$

Algorithm: Topological Disk

Input: A topological disk M, an interior point $p \in M$
Output: Riemann mapping $\phi : M \to mathbbD$, maps M to the unit disk and p to the origin

1. Punch a small hole at p in the mesh M,
2. Use the algorithm for topological annulus to compute the conformal mapping.

Slide 1

Multiply connected domains

Slide 2

Multiply-Connected Annulus

Definition (Multiply-Connected Annulus)

Suppose S is a surface of genus zero with multiple boundaries, then S is called a multiply connected annulus.

Theorem

Suppose S is a multiply connected annulus with a Riemannian metric $\mathbf{g}$, then there exists a conformal mapping $\phi : S \to \mathbb{C}$, which maps S to the unit disk with circular holes. The radii and the centers of the inner circles are the conformal module of S. Such kind of conformal mapping are unique up to Möbius transformations.

Slide 3

Algorithm: Multiply-Connected Annulus

Input: A multiply-connected annulus M,

$$\partial M = \gamma_0 - \gamma_1, \cdots, \gamma_n.$$

Output: a conformal mapping $\phi : M \to \mathbb{A}$, $\mathbb{A}$ is a circle domain.

1. Fill all the interior holes γ_1 to γ_n
2. Punch a hole at γ_k, $1 \le k \le n$
3. Conformally map the annulus to a planar canonical annulus
4. Fill the inner circular hole of the canonical annulus
5. Repeat step 2 through 4, each round choose different interior boundary γ_k. The holes become rounder and rounder, and converge to canonical circles.
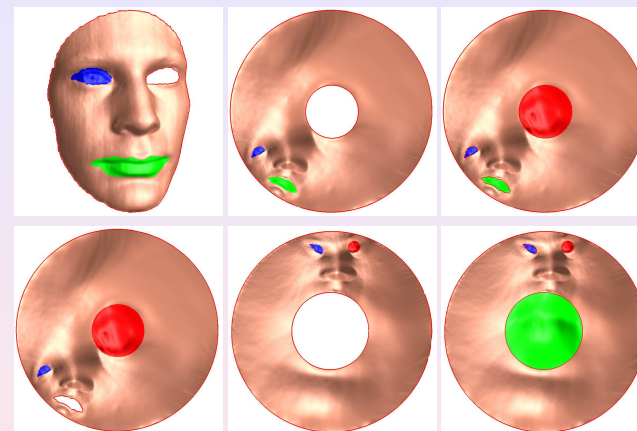
Slide 4

Koebe's Iteration - I

Figure: Koebe's iteration for computing conformal maps for multiply connected domains.

Koebe's Iteration - II
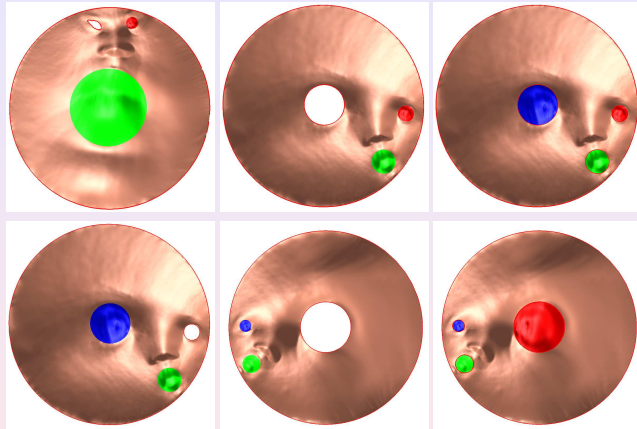
Figure: Koebe's iteration for computing conformal maps for multiply connected domains.

Koebe's Iteration - III
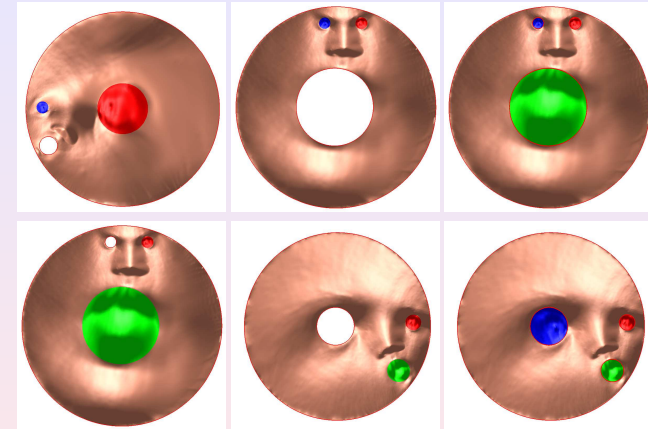
Figure: Koebe's iteration for computing conformal maps for multiply connected domains.

Convergence Analysis

Theorem (Gu and Luo 2009)

Suppose genus zero surface has n boundaries, then there exists constants $C_1 > 0$ and $0 < C_2 < 1$, for step k, for all $z \in \mathbb{C}$,

$$|f_k \circ f^{-1}(z) - z| < C_1 C_2^{2[\frac{k}{n}]},$$

where f is the desired conformal mapping.

W. Zeng, X. Yin, M. Zhang, F. Luo and X. Gu, "Generalized Koebe's method for conformal mapping multiply connected domains", Proceeding SPM'09 SIAM/ACM Joint Conference on Geometric and Physical Modeling, Pages 89-100.

Topological Torus

Topological torus
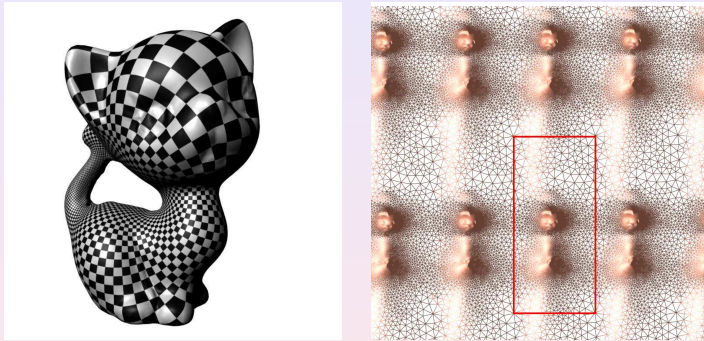
Figure: Genus one closed surface.

Algorithm: Topological Torus

Input: A topological torus M

Output: A conformal mapping which maps M to a flat torus $\mathbb{C}/\{m + n\alpha | m, n\mathbb{Z}\}$

1. Compute a basis for the fundamental group $\pi_1(M)$, $\{\gamma_1, \gamma_2\}$.
2. Slice the surface along γ_1, γ_2 to get a fundamental domain $\bar{M}$,
3. Set the target curvature to be 0 everywhere
4. Run Ricci flow to get the flat metric
5. Isometrically embed $\tilde{S}$ to the plane

Hyperbolic Ricci Flow

Computational results for genus 2 and genus 3 surfaces.
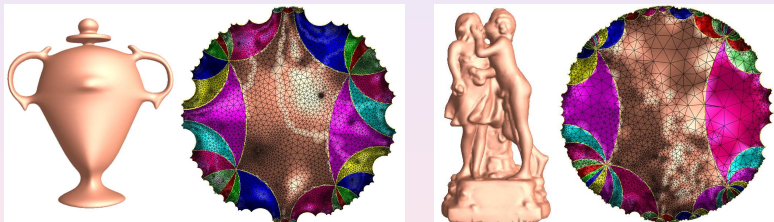
Hyperbolic Koebe's Iteration
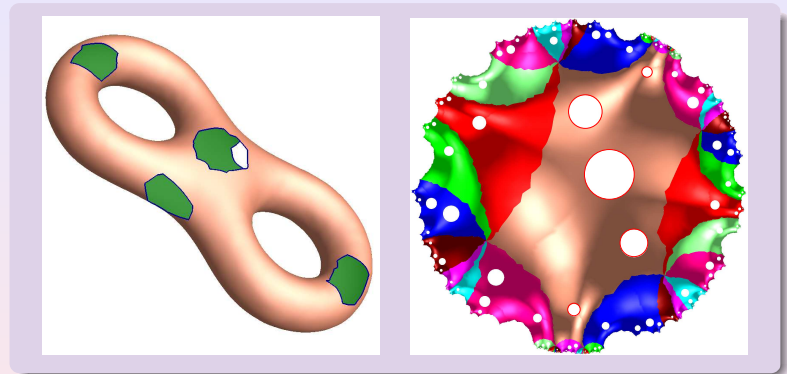
M. Zhang, Y. Li, W. Zeng and X. Gu. "Canonical conformal mapping for high genus surfaces with boundaries", Computer and Graphics, Vol 36, Issue 5, Pages 417-426, August 2012.

Differential Operators and Spaces for Shape Modeling

Laplacian Operator and Spectral Processing

G. Patanè, X.D. Gu, X.S. Li

Functions on 3D shapes

- **Laplace-Beltrami operator**
  - Harmonic equation
    - Discretization & properties
  - Laplacian eigenproblem
    - Discretization & properties
  - Heat diffusion equation
    - Discretization & properties
    - Spectrum-free computation
    - Heat diffusion distances
- **Applications**
  - Shape analysis and comparison

Functions on 3D shapes: discrete case

- Define f:M➤R on the mesh vertices of M and extend f to the edges and faces by using barycentric coordinates.

$$f$$

$$\max(f)$$

$$\subset \mathbf{R}$$

$$\mathcal{M}$$

$$\min(f)$$
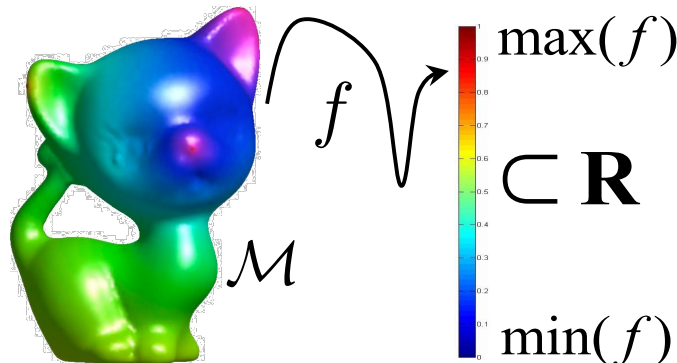
Laplace-Beltrami operator

- Continuous case
$$\Delta f = \mathrm{div}(\mathrm{grad})f$$

- Harmonic equation
$$\Delta f = 0$$

- Laplacian eigenvalue problem
$$\Delta f = \lambda f$$

- Heat diffusion equation
$$\partial_t F(\cdot, t) = \Delta F(\cdot, t)$$

Discrete Laplacians

- We represent the Laplacian matrix for meshes and point sets in a "unified" way as

$$\tilde{L} = B^{-1}L$$

L symm., positive semi-definite

B symm., positive definite

Stiffness matrix

$$L(i,j) := \begin{cases} w(i,j) := \frac{\cot \alpha_{ij} + \cot \beta_{ij}}{2} & j \in N(i), \\ -\sum_{k \in N(i)} w(i,k) & i = j, \\ 0 & \text{else,} \end{cases}$$

Mass matrix

$$B(i,j) := \begin{cases} \frac{|t_r| + |t_s|}{12} & j \in N(i), \\ \frac{\sum_{k \in N(i)} |t_k|}{6} & i = j, \\ 0 & \text{else,} \end{cases}$$
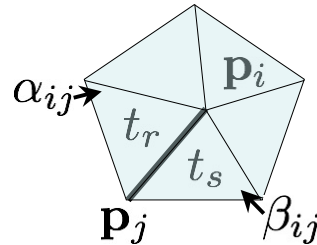
Discrete Laplacians

- **B area-driven matrix**
  - Linear FEM weights
    - [Reuter2006,Vallet2008]
  - Voronoi-cotg weights   **T-mesh**
    - [Desbrun1999]
  - Mean-value weights
    - [Floater2003]
  - Polygonal weights   **Polyg-mesh**
    - [Alexa2011]
  - Voronoi-exp weights   **Points**
    - [Liu2012]
- **B=I** (Euclidean product on a 3D shape)
  - Cotg weights   **T-mesh**
    - [Pinkall1999]
  - Exp weights   **Points**
    - [Belkin2003-06-08]

Harmonic functions

Smooth functions with a (generally) low number of critical points are achieved by solving the Laplace-Beltrami equation with Dirichlet boundary conditions.

$$\begin{cases} \Delta f = 0 & \mathbf{p} \in \mathcal{M} \\ f(\mathbf{p}) = g(\mathbf{p}), & \mathbf{p} \in \mathcal{B} \subset \mathcal{M} \end{cases}$$

$$\begin{cases} \tilde{L}\mathbf{f} = \mathbf{0} & \mathbf{f} := (f(\mathbf{p}_i))_{i=1}^n \\ f(\mathbf{p}_i) = \alpha_i & i \in \mathcal{I} \end{cases}$$

Harmonic functions
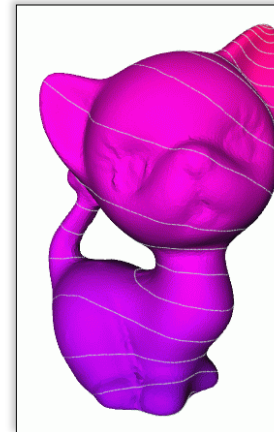
$m = 1, M = 1, s = 2$ $m = 3, M = 3, s = 6$

$m = 2, M = 2, s = 4$

Harmonic functions: properties

- The number of critical points depends on
  - the Dirichlet boundary conditions
  - the genus of the input surface, according to the Euler formula $s = m + M - \chi(\mathcal{M})$
- If f is harmonic and has 1 min and 1 max (i.e., 2 Dirichlet boundary conditions),
  - f has 2g saddles, g=genus of M
  - f has a minimal number of critical points (i.e., 2+2g)
  - saddles are located on the topological handles of M
- $f \in_{\approx} C^2(M, \mathbf{R})$.

Harmonic functions: properties

- **Stability:** Numerical instabilities might be introduced by its discretization:
  - the cotangent weights are negative if $\alpha_{ij} + \beta_{ij} > \pi$
  - the mean-value weights are always positive and more stable than the cotangent weights.
- **Degree of freedom:** the choice of the Dirichlet boundary conditions.
- **Efficiency:** solution of a sparse linear system O(nlogn)
- **Invariance:** f is invariant w.r.t. isometries (linear FEM, Voronoi-cotg weights).

Harmonic functions: properties

- Harmonic functions with the same Dirichlet boundary conditions: different postures of the same shape.

Laplacian eigenproblem

- Linear finite elements (*weak formulation*) yield the **generalized eigenvalue problem** [Reuter04,Vallet08]

$$L\mathbf{f} = \lambda B \mathbf{f}$$

  - L **stiffness matrix** with cotangent weights
  - B **mass matrix**, which
    - encodes the triangle areas
    - defines the scalar product $\langle \mathbf{f}, \mathbf{g} \rangle_B := \mathbf{f}^T B \mathbf{g}$ on the space of piecewise linear scalar functions on the input surface.

Laplacian eigenfunctions

- The generalized eigensystem of (L,B)

$$Lx_i = \lambda_i Bx_i, \qquad \langle x_i, x_j \rangle_B = \delta_{ij}$$

defines a set of (n-1) non-trivial, **smooth**, **shape-intrinsic, isometry-invariant** maps.
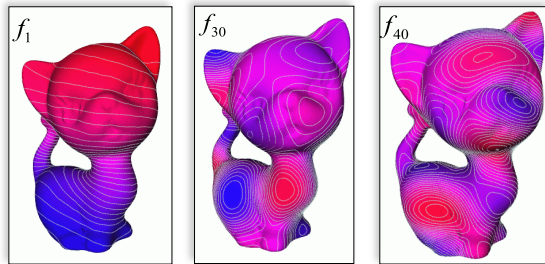
Laplacian eigenfunctions

- **Smoothness:** the first eigenvectors correspond to smooth and slowly varying functions, while the last ones show rapid oscillations (increasing number of critical points).
- **Shape-driven properties:** Laplacian eigenfunctions
  - are intrinsic to the input shape
  - identify shape features at different scales (*nodal domains*).
- **Stability:** the switch of the eigenfunctions might happen regardless the quality of the mesh discretization.

Laplacian eigenfunctions: switch

$\lambda_{21} > \lambda_{22}$

$\lambda_{37} = 0.015696$ $\lambda_{38} = 0.015493$

$\lambda_{37} > \lambda_{38}$
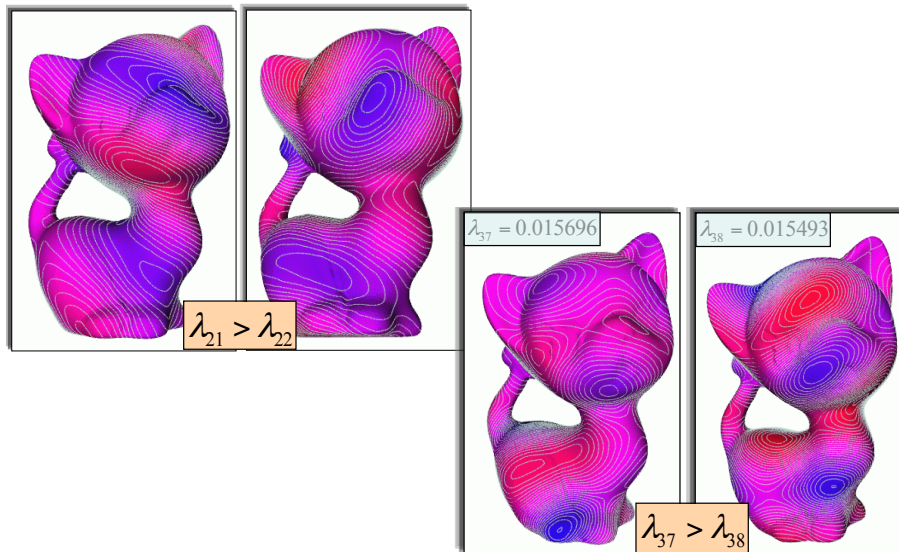
Laplacian eigenfunctions: robustness
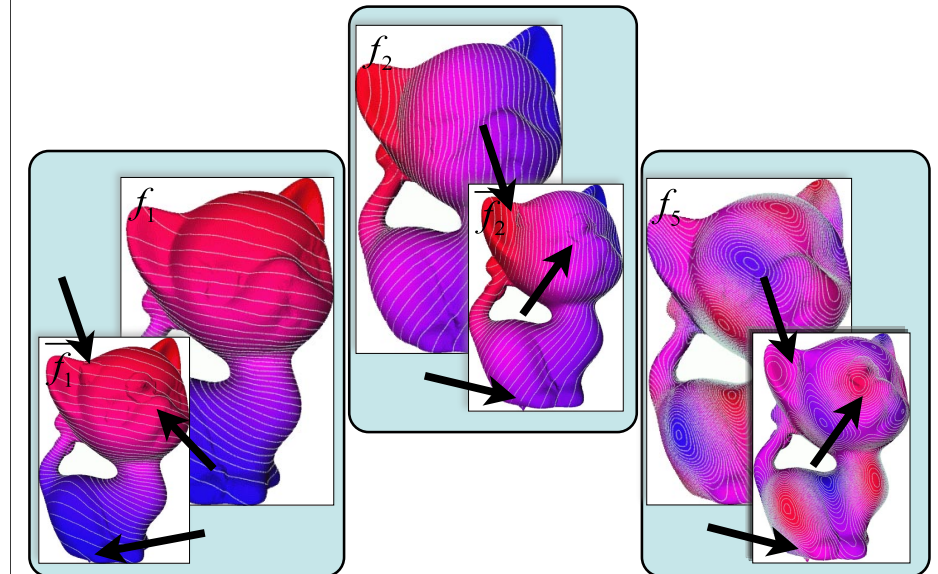
Laplacian eigenfunctions

- **Related work:** properties of the Laplacian spectrum have been investigated for several applications, such as
  - data reduction [Belkin03-08,...]
  - compression [Karni,...]
  - discrete differential forms [Desbrun99-05,Gu03,...]
  - local/global parameterization [Floater,Patane04-07,Zhang05,...]
  - quadrilateral remeshing [Dong06,...]
  - shape analysis [Biasotti07,...]
  - shape processing & deformation [Levy06,Vallet08,Zhang07,...]
  - shape comparison and correspondence [Reuter05-07,Rustamov07,Jain06-07,Wardetzky07,...]
  - ...

Heat diffusion equation
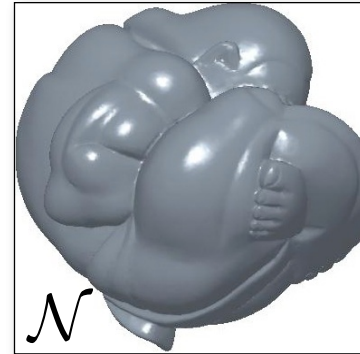
$$\begin{cases} (\partial_t + \Delta) H(\cdot, t) = 0 \\ H(\cdot, 0) = h \end{cases}$$

$$\Delta \psi_i = \lambda_i \psi_i$$

$$H(\mathbf{x}, t) = K_t(\mathbf{x}, t) \star h$$

$$K_t(\mathbf{x}, \mathbf{y}) = \sum_{i=0}^{+\infty} \exp(-\lambda_i t) \psi_i(\mathbf{x}) \psi_i(\mathbf{y})$$

Applications

- Applications of the heat diffusion kernel and distance
  - **multi-scale representations** of functions [Rosenberg97,Patane10-13]
  - **shape segmentation** [DeGoes08,Gebal08]
  - **shape comparison** with HK shape signatures [Bronstein09-11,Memoli09,Ovsjanikov10,Sun09]
    - intrinsic to the shape
    - isometry-invariant
    - multi-scale (local vs global details)
  - **diffusion distances** [Coifman06] for
    - data matching [Lafon06]
    - gradient [Wang09], critical points computation [Luo09]
  - **dimensionality reduction** [Belkin03,Roweis00,Xiaoa10,Tenenbaum00]
  - **clustering** [Chapelle03]
  - ...

Discrete Laplacians

- We represent the Laplacian matrix for meshes and point sets in a "unified" way as

$$\tilde{L} = B^{-1} L$$

L symm., positive semi-definite

B symm., positive definite
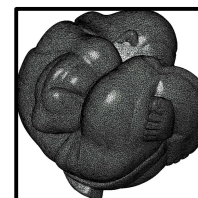
$$\begin{cases} (\partial_t + \tilde{L})\mathbf{F}(t) = \mathbf{0} \\ \mathbf{F}(0) = \mathbf{f} \end{cases} \qquad \mathbf{F}(t) := (F(\mathbf{p}_i, t))_{i=1}^n$$

Heat kernel discretization

- On the space of functions defined on P, we consider the B-scalar product $\langle \mathbf{f}, \mathbf{g} \rangle_B := \mathbf{f}^T B \mathbf{g}$.

- Using the generalized eigensystem of (L,B), the solution is

$$F(\cdot, t) = K_t \mathbf{f} \qquad K_t := X D_t X^T B$$

$$\boxed{K_t = \exp(-t B^{-1} L)}$$

Properties

- The resulting discrete heat kernel is
  - **self-adjoint** with respect to the B-scalar product
  - **stable** to noise, irregular sampling
  - **isometry-invariant** $\qquad K_t(\alpha\mathcal{M}) = K_t(\mathcal{M})$
  - **intrinsically scale-covariant** (i.e., with no a-posteriori normalization) $K_t(\alpha\mathcal{M}) = K_{\alpha^2 t}(\mathcal{M})$
  - **scale-invariant** through a normalization of the Laplacian eigenvalues
  - **higher robustness for shape comparison**, i.e., it improves robustness of matching based on HK descriptors [SHREC10]
  - **consistent**: if the linear FEM mass matrix B is lumped to D, then K_t equals the kernel $K_t^* = X D_t X^T D$, which holds for $L := D^{-1} W$.

Example: robustness

Sampling

Noise

Off-set

Deformation
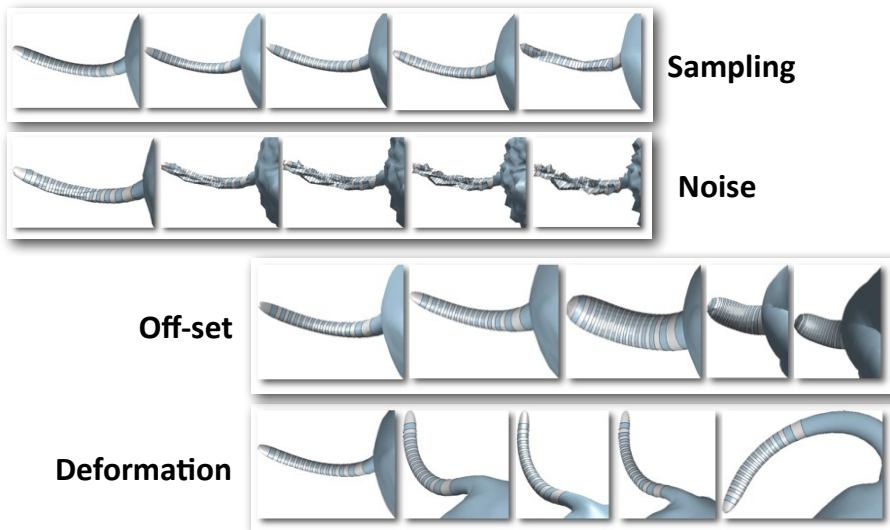
Example: dist. robustness
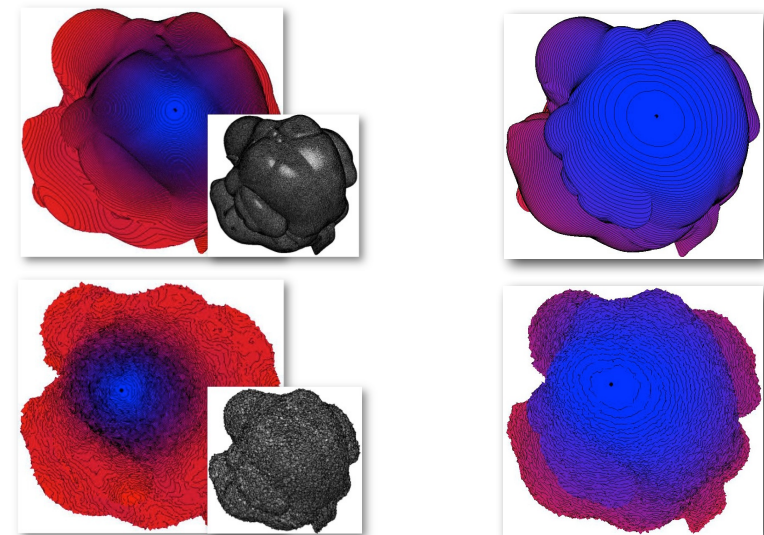
Example: dist. robustness
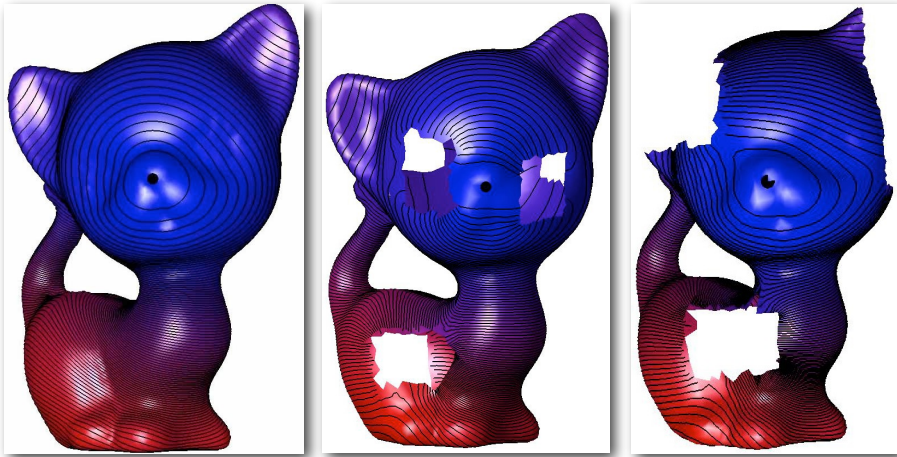
Previous work

- **Truncated spectral approximations** of the HK consider the contribution of the first k Laplacian eigenpairs related to the smaller eigenvalues.
- **Main motivations**
  - the evaluation of the whole spectrum is computationally unfeasible
    - $O(kn)$ to $O(n^3)$, n points (*matrix sparsity*)
    - $O(kn)$ memory for storing k Laplacian eigenvectors (*large k*)
  - the filter factors exponentially tend to zero as the eigenvalues and/or the time parameter increase.

Previous work

- Approximate the HK with **multi-resolutive prolongation operators** [Vaxman10]
  - using k eigenpairs on a specific level of a multi-resolutive shape representation
  - selecting k according to time and the shape resolution in the hierarchy
  - prolongating the HK from a given resolution to the input shape.
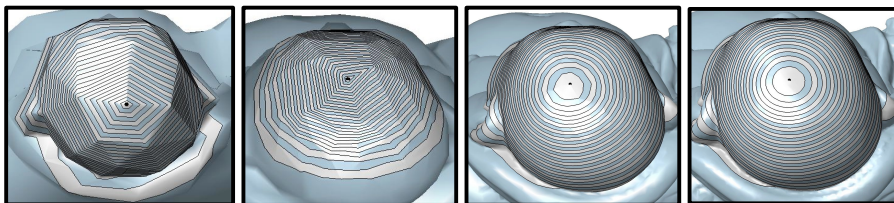
Main limitations

- Need to select and adapt the number of eigenpairs to
  - the shape resolution in the hierarchy
  - the temporal parameter.
- No "exact" computation of the heat kernel; i.e., extraction of the whole Laplacian spectrum.
- No estimation of the approximation accuracy with respect to the selection of k eigenpairs.
- Focus on shapes represented as triangle meshes.

Aims

- Unified, robust discretization and **spectrum-free computation** of the heat kernel with respect to the discretization of the
  - input 3D shape
  - Laplace-Beltrami operator.
- No selection of input parameters.
- High approximation accuracy 10^{-r} (r:=5,7), which can be adjusted through the degree of the Padè-Chebyshev rational approximation.

Patanè G. **wFEM Heat Kernel: Discretization and Applications to Shape Analysis and Retrieval.** Computer Aided Geometric Design. In press, 2013.

Chebyshev approximation

- Compute the (r,r)-degree rational function $c_{rr}(x)$ of e^x with respect to the l_∞-norm

$$\exp(x) \approx \alpha_0 + \sum_{i=1}^{r} \alpha_i (x - \theta_i)^{-1}$$

coeff.   **poles**

- compute the approximation of $K_t := \exp(-tB^{-1}L)$

$$\exp(-tB^{-1}L)\mathbf{f} \approx \alpha_0 \mathbf{f} + \sum_{i=1}^{r} \alpha_i (-tB^{-1}L - \theta_i I)^{-1}\mathbf{f}$$

$$:= \mathbf{g}_i$$

Chebyshev approximation

- Solve r sparse, symmetric linear systems

$$(tL + \theta_i B)\mathbf{g}_i = -B\mathbf{f}$$

- Spectrum-free computation of the heat diffusion kernel

$$K_t \mathbf{f} \approx \alpha_0 \mathbf{f} + \sum_{i=1}^{r} \alpha_i \mathbf{g}_i$$

- **Solution:** iterative solvers or pre-factorization of (L,B).
- **Properties**
  - Independency of the shape and Laplacian discretization
  - No input parameters (*degree r fixed*).

Numerical accuracy & stability

- **Accuracy** For a (r,r) Chebyshev polynomial approx.,
  - solution of r sparse and symmetric linear systems (e.g., r=5,7)
  - l_2 error between e^c and its rational approximation is lower than $\sigma_{rr} \approx 10^{-r}$ (*unif. rational Cheb. constant*).
- **Stability**
  - The Chebyshev approx. might be unstable if $||tC||_2$ is large.
  - From the upper bound $\|tB^{-1}L\|_2 \leq t\lambda_{\max}(L)\lambda_{\min}^{-1}(B)$ a well-conditioned matrix B guarantees that $||tB^{-1}L||_2$ is bounded and low.

Example: numerical stability
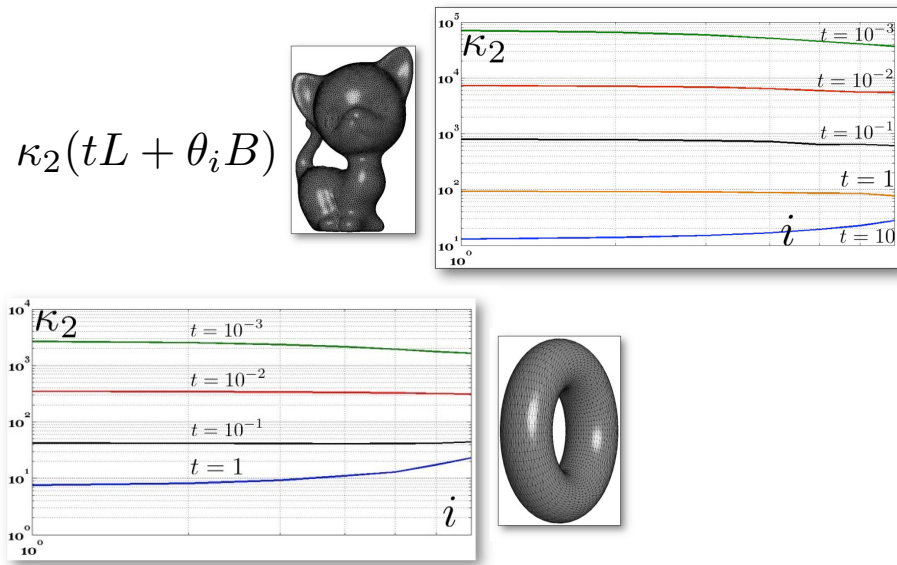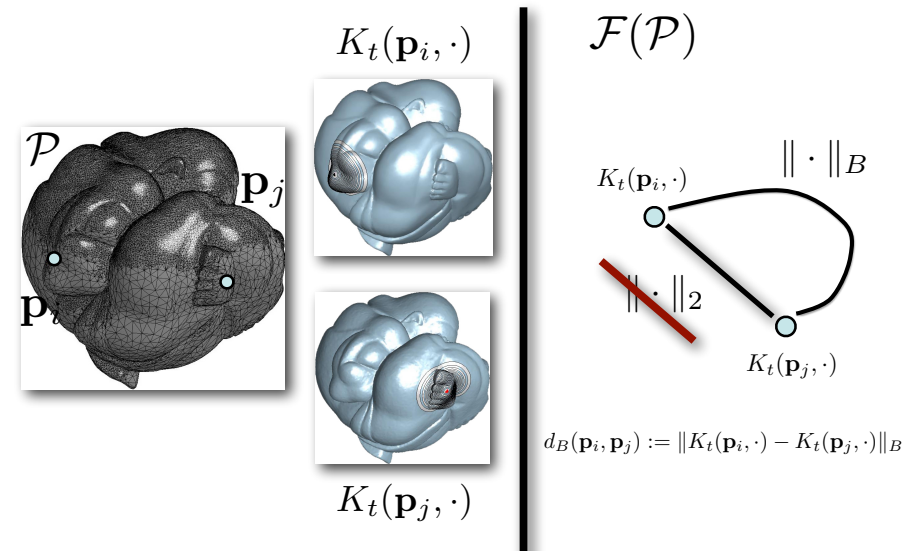
$\kappa_2(tL + \theta_i B)$

κ_2 $t = 10^{-3}$ $t = 10^{-2}$ $t = 10^{-1}$ $t = 1$ $t = 10$ i

κ_2 $t = 10^{-3}$ $t = 10^{-2}$ $t = 10^{-1}$ $t = 1$ i

Heat diffusion distance

$K_t(\mathbf{p}_i, \cdot)$ $\mathcal{F}(\mathcal{P})$

$\mathcal{P}$ $\mathbf{p}_j$ $\mathbf{p}_i$

$K_t(\mathbf{p}_j, \cdot)$

$K_t(\mathbf{p}_i, \cdot)$ $\|\cdot\|_B$ $\|\cdot\|_2$ $K_t(\mathbf{p}_j, \cdot)$

$d_B(\mathbf{p}_i, \mathbf{p}_j) := \|K_t(\mathbf{p}_i, \cdot) - K_t(\mathbf{p}_j, \cdot)\|_B$

Heat diffusion distance

- The B-scalar product induces the diffusion distance

$$d_B(\mathbf{p}_i, \mathbf{p}_j) := \|K_t(\mathbf{p}_i, \cdot) - K_t(\mathbf{p}_j, \cdot)\|_B^2$$
$$= \sum_{l=1}^{n} \exp(-2\lambda_l t) |\langle \mathbf{x}_l, \mathbf{e}_i - \mathbf{e}_j \rangle_B|^2$$

Heat diffusion distance

- The B-scalar product induces the diffusion distance

$$d_B(\mathbf{p}_i, \mathbf{p}_j) := \|K_t(\mathbf{p}_i, \cdot) - K_t(\mathbf{p}_j, \cdot)\|_B^2$$
$$= \sum_{l=1}^{n} \exp(-2\lambda_l t) |\langle \mathbf{x}_l, \mathbf{e}_i - \mathbf{e}_j \rangle_B|^2$$

- Previous work

$$d(\mathbf{p}_i, \mathbf{p}_j) = \sum_{l=1}^{n} \exp(-\lambda_l t) |\langle \mathbf{x}_l, \mathbf{e}_i - \mathbf{e}_j \rangle_2|^2$$

Heat diffusion distance

- The spectrum-free computation of the heat diffusion distance is based on the Chebyshev approximation of the heat kernel.
- Expressing the diffusion distance in terms of K_{2t} and B

$$d_B^2(\mathbf{p}_i, \mathbf{p}_j) = \mathbf{e}_i^T B K_{2t} \mathbf{e}_i - 2\mathbf{e}_i^T B K_{2t} \mathbf{e}_j + \mathbf{e}_j^T B K_{2t} \mathbf{e}_j$$

$$\mathbf{e}_i^T B K_{2t} \mathbf{e}_j$$

Chebyshev approximation

Example: comput. cost
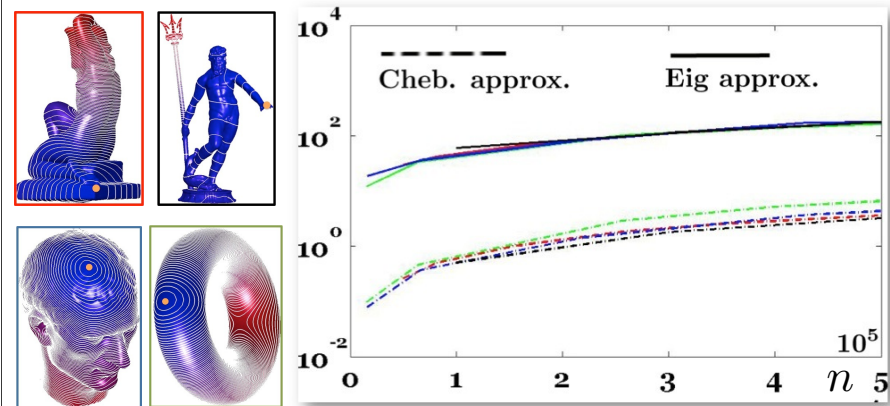
Example: comput. cost

Acquarius Fig. 9(a)				Neptune Fig. 9(b)			
n	Eigs	Cheb.	$\times$	n	Eigs	Cheb.	$\times$
5K	30.06	0.26	115	10K	59.65	0.50	119
25K	97.25	1.83	53	30K	111.28	1.78	62
35K	130.39	2.61	49	50K	176.47	3.21	54
50K	173.78	3.60	48	100K	372.16	7.44	50
Torus Fig. 9(c)				Julius Fig. 9(d)			
n	Eigs	Cheb.	$\times$	n	Eigs	Cheb.	$\times$
2K	12.00	0.01	1200	2K	18.47	0.08	230
6K	33.28	0.45	73	7K	35.89	0.37	97
26K	100.88	2.89	34	22K	82.47	1.42	58
49K	140.00	5.14	33	43K	173.52	3.71	46
58K	186.06	7.92	23	50K	174.89	4.34	40

wFEM HK & shape comparison

- We have compared HK- and wFEM HK-based shape descriptors.
- **Data set**: 1184 shapes (13 transf.)
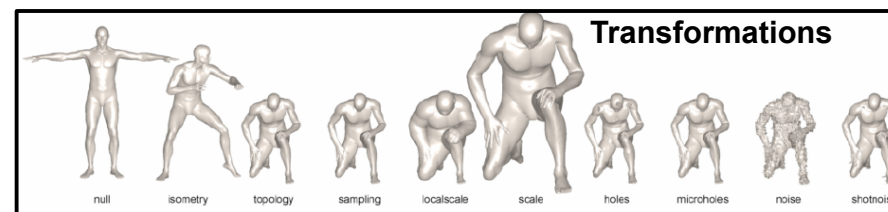
BRONSTEIN, A. M., BRONSTEIN, M. M., CASTELLANI, U., FALCIDIENO, B., FUSIELLO, A., GODIL, A., GUIBAS, L., KOKKINOS, I., LIAN, Z., OVSJANIKOV, M., PATANÈ, G., SPAGNUOLO, M., AND TOLDO, R. 2010. Shrec 2010: robust large-scale shape retrieval benchmark. *Eurographics Workshop on 3D Object Retrieval*.

BRONSTEIN, A. M., BRONSTEIN, M. M., BUSTOS, B., CASTELLANI, U., CRISANI, M., FALCIDIENO, B., GUIBAS, L. J., I. KOKKINOS, V. M., ISIPIRAN, I., OVSJANIKOV, M., PATANÈ, G., SPAGNUOLO, M., AND SUN, J. 2010. Shrec 2010: robust large-scale shape retrieval benchmark. *Eurographics Workshop on 3D Object Retrieval*.

wFEM- vs HK-based shape descr.

- Comparison results for 5 methods.

- **DHK1**: [BBOG10]
- **DHK2**: Ours
- **SHK1-2**: [SOG09]

[BBOG10] BRONSTEIN A. M., BRONSTEIN M. M., OVS-
JANIKOV M., GUIBAS L. J.: ShapeGoogle: geometric words
and expressions for invariant shape retrieval. *TOG (in review)*
(2010). 4

[SOG09] SUN J., OVSJANIKOV M., GUIBAS L.: A concise and
provably informative multi-scale signature based on heat dif-
fusion. In *Eurographics Symposium on Geometry Processing
(SGP)* (2009). 2, 4

[JH99] JOHNSON A., HEBERT M.: Using spin images for effi-
cient object recognition in cluttered 3D scenes. *IEEE Transac-
tions on Pattern Analysis and Machine Intelligence* 21, 5 (1999),
433–449. 4, 5

Transform.	Strength				
	≤ 1	≤ 2	≤ 3	≤ 4	≤ 5
Isometry	DHK2	DHK2	DHK2	DHK2	DHK2
Topology	DHK2	DHK2	DHK2	DHK2	DHK2
Holes	DHK2	DHK2	DHK2	DHK2	DHK1
Micro holes	DHK2	DHK2	DHK2	DHK2	DHK2
Scale	SHK2	SHK2	SHK2	SHK2	SHK2
Local scale	DHK2	DHK2	DHK2	DHK2	DHK2
Sampling	DHK2	DHK2	DHK2	DHK2	DHK2
Noise	DHK1	DHK1	DHK2	SHK1	SHK2
Shot noise	DHK2	DHK2	DHK2	DHK2	DHK2
Average	DHK2	DHK2	DHK2	DHK2	DHK2

Table 16: *Winning feature description algorithms across trans-
formation classes and strengths. DHK1=dense heat kernel signa-
tures using cotangent weight discretization, SHK2=sparse heat ker-
nel signatures based on features detected by HK2.*

From Surface- to Volume-based Shape Modeling and Analysis

Volumetric approximation
and main approaches

G. Patanè, X.D. Gu, X.S. Li

Volumetric approximation

- **Volumetric approximation**
  - Piecewise linear approximations
  - Radial basis functions
  - Harmonic volumetric mapping
  - Moving least-squares
  - Constrained (topology-driven) approximation
  - Local approximation with RBFs
- **Applications**
  - Image & data resampling
  - Shape correspondences
  - Biomedical applications

Volumetric approximation - Motivations

- **Shape modeling** handles a 3D shape as a 2-manidold, which describes the boundary shape (e.g., mesh, point set, …).
- A volumetric **surface representation** is more suited to handle the shape complexity.
- A volumetric **signal representation** is more suited to analyze complex phenomena measured on the input shape.
- Volumetric approximation of shape geometry and scalar functions will be handled using a **signal-like approach**.
- …
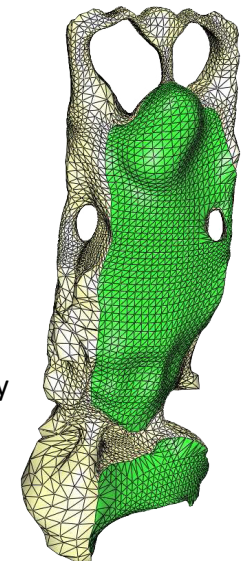
Volumetric approximation - Motivations

We will address
- the **integration** of surface- and volume-based shape information for the approximation of scalar functions defined on surfaces
- different **volumetric approximations**
  - piecewise linear approximation
  - smooth approximation
  - constrained approximation
  - local approximation
- the use of several **approximation constraints**; e.g.,
  - smoothness conditions
  - interpolating constraints
  - preservation of critical points and feature values at both a local and global level.

Approximation problem

- **Input:** a discrete map $f:M \rightarrow R$, defined on a set $M:=\{p_i\}_{i=1}^n$ of points of R^d, which have been sampled on
  - a 2D image
  - a 3D shape
  - a volumetric domain
  - d-dimensional data for $M \subseteq R^d$.

- **Output:** compute $F:R^d \rightarrow R$ that locally interpolates or approximates the f-values.
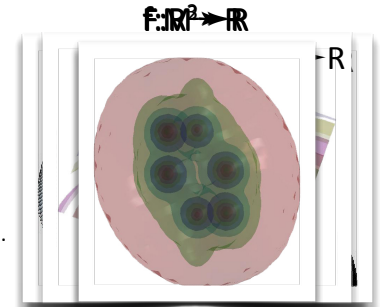
Motivations

- Approximating discrete maps on R^d is important for
  - providing fast computation of volumetric (e.g., Laplacian eigenmaps) shape descriptors

Motivations

- resampling images and volumetric data

$M \subseteq R^2$ $f:M \rightarrow R$ $M \subseteq R^3$ $f:M \rightarrow R$
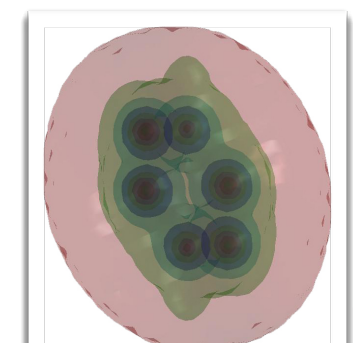
$F:R^2 \rightarrow R$ $F:R^3 \rightarrow R$

Motivations

- extending maps from shapes to volumes

Input PL function on T-mesh

Smooth volumetric function

$f : \mathcal{M} \rightarrow \mathbb{R}$

$F : \mathbb{R}^3 \rightarrow \mathbb{R}$
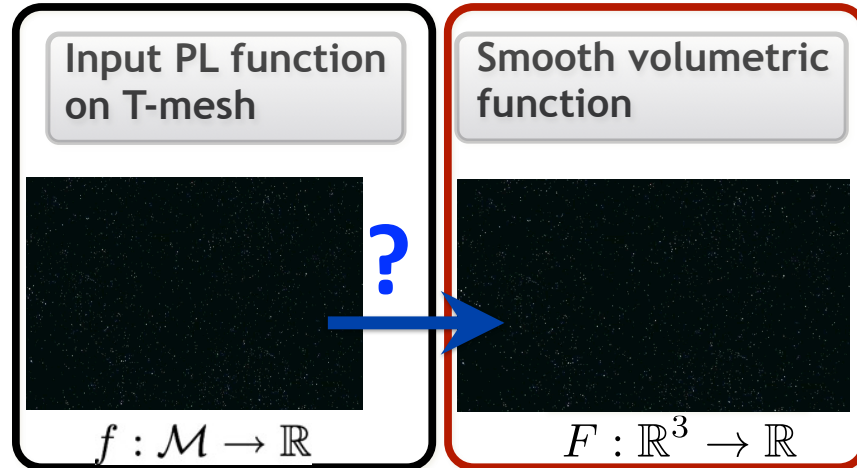
Motivations

- identifying correspondences between shapes
- computing the cross shape parameterization

Volumetric mapping (both surface points and interior points)
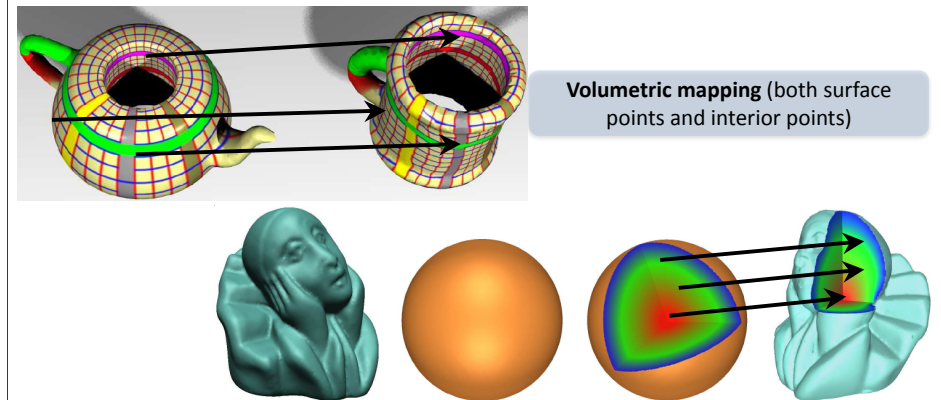
Motivations

- studying phenomena measured on surfaces and that act in the surrounding space.
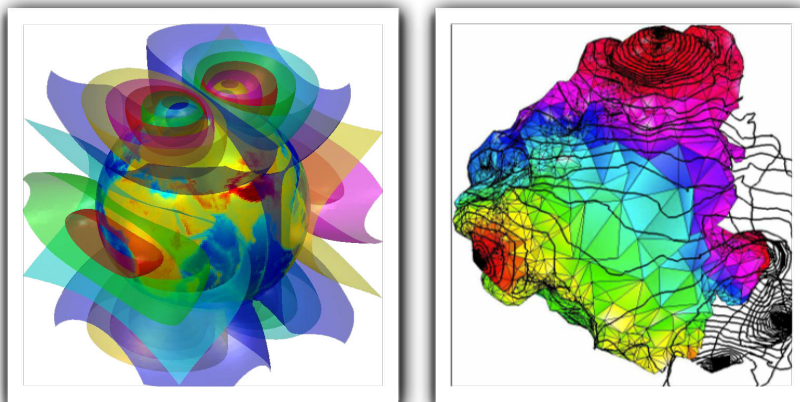
Desired properties

- The volumetric approximation $F:\mathbb{R}^3 \rightarrow \mathbb{R}$ of $f:M \rightarrow \mathbb{R}$ should be
  - **locally computed**
  - **independent of**
    - **any underlying tessellation** and **parameterization domain** (*meshless approximation*)
    - **dimension** of the input data
  - **accurate**
    - by combining interpolating and least-squares constraints on the f-values (*constraints' flexibility*)
    - by improving the accuracy of linear precision and MLS methods with polynomial basis functions (*higher extrapolation capabilities*)
  - **computationally efficient** through the solution of a small and well-conditioned linear system.

Desired properties

- The volumetric approximation $F:R^3 \to R$ of $f:M \to R$
  - at **global level**
    - preserves the features of $f:M \to R$; e.g., critical points, f-values, smoothness, harmonicity,…
    - induces a correspondence with its surface-based map f
  - at **local level**
    - preserves the details of f at a given accuracy
  - at **computational level**
    - is efficiently computable; e.g., selection of RBFs, f-values, etc.

Main approaches

- **Piecewise-linear** approximations with generalized barycentric
- **Smooth** approximations
  - Partition of the Unity
  - Radial Basis Functions
  - Moving Least-Squares
- **Local** approximation with RBFs
- **Constrained** approximations
  - Critical points' preservation

Main approaches

- **Piecewise-linear approximations:**
  - *Barycentric coordinates*: [Rustamov11]
- **Smooth approximations:**
  - *Radial basis functions*: [Aronszajin50,Dyn86,Micchelli86, Poggio90,Wendland95], [Morse01,Patanè06,Shen05,Turk02], [Adams09,Weiler05,Jang04-06]
  - *Implicits*: [Boomenthal97,Hart99,Pasko95/98]
  - *Volume parameterization*: [Li10,Martin08]
  - *Moving Least-Squares*: [Adamson03,Alexa01,Amenta04,Fleishman03,Guennebaud07,Jin09,Levin98,Pauly02-03], [Carr01,Dey05,Shen04,Walder06,Xie04]
  - *Partition of the Unity*: [Ohtake03/05]
- **Constrained & local volumetric approximations**: [Jin09,Patanè09/12]

Linear precision methods

- Since $f:M \to R$ is known at the vertices of the T-mesh, we consider the function $F:R^3 \to R$

$$F(\mathbf{p}) := \sum_{i=1}^{n} f(\mathbf{p}_i)\varphi_i(\mathbf{p})$$

Barycentric coordinates of **p**

Properties

$\varphi_i(\mathbf{p}_j) = \delta_{ij}$	**Lagrange property**
$\sum_{i=1}^{n} \varphi_i(\mathbf{p}) = 1$	**Partition of the Unity**
$\sum_{i=1}^{n} \varphi_i(\mathbf{p})\mathbf{p}_i^{(x)} = \mathbf{p}_i^{(x)}$	**Affine combination**

Generalized barycentric coordinates

- Main **properties** of the volumetric approximation with barycentric coordinates
  - linear precision
  - piecewise linear continuity
  - fast computation
  - …
- **Applications**
  - computation of volumetric shape descriptors through interpolation of surface-based Laplacian eigenfunctions
  - surface and volume parameterization.

Volumetric approximation with RBFs

- Compute the function $F: \mathbb{R}^3 \to \mathbb{R}$ that satisfies the **interpolating conditions**

$$F(\mathbf{p}_i) = f(\mathbf{p}_i) \quad i = 1, \ldots, n$$

$\mathbf{p}_i$

$\|\mathbf{p} - \mathbf{p}_i\|_2$

$\mathbf{p}$
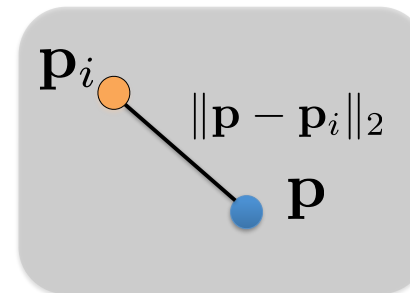
$\varphi_i(\mathbf{p}) := \varphi(\|\mathbf{p} - \mathbf{p}_i\|_2)$

Basis function centered at $\mathbf{p_i}$

$\varphi : \mathbb{R} \to \mathbb{R}$

Kernel function

Volumetric approximation with RBFs

- The solution F is a linear combination of RBFs centered at the points of M

$$F(\mathbf{p}) = \sum_{k=1}^{n} \alpha_k \varphi_k(\mathbf{p})$$

Unknown coefficients

$$A\alpha = \mathbf{f}$$

$A = (\varphi_i(\mathbf{p}_j))_{i,j=1}^n$

$\alpha := (\alpha_i)_{i=1}^n$

$\mathbf{f} := (f(\mathbf{p}_i))_{i=1}^n$

Volumetric approximation with RBFs

- The kernel properties (e.g., compact support, positive definiteness, etc) determine the
  - properties of the Gram matrix;
    - sparsity
    - symmetry
    - positive-definiteness
  - properties of the solution (e.g., uniqueness)
  - selection of the solver; e.g.,
    - direct solvers
    - iterative solvers (e.g., conjugate gradient←Gram matrix is symmetric and positive definite).

Volumetric approximation with RBFs

- Select a set **C** of centers; e.g., apply PCA, sparsification, clustering, …

- Consider the corresponding RBFs and approximation

$$F(\mathbf{p}) = \sum_{\mathbf{p}_i \in \mathcal{C}} \alpha_i \varphi_i(\mathbf{p})$$

- Minimize the least-square error

LS error

$$\mathcal{E} := \sum_{i=1}^{n} |F(\mathbf{p}) - f(\mathbf{p}_i)|^2$$

Volumetric approximation with RBFs

- **Cons**
  - center selection
  - time-consuming update of the approximation
  - …

$$\Phi : n \times k \qquad (\Phi^T \Phi)\alpha = \Phi^T \mathbf{f}_k$$

Gram matrix $\qquad k \times k,\ k := |\mathcal{C}|$

- **Pro**
  - reduction of the noise effects on the final approximation
  - reduction of the computational cost, which is proportional to the number of selected centers instead of input points
  - …

MLS approximation

$$f : \mathcal{M} \rightarrow \mathbb{R}$$

$\mathbf{p}_1$

$W(\mathbf{p}, \mathbf{p}_1)$

$\mathbf{p}$ $W(\mathbf{p}, \mathbf{p}_i)$

$W(\mathbf{p}, \mathbf{p}_2)$ $\mathbf{p}_i$

$\mathbf{p}_2$

$\mathcal{M}$

LS error

$$\mathcal{E} := \sum_{i=1}^{n} |F(\mathbf{p}) - f(\mathbf{p}_i)|^2$$

$$F(\mathbf{p}) = ?$$

Weighted LS

$$\mathcal{E} := \sum_{i=1}^{n} W(\mathbf{p}, \mathbf{p}_i)|F(\mathbf{p}) - f(\mathbf{p}_i)|^2$$
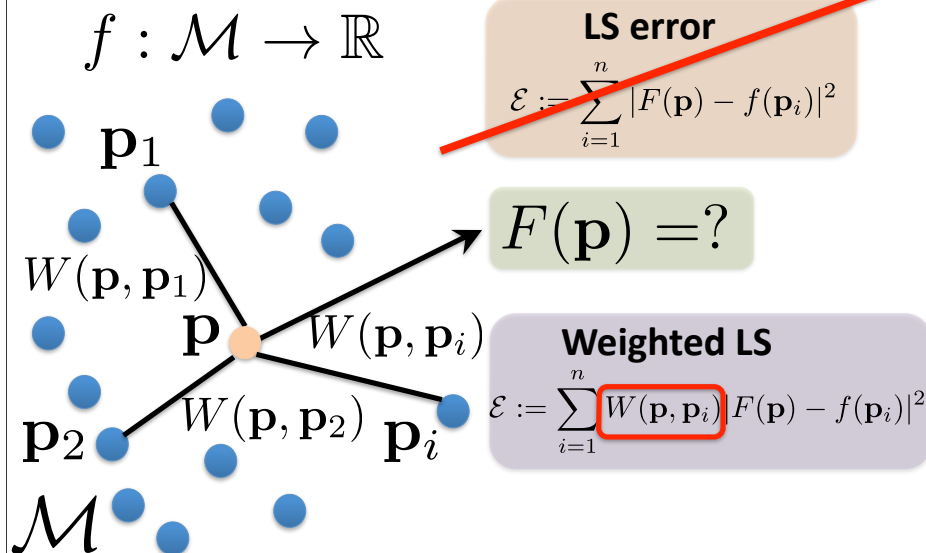
MLS approximation

- F(**p**) is a polynomial function of degree at most r

$$F(x, y, z) := \sum_{\alpha + \beta + \gamma = r} C_{\alpha, \beta, \gamma} x^\alpha y^\beta z^\gamma$$

- The normal equation depends on the evaluation point **p**

$$\left[\Phi^T W(\mathbf{p}) \Phi \right] \alpha = \Phi^T W(\mathbf{p}) \mathbf{f}$$

Pol. Gram matrix Weights Input f-values

MLS approximation

- Approximation with polynomial functions
  - choice of the polynomial degree?
    - usually degree $r=2$ or $r=3$ in x, y, z
    - numerical instabilities with higher polynomial degrees
    - growth of the number of unknowns with r
  - no use of interpolating constraints
    - polynomial degree is *a-priori* fixed
    - number of local constraints depends on the sampling density
    - only least-squares constraints → no interpolating conditions
  - ...

Example

Example

Example

[Input] [Loc. ap.] [APSS] [RIMLS]
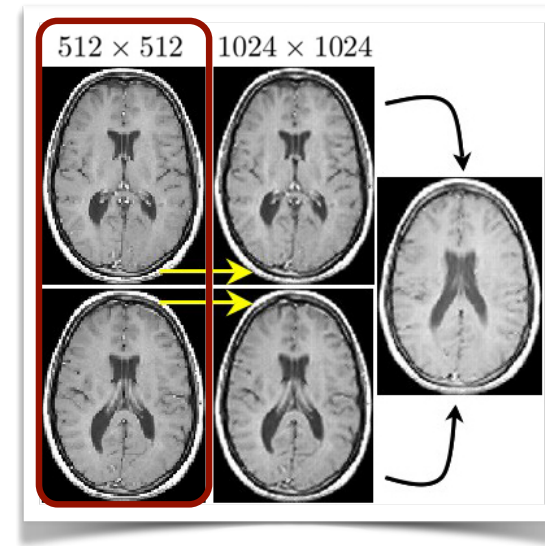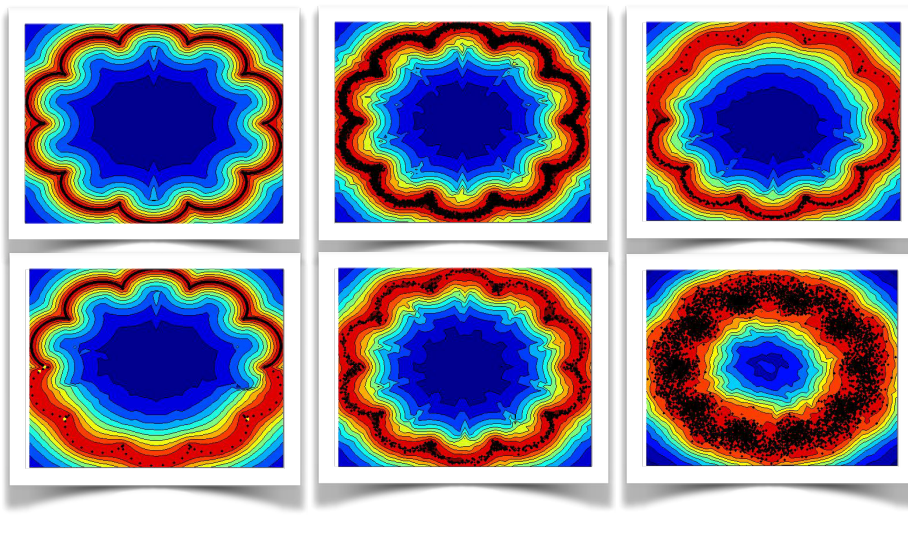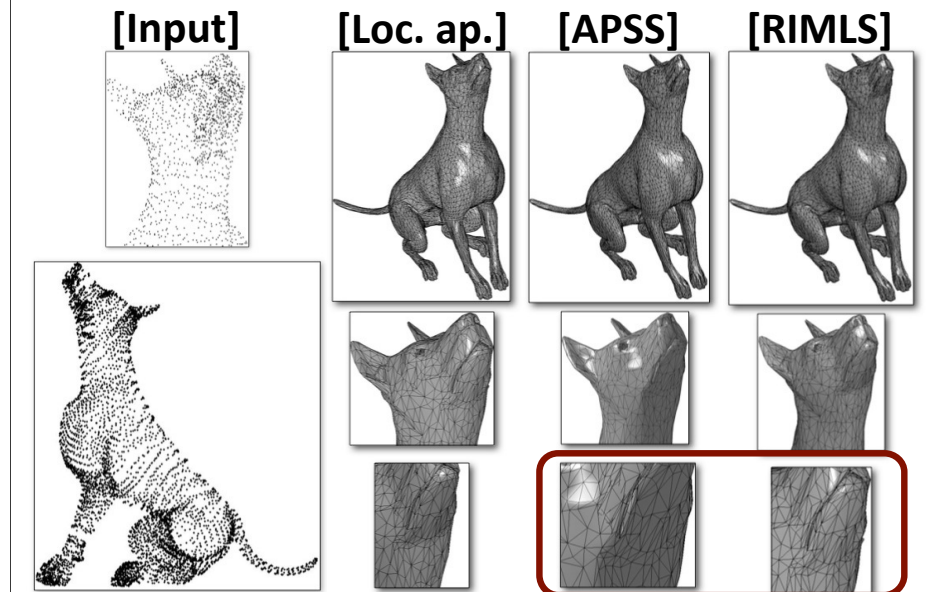
Constrained volumetric approximation

- **Idea**: emphasis on
  - **critical points' preservation**; i.e., preservation of the topological behavior of the input scalar function
  - selection of a generally low number of interpolation conditions (**center selection**)
  - generation of a **hierarchy** of surface- and volume-based approximations of the input map.
- The approximation error can be locally reduced with additional interpolating/least-squares constraints.

Patanè G, Spagnuolo M., Falcidieno B. **Topology- and error-driven extension of scalar functions from surfaces to volumes** ACM Transactions on Graphics, 2009. SIGGRAPH 2010, Los Angeles − USA

Topology-driven approximation

Input PL function on T-mesh

Smooth volumetric function

f, h same critical points

Global support

$h : \mathcal{M} \rightarrow \mathbb{R}$

$f : \mathcal{M} \rightarrow \mathbb{R}$ $g : \mathbb{R}^3 \rightarrow \mathbb{R}$ $h := g_{\mathcal{M}}$
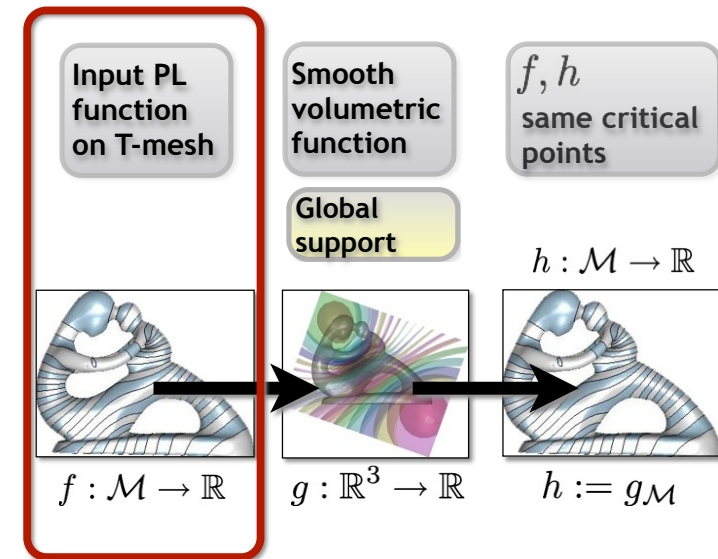
Properties

- The topology-driven approximation
  - at **global level**
    - preservation of topological features (critical points) of $f{:}M{\rightarrow}R$
    - hierarchy of surface-based approx. and volumetric extensions of f
  - at **local level**
    - preservation of details of f at a given accuracy
  - at **computational level**
    - efficiently selection of of RBF centers used by the approximation.
- **Related work**
  - Morse theory: [Banchoff67,Bajaj98,Biasotti09,Bremer04, Dey06,Edelsbrunner04-06,Hart98,Liu07,Milnor63,Ni04, Pascucci04,Patane09,Weber02]

Topology-driven approximation

- **Problem statement:** Given a PL scalar function $f{:}M{\rightarrow}R$, extend f to a volumetric function $g{:}R^3{\rightarrow}R$ such that
  - g is smooth: $g \in C^k$
  - g is globally supported (*topology-driven extension*)
  - the PL scalar function $h{:}M{\rightarrow}R$, with $h(\mathbf{p}_i){=}g(\mathbf{p}_i)$, i=1,...,n,
    - has a "smooth" behavior on M
    - has the same critical points of f (*topology-driven approximation*)
    - preserves the details of f within a given error.

Idea-behind 1D case
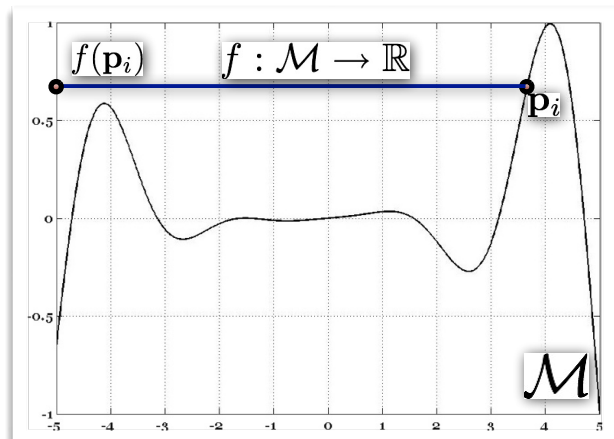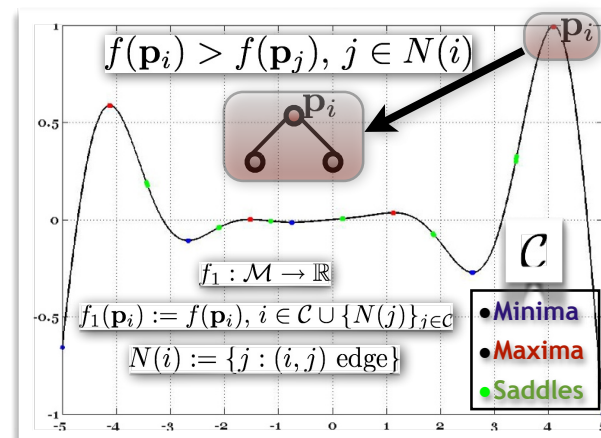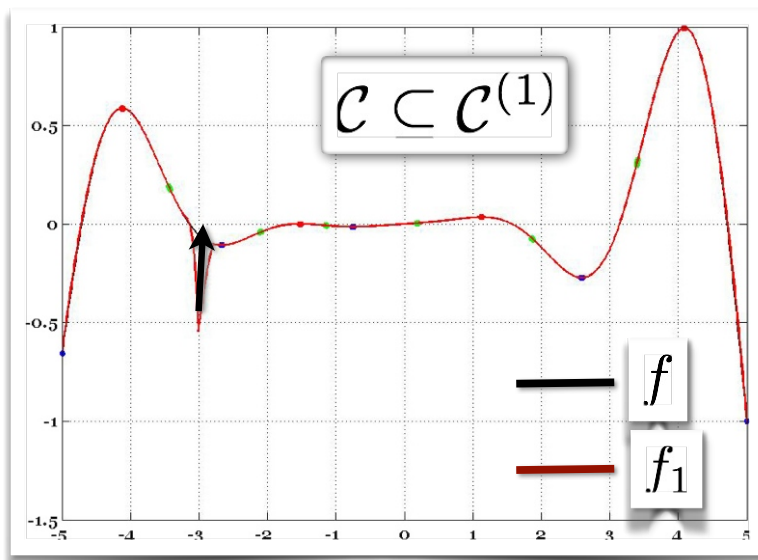
$f(\mathbf{p}_i)$ $f : \mathcal{M} \to \mathbb{R}$ $\mathbf{p}_i$

$\mathcal{M}$

Idea-behind 1D case

$f(\mathbf{p}_i) > f(\mathbf{p}_j), \; j \in N(i)$

$\mathbf{p}_i$

$\mathbf{p}_i$

$f_1 : \mathcal{M} \to \mathbb{R}$

$f_1(\mathbf{p}_i) := f(\mathbf{p}_i), \; i \in \mathcal{C} \cup \{N(j)\}_{j \in \mathcal{C}}$

$N(i) := \{j : (i,j) \text{ edge}\}$

$\mathcal{C}$

- Minima
- Maxima
- Saddles

Idea-behind 1D case

$\mathcal{C} \subset \mathcal{C}^{(1)}$

f

f_1

Idea-behind 1D case

$f_2 : \mathcal{M} \to \mathbb{R}$

$f_2(\mathbf{p}_i) := f(\mathbf{p}_i),$
$i \in \mathcal{C}^{(1)} \cup \{N(j)\}_{j \in \mathcal{C}^{(1)}}$

f

f_2

Idea-behind 1D case

$g : \mathbb{R}^2 \to \mathbb{R}$

$\mathcal{M}$

Topology-driven approximation

$f : \mathcal{M} \to \mathbb{R}$

Approximation hierarchy

Stop condition?

g_1 g_2 g_3

f_1 f_2 f_3
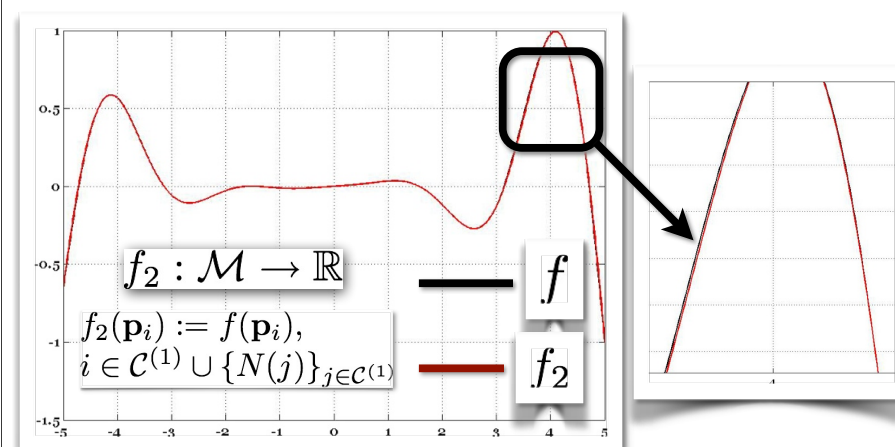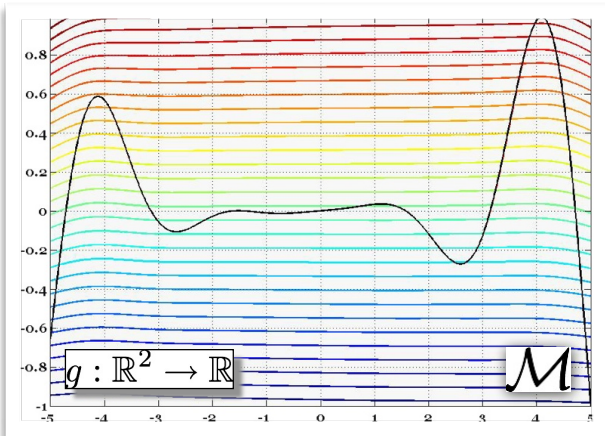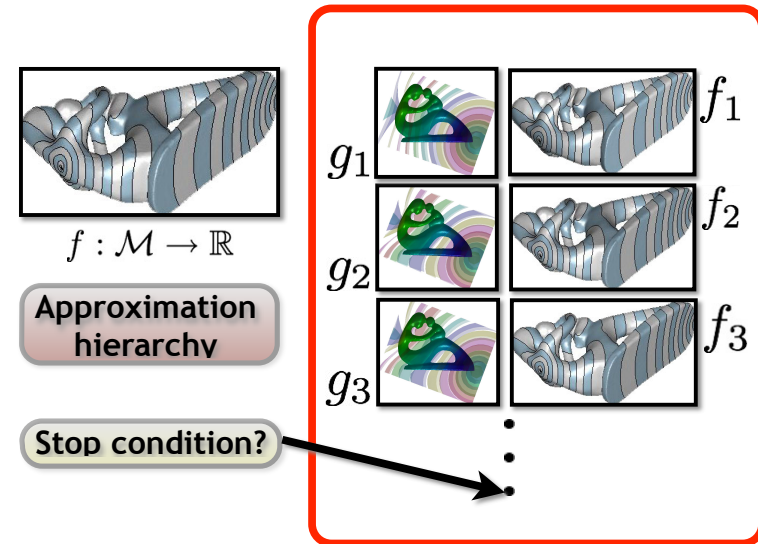
Topology-driven approximation

- Variation of the critical points.

- Minima
- Maxima
- Saddles

$\mathcal{C} \subseteq \mathcal{C}^{(k)} \subseteq \mathcal{C}^{(k+1)}$

$8 + s(k)$ > 0

$M + M(k)$ > 0

$M\mathcal{C}^{(k)} \equiv \mathcal{C}$ $m(k) = 0$

$k \geq 1$

Num. critical points of $f^{(k)}$

Iteration k
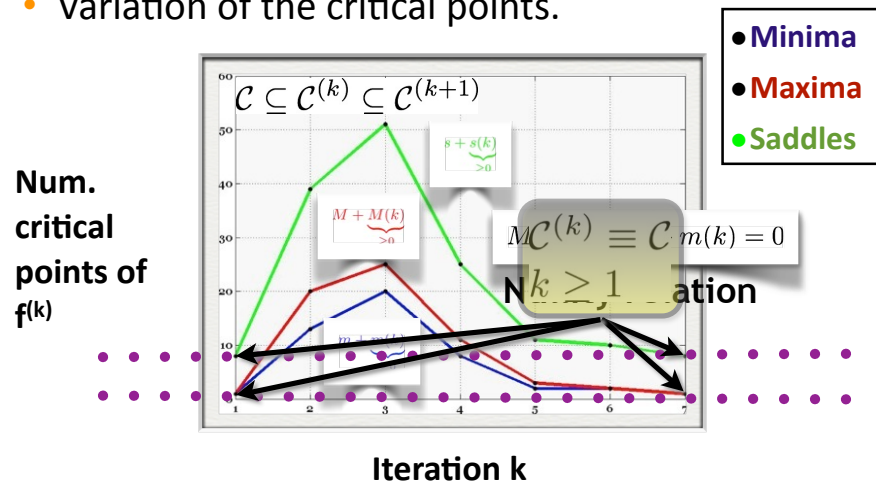
Topology-driven approximation

- The number and position of the selected centers (interpolation conditions) depend on the critical points and behavior of the input function.

Approx. error

$\|f - f_k\|_\infty$

Num. RBFs

Num. iterations

Num. iterations

Example

f
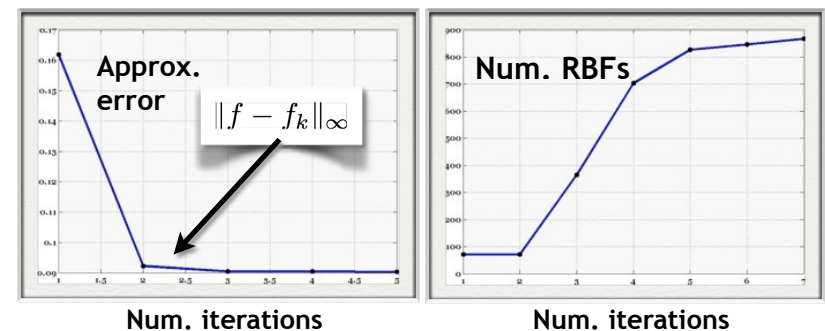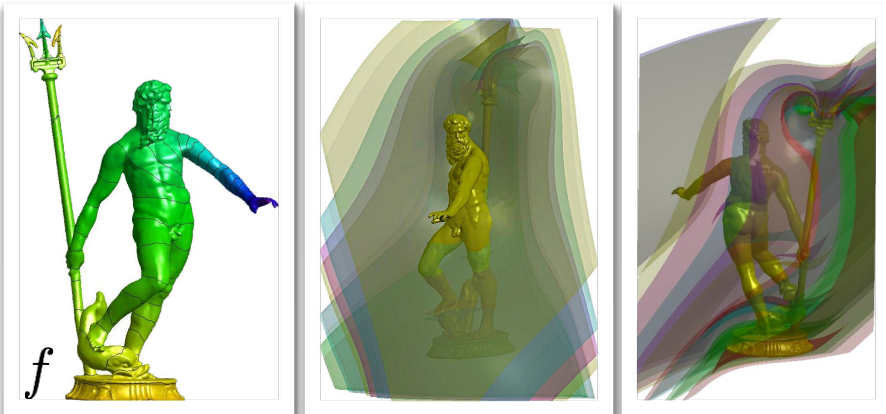
Topology-driven approximation

- **Computational cost:** at each step k,
  - critical points' classification: O(n), with n vertices
  - matrix construction: $O(r_k^2)$, with r_k number of selected centers
  - iterative solution of the linear system: $O(r_k^2)$
- **Properties:** The topology-driven approximation is computed through an iterative process, which
  - converges in a finite number of steps
  - avoids stop conditions based on thresholds
  - can be applied to n-dimensional data equipped with a map
  - can be coupled with error-driven/weak constraints

From Cross-Surface Mapping to Cross-Volume Mapping

G. Patanè, X.D. Gu, **X.S. Li**

Cross-shape Mapping: From Surface to Volume

- ❑ Cross-shape mapping
  - ❑ A bijective map between two given shapes
  - ❑ A modeling technique to obtain the parametric representation on suitable domain, or to establish one-to-one correspondence
  - ❑ Can facilitate many tasks in graphics, vision, visualization

Main Contents:
1) Cross-surface mapping computation
2) Cross-volume mapping computation
3) An example : Polycube mapping
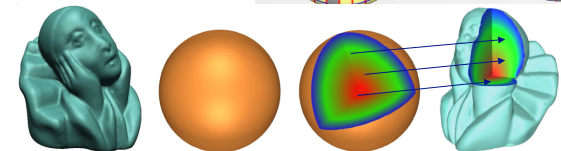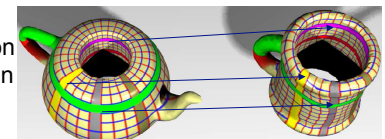
Cross-surface Mapping

- Criteria
  - Bijectivity: no flip-overs, no degeneracy
  - Mapping Distortions: length, angle, and area/volume distortion
  - Feature/Structure Alignment

Computing Cross-Surface Maps
- Parameterization of surface patches (topological disks) have been extensively studied, many effective algorithms developed
  - [Floater and Hormann 2005], [Sheffer et al. 2006], [Hormann et al. 2007]
- Solid objects widely exist in scientific applications; their boundaries are closed surfaces and may possess nontrivial topology
  - We discuss the mapping between closed surfaces, and then extend it to volume shapes

Cross-surface Mapping (Genus-0 Surfaces)

- Explicitly solving a deformation, $f:M1 \rightarrow M2$,
  - ✓ Effective for shapes differ by small deformation
  - ❖ Local minima (good initial estimate important); non-linear geometric constraints expensive to enforce
- Implicitly composing two parameterizations over a common domain, $g:D \rightarrow M1, h:D \rightarrow M2, f = h \cdot g\hat{}-1$.
  - Popular common domains: e.g. sphere, cube, polycubes…
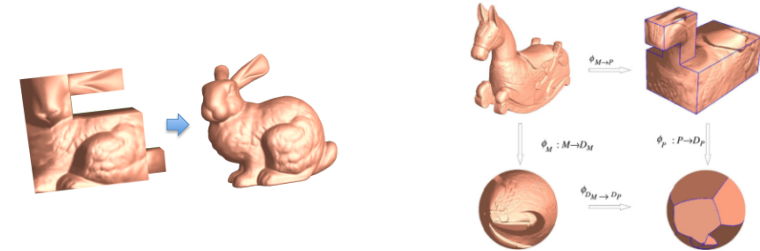
Spherical Parameterization of Genus-0 Surface

(a) (b) (c) (d) (e) (f)
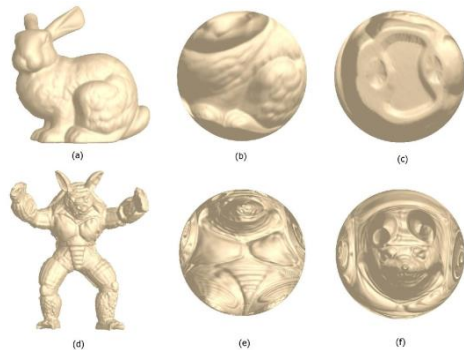
Image from [S. Wan, T. Ye, M. Li, H. Zhang, X. Li, "Efficient Spherical Parameterization Using Progressive Optimization," Proc. of Computational Visual Media Conference, pp. 170-177, 2012.]

- Applications:
  - Inter-surface Mapping
  - Spherical Harmonics Decomposition

Cross-surface Mapping (High-genus Surfaces)

- Explicit deformation: challenging when with multiple handles
- Implicit composition of parameterizations
  1) Composing *local* parameterization through *divide-and-conquer*
  2) Composing two *global* parameterizations on a common domain

Genus-2

Genus-3
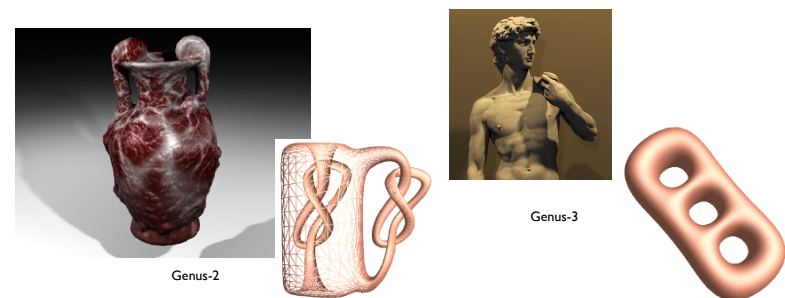
Cross-surface Mapping (High-genus Surfaces)

- ❑ **Explicit** deformation: challenging when with multiple handles
- ❑ **Implicit** composition of parameterizations
  1) Composing *local* parameterization through *divide-and-conquer*
  2) Composing two *global* parameterizations on a common domain

Genus-2

Genus-3
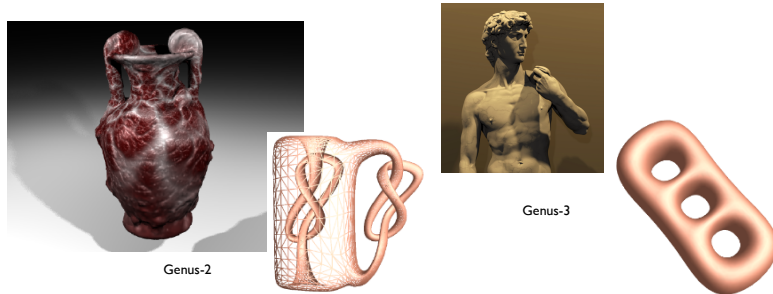
D & C: General Pipeline

A general computation pipeline:
1) <u>Partitioning</u>: Consistently segment the two surfaces into simple patches
2) <u>Local Mapping</u>: Compute cross-patch mappings between corresponding local patches
3) <u>Global Composition</u>: Stitch the local maps together and apply some post-processing to remove the artifacts
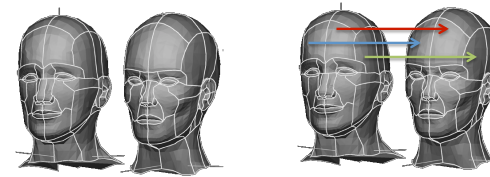
D & C: Partitioning

Consistent Decomposition

1. Manual Design

2. Land Markers + Auto Boundary Tracing

Dual Graphs of the two Decompositions
→ Isomorphic

[Decarlo and Gallier, GI'96]
[Gregory et. al. CA'98]
[Zockler et al. VC'00]

[Schreiner et. al. SIG'04]

[Kraevoy and Sheffer SIG'04]
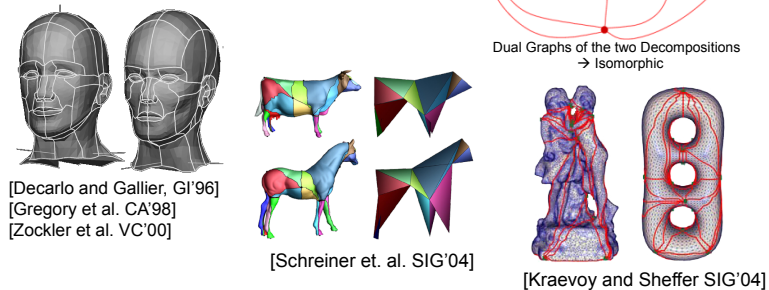
[Lee et. al. SIG'99] , [Kanai et al. VC'98], [Praun et al. SIG'01],
[Kraevoy and Sheffer SIG'04], [Schreiner et al. SIG'04] [Kwok et al. TVCG'11]

D & C: Data Partitioning

Consistent Decomposition

1. Manual Design

2. Land Markers + Auto Boundary Tracing

- ✓ **Intuitive, flexibly align semantic features.**
- ✗ **Manual, not easy for surfaces with complex topology.**

Dual Graphs of the two Decompositions
→ Isomorphic

[Decarlo and Gallier, GI'96]
[Gregory et. al. CA'98]
[Zockler et al. VC'00]

[Schreiner et. al. SIG'04]

[Kraevoy and Sheffer SIG'04]

[Lee et. al. SIG'99] , [Kanai et al. VC'98], [Praun et al. SIG'01],
[Kraevoy and Sheffer SIG'04], [Schreiner et al. SIG'04] [Kwok et al. TVCG'11]

A Topology-Driven Auto Consistent Decomposition
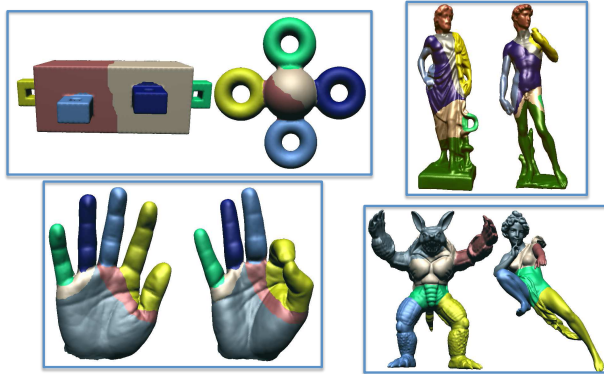
☐ A Topology-driven Top-Down Approach: Canonical Pants Decomposition:
[Li, Gu, Qin, "Surface Mapping using Consistent Pants Decomposition," 15(4):558 – 571, TVCG 2009]

Pants Decomposition

A Topology-driven Top-Down Approach: Canonical Pants Decomposition
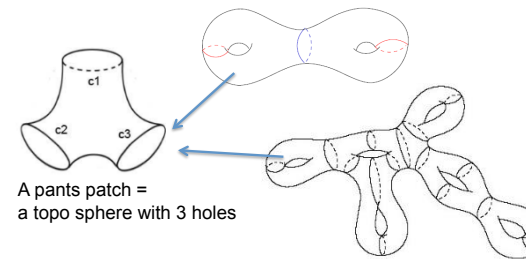
A pants patch =
a topo sphere with 3 holes

A uniform decomposition scheme for surfaces with non-trivial topology
➢ a genus-g surface with b boundaries → $2g+b-2$ Pants Patches
➢ dual graphs are simple : every node is valence-3

[Li, Gu, Qin, "Surface Mapping using Consistent Pants Decomposition," TVCG 2009]
[Zhang, Li, "Optimizing Geometry-aware Pants Decomposition," PG2012]

Canonical Pants Decomposition

Decompose a surface → base patch + handle patches
Decompose base patch and handle patches to pants

"waist": Topologically: bound the handle
Geometrically: short, smooth loop

"legs"
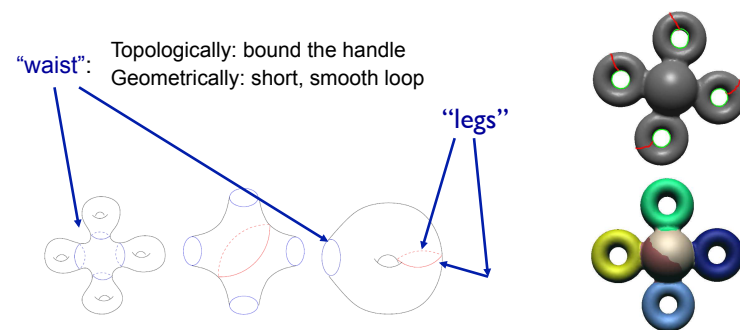
[Li, Gu, Qin, "Surface Mapping using Consistent Pants Decomposition," TVCG 2009]

Canonical Pants Decomposition Results

Enumerating Pants Decompositions

- A compact orientable surface admits infinitely many topologically different Pants Decompositions. [Hatcher et.al 2000]
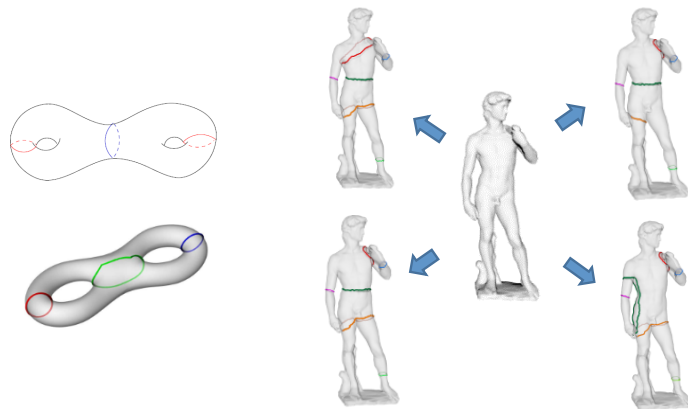
Topological Operations

We can use two operations to traverse among topologically different Pants Decompositions

1) **Simple move (S-move)**
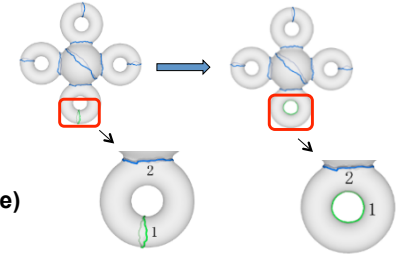
2) **Associativity Move (A-move)**
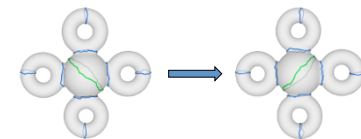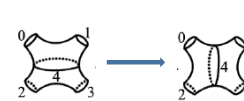
[Zhang, Li, "Optimizing Geometry-aware Pants Decomposition," PG2012]

Topologically Consistent Surface Decomposition

With these two operations,
We can enumerate the space of pants decompositions.

Geometric properties can be incorporated in the search of a desirable decomposition.
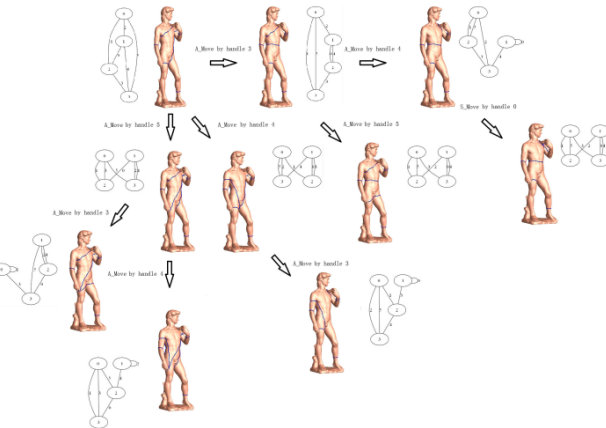
[Li, Gu, Qin, "Surface Mapping using Consistent Pants Decomposition," TVCG 2009]
[Zhang, Li, "Optimizing Geometry-aware Pants Decomposition," PG2012]

Step 2: Local Mapping

S_1 and S_2 (genus # = g, boundary # = b)

Consistent pants decomposition

Consistent pants sets: (χ = 2g-2+b)
$\{P_1^1, P_1^2, …, P_1^x\}$ and
$\{P_2^1, P_2^2, …, P_2^x\}$

match the corresponding pairs of pants

Piecewise surface mapping

D & C: Local Mapping

- Slice each pants patch into 2 topological hexagons
- Get the cross-patch mapping by composing the parameterizations on the planar hexagon domains
- Simple dual graph → consistent boundary mapping condition easy to enforce

$$\partial\Omega = \partial\Omega_1 \cup \partial\Omega_2$$

$$\partial M = \partial M_1 \cup \partial M_2$$

$$f = \varphi_1^{-1} \cdot \psi_1 \cup \varphi_2^{-1} \cdot \psi_2$$
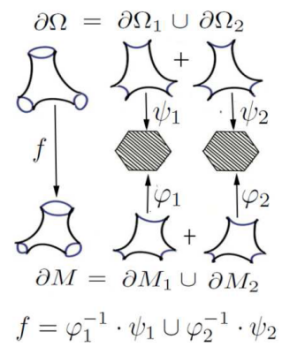
Surface Mapping Results

Some Cross-Surface Mapping Results

Cross-surface Mapping (High-genus Surfaces)

- Explicit deformation: challenging when with multiple handles
- Implicit composition of parameterizations
    1) Composing *local* parameterization through *divide-and-conquer*
    2) Composing two *global* parameterizations on a common domain

Genus-2

Genus-3
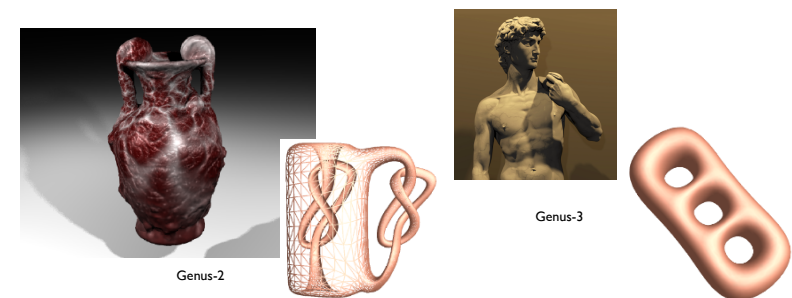
Compose Global Map via Fundamental Domains

Slice surfaces open → fundamental domains → parameterization

1) Compute a set of *2g* loops (a canonical homology basis)
2) Slice surface open to a disk (*4g*-gon)
3) Parameterize sliced surfaces over the planar disk
4) Compose the parameterizations
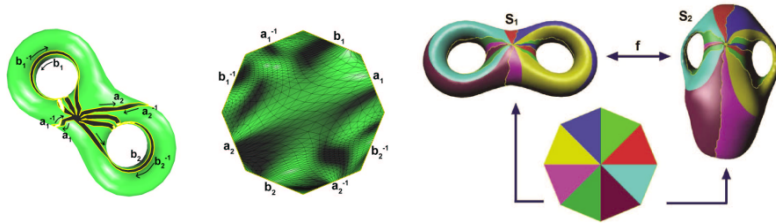
❑ Global Harmonic Mapping under Uniformization Metric:
[Li et al., "Globally Optimal Surface Mapping for Surfaces with Arbitrary Topology," TVCG 2008]

Solving a Global Harmonic Mapping

Goal:
To solve a quasi-conformal map that minimizes the stretching

Difficulty:
Direct optimization always gets trapped by local minima

Approach: (Uniformization Metric)

1. Conformally deform the target surface to its uniformization metric
   ❑ for surfaces with non-trivial topology (g>=1)
      → constant non-positive curvature everywhere
2. Under this metric, reduce harmonic energy
   ❑ The global harmonic map is unique in each homotopy class [Schoen and Yau 78]

[Li et al., "Globally Optimal Surface Mapping for Surfaces with Arbitrary Topology," TVCG 2008]

Some Mapping Results

Genus-1 Surface Map Optimization
Based on Flat Metric

Genus-g (g>1) Surface Map Optimization
Based on Hyperbolic Metric
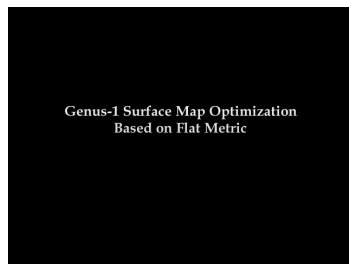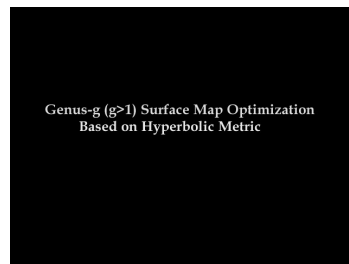
Video: G=1, Star → Rocker-arm   Video: G=2, Vase → 2-Torus

[Li et al., "Globally Optimal Surface Mapping for Surfaces with Arbitrary Topology," TVCG 2008]

Local Optima vs. Global Optima

Optimization under Euclidean Metric: Optimization under Uniformization Metric
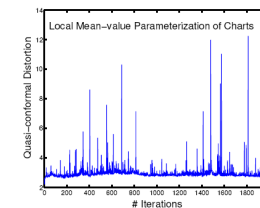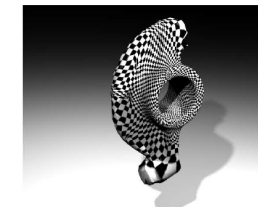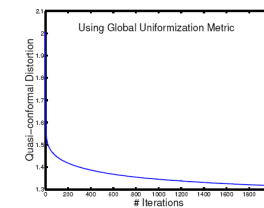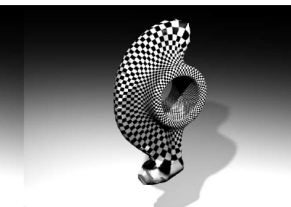
Local Optima vs. Global Optima
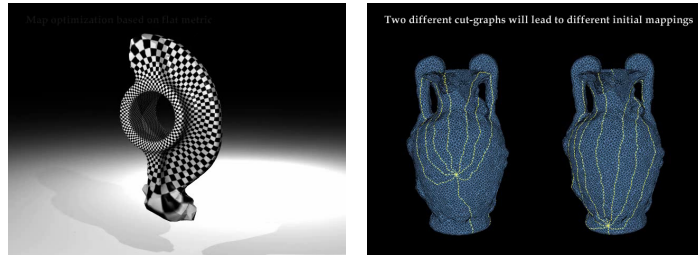
Cross-volume Mapping

❑ To establish a bijective map between two given solid shapes
❑ Boundary condition: boundary surface mapping

  (a)   (b)   (c)   (d)   (e)   (f)
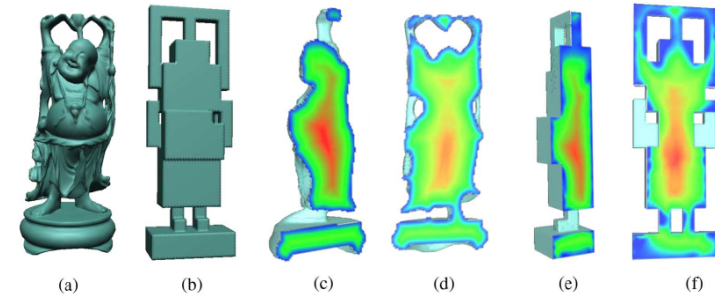
X. Li, X. Guo, H. Wang, Y. He, X. Gu, H. Qin, "Harmonic Volumetric Mapping for Solid Modeling Applications", in Proc. of ACM Solid and Physical Modeling Symposium (SPM), pp. 109-120, 2007.

Volumetric Harmonic Mapping

A harmonic (volumetric) map:

$$f : M_1 \rightarrow M_2$$

$$\begin{cases} \Delta f = 0 & p \in M_1 \\ f(p) = g(p) & p \in \partial M_1 \end{cases}$$

where $\Delta = \dfrac{\partial^2}{\partial x^2} + \dfrac{\partial^2}{\partial y^2} + \dfrac{\partial^2}{\partial z^2}$

$$\Delta f = 0, \quad f = (f_0, f_1, f_2) \implies \Delta f_i = 0, \quad (i = 1,2,3)$$

Physical Intuition:
❑ To deform a solid rubber whose boundary deformation is determined by a surface mapping.
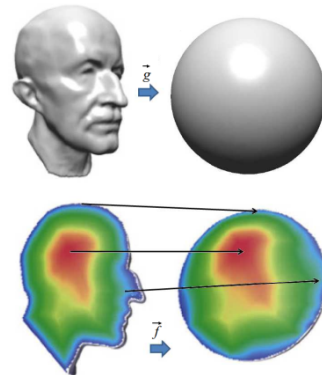
Kernel of Harmonic Functions

Kernel Function of 3D Laplacian Operator Δ: $\quad K(x,x') = \dfrac{1}{4\pi} \dfrac{1}{|x - x'|}$

A harmonic map $f_i(P)$ can be approximated by

$$f_i(\vec{w}, \vec{Q}; P) = \sum_{n=1}^{N_e} w_n K(P, Q_n) \quad , P \in M_1$$

A Physical Model:
❑ Harmonic field ← an electrical potential field
  ❑ The potential at a point, , is determined by a set of electronic particles
  ❑ Degree-of-Freedom: their positions and charge amounts
  ❑ Constraints: the boundary mapping

Solving these 3 Electrical Potential Fields

Solve this by a collocation method:

Sample n_s singularity points outside the model domain
Sample n_c collocation points on the model boundary surface

Solve a linear system

$$A_{n_c \times n_s} x_{n_s \times 1} = b_{n_c \times 1}$$

The system is dense and usually ill-conditioned

Approaches to improve numerical stability:
- SVD, with insignificant eigenvalues truncated
- Adaptively inserting new singularity points and removing least effective ones
- Add a regularization term, solved by LU
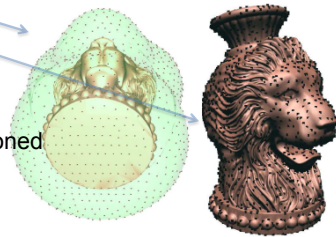
Feature Alignment

To support matching of corresponding feature points, curves, or iso-surfaces
- Treated as soft constraints, directly added into the system

Mapping M_1 (with skeleton K_1) and M_2 (with K_2)
- Feature curves matching → isomorphic skeleton graphs
- Compute $f : M_1 \rightarrow M_2$, enforcing alignment of corresponding nodes on skeletons K_1 and K_2
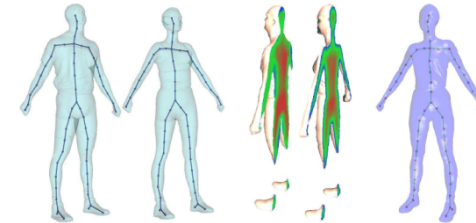
Feature Alignment

To support matching of corresponding feature points, curves, or iso-surfaces
- Treated as soft constraints, directly added into the system

Mapping M_1 (with feature surface S_1) and M_2 (with S_2)
- Feature surface mapping → compatible surface meshes
- Compute $f : M_1 \rightarrow M_2$, enforcing alignment of corresponding vertices on S_1 and S_2
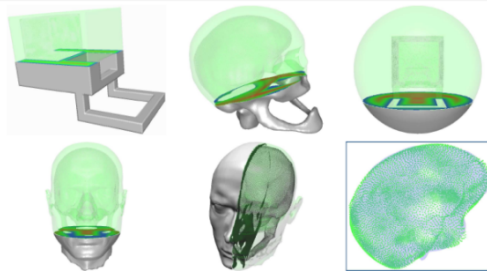
Volumetric Mapping Results

(a) Sphere (b) Max-Planck (c) Distance Field D_1 (d) Transferred D_1

(e) Omotondo (f) Distance Field D_2 (g) Transferred D_2 (h) Color-bar

Volumetric Mapping Results (cont.)

(a) Polycube   (b) Two-torus   (c) Distance Field D_3 (d) Transferred D_3

(e) Polycube   (f) Kitten   (g) Distance Field D_4 (h) Transferred D_4

Volumetric Mapping Results (cont.)

Max

Min

Depth value
Color-coding
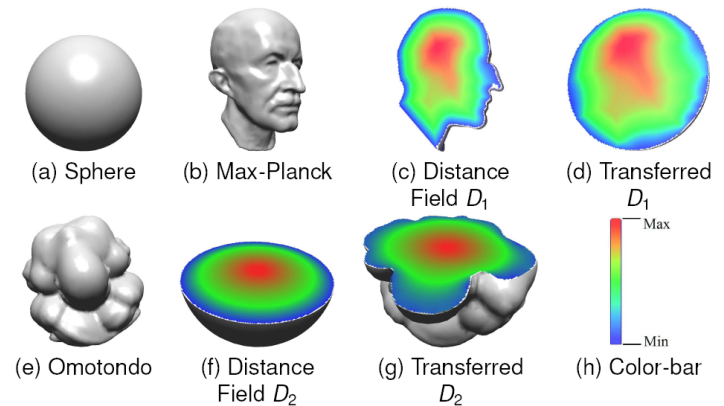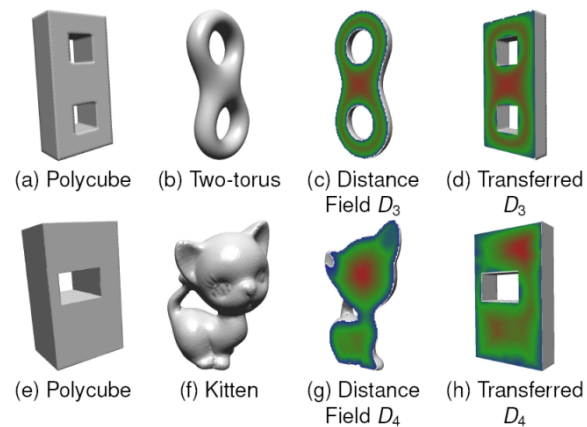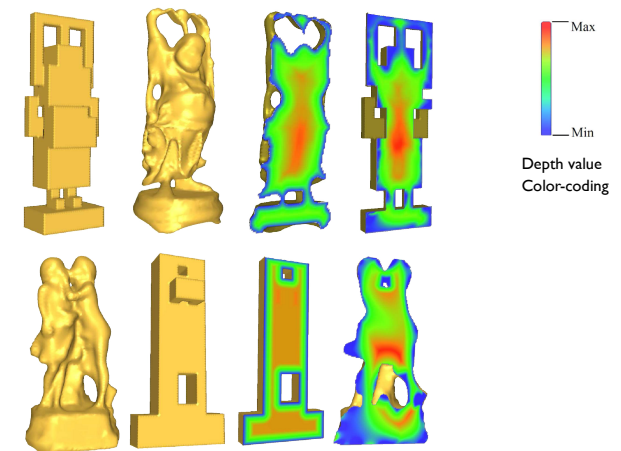
Volumetric Mapping Applications:
-- Meshing
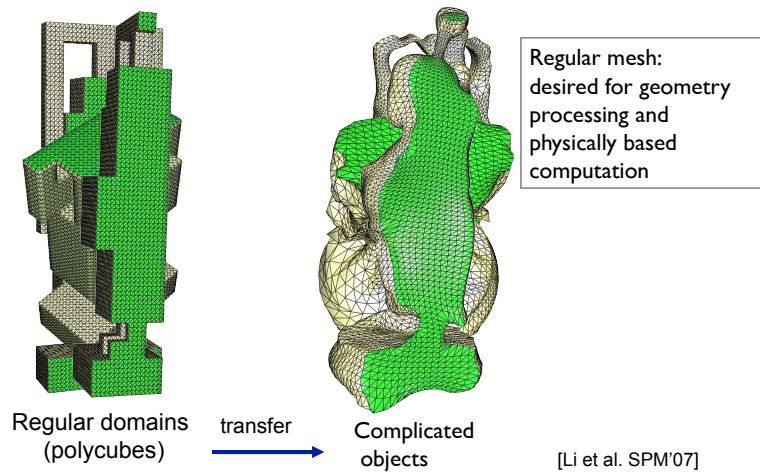
Regular mesh: desired for geometry processing and physically based computation

Regular domains (polycubes)   transfer   Complicated objects   [Li et al. SPM'07]

Mapping Complex Volume via Divide-and-Conquer

❑ For solid shapes with complex geometry or inhomogeneous structures
- ❑ Global harmonic mapping
  - ❑ Bijectivity usually not guaranteed
  - ❑ Complex feature structures difficult to handle
- ❑ Mapping via Divide-and-Conquer
  1) Decompose the solid into solvable sub-parts
  2) Solve individual sub-mappings locally
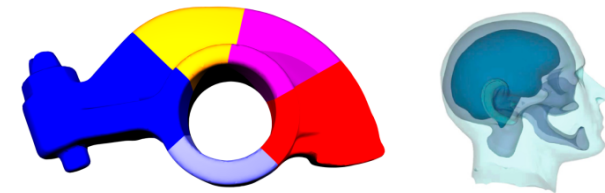
Star Decomposition for Volume Shapes

❑ Bijective Harmonic Parameterization can be constructed on star-shaped regions
[Xia et al. "Parameterization of Star Shaped Volumes Using Green's Functions," GMP'10]

[Yu and Li, "Computing Guarding and Star Decomposition," Computer Graphics Forum, 2011]

Mapping Complex Volume via Divide-and-Conquer

❑ For solid shapes with complex geometry or inhomogeneous structures
- ❑ Global harmonic mapping
  - ❑ Bijectivity usually not guaranteed
  - ❑ Complex feature structures difficult to handle
- ❑ Mapping via Divide-and-Conquer
  1) Decompose the solid into solvable sub-parts
  2) Solve individual sub-mappings locally
  3) Need to consider the smoothness of the transitions across partitioning boundaries → Harmonic maps only offer C^0 continuity

---
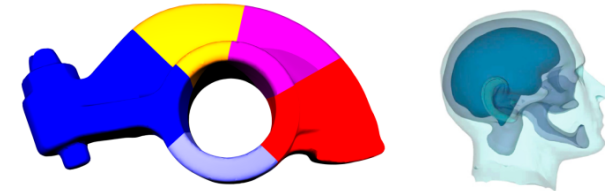
A Biharmonic Volumetric Mapping Model

To solve $\Phi : \Omega \rightarrow M \quad \Omega, M \subset R^3$

$$\begin{cases} \nabla^4 \Phi = 0, & \text{in } \Omega, \quad \Phi = f, \quad \text{on } \partial\Omega, \quad \partial\Phi/\partial n = g, \quad \text{on } \partial\Omega, \end{cases}$$
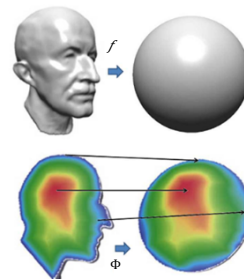
n : the surface normal on the domain boundary
$\partial\Phi/\partial n$: the outward normal derivative
f : surface mapping from $\partial\Omega$ to ∂M
g : derivative along the normal direction on each boundary points

$\Phi = (\phi_x, \phi_y, \phi_z)$: along x, y, z axis directions, each ϕ_i is a biharmonic function

---

MFS Kernels for Biharmonic Function

A biharmonic Function $\phi(x)$ can be approximated by:
$$\phi(\mathbf{h}, \mathbf{b}, \mathbf{Q}, \mathbf{x}) = \sum_{j=1}^{n_s} h_j \, H(\mathbf{q}_j, \mathbf{x}) + \sum_{j=1}^{n_s} b_j \, B(\mathbf{q}_j, \mathbf{x})$$

❑ Kernels:
- ❑ $H(\mathbf{q}_j, \mathbf{x}) = 1/4\pi|\mathbf{q}_j - \mathbf{x}|$: harmonic kernel
- ❑ $B(\mathbf{q}_j, \mathbf{x}) = |\mathbf{q}_j - \mathbf{x}|/8\pi$: biharmonic kernel

❑ Singularity Points
- ❑ $\mathbf{Q} = \{\mathbf{q}_1, ..., \mathbf{q}_{n_s}\}$: a $3n_s$-D vector, indicating the singularity points sampled outside Ω
- ❑ $\mathbf{q}_j = [q_{3j-2}, q_{3j-1}, q_{3j}]^T \in R^3$ is the 3D position of a singularity point

❑ Unknown:
- ❑ $\mathbf{h}, \mathbf{b}$: harmonic and bihamronic coefficients to solve

Solve each using Methods of Fundamental Solutions (MFS)

Biharmonic Volumetric Mapping Examples

Ω M Harmonic Map   Biharmonic Map

Solve each   using Methods of Fundamental Solutions (MFS)

Biharmonic Volumetric Mapping Examples

(a) Domain   (b) Target   (c) Harmonic   (d) Biharmonic

(e) Harmonic   (f) Biharmonic

[Xu et al. "Biharmonic Volumetric Mapping using Fundamental Solutions," TVCG, 19(5): 787-798, 2013]

Solve each   using Methods of Fundamental Solutions (MFS)

Biharmonic Volumetric Mapping Examples

(a)   (b)   (c)

Biharmonic

Harmonic

(d)   (e)
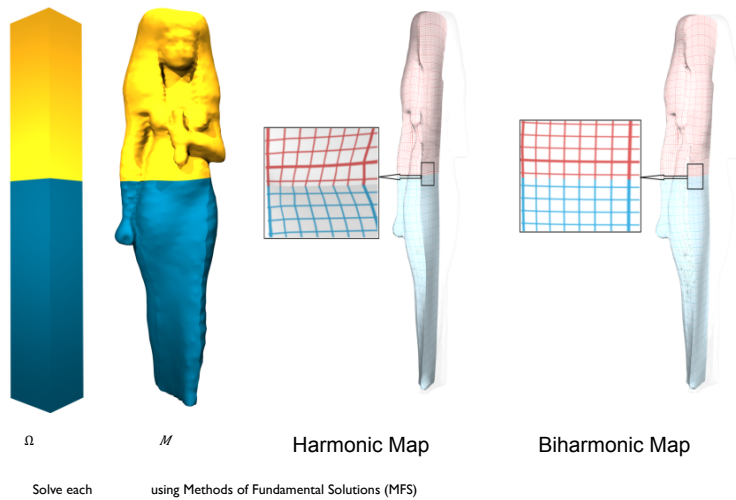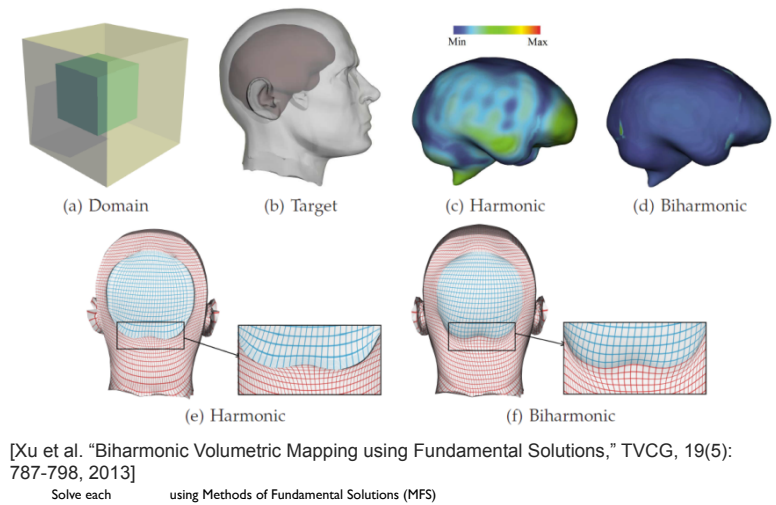
Solve each   using Methods of Fundamental Solutions (MFS)
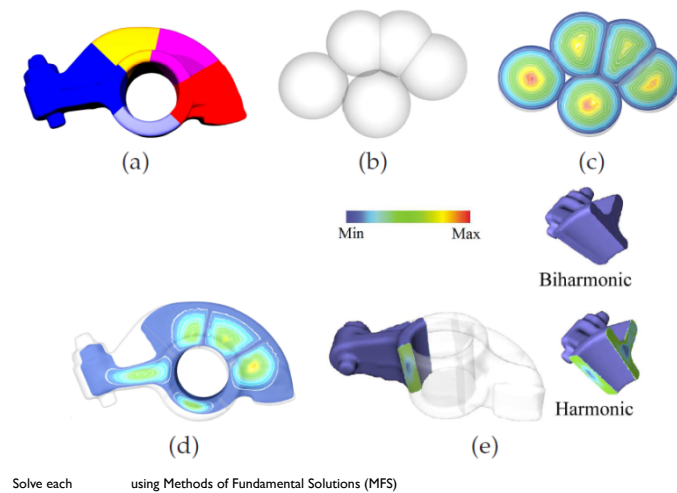
Polycube Parameterization
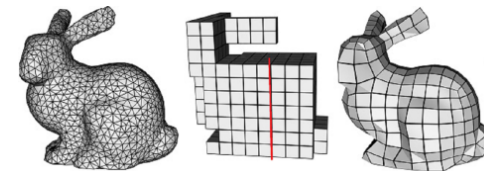
Polycube Parameterization: Definition & Motivation

- ❑ A Polycube is
  - ❑ A shape composed of a set of cubes that are attached face to face, or
  - ❑ more formally, a 3D manifold that is an orthogonal polyhedron.
- ❑ A polycube parameterization of a (surface/solid) model M is a bijective map from a polycube (surface/solid) P to M
- ❑ Polycube as a desirable parametric domain:
  - ➢ Regularity

    desirable for functional design and mesh generation
  - ➢ Good approximation to model

    lowly-distorted (less stretching) parameterization
- ❑ Many Applications:
  - ❑ Spline construction
  - ❑ Hex-meshing
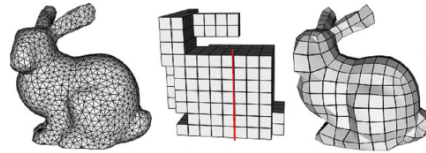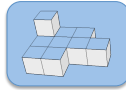
Contents

- ❑ A Brief Review on Existing Methods
- ❑ A Polycube Surface Mapping Algorithm
- ❑ A Polycube Volumetric Mapping Algorithm
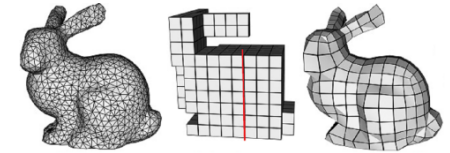
Related Work: Polycube Construction

- ❑ Manual/Semi-automatic Polycube Construction:
  - ❑ [Tarini et al. SIG'04]: Interactive Cube Assembly
  - ❑ [Wang et al. SPM'07]: CSG
  - ❑ [Li et al. SMI'10]: Surface Segmentation for Generalized Polycube
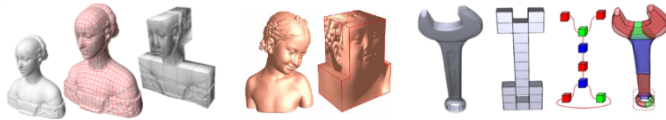
- ❑ Automatic Polycube Construction:
  - ❑ [Lin et al. GMP'08]: Reeb-graph
  - ❑ [He et al. SMI'09]: Horizontal scanning
  - ❑ [Gregson et al. SGP'11]: Rotational-driven Deformation
  - ❑ [Yu et al. SPM'13]: Homotopic Morphological Optimization
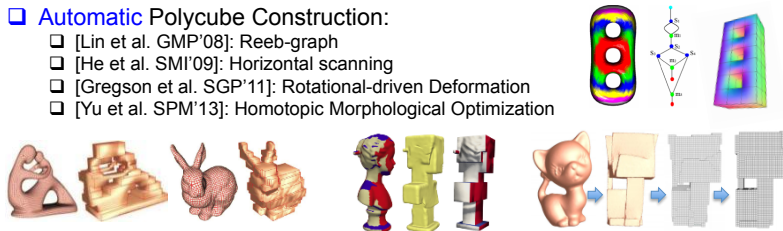
Related Work: Polycube Mapping

- ❑ Polycube Surface Mapping
  - ❑ [Tarini et al. SIG'04]: Spatial projection
  - ❑ [Lin et al. GMP'08, Xia et al. I3D'11, Li et al. SMI'10, Wan et al. SMI'11]: Surface partitioned into topological disks + disk parameterization
  - ❑ [He et al. SMI'09]: Surface partitioned into patches with holes + discrete Ricci flow
  - ❑ [Wang et al. SPM'07]: Global surface-polycube mapping by composing intrinsic global parameterization on the fundamental domain
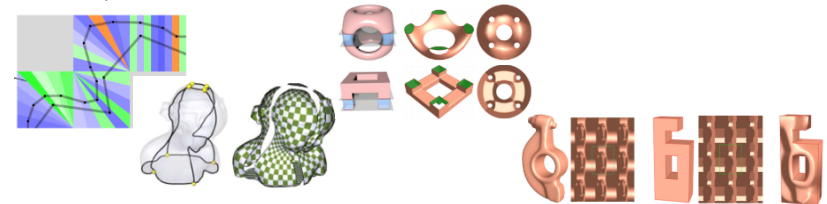
Related Work: Polycube Mapping

❑ Polycube Surface Mapping
  ❑ [Tarini et al. SIG'04]
  ❑ [Lin et al. GMP'08, Xia et al. I3D'11, Li et al. SMI'10, Wan et al. SMI'11]
  ❑ [He et al. SMI'09]
  ❑ [Wang et al. SPM'07]
❑ Polycube Volumetric Mapping
  ❑ Harmonic Mapping
    ❑ FEM: [Xia et al. SMI'10, Han et al. SPM'10, Li et al. TVCG'13]
    ❑ MFS: [Li et al. SPM'07, Li et al. SMI'10]
  ❑ Bi-harmonic Mapping
    ❑ [Xu et al. TVCG'13]
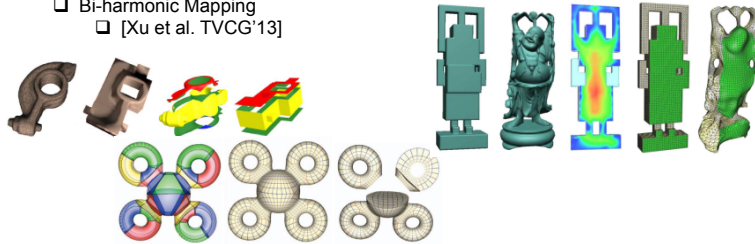
What is a Desirable Polycube Map?

❑ Effective automatic polycube construction remains challenging:
  Need to solve:
  ➢ A good polycube domain
  ➢ A low-distortion mapping
❑ A **Good** Polycube Domain:
  ❑ Composed by only a few cubic subparts, i.e, few corner points (singularities)
  ❑ Capturing shape features

Input | Too many corner points | Too simple to capture shape features
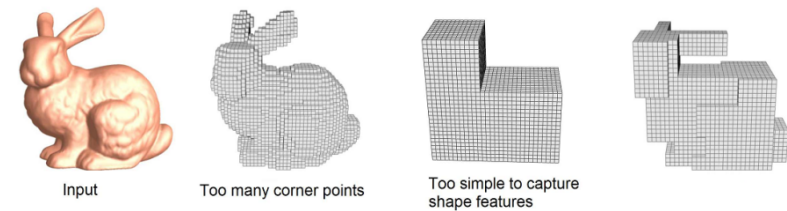
Polycube Domain Construction

Polycube domain shape determines:
➔ boundary surface mapping, quality of the boundary quad-mesh
➔ consequently, quality of the constructed hex-mesh

Which one is better?
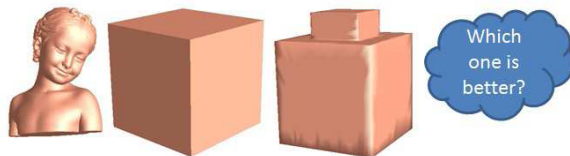
• Geometric Similarity VS Domain Simplicity
  ▪ Simpler domain ➔ fewer singularities
  ▪ More complex domain ➔ better approximate shape geometry

Polycube Mapping via Horizontal Scanning

[He et al. SMI'09]
1) Partition the model using a sweeping horizontal plane
2) Construct axis-aligned polygons to approximate patch boundaries
3) Flatten the surface patch and polycube patch
4) Map the flattened patch pair using planar harmonic maps
➔Could generate well-approximated polycube domain, but with many singularities
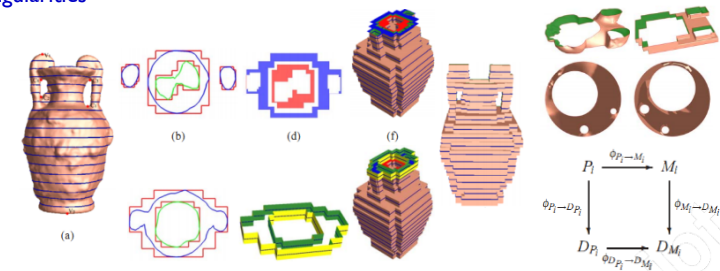
A Simultaneous Optimization on PC Domain Shape and Surface Mapping

[Wan et al. "A Topology-preserving Optimization Algorithm for Polycube Mapping," SMI'11]

Polycube domain shape optimization guided by mapping distortion

- ❑ Aims to optimize both
  1) Polycube Domain Shape (without adding/deleting corners)
  2) Polycube Surface Mapping
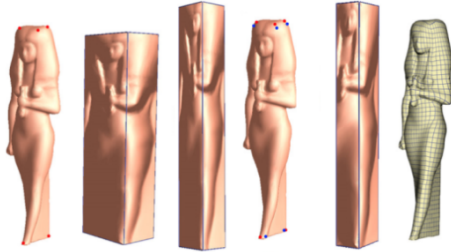
Polycube Construction by Voxelization

- ▪ When each facet's corner mapping is determined:
- ▪ Partition M and P into sub-patches: $f_{lk}: M_{lk} \to P_{lk}$
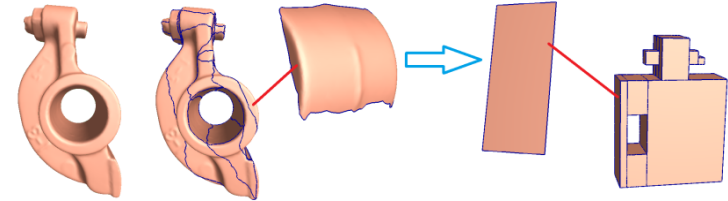
Discrete harmonic mapping energy for patch M_{lk} :

on l-th axis: $H_{kll}(f) = \sum_{(v_{li}, v_{lj}) \in E(M_{lk})} 1/2 \ w_{lij} (f_{ll}(v_{li}) - f_{ll}(v_{lj}))^2$

where w_{lij} is the well known cotangent weight ([Eck et al.'95])
v_{li}, v_{lj} are vertices, f_{ll} is the l-th component of the map f

- • Total harmonic energy:

Piecewise Polycube Surface Maps

- ❑ When the mapping of each facet's corners is determined:
  - ❑ We can trace the shortest paths to connect corners
  - ❑ M and P partitioned into sub-patches: $f_{lk}: M_{lk} \to P_{lk}$
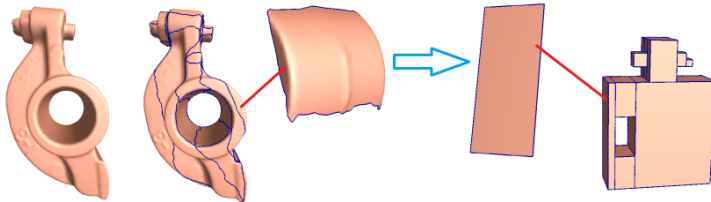
Discrete harmonic mapping energy for patch M_{lk} :

on l-th axis: $H_{lk1l}(f) = \sum_{(v_{li}, v_{lj}) \in E(M_{lk})} 1/2 \ w_{lij} (f_{ll}(v_{li}) - f_{ll}(v_{lj}))^2$
where w_{lij} is the well known cotangent weight ([Eck et al.'95])
v_{li}, v_{lj} are vertices, f_{ll} is the l-th component of the map f

- • Total harmonic energy:

Piecewise Polycube Surface Maps (cont.)

We also measure the area-stretching of the map f:

$$A = \sum_{k=1}^{N} \left(\sum_{(v_i, v_j, v_h) \in F(M_k)} \frac{(Area_P(U_i, U_j, U_h))^2}{Area_M(X_i, X_j, X_h)} \right),$$

The final mapping energy to minimize:

$$E(f) = H(f) + \alpha A(f)$$

where the mapping function f is determined by the corner points of P and their images on M

Optimization Algorithm (Overview)

Directly minimizing E = simultaneously optimizing the polycube domain shape
as well as the surface mapping

$$E(X_1, X_2, ..., X_{3N_c}, U_1, U_2, ..., U_{3N_c})$$

where $(U_{3i-2}, U_{3i-2}, U_{3i-2})$ is a corner point,

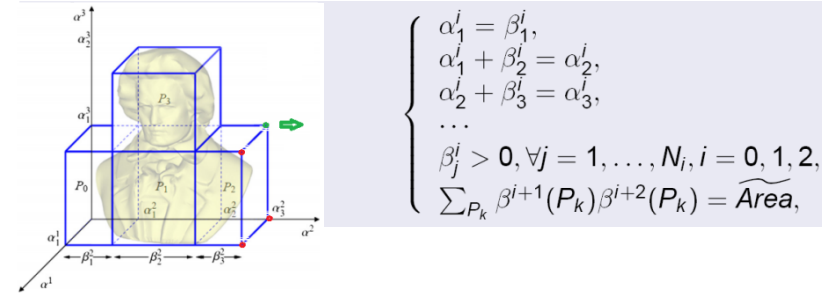and $(X_{3i-2}, X_{3i-2}, X_{3i-2})$ is its pre-image on the surface

is nonlinear, and the derivatives of   over   is unknown,

❑ The geometric constraints are also complicated

   ❑ directly solving this optimization is very expensive

   ❑ Approach: to optimize   over and iteratively

Optimizing Polycube Domain Shape

Optimizing domain shapes $\{ U_i \}$ to reduce E

❑ Subject to the following constraints

  1) Each cube facet has planarity

  2) Consistency between adjacent facets

  3) Preserving total area

$$\begin{cases} \alpha_1^i = \beta_1^i, \\ \alpha_1^i + \beta_2^i = \alpha_2^i, \\ \alpha_2^i + \beta_3^i = \alpha_3^i, \\ \cdots \\ \beta_j^i > 0, \forall j = 1, \ldots, N_i, i = 0, 1, 2, \\ \sum_{P_k} \beta^{i+1}(P_k)\beta^{i+2}(P_k) = \widetilde{Area}, \end{cases}$$

Optimizing Polycube Domain Shape (Cont.)

Quartic Energy with Bounded Linear Constraints

$$\begin{aligned} \min \quad & E(\mathbf{x}) \\ \text{s. t.} \quad & \mathbf{x} \in \Omega := \{ \mathbf{x} : A\mathbf{x} = \mathbf{b}, \ \mathbf{b_l} \leq \mathbf{x} \leq \mathbf{b_u} \}, \end{aligned}$$

Barzilai-Borwein gradient projection optimization algorithm

A first-order, non-monotone gradient projection algorithm
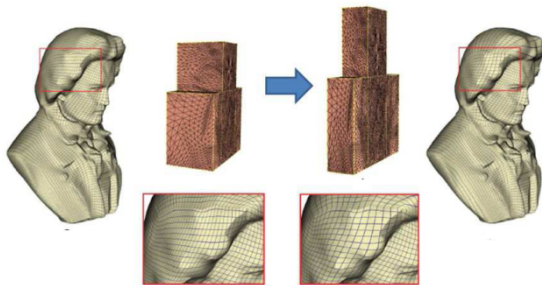
Optimizing Polycube Surface Mapping

Optimizing $\{X_i\}$, the corner points on the model

   When pre-images of corners move, we don't have close form of E

   (need to retrace shortest paths, and re-compute piecewise harmonic maps)

   ❑Optimized upon a local parametric (u,v) chart centered on each corner,

   ❑Nonlinear optimization with $2N_C$ parameters

   ❑No gradient information
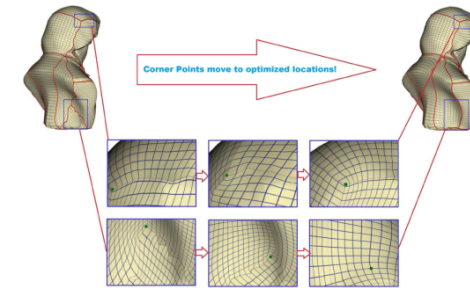
Optimizing Polycube Surface Mapping (Cont.)

Objective function (once sub-patches are segmented)

Bounded summation of signed squares of functions

$$\min \Phi(\mathbf{x}) = \sum_i^m \text{sgn}(i)\, f_i^2(\mathbf{x}), \quad \text{s.t. } \mathbf{b_l} \leq \mathbf{x} \leq \mathbf{b_u},$$

- ❑ An efficient derivative-free optimization solver
  (Locally, O(n) evaluation to initialize the quadratic model; each iteration needs 1 evaluation to update the model)
- ❑ Efficient re-evaluations of harmonic mapping
  - ❑ Harmonic maps need to be recomputed whenever corners move
  - ❑ Fast harmonic field updating [Xu et al. SMI'09]
    By Dynamic supernodal Choleskey update/downdate [Davis et al. 2009]
  (Initial cost O(n^3) ; O(k) each additional evaluation, k ~ length of shortest path (O($\sqrt{n}$)))

[Wan, Yin, Zhang, Zhang, Li, "A Topology-Preserving Optimization Algorithm for Polycube Mapping," Comp. & Graph., 35(3):639-649, 2011]

Optimizing Polycube Surface Mapping (Cont.)

Optimizing (moving) the corner points on the model
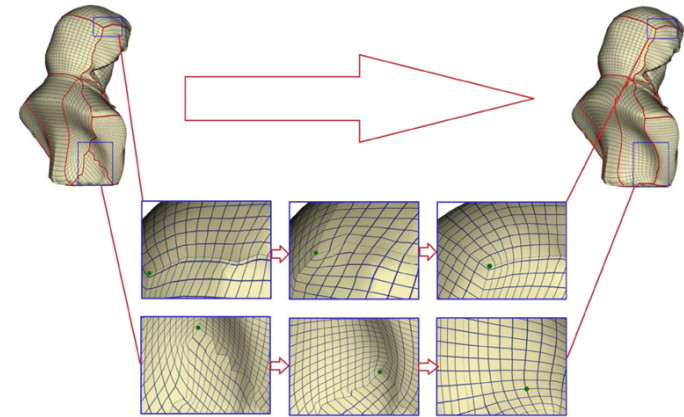
Some Optimization Results
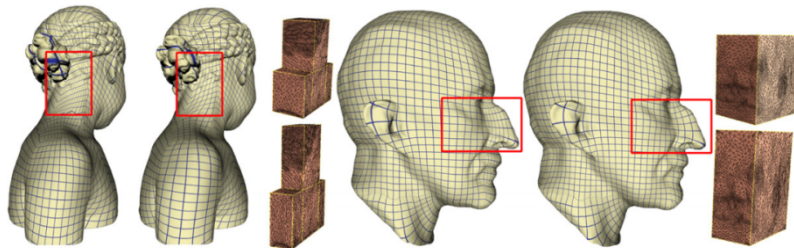
Cross-Shape Mapping via Polycube Domain

Optimizing a Common Polycube Domain of Multiple Objects
→ Compatible Parameterization of Multiple Models
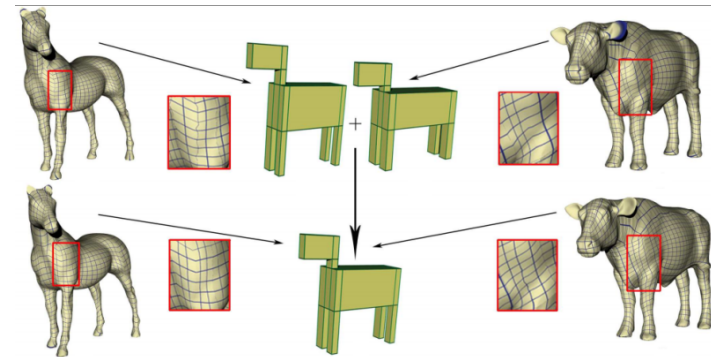
Quad-Meshing via Polycube Mapping

Quad/hex-meshes can be constructed on the polycube P

With a polycube parameterization $f\colon P \boxed{x} M$, this regular tessellation can be transferred onto the given model M
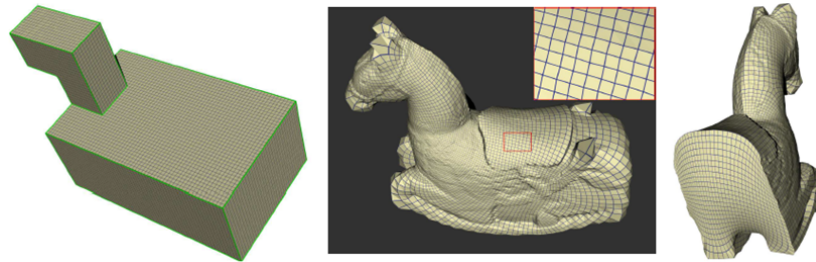

Some Results
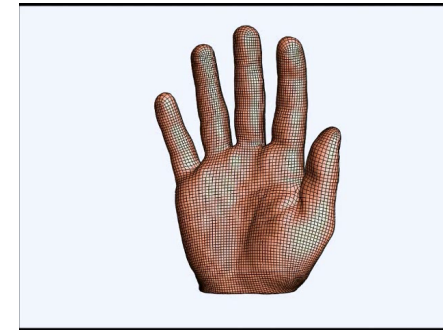
[Video]

[Shenghua Wan, Zhao Yin, Kang Zhang, Hongchao Zhang, Xin Li, "A Topology-Preserving Optimization Algorithm for Polycube Mapping," Computers & Graphics (CAG), (SMI'11), Volume 35, Issue 3, Pages 639-649, 2011.]

Optimizing Polycube Domain Construction
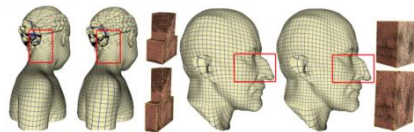
[Wan, Yin, Zhang, Zhang, Li, "A Topology-preserving Optimization Algorithm for Polycube Mapping," SMI'11]

➤ Optimizing not only the stretching of the polycube, but also the layout of the polycube domain
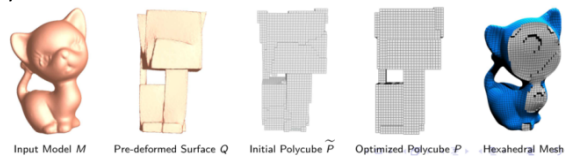
Input Model M Pre-deformed Surface Q Initial Polycube $\widetilde{P}$ Optimized Polycube P Hexahedral Mesh

[Yu, Wan, Zhang, Li, "Optimizing Polycube Domain Construction for Hexahedral Remeshing," SIAM SPM'2013]

Optimizing Polycube by Morphological Operations

[Yu, Wan, Zhang, Li, "Optimizing Polycube Domain Construction for Hexahedral Remeshing," SIAM SPM'2013]

Given a solid model M (with boundary S), to construct a desirable solid polycube domain Ω (with boundary P) and the mapping $f\colon M \to \Omega$
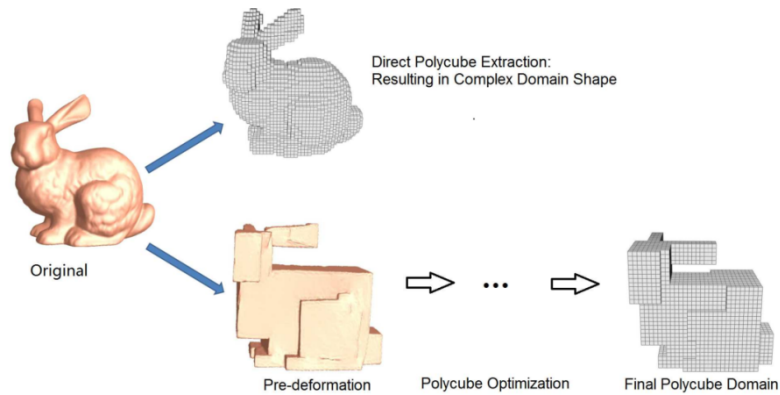
A 3-steps optimization algorithm:
1) Pre-deformation
2) Polycube construction and optimization
3) Mapping computation

Input Model M Pre-deformed Surface Q Initial Polycube $\widetilde{P}$ Optimized Polycube P Hexahedral Mesh
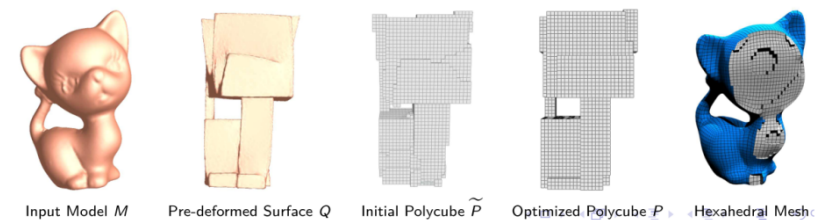
Step 1: Pre-deformation - Motivation

Polycube directly extract from M will lead to complex domain.

Starting with an axis-aligned shape will get to a simpler shape.

Direct Polycube Extraction:
Resulting in Complex Domain Shape

Original

Pre-deformation   Polycube Optimization   Final Polycube Domain

Step 1: Pre-deformation - Computation

Apply the rotational-driven deformation on S [Gregson et al. CGF11]

❑ Cluster S to six types of patches based on minimal rotations to axes ($\pm X, \pm Y, \pm Z$).

❑ Use the minimal rotation to deform the surface (solving a Poisson equation).

❑ Iteratively conduct the deformation until it converges.

Pre-deformation Result:
a *Pseudo-Polycube*

❑ Geometrically axis-aligned, but not topologically invalid (corners not always valence-3)

➢ Need to extract correct Polycube structure from pseudo-polycube.
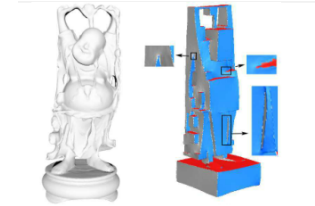
Step 2: Polycube Construction

Extract the polycube P from the pseudo-polycube Q by voxelization

❑ Need to select voxel size to

  ❑ Capture topological features without getting too fine grid

  ❑ Analyze the height functions on Q to decide the voxel size:

  1) Detect critical points in x, y, z directions, and in each direction cluster nearby critical points using a representative;

  2) In each direction, separate the range of height function using the value of the critical points.

  3) Choose $1/3$ of the minimal interval as the voxel size.

Pseudo-Polycube Q Representative Critical Points   Initial Polycube $\widetilde{P}$
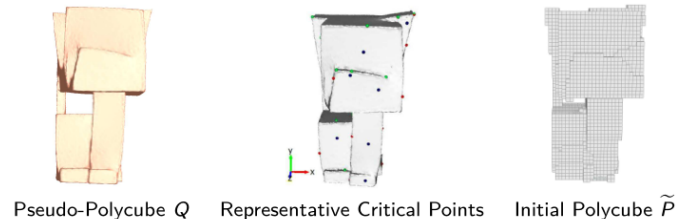
Step 3: Polycube Optimization

The voxelization results can be further simplified

Inspired by the morphological operations, we propose a polycube optimization algorithm
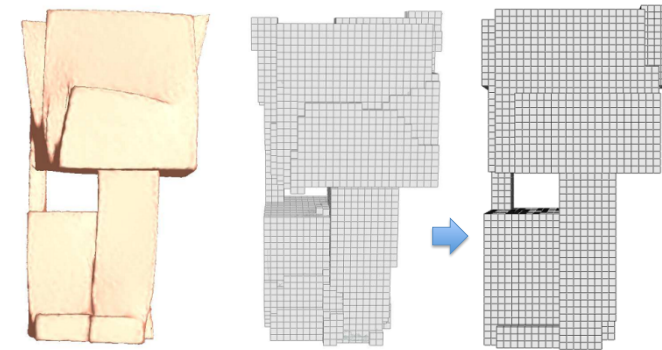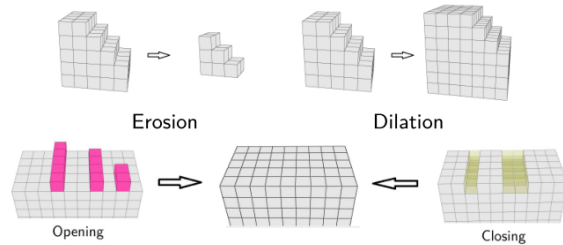
Morphological Operations

Erosion: Removes a layer of boundary cells

Dilation: Inserts a new layer of boundary cells

Opening: An erosion followed by a dilation

Closing: A dilation followed by an erosion

Erosion   Dilation

Opening   Closing

However, morphological operations could not preserve topology.
Need: Topology-preserving morphological operations

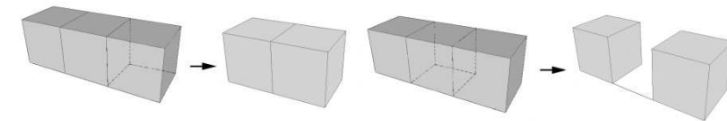## Homotopic Morphology: Simple Removal

Define the *Simple Removal* [Zhou et al. TVCG07].

If a k-D element is shared by one $(k+1)$-D element,

❑ Simple element: the k-D element

❑ Witness: the $(k+1)$-D element

Simple Removal: a simple element can only be removed together with it's witness

→ Iteratively applying simple removal won't change the topology.

Homotopic Morphological Operations

Based on *Simple Removal*, we can define:

❑ Homotopic erosion: An erosion on boundary layer of P that only remove simple removable voxels

❑ Homotopic dilation: A dilation can be seen as an erosion on the dual space of R^3 / P

❑ Homotopic opening: A homotopic erosion followed by a homotopic dilation

❑ Homotopic closing: A homotopic dilation followed by a homotopic erosion

Ordinary mophological operations (incorrect)
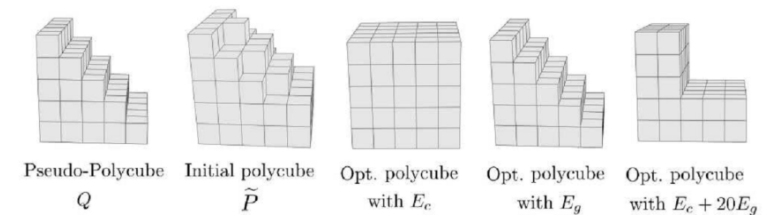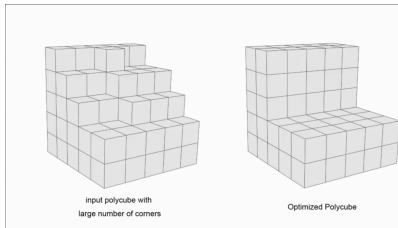
Homotopic morphological operations (correct)

Step 3: Polycube Optimization

A good polycube should: (1) be simple, and (2) be similar to the pseudo polycube
We define the following energy:

❑ Domain Simplicity: (Corner Number, smaller is simpler)

❑ Geometric Deviation: where is the distance from vertex to

, where is the weight to balance simplicity and similarity

Video: Polycube Optimization Example

Pseudo-Polycube Q | Initial polycube $\widetilde{P}$ | Opt. polycube with E_c | Opt. polycube with E_g | Opt. polycube with $E_c + 20E_g$

Step 3: Polycube Optimization

A good polycube should: (1) be simple, and (2) be similar to the pseudo polycube

We define the following energy:

- ❑ Domain Simplicity: (Corner Number, smaller is simpler)
- ❑ Geometric Deviation: where is the distance from vertex to

, where is the weight to balance simplicity and similarity

Video: Polycube Optimization Example

input polycube with
large number of corners

Optimized Polycube

Step 4: Parameterization: Initial Surface Map

Polycube Surface Map: boundary condition of volumetric map
1) Direct projection ($Q \rightarrow P$), with geometric similarity
2) Local relaxation is applied (on P, locally flattened) to reduce the mapping distortion and flip-overs.
   - ❑ Most flip-overs will be eliminated (even a few local flip-overs exist, won't change the boundary condition and hence won't affect volumetric mapping computation).

Before Relaxation   After Relaxation
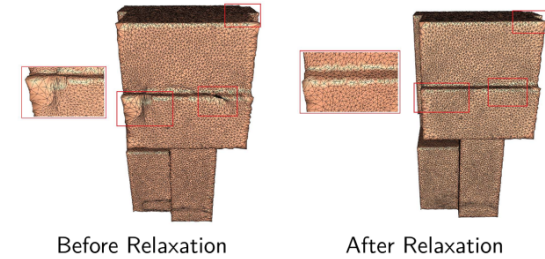
Step 4: Parameterization: Volumetric Mapping

Optimizing Volumetric Parameterization:
- ❑ Near boundary: gradient aligned with surface normal.
- ❑ Interior region: gradients smooth and orthornomal.

Frame Field X to Guide Parameterization on M
- ❑ Composed of 3 perpendicular unit vector fields.
- ❑ In each tetrahedron the frame is $X_i = (x_{i1}, x_{i2}, x_{i3})$

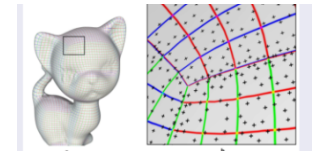Volumetric Parameterization following a given Frame Field

$$E = \sum_{j} \sum_{k=1}^{3} (\|\nabla u_j^k - X_j^k\|^2) \cdot vol(t_j),$$

[Nieser, Reitebuch, and Polthier, "Cubecover parameterization of 3d volumes," CGF, 30(5), 2011.]

Step 4: Parameterization: Frame Field Solving

Setting Boundary Frames
- ❑ Initially determined by polycube surface map
- ❑ Optimized on tangent plane with interior frames


Interior Frame Field Smoothing
- ❑ In i-th tet, frame $X_i \leftarrow (\alpha_i, \beta_i, \gamma_i)$.
- ❑ Intuitively, small changes on Euler angles on adjacent frames indicates better smoothness.
- ❑ We define a simple smoothness energy (similar to [Li et al. TOG12], but without considering rotational symmetry):

$$C_S = \sum_{i} \sum_{j \in N(i)} [(\alpha_i - \alpha_j)^2 + (\beta_i - \beta_j)^2 + (\gamma_i - \gamma_j)^2]$$

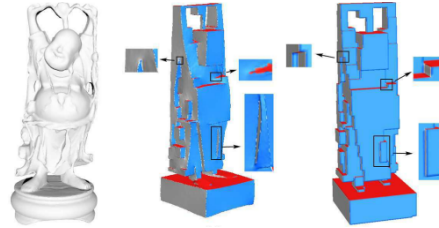## Results and Comparisons: Polycube Construction

Compared with [He et al. SMI09]
- ❑ Our constructed polycube domains are much simpler
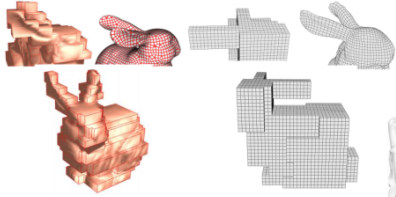
Compared with [Gregson et al. SGP11]
- ❑ Our algorithm is more robust on complex models.

Results and Comparisons: Mapping Distortion

Mapping distortion can measured using the quality of the constructed hexahedral mesh.

A few common criteria on element shape (*angle distortion*) and element uniformity (*volume distortion*):

- ❑ Scaled Jacobian ζ
- ❑ Dihedral angles (the average value α and standard deviation $\sigma{\downarrow}\alpha$)
- ❑ Volume distortion $D{\downarrow}v$
- ❑ # of sin...
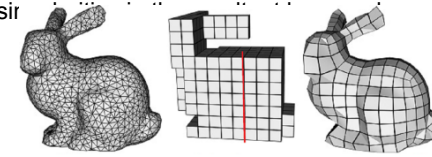
[W. Yu, K. Zhang, S. Wan, X. Li, "Optimizing Polycube Domain Construction for Hexahedral Remeshing," Computer-aided Design, (SIAM/ACM Conference on Geometric & Physical Modeling GD/SPM13), Vol. 46, Pages 258-68, 2013.]

Results and Comparisons: Hexahedral Meshing

Models	#Hexes	$\bar{\zeta}$	$\bar{\alpha}\ /\ \sigma_\alpha$	D_v	$D_g (10^{-7})$	N_h
Bunny [Gregson et al. 2011]	82k	0.930	89.99 / 29.97	-	-	405
Bunny [Li et al 2012]	134k	0.935	89.99 / 27.79	-	-	234
Bunny (ours)	80k	0.938	89.99 / 11.43	0.997	0.04	211
Rocker-arm [Nieser et al. 2011]	36k	0.950	90.00 / 8.40	-	-	-
Rocker-arm [Gregson et al. 2011]	18K	0.899	-	-	-	-
Rocker-arm [Li et al. 2012]	11K	0.866	89.98 / 37.31	-	-	866
Rocker-arm (ours)	18k	0.931	90.00 / 12.75	0.997	0.02	200
Fertility [Gregson et al. 2011]	20k	0.911	90.00 / 29.62	-	-	432
Fertility [Li et al. 2012]	14K	0.911	90.00 / 29.36	-	-	339
Fertility (ours)	18k	0.914	89.99 / 10.41	0.993	4.23	366
Hand [Nieser et al. 2011]	5k	-	90.00 / 10.30	-	-	-
Hand [Gregson et al. 2011]	12k	0.928	-	-	-	-
Hand (ours)	10k	0.937	89.88 / 12.88	0.994	2.06	110
3-Torus (ours)	25k	0.927	89.99 / 10.31	0.996	2.36	944
Kitten (ours)	16k	0.923	89.98 / 12.18	0.997	0.12	941

**vs** ❑ Gregson, Sheffer, and Zhang. All-hex mesh generation via volumetric polycube deformation. CGF, 30(5), 2011.

❑ Nieser, Reitebuch, and Polthier. Cubecover parameterization of 3d volumes. CGF, 30(5), 2011.

❑ Li, Liu, Xu, Wang, and Guo. All-hex meshing using singularity-restricted Field. ACM Trans. Graph., November 2012.

Results and Comparisons: Hexahedral Meshing

Models	#Hexes	$\bar{\zeta}$	$\bar{\alpha}\ /\ \sigma_\alpha$	D_v	$D_g (10^{-7})$	N_h
Bunny [Gregson et al. 2011]	82k	0.930	89.99 / 29.97	-	-	405
Bunny [Li et al 2012]	134k	0.935	89.99 / 27.79	-	-	234
Bunny (ours)	80k	0.938	89.99 / 11.43	0.997	0.04	211
Rocker-arm [Nieser et al. 2011]	36k	0.950	90.00 / 8.40	-	-	-
Rocker-arm [Gregson et al. 2011]	18K	0.899	-	-	-	-
Rocker-arm [Li et al. 2012]	11K	0.866	89.98 / 37.31	-	-	866
Rocker-arm (ours)	18k	0.931	90.00 / 12.75	0.997	0.02	200
Fertility [Gregson et al. 2011]	20k	0.911	90.00 / 29.62	-	-	432
Fertility [Li et al. 2012]	14K	0.911	90.00 / 29.36	-	-	339
Fertility (ours)	18k	0.914	89.99 / 10.41	0.993	4.23	366
Hand [Nieser et al. 2011]	5k	-	90.00 / 10.30	-	-	-
Hand [Gregson et al. 2011]	12k	0.928	-	-	-	-
Hand (ours)	10k	0.937	89.88 / 12.88	0.994	2.06	110
3-Torus (ours)	25k	0.927	89.99 / 10.31	0.996	2.36	944
Kitten (ours)	16k	0.923	89.98 / 12.18	0.997	0.12	941

❑ Gregson, Sheffer, and Zhang. All-hex mesh generation via volumetric polycube deformation. CGF, 30(5), 2011.

vs ❑ Nieser, Reitebuch, and Polthier. Cubecover parameterization of 3d volumes. CGF, 30(5), 2011.

❑ Li, Liu, Xu, Wang, and Guo. All-hex meshing using singularity-restricted Field. ACM Trans. Graph., November 2012.

Results and Comparisons: Hexahedral Meshing

Models	#Hexes	$\bar{\zeta}$	$\bar{\alpha}$ / σ_α	D_v	$D_g (10^{-7})$	N_h
Bunny [Gregson et al. 2011]	82k	0.930	89.99 / 29.97	-	-	405
Bunny [Li et al 2012]	134k	0.935	89.99 / 27.79	-	-	234
Bunny (ours)	80k	0.938	89.99 / 11.43	0.997	0.04	211
Rocker-arm [Nieser et al. 2011]	36k	0.950	90.00 / 8.40	-	-	-
Rocker-arm [Gregson et al. 2011]	18K	0.899	-	-	-	-
Rocker-arm [Li et al. 2012]	11K	0.866	89.98 / 37.31	-	-	866
Rocker-arm (ours)	18k	0.931	90.00 / 12.75	0.997	0.02	200
Fertility [Gregson et al. 2011]	20k	0.911	90.00 / 29.62	-	-	432
Fertility [Li et al. 2012]	14K	0.911	90.00 / 29.36	-	-	339
Fertility (ours)	18k	0.914	89.99 / 10.41	0.993	4.23	366
Hand [Nieser et al. 2011]	5k	-	90.00 / 10.30	-	-	-
Hand [Gregson et al. 2011]	12k	0.928	-	-	-	-
Hand (ours)	10k	0.937	89.88 / 12.88	0.994	2.06	110
3-Torus (ours)	25k	0.927	89.99 / 10.31	0.996	2.36	944
Kitten (ours)	16k	0.923	89.98 / 12.18	0.997	0.12	941

- ❑ Gregson, Sheffer, and Zhang. All-hex mesh generation via volumetric polycube deformation. CGF, 30(5), 2011.
- ❑ Nieser, Reitebuch, and Polthier. Cubecover parameterization of 3d volumes. CGF, 30(5), 2011.
- ❑ Li, Liu, Xu, Wang, and Guo. All-hex meshing using singularity-restricted Field. ACM Trans. Graph., November 2012.

vs

Video: Hexahedral Meshing Results
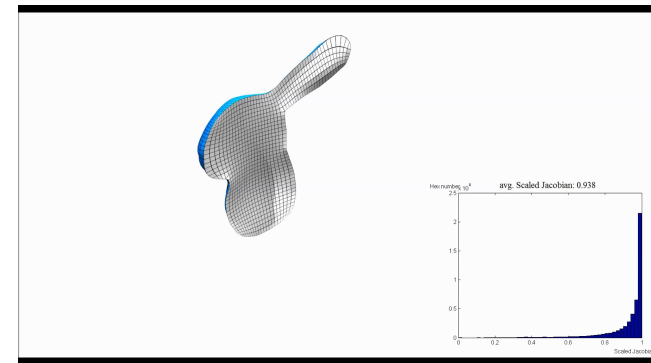
[Video]

[W. Yu, K. Zhang, S. Wan, X. Li, "Optimizing Polycube Domain Construction for Hexahedral Remeshing," Computer-aided Design, (SIAM/ACM Conference on Geometric & Physical Modeling GD/SPM13), Vol. 46, Pages 258-68, 2013.]
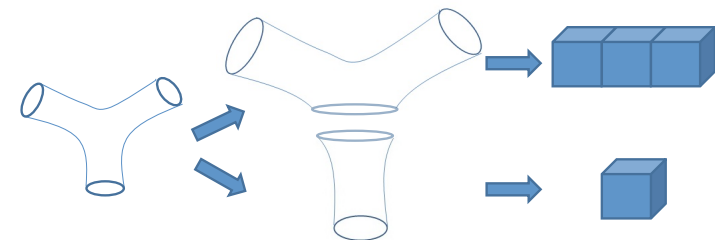

Generalized Polycube (GPC)

- ❑ [Li et al. SMI10] [Li et al. TVCG13]
- ❑ A GPC is a 3D manifold topologically glued by a set of cubes, where
  - ❑ Any pair of facets can be glued
  - ❑ Axis-alignment not required
  - ❑ Realization in 3D space not require
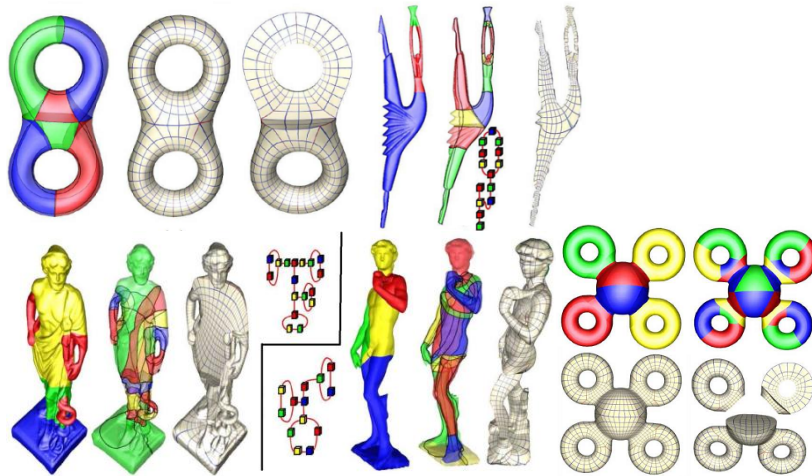 - ❑ Represented by a GPC graph

---
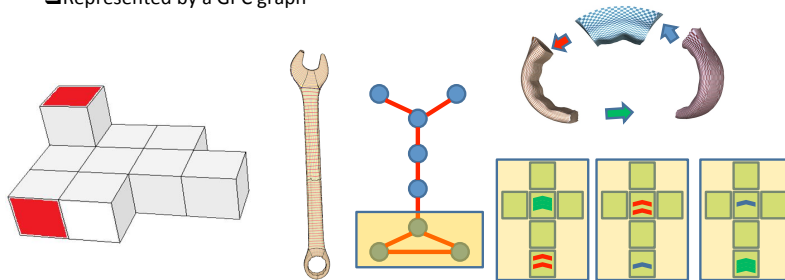
A Topological GPC Construction Approach

- ❑ [Li et al. SMI10] [Li et al. TVCG13]
- ❑ By a topological cube decomposition generated based on the surface pants decomposition
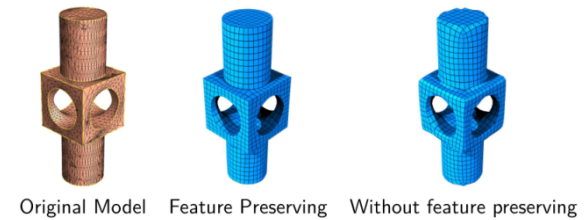

Bo Li, Xin Li, Kexiang Wang, Hong Qin, "Surface Mesh to Volumetric Spline Conversion with Generalized Poly-cubes," IEEE Trans. on Visualization and Computer Graphics (TVCG), 2013.

Some GPC Parameterization Results

Applications

G. Patanè, X.D. Gu, **X.S. Li**

Limitations of Parameterization on Polycube Domains

- ❑ Big distortion near polycube corners.
- ❑ Constructing an Optimal Polycube/GPC Domain which Minimizes the Mapping Distortion is still challenging
  - ❑ Now people solve them separately;
  - ❑ Optimizing them simultaneously is very expensive
- ❑ Modeling complex feature curves on polycube domain may be challenging

Original Model   Feature Preserving   Without feature preserving

Contents

1) Shape Analysis and Retrieval
2) Medical Applications
   a. Spatiotemporal Parameterization of Medical Scans → Respiratory Motion Modeling in Lung Tumor Radiotherapy
   b. Brain Matching and Analysis
   c. 3D Body Scanning for Medical Diabetes Diagnosis
3) Forensic Skull Restoration and Facial Reconstruction
4) Optimal Autonomous Robotic Pipeline Inspection Planning

Shape Comparison and Retrieval

With least-distorted registration, we can measure bending difference and stretching ratio

Mean curvature: H_1

Mean curvature: H_2

Bending difference: $\delta H = H_1 - H_2$

Stretching ratio: $\lambda = A_1 / A_2$
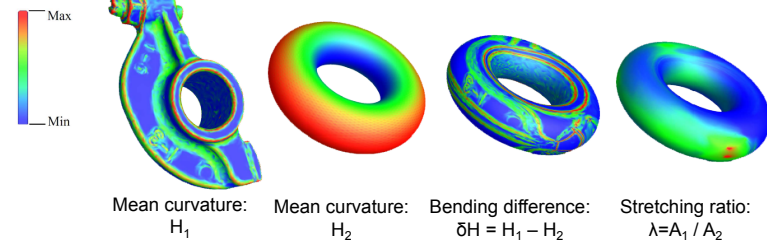
Conformal Representation Theory:

Shape difference : $D = \int_{S1/2} 1 \equiv (\delta H \tau_2 + \lambda \tau_2) ds$

[Li, Bao, Guo, Jin, Gu, Qin, Globally Optimal Surface Mapping for Surfaces with Arbitrary Topology, IEEE Transactions on Visualization and Computer Graphics, 2008]

(please check [Li et al. TVCG' 08] for details)

Shape Comparison and Retrieval

Motion and deformation analysis for temporal sequences

deformation energy
→
shape difference
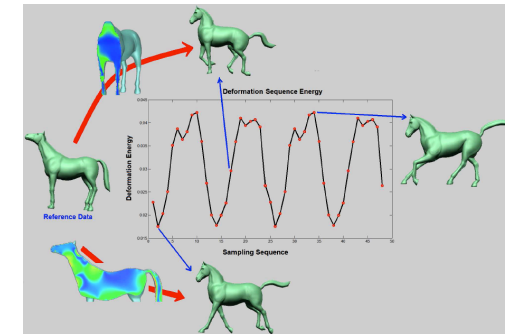
[Li, Guo, Wang, He, Gu, Qin, "Meshless Harmonic Volumetric Mapping using Fundamental Solution Methods," IEEE Transactions on Automation Science and Engineering (TASE), 6(3):409 - 422, 2009]

(please check [Li et al. TVCG' 08] for details)

Shape Comparison and Retrieval
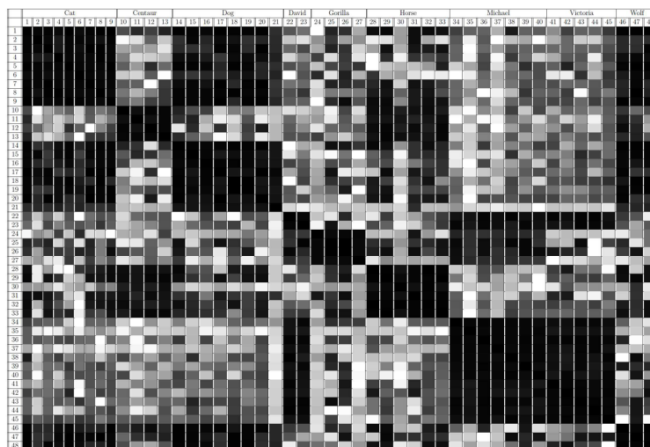
Shape comparison of 48 models in the TOSCA dataset.
- **Black** indicates the smaller difference.
- **Black blocks** indicate similar groups of models.

[W. Yu and X. Li, "Computing 3D Shape Guarding and Star Decomposition," Computer Graphics Forum 2011]

(please check [Li et al. TVCG' 08] for details)

Motion Modeling for Radiotherapy Management

- Motion Modeling for Lung Cancer Radiotherapy:
  - Most lung-cancer (most common cause of cancer-related deaths in the US) patients will take Radiotherapy Treatment, in which external beam applies radiation on the tumor
  - Goal: to radiate only the tumor; avoid damaging surrounding tissue/organs
  - Difficulty in capturing their geometry and trajectory:
    - Complicated spatial relationship of the tumor with normal tissue structures (spinal cord, heart, trachea…)
    - Respiratory cycle involves movement of normal tissues → heavily influences the tumor's motion and its deformation
  - With the advancing hardware to shape the radiation from different directions
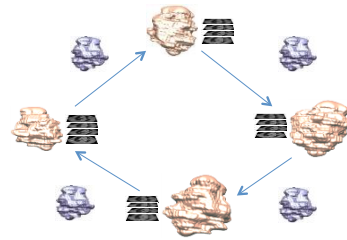 - → Pressing need for Radiotherapy Management

[Iyengar, Li et al. "Toward More Precise Radiotherapy Treatment of Lung Tumors," IEEE Computer, Vol. 45, Issue 1, pp. 59-65, 2012]
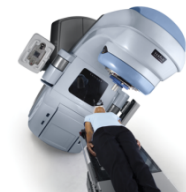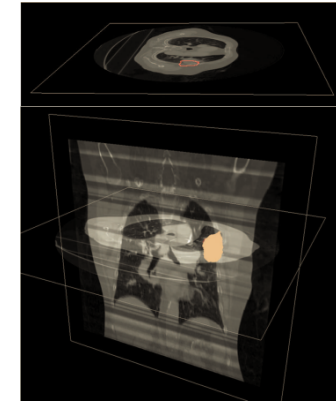
4D Parameterization Problem

❑ Input:
  ❑ 4D images (a sequence of volumetric CT images) $I_1, I_2, \ldots I_n$ scanned during several respiratory cycles
❑ Output:
  ❑ A 4D parameterization of the irradiation volume $V(t,x,y,z)$
    ❑ Given t → the location + shape of corresponding tumor/organs

❑ The reconstructed deformation model
  ❑ Can analyze the motion and deformation of the organs during the respirations $V(t,x,y,z), t<n$
  ❑ Can predict the geometry and trajectory of the organs, and guide the radiation beam $V(t,x,y,z), t>n$

Computation Pipeline

A computational framework:

1) **Segment geometries from images (important volume regions, important iso-surfaces)**
2) Build Adaptive FEM meshes
3) Compute cross-volumetric mapping and the temporally deforming model

---
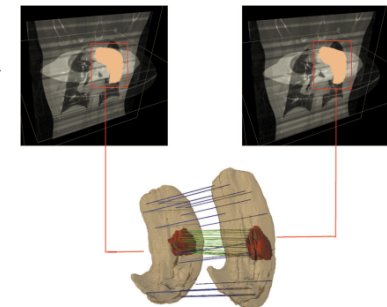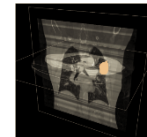
Computation Pipeline

A computational framework:

1) Segment geometries from images (important volume regions, important iso-surfaces)
2) **Build Adaptive FEM meshes**
3) Compute cross-volumetric mapping and the temporally deforming model

---

Computation Pipeline

A computational framework:

1) Segment geometries from images (important volume regions, important iso-surfaces)
2) Build Adaptive FEM meshes
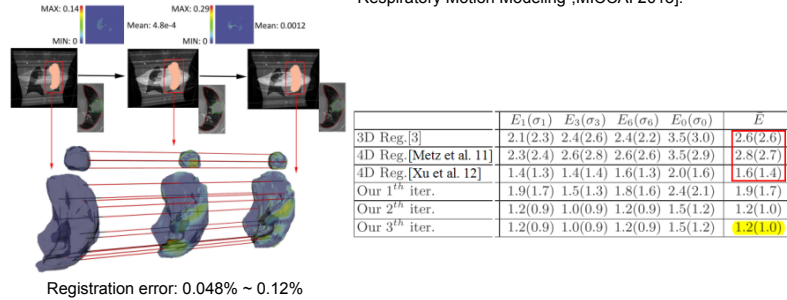3) **Compute cross-volumetric mapping and the temporally deforming model**

[H. Xu, X. Li, "Consistent Feature-aligned 4D Image Registration for Respiratory Motion Modeling," International Symposium on Biomedical Imaging, 2013.]

## Matching Accuracy on Motion Modeling

A 4D (3D + t) matching algorithm to register the dynamic volume image scans: the constructed deformable geometry can approximate the respiratory motion of the lung tumor and organs in the radiotherapy treatment planning and optimization

[Xu and Li, "A Symmetric 4D Registration Algorithm for Respiratory Motion Modeling",MICCAI 2013].

	$E_1(\sigma_1)$	$E_3(\sigma_3)$	$E_6(\sigma_6)$	$E_0(\sigma_0)$	$\bar{E}$
3D Reg.[3]	2.1(2.3)	2.4(2.6)	2.4(2.2)	3.5(3.0)	2.6(2.6)
4D Reg.[Metz et al. 11]	2.3(2.4)	2.6(2.8)	2.6(2.6)	3.5(2.9)	2.8(2.7)
4D Reg.[Xu et al. 12]	1.4(1.3)	1.4(1.4)	1.6(1.3)	2.0(1.6)	1.6(1.4)
Our 1th iter.	1.9(1.7)	1.5(1.3)	1.8(1.6)	2.4(2.1)	1.9(1.7)
Our 2th iter.	1.2(0.9)	1.0(0.9)	1.2(0.9)	1.5(1.2)	1.2(1.0)
Our 3th iter.	1.2(0.9)	1.0(0.9)	1.2(0.9)	1.5(1.2)	1.2(1.0)

Registration error: 0.048% ~ 0.12%

DIR-LAB Benchmark: Anatomical landmarks provided for matching accuracy assessment.

Matching Accuracy on Motion Modeling

(a) S_1 from I_1 (b) $F^{1,6}(S_1)$ on I_6 (c) I_1 (d) $d(F^{1,6}(I_1), I_1)$ (e) $H(F^{1,6}(I_1), I_6)$
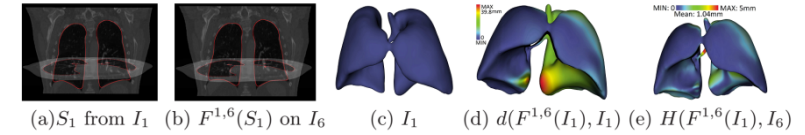
	$D_1(\sigma_1)$	$D_2(\sigma_2)$	$D_3(\sigma_3)$	$D_4(\sigma_4)$	$D_5(\sigma_5)$	$D_6(\sigma_6)$	$D_7(\sigma_7)$	$D_8(\sigma_8)$	$D_9(\sigma_9)$	$D_0(\sigma_0)$	$\bar{D}$
3D Reg.[2]	3.6(2.3)	2.3(1.8)	2.1(1.7)	2.2(2.0)	2.4(2.3)	2.9(2.4)	2.8(2.3)	2.1(1.7)	2.1(1.5)	2.7(2.1)	2.5
4D Reg.[2]	3.8(2.3)	2.6(2.0)	2.2(1.8)	2.2(2.0)	2.5(2.2)	2.9(2.3)	2.8(2.3)	2.2(1.8)	2.2(1.5)	2.8(2.2)	2.6
4D Reg.[7]	2.1(1.6)	1.8(1.5)	1.6(1.3)	1.6(1.2)	2.1(1.4)	2.4(1.7)	2.1(1.6)	1.7(1.0)	1.6(1.2)	1.9(1.6)	1.9
Our 1th iter.	1.9(1.4)	1.6(1.2)	1.6(1.3)	1.8(1.5)	2.0(1.7)	2.0(1.7)	2.0(1.6)	1.6(1.2)	1.7(1.1)	2.2(1.6)	1.9
Our 2th iter.	1.1(0.8)	1.2(0.9)	1.3(0.9)	1.2(0.8)	1.5(0.9)	1.5(1.0)	1.4(1.1)	1.1(0.6)	1.2(0.8)	1.2(0.8)	1.3
Our 3th iter.	1.1(0.8)	1.2(0.9)	1.3(0.9)	1.2(0.8)	1.5(0.9)	1.5(1.0)	1.4(1.1)	1.1(0.6)	1.2(0.8)	1.2(0.8)	1.3

POPIVAND Benchmark: Anatomical landmarks provided for matching accuracy assessment.

[Xu and Li, "A Symmetric 4D Registration Algorithm for Respiratory Motion Modeling," MICCAI 2013].

A Motion Modeling Result

A 4D (3D + t) matching algorithm to register the dynamic volume image scans: the constructed deformable geometry can approximate the respiratory motion of the lung tumor and organs in the radiotherapy treatment planning and optimization
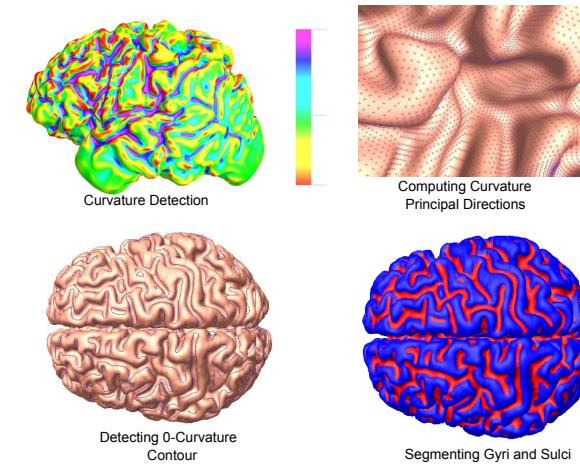

Tracking the Lung's Respiratory

Motion Using a Parameteric

Deforming 3D Surface

[Xu and Li, "A Symmetric 4D Registration Algorithm for Respiratory Motion Modeling," MICCAI 2013].
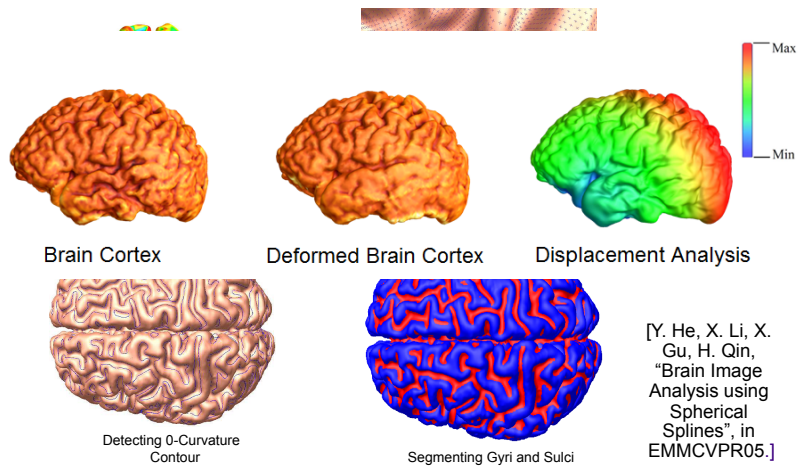
For more details, please visit:
http://www.ece.lsu.edu/xinli/CBiomedicine/TumorTracking.html

Brain Cortex Modeling, Matching, and Analysis

Curvature Detection

Computing Curvature Principal Directions

Detecting 0-Curvature Contour

Segmenting Gyri and Sulci

[Y. He, X. Li, X. Gu, H. Qin, "Brain Image Analysis using Spherical Splines", in EMMCVPR05.]
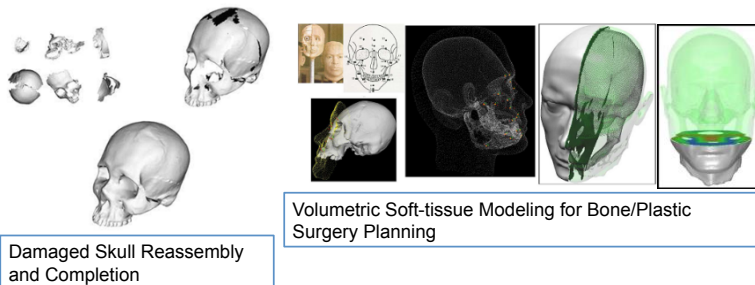
Brain Cortex Modeling, Matching, and Analysis

Brain Cortex

Deformed Brain Cortex

Displacement Analysis

Detecting 0-Curvature Contour

Segmenting Gyri and Sulci

[Y. He, X. Li, X. Gu, H. Qin, "Brain Image Analysis using Spherical Splines", in EMMCVPR05.]

3D Body Scanning for Diabetes Diagnosis

Real-time Human Body Scan

Reconstructed Digital Model
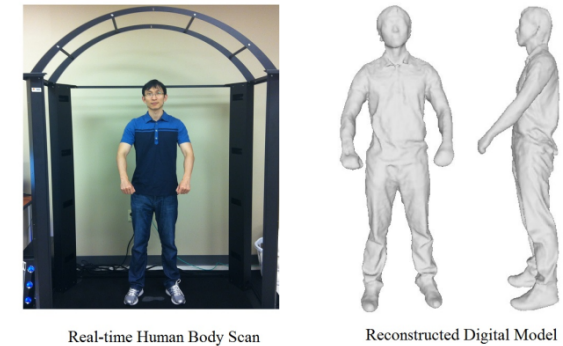
❑ Inexpensive real-time 3D body scanning system
❑ Digital body size and volume measurement can be conducted to replace the traditional physical measurement.
❑ Desirable accuracy (circumference errors < 2cm)
❑ Efficient measurement and posture/motion analysis on diabetes patients.

Skull and Facial Modeling and Restoration

❑ Restoring Fragmented Geometries, Synthesizing Constrained Geometry

Volumetric Soft-tissue Modeling for Bone/Plastic Surgery Planning

Damaged Skull Reassembly and Completion

❑ Shape Modeling Problems
    ❑ Fragmented skull reassembly and damaged skull completion
    ❑ Facial tissue reconstruction from skull

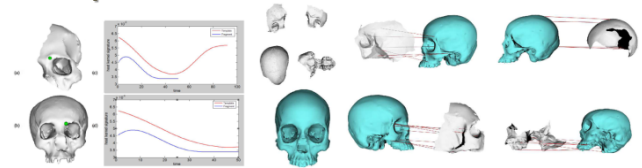## Skull Reassembly and Completion

❑ Fragmented Skull Reassembly
    ❑ Fragments reassembly guided by template:
        ❑ Partial cross-shape mapping (between template and fragments)

[Wei, Yu, Li, "Skull Assembly and Completion using Template-based Surface Matching," 3DIMPVT 2011]

Skull Reassembly and Completion

❏ Fragmented Skull Reassembly
    ❏ Fragments reassembly guided by template:
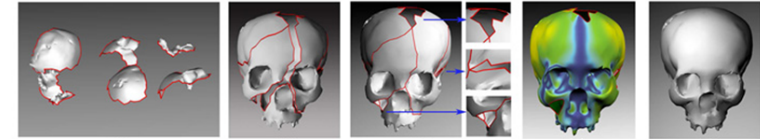   ❏ Partial cross-shape mapping (between template and fragments)
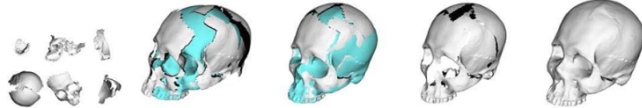
[Wei, Yu, Li, "Skull Assembly and Completion using Template-based Surface Matching," 3DIMPVT 2011]

[Yu, Li, "Fragmented Skull Modeling using Heat Kernels," GMP 2012.]

Skull Reassembly and Completion

❏ Fragmented Skull Reassembly
    ❏ Fragments reassembly guided by template:
        ❏ Partial cross-shape mapping (between template and fragments)
    ❏ Fragments reassembly guided by break-region analysis
        ❏ Partial region matching (between adjacent fragments)

[Yin, Wei, Manhein, Li, "An Automatic Assembly and Completion Framework for Fragmented Skulls," ICCV 2011]

Skull Reassembly and Completion

❏ Fragmented Skull Reassembly
    ❏ Fragments reassembly guided by template:
        ❏ Partial cross-shape mapping (between template and fragments)
    ❏ Fragments reassembly guided by break-curve analysis
        ❏ Partial region matching (between adjacent fragments)
❏ Damaged Skull Completion
    ❏ Iterative symmetry + template guided model completion
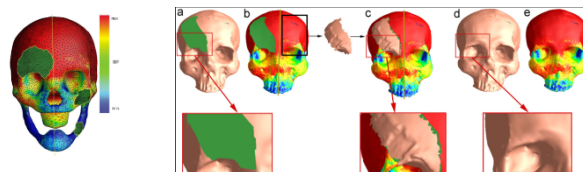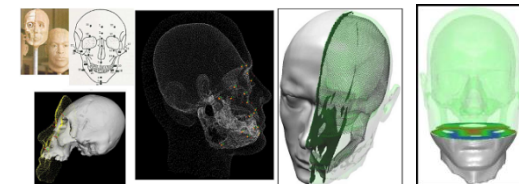

Facial Tissue Modeling
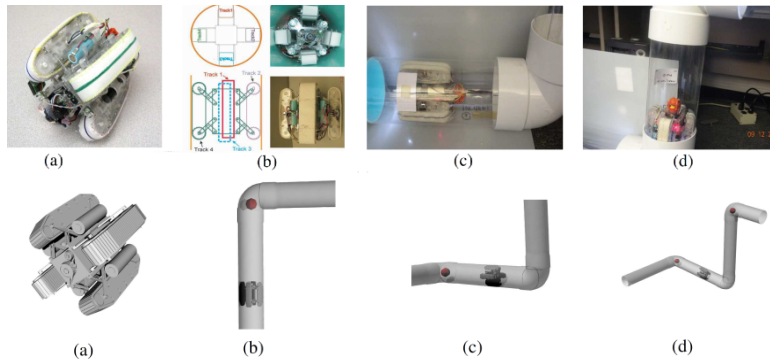
❏ Current Practice: Manual Reconstruction using clay models

Image from http://www.joshharker.com/?page_id=81
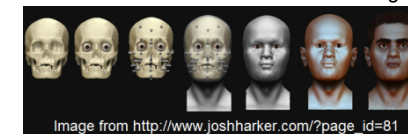
❏ Soft-tissue modeling based on volumetric mapping, using cross-skull surface matching as boundary constraints

Autonomous Robotic Exploration Planning

X. Li, W. Yu, X. Lin, and S. S. Iyengar. "On Optimizing Autonomous Pipeline Inspection in 3D Environment,"
IEEE Transactions on Robotics (TRO), vol. 28, no. 1, pp. 223-233, 2012.

Acknowledgments